



HAL
open science

Plasmonic Cu nanoparticles inclusion in ZnO and Cu₂O matrices for enhanced photoconversion of all-oxide optoelectronics

Yerila Rodríguez-Martínez

► **To cite this version:**

Yerila Rodríguez-Martínez. Plasmonic Cu nanoparticles inclusion in ZnO and Cu₂O matrices for enhanced photoconversion of all-oxide optoelectronics. Materials Science [cond-mat.mtrl-sci]. Université de Lorraine; Universidad de La Habana (Cuba), 2023. English. NNT : 2023LORR0208 . tel-04537047

HAL Id: tel-04537047

<https://hal.univ-lorraine.fr/tel-04537047v1>

Submitted on 29 Jan 2025

HAL is a multi-disciplinary open access archive for the deposit and dissemination of scientific research documents, whether they are published or not. The documents may come from teaching and research institutions in France or abroad, or from public or private research centers.

L'archive ouverte pluridisciplinaire **HAL**, est destinée au dépôt et à la diffusion de documents scientifiques de niveau recherche, publiés ou non, émanant des établissements d'enseignement et de recherche français ou étrangers, des laboratoires publics ou privés.



**UNIVERSITÉ
DE LORRAINE**

**BIBLIOTHÈQUES
UNIVERSITAIRES**

AVERTISSEMENT

Ce document est le fruit d'un long travail approuvé par le jury de soutenance et mis à disposition de l'ensemble de la communauté universitaire élargie.

Il est soumis à la propriété intellectuelle de l'auteur. Ceci implique une obligation de citation et de référencement lors de l'utilisation de ce document.

D'autre part, toute contrefaçon, plagiat, reproduction illicite encourt une poursuite pénale.

Contact bibliothèque : ddoc-theses-contact@univ-lorraine.fr
(Cette adresse ne permet pas de contacter les auteurs)

LIENS

Code de la Propriété Intellectuelle. articles L 122. 4

Code de la Propriété Intellectuelle. articles L 335.2- L 335.10

http://www.cfcopies.com/V2/leg/leg_droi.php

<http://www.culture.gouv.fr/culture/infos-pratiques/droits/protection.htm>

THÈSE

pour l'obtention du titre de

DOCTEUR DE L'UNIVERSITÉ DE LORRAINE

Spécialité : Science des Matériaux

DOCTEUR DE L'UNIVERSITÉ DE LA HAVANE

Spécialité : Sciences Physiques

Présentée par

Yerila RODRÍGUEZ MARTÍNEZ

Plasmonic Cu nanoparticles inclusion in ZnO and Cu₂O matrices for enhanced photoconversion of all-oxide optoelectronics

Soutenue publiquement le 7 décembre 2023 à Nancy devant le jury composé de :

| | | |
|-----------------------|--------------------|---|
| Directeurs de thèse : | Lídice VAILLANT | Directrice de recherches, IMRE Université de La Havane, La Havane |
| | David HORWAT | Professeur des universités, IJL Université de Lorraine, Nancy |
| Rapporteurs : | Angélique BOUSQUET | Maître de Conférences, ICCF Université Clermont Auvergne, Aubière |
| | Alberto VOMIERO | Professeur Université de technologie de Luleå, Luleå |
| Président : | Nicolas MARTIN | Professeur des universités, FEMTO ST Université de Franche-Comté, Besançon |
| Membre invité : | Claudia DE MELO | Maître de Conférences, ICMN Université d'Orléans, Orléans |

THESIS

in order to become

DOCTOR FROM UNIVERSITY OF LORRAINE

Academic field: Materials Science

DOCTOR FROM UNIVERSITY OF HAVANA

Academic field: Physics Sciences

Presented by

Yerila RODRÍGUEZ MARTÍNEZ

Plasmonic Cu nanoparticles inclusion in ZnO and Cu₂O matrices for enhanced photoconversion of all-oxide optoelectronics

Defended on December 7th, 2023, in Nancy, in front of the following committee:

| | | |
|-----------------|--------------------|--|
| Supervisors: | Lídice VAILLANT | Titular researcher, IMRE University of Havana, Havana |
| | David HORWAT | Professor, IJL University of Lorraine, Nancy |
| Reviewers: | Angélique BOUSQUET | Associate Professor, ICCF University Clermont Auvergne, Aubière |
| | Alberto VOMIERO | Professor Luleå University of Technology, Luleå |
| President: | Nicolas MARTIN | Professor, FEMTO ST University of Franche-Comté, Besançon |
| Invited member: | Claudia DE MELO | Associate Professor, ICMN University of Orléans, Orléans |

Abstract

In this work we present the results on in-situ growth of plasmonic copper (Cu) nanoparticles (NPs) into a p-Cu₂O matrix by using reactive magnetron sputtering of a Cu target and adjusting the oxygen flowrate. It was possible to observe, for oxygen-poor conditions, the formation of CuNPs-Cu₂O composites presenting the signature of the localized surface plasmon resonance (LSPR) phenomenon. Devices based on the studied nanocomposites interfaced with zinc oxide (ZnO) were characterized by J-V and spectral photocurrent measurements, showing a photocurrent density increase under optical illumination as a result of the plasmonic particles incorporation and consequent hot carriers injection. In the second part of the manuscript, the results about the rapid thermal annealing (RTA) of the CuNPs-Cu₂O composites under oxygen-poor conditions and their properties evolution when temperature increases are presented. At temperature higher than 150 °C it was possible to see a copper segregation towards the surface, increase in the crystal preferential orientation of Cu₂O and improvement of the LSPR signal. Electrical response of devices constituted by the composite layers interfaced with ZnO and annealed at 200 °C showed a further increase in the photocurrent resulting from the LSPR of Cu NPs at the devices surface. Finally, the synthesis of Cu nanoparticles through a gas aggregation source (GAS) and the subsequent fabrication of ZnO-CuNPs multilayer structure with plasmonic response were studied. The resulted composite revealed LSPR response and the presence of Cu particles acting as nucleation points for highly oriented ZnO conical grains.

Résumé

Dans ce travail, nous présentons dans une première partie les résultats de la croissance in situ de nanoparticules (NPs) plasmoniques de cuivre (Cu) dans une matrice de p-Cu₂O en utilisant la pulvérisation cathodique magnétron réactive d'une cible de Cu et en ajustant le débit d'oxygène. Il a été possible d'observer, dans des conditions pauvres en oxygène, la formation de films composites CuNPs-Cu₂O présentant la signature du phénomène de résonance plasmon de surface localisée (LSPR). Les dispositifs basés sur les nanocomposites étudiés interfacés avec de l'oxyde de zinc (ZnO) ont été caractérisés par des mesures J-V et des mesures spectrales de photocourant, montrant une augmentation de la densité de photocourant sous illumination optique comme conséquence de l'incorporation des particules plasmoniques et de l'injection conséquente de porteurs chauds. La deuxième partie du manuscrit présente les résultats du recuit thermique rapide (RTA) des films composites CuNPs-Cu₂O dans des conditions pauvres en oxygène et l'évolution de leurs propriétés lorsque la température augmente. Après un recuit à une température de recuit supérieure à 150 °C, il a été possible de constater une ségrégation du cuivre vers la surface, une augmentation de l'orientation cristalline préférentielle du Cu₂O et une amélioration du signal LSPR. La réponse électrique des dispositifs constitués des composites interfacés avec ZnO puis recuits à 200 °C a montré une augmentation supplémentaire du photocourant en raison de la LSPR des nanoparticules de Cu à la surface des dispositifs. Enfin, la synthèse de nanoparticules de Cu par une source d'agrégation de gaz (GAS) et la fabrication ultérieure de structures multicouches ZnO-CuNPs avec une réponse plasmonique ont été étudiées. Le composite obtenu a révélé une réponse LSPR et la présence de particules de Cu agissant comme points de nucléation pour des grains coniques de ZnO hautement orientés.

Résumé étendu

Le taux élevé de consommation d'énergie actuel est indéniablement l'un des défis les plus pressants de l'humanité, au même titre que les conséquences environnementales des activités humaines et l'épuisement des combustibles fossiles. Pour résoudre ces problèmes, une solution viable consiste à développer et à utiliser des dispositifs alimentés par des sources d'énergie renouvelables, comme les cellules solaires et d'autres outils optoélectroniques utilisés pour la surveillance environnementale et industrielle, la production d'hydrogène par photocatalyse et la séparation de l'eau. Toutefois, la création de ces dispositifs pose plusieurs problèmes, notamment la nécessité d'utiliser des matériaux non toxiques et abondants sur Terre, ainsi que celle de diminuer des coûts de production pour permettre de rendre la technologie plus accessible. En outre, les recherches en cours visent à améliorer l'efficacité de ces dispositifs en acquérant une meilleure compréhension des processus physiques sous-jacents.

Les semi-conducteurs à base d'oxydes métalliques constituent une catégorie prometteuse de matériaux pour la construction de dispositifs optoélectroniques. Ils offrent plusieurs avantages, notamment la non-toxicité, la rentabilité et des propriétés électriques et optiques favorables. Parmi ces matériaux, l'oxyde de cuivre Cu_2O a suscité un grand intérêt en raison de sa capacité à absorber la lumière visible et de sa conductivité électrique de type p. Diverses méthodes peuvent être employées pour synthétiser Cu_2O , qu'elles soient ou non basées sur le vide. Bien que les prévisions théoriques suggèrent des rendements de conversion d'énergie élevés d'environ 20 % pour les dispositifs de photo-conversion basés sur un absorbeur Cu_2O , les performances pratiques sont actuellement inférieures à environ 8,4 %, ce qui indique qu'il est possible d'améliorer leur conception et leur fonctionnalité. De nombreuses études portent sur des hétérojonctions à base de Cu_2O associées à des matériaux tels que l'oxyde de zinc (ZnO), un matériau de type n bien connu, doté d'une large bande interdite, d'une énergie de liaison des

excitons élevée et d'excellentes propriétés photoconductrices. Ces caractéristiques le rendent prometteur pour les cellules solaires et d'autres applications optoélectroniques.

Par ailleurs, les nanocomposites plasmoniques, qui se composent d'une matrice semi-conductrice dans laquelle sont intégrées des nanoparticules métalliques (NPs), ont attiré l'attention pour la collecte d'énergie. Ces nanocomposites combinent les propriétés optiques et électriques des matériaux hôtes avec les effets quantiques présentés par les particules à l'échelle nanométrique, tels que le phénomène de résonance plasmon de surface localisée (LSPR). Alors que les recherches antérieures dans le domaine de la plasmonique se sont concentrées sur des métaux coûteux comme l'or (Au) et l'argent (Ag) en raison, respectivement, d'une excellente stabilité chimique et d'une forte réponse plasmonique, des alternatives plus économiques comme le cuivre (Cu) sont apparues comme des options intéressantes. Le cuivre possède des propriétés plasmoniques dans le spectre visible et offre des avantages tels que l'abondance, la non-toxicité et la recyclabilité. Le cuivre s'est également révélé prometteur dans le transfert efficace de porteurs de charge "chauds" vers divers semi-conducteurs à base d'oxyde métallique, ce qui élargit la gamme de ses applications potentielles.

L'incorporation de nanoparticules de cuivre métallique dans des dispositifs de photoconversion est le thème central de cette thèse en raison de leur capacité à générer des porteurs de charge supplémentaires par l'effet LSPR lorsqu'ils sont exposés à la lumière, lesquels peuvent ensuite être transférés au semi-conducteur en contact avec elles. Cependant, l'intégration de NP de cuivre métallique dans des oxydes métalliques semi-conducteurs comme le Cu_2O et le ZnO présente des défis complexes, notamment les risques d'agrégation et d'oxydation des particules, qui limitent leur réponse plasmonique. Cela souligne le besoin de techniques de synthèse innovantes.

En résumé, l'objectif principal de cette thèse est de faire croître des nanoparticules plasmoniques de Cu et des semi-conducteurs d'oxyde métallique afin de créer des composites et des hétérostructures multicouches pour des applications optoélectroniques. Diverses conceptions d'hétérostructures de Cu_2O et de ZnO sont explorées afin de déterminer l'emplacement optimal de ces nanoparticules dans les dispositifs de photo-conversion. Le manuscrit est structuré en cinq chapitres, suivis des conclusions générales et des perspectives. Une annexe fournit des informations supplémentaires pour approfondir les résultats présentés.

Le Chapitre 1 présente une vue d'ensemble de l'état de l'art des semi-conducteurs à base d'oxydes métalliques pour applications photovoltaïques, en particulier ZnO et Cu₂O. Un résumé des principales propriétés optiques, structurales et électriques de ces matériaux sera présenté. En outre, le phénomène de résonance plasmon de surface localisée est décrit d'un point de vue général, en mettant l'accent sur son application en optoélectronique, en particulier dans les cellules solaires. Les principales méthodes de dépôt utilisées pour l'inclusion de nanoparticules plasmoniques métalliques et les principaux défis sont également présentés.

Le Chapitre 2 présente une vue d'ensemble de la méthode de pulvérisation utilisée pour produire des couches d'oxydes métalliques et de composites plasmoniques, ainsi que les principes essentiels qui sous-tendent les techniques de caractérisation employées dans l'étude. Les matériaux et les dispositifs étudiés dans cette thèse ont été synthétisés par différentes méthodes. Le dépôt d'oxydes métalliques (ZnO, Cu₂O) et de composites plasmoniques CuNPs-Cu₂O a été réalisé par pulvérisation cathodique magnétron réactive à courant continu, tandis que pour la fabrication de couches multiples de nanoparticules de Cu et ZnO, une source d'agrégation de gaz (GAS) a été intégrée. Le traitement thermique des composites CuNPs-Cu₂O a été effectué à l'aide d'un four de recuit thermique rapide (RTA). La structure cristalline de tous les échantillons a été étudiée par diffraction des rayons X (XRD) et la caractérisation optique a été réalisée par spectrophotométrie UV-Vis-NIR et spectroscopie ellipsométrique. L'analyse de la composition et l'étude de la morphologie des films ont été réalisées par microscopie électronique à balayage (MEB) et microscopie électronique en transmission (MET). La résistivité des films a été calculée en utilisant la méthode de la sonde quatre pointes. La caractérisation des dispositifs a été réalisée à partir des courbes J-V dans l'obscurité et sous intensité lumineuse 1 soleil. Le photocourant spectral (SP) et la spectroscopie d'impédance (IS) ont également permis de comprendre le comportement des dispositifs.

Le Chapitre 3 présente une méthode de synthèse en une seule étape de nanoparticules de cuivre plasmoniques intégrées dans une matrice de Cu₂O semi-conductrice de type p par pulvérisation magnétron réactive à courant continu. En contrôlant le débit d'oxygène pendant le processus de pulvérisation de la cible de cuivre, l'oxydation des atomes de cuivre est limitée, ce qui permet d'obtenir une couche composite CuNPs-Cu₂O. Lorsque le matériau composite est déposé orthogonalement à l'axe de la cible et à un débit d'oxygène de 4 sccm, une croissance en colonnaire avec une orientation préférentielle de la matrice de Cu₂O selon [100] et une faible interconnectivité des particules de Cu sont observées par l'analyse microstructurale [100]. Dans

ce cas, la taille des NPs est estimée à environ 4 nm. D'autre part, lorsque le débit d'oxygène (OFR) est le plus faible, on obtient une matrice nanocristalline avec des nanodomains de cuivre connectés et une taille plus importante (environ 7 nm). Des valeurs de résistivité de l'ordre, respectivement, de 10^{-4} et $10 \Omega \cdot \text{cm}$ pour des OFR de 2 sccm et 4 sccm confirment la présence plus importante de particules de Cu métalliques et leur connexion dans le premier cas. La réponse LSPR est présente dans les deux composites à base de Cu, avec une seule bande d'absorption proche de 2 eV. Les mesures ellipsométriques corroborent le comportement hybride de l'échantillon synthétisé avec une valeur d'OFR inférieure (métallique + plasmonique) et la nature plasmonique de l'échantillon synthétisé avec un de 4 sccm.

L'influence de la position de l'échantillon par rapport à l'axe de la cible de Cu sur les propriétés du film est également analysée. À une plus grande distance entre l'échantillon et l'axe de la cible, pour les deux OFR, la croissance ordonnée de la matrice Cu_2O avec une orientation préférentielle [100] est plus faible, ce qui est associé à une énergie plus faible des ions d'oxygène frappant la surface du film en cours de croissance. En outre, une taille de particules plus faible, attribuée à un rapport de compositions O/Cu plus élevé, et une réponse LSPR plus faible sont observées à cette position. La résistivité des composites dépend également de la position de l'échantillon. Elle atteint des valeurs plus élevées loin de l'axe de la cible et diminue au fur et à mesure que l'échantillon s'en rapproche. Ce comportement est également associé au rapport des atomes O/Cu atterrissant sur la surface du film. Ces résultats sont discutés en relation avec la variation de microstructure des films obtenus.

Deux hétérojonctions semi-transparentes à base de composites ont également été fabriquées par pulvérisation magnétron réactive : n-ZnO/CuNPs- Cu_2O et n-ZnO/CuNPs- $\text{Cu}_2\text{O}/\text{p-Cu}_2\text{O}$. Les hétérojonctions présentent un comportement de redressement selon des mesures électriques macroscopiques. Il a également été démontré que les composites CuNPs- Cu_2O améliorent la photoconversion lorsqu'ils sont insérés à l'interface des hétérojonctions n-ZnO/p- Cu_2O . Cette amélioration est associée à l'injection et à la collecte de porteurs chauds suite à la désexcitation de la LSPR au niveau des nanodomains plasmoniques de Cu et à l'augmentation de l'intensité du champ proche. La méthode présentée peut être facilement transférée à large échelle et est compatible avec l'industrie de la microélectronique.

Le Chapitre 4 étudie le recuit thermique des composites plasmoniques et des hétérostructures à incluant ces composites plasmoniques, en se concentrant sur l'utilisation d'un four à recuit

thermique rapide (RTA) dans des conditions pauvres en oxygène pour limiter l'oxydation des nanoparticules de cuivre et exploiter l'effet LSPR. Ce chapitre comprend une étude complète de la microstructure, de la morphologie, des propriétés optiques, de la caractérisation J-V et des mesures de spectroscopie d'impédance des dispositifs plasmoniques recuits.

Les composites CuNPs-Cu₂O élaborés en utilisant un OFR de 4 sccm ont été traités à différentes températures (150 °C, 200 °C, 250 °C et 300 °C) dans des conditions pauvres en oxygène pour éviter l'oxydation des NPs. Avec l'augmentation de la température, on observe une amélioration de l'orientation préférentielle de la matrice Cu₂O selon [100] ainsi qu'une ségrégation et une coalescence du Cu métallique à la surface du composite. La taille latérale moyenne des particules passe de 90 nm à 150 nm environ avec l'augmentation de la température. Une amélioration de la réponse LSPR est mise en évidence pour les échantillons traités par rapport aux composites non recuits, atteignant une valeur maximale à 200 °C. Un meilleur ordonnancement de la structure cristalline de la matrice Cu₂O est mis en évidence par les calculs d'énergie d'Urbach qui montrent des valeurs plus faibles à mesure que la température augmente, ce qui indique une plus faible densité de défauts structuraux. En outre, un lien est observé entre les propriétés structurales et optiques (intensité de la bande d'absorption plasmon) des composites traités thermiquement et la consommation de la cible. L'étude montre que, dans le cas de cibles érodées, la réponse plasmonique la plus efficace est obtenue lorsque les films sont placés de manière décalée par rapport à l'axe de la cible.

Des dispositifs semi-transparents n-ZnO/CuNPs-Cu₂O et n-ZnO/CuNPs-Cu₂O/p-Cu₂O ont également été traités thermiquement à 200 °C dans les mêmes conditions pauvres en oxygène. Des hétérostructures n-ZnO/p-Cu₂O présentant des particules de Cu à la surface (n-ZnO/p-Cu₂O/CuNPs), en interface avec le contact arrière en or, ont été obtenues dans les deux cas. Les mesures électriques (J-V) montrent une densité de courant de court-circuit cinq fois supérieure à la valeur obtenue pour un dispositif de référence en n-ZnO/p-Cu₂O lorsque le dispositif modifié thermiquement présente une plus grande quantité de NP de Cu à la surface (dispositif recuit n-ZnO/CuNPs-Cu₂O). Ce résultat est associé à une injection plus importante de porteurs chauds, mise en évidence par une densité de courant en polarisation inverse plus élevée. Des mesures d'impédance et une modélisation ont été réalisées, indiquant un lien étroit entre des valeurs de densité de courant en court-circuit, J_{sc} plus élevées et la présence de NP de Cu plasmoniques induisant un transfert de charges plus important. Parallèlement, un lien a été établi entre, d'une part, la minimisation des défauts et la recombinaison et, d'autre part,

l'obtention d'une valeur plus élevée de tension en circuit ouvert, V_{oc} . Enfin, il a été démontré que les particules plasmoniques positionnées plus près du contact arrière, après recuit, présentent une meilleure génération de photocourant par rapport aux particules situées plus près de la jonction p-n.

Le Chapitre 5 décrit la synthèse de nanoparticules de cuivre à l'aide d'une source d'agrégation de gaz (GAS) et la construction de structures multicouches ZnO-CuNPs par croissance séquentielle de films minces de ZnO par pulvérisation réactive et de nanoparticules de Cu par GAS. Il analyse les variations de la densité des nanoparticules pendant le dépôt et inclut des analyses HRTEM et EELS pour confirmer la formation réussie de l'hétérostructure. L'ellipsométrie spectroscopique est utilisée pour valider la présence de bandes d'absorption liées au plasmons de surface et associées aux nanoparticules de Cu.

Il est démontré que la densité des particules augmente avec le temps de dépôt dans les deux cas, avec une augmentation moins abrupte dans le cas de rotation du porte-substrats en raison de l'arrivée d'une plus petite quantité de nanoparticules par unité de temps. Par ailleurs, la taille latérale des particules n'est pas affectée par le temps de dépôt, présentant des distributions bimodales avec des pics autour de 2,5 nm et 11,5 nm dans tous les échantillons. Cette étude donne un aperçu des possibilités de contrôler et de manipuler la distribution des nanoparticules dans la future structure multicouche.

Les structures multicouches ZnO-CuNPs présentant des caractéristiques plasmoniques ont été obtenues par un processus de croissance séquentiel, impliquant le dépôt de couches minces de ZnO par pulvérisation magnétron réactive et l'introduction de nanoparticules de Cu par le biais de la GAS. Les analyses HRTEM et EELS ont permis de confirmer la formation réussie de l'hétérostructure et fournissent des informations précieuses sur ses caractéristiques structurales et chimique. Il est possible d'identifier des nanoparticules à différentes hauteurs du film coïncidant avec l'origine des grains de ZnO bien orientés. Cette observation suggère que les nanoparticules de Cu peuvent servir de sites de nucléation, favorisant un meilleur ordonnancement au sein de la matrice du film mince, même à des niveaux d'épaisseur très faibles. D'autre part, l'ellipsométrie spectroscopique est utilisée pour valider la présence de la bande d'absorption plasmon autour de 1.5 eV associée aux nanoparticules de cuivre dans la structure multicouche. Cette technique spectroscopique permet d'évaluer les propriétés plasmoniques et leur corrélation avec la configuration fabriquée.

Acknowledgements

Completing this thesis in cotutela between the University of Havana and the University of Lorraine was, from the beginning, a true challenge. From bureaucratic obstacles to an endless period of pandemic, many difficulties had to be overcome so that it could finally materialize. Moreover, managing to organize and carry out research work between two laboratories separated by more than 7000 km required very hard work and discipline, which put to the test the significance that the results achieved in this thesis have for me. However, all of this would not have been possible without the support of many people in both Cuba and France, whom I would like to deeply thank:

To my thesis advisors, Lídice Vaillant and David Horwat, I am grateful for your solid support from the very beginning of this journey. Li, thank you for standing by my side in every battle, for your invaluable advice on work and life, for being an example of resilience, and for your confidence in me. David, thank you for giving me the excellent opportunity to work with you, for your support at every moment, regardless of the circumstances, for our interesting discussions and your enthusiasm, especially in these recent months of immense pressure and uncertainty.

I would like to sincerely thank to all the people who have collaborated directly with this work and made possible the publication of part of the presented results: Jaafar Ghanbaja (IJL), Sylvie Migot (IJL), Yann Battie (LCP-A2MC, Institut Jean Barriol) and Sidi Hamady (CentraleSupélec, LMOPS). Your contribution was undoubtedly fundamental as well as our discussions.

To my husband, the person who has demonstrated the most love and confidence in me, who has been by my side in every challenge, lifting me up from the deepest falls and celebrating every achievement. Thank you, my love, for so much; we continue to pave our own paths.

Thanks to my family, especially my parents and in-laws, for the love, trust, and unconditional support. You have undoubtedly been a fundamental pillar in achieving all my goals.

I have no words to thank Claudia and Alejandro. Thank you for welcoming me into your home without hesitation, for the encouragement, valuable advice, assistance, and countless enjoyable moments that made me feel like family.

Thanks also to the rest of my friends in Nancy: Alexis, Zil, Adrián, Agathe, Carlos, Raya, Mariana and Yohana, for all the support in various circumstances, both personal and professional, for the endless advice, countless laughs, and good times. Your company has undoubtedly been one of the best things I take away from these years.

A special thanks to my mates and friends at the PV lab in Havana: to Rene for advice of all kinds, unconditional assistance in every technical challenge, and his contagious enthusiasm for every task. I also appreciate the help of the rest of my younger colleagues, especially Jesús, Silvia, Josué Benavides and Josué Aguilar, for always responding with a "yes" to any circumstance when I needed them.

Thanks to all the people at IMRE who contributed their bit during this time. Thanks to Nancy Martínez, Anabel Lam and Ricardo Pila for all the bureaucratic arrangements and the effort made to carry out this thesis in cotutela.

To the professors at the Physics Faculty in Havana, especially Mulet, Arbelio, Aimé, Maruchi and Maite and younger colleagues with whom I shared nice moments and from whom I received support in one way or another.

Thanks to the members of the "Functional Thin Films and Applications" team of the IJL, especially Jean-François Pierson, Brigitte Vigolo, David Pilloud, Stéphane Suire, Stéphanie Bruyere and Silvère Barrat, for every help received during my stays in Nancy.

I also thank the IJL competence centers (CC) where I could characterize my samples. To Pascal Boulet from the CC-XGamma for his help with the XRD measurements; Sébastien Hupont

from the CC-Optique Lasers CC for his trainings to achieve optical measurements, nice talks and French practice; Jaafar Ghanbaja and Sylvie Migot from the CC-3M for analysing too many samples, obtain beautiful micrographs and spend nice moments; Christine Gendarne from the CC-3M for keeping the SEM working for us; Laurent Badie and the members of the CC-MiNaLor for the trainings received in the cleanroom and for sharing with me this incredible working space.

I'd also like to acknowledge Stéphane Cuynet and Yann Battie for accepting to be part of my follow-up committee and for the interesting discussions.

Thanks to Chistine Sartori, Valérie Madeline, Martine Tailleur and Ferdally Jacobs for all their help with the administrative aspect during these years at IJL. Likewise, I thank the administrative work and support of Mercedes Coderch (Mercy) from the Physics Faculty and Lissette Navarrete from IMRE in Havana.

I'm immensely grateful to the Cooperation and Cultural Action Service (SCAC) of the French Embassy in Havana and Campus France for the financial support and for following-up my stays in Nancy. Also, I thank Flavio Soldera for the invitation to carry out research and teaching activities within the Erasmus Mundus master Project AMASE, which meant an important financial support for performing more experiments. I also would like to acknowledge to the Abdus Salam International Centre for Theoretical Physics (ICTP) for awarding me the ICTP ATAP Programme scholarship to spend these last months in France and defend my PhD. Likewise, thanks to the 202 team for your support for participating in the PLATHINIUM'23 conference and carry out measurements in Metz during these years.

Lastly, I would like to thank the members of the jury for agreeing to be part of my thesis defence and for the time they will spend on assessing my work.

Contents

| | |
|---|----|
| Introduction | 1 |
| CHAPTER 1 | 5 |
| General Overview | 5 |
| 1.1 Metal oxides semiconductors and devices..... | 9 |
| 1.1.1 Cu ₂ O basic properties..... | 10 |
| 1.1.2 ZnO basic properties. | 14 |
| 1.1.3 ZnO/Cu ₂ O based devices. | 16 |
| 1.2 Metal nanoparticles and plasmonic devices..... | 17 |
| 1.2.1 Localized surface plasmon resonance effect..... | 18 |
| 1.2.2 Tuning of the plasmonic response by controlling particles properties..... | 20 |
| 1.2.3 Plasmonic devices for optoelectronic applications. | 22 |
| CHAPTER 2 | 27 |
| Synthesis and characterization methods | 27 |
| 2.1 Deposition methods and films preparation. | 31 |
| 2.1.1 Sputtering technique..... | 31 |
| 2.1.2 Gas Aggregation Source. | 36 |
| 2.1.3 Rapid Thermal Annealing system. | 38 |
| 2.2 Characterization of the films..... | 40 |
| 2.2.1 X- Rays Diffraction..... | 40 |
| 2.2.2 UV-Vis-NIR spectroscopy..... | 42 |
| 2.2.3 Ellipsometric spectroscopy. | 45 |
| 2.2.4 Four-Point Probe method. | 47 |
| 2.2.5 Scanning Electron Microscopy. | 48 |

| | |
|--|-----------|
| 2.2.6 Transmission Electron Microscopy..... | 49 |
| 2.2.7 Current – Voltage characteristics | 52 |
| 2.2.8 Modulated Photocurrent Spectroscopy. | 55 |
| 2.2.9 Impedance Spectroscopy..... | 56 |
| CHAPTER 3 | 59 |
| Reactively-sputtered plasmonic composites based on Cu nanoparticles and metal oxides semiconductors | 59 |
| 3.1 Introduction..... | 63 |
| 3.2 Cu-O films deposition..... | 64 |
| 3.2.1 Characterization of CuNPs-Cu ₂ O composites: oxygen flowrate dependence. | 67 |
| 3.2.2 Characterization of CuNPs-Cu ₂ O composites: substrate position dependence. | 75 |
| 3.3 Devices fabrication | 82 |
| 3.3.1 Photocurrent enhancement with plasmonic particles incorporation. | 83 |
| 3.3.2 Performance enhancement of the nanocomposites. | 88 |
| Chapter conclusions | 89 |
| CHAPTER 4 | 91 |
| Influence of thermal annealing on the properties of CuNPs-Cu₂O composites and photoconversion devices | 91 |
| 4.1 Introduction..... | 95 |
| 4.2 Study of the influence of thermal annealing on the properties of CuNPs-Cu ₂ O composites and related devices. | 96 |
| 4.2.1 CuNPs-Cu ₂ O films growth and annealing. | 96 |
| 4.2.2 Characterization of CuNPs-Cu ₂ O composites annealed in oxygen-poor conditions. | 97 |
| 4.2.3 Influence of the thermal annealing on plasmonic devices performance. | 102 |
| Chapter conclusions | 113 |

| | |
|---|-----|
| CHAPTER 5 | 107 |
| Synthesis of Cu NPs via a Gas Aggregation Source and fabrication of ZnO-CuNPs composites exhibiting LSPR | 107 |
| 5.1 Introduction..... | 119 |
| 5.2 Copper nanoparticles by GAS | 120 |
| 5.3 ZnO-CuNPs multilayers composites by GAS..... | 124 |
| 5.3.1 ZnO-CuNPs multilayers deposition. | 124 |
| 5.3.2 Structural and morphological properties of ZnO-CuNPs multilayers..... | 126 |
| 5.3.3 Optical response of ZnO-CuNPs multilayers..... | 128 |
| 5.4 Studies in progress | 130 |
| 5.4.1 Electrical response of ZnO-CuNPs based devices. | 130 |
| Chapter conclusions | 132 |
| Conclusions and Perspectives | 133 |
| Annexes | 139 |
| References | 149 |
| Curriculum vitae | 173 |

Introduction

Today's rapidly increasing energy consumption, magnified by the environmental repercussions of human actions and the depletion of fossil fuel reserves, is undeniably a pressing issue for humanity. The development and use of renewable energy sources-based devices, such as solar cells, and other optoelectronic devices with applications in environmental and industrial monitoring, like the photocatalytic H₂ generation and H₂O splitting, are some of the alternatives to help address the aforementioned concerns. Among the challenges encountered in the development of these devices is the use of materials composed by elements abundant in the Earth's crust, non-toxic and whose production costs are falling steadily, thereby reducing the price of access to these technologies. In addition, the scientific community continues to explore new prototypes and works on the basis of a better understanding of the physical processes taking place in them, with the aim of continuing to increase efficiency.

Metal oxide semiconductors offer advantages such as non-toxicity (in most of the cases), cost-effectiveness, and favourable electrical and optical properties, making them standout options for building optoelectronic devices. Among these materials, Cu₂O has gained significant interest for various applications due to its absorption in the visible range of the electromagnetic spectrum and its p-type conductivity. Furthermore, Cu₂O can be synthesized using various

techniques, both vacuum-based and non-vacuum methods. Nevertheless, even though theoretical projections suggest power conversion efficiencies approaching 20% of Cu₂O-based photoconversion devices, the current practical performance remains relatively modest at 8.4% [1]. This suggests that there is considerable potential for enhancing the design and functionality of these devices. An important amount of studied Cu₂O-based heterojunctions includes ZnO semiconductor as a suitable partner. This well-known n-type material presents a wide bandgap, large exciton binding energy (60 meV) and excellent photoconductive properties. Besides, the band alignment of these materials aids in the separation of photogenerated electrons and holes, making them promising for solar cells and other optoelectronic applications.

Plasmonic nanocomposites, on the other hand, consisting in a semiconductor matrix embedding metal nanoparticles (NPs), have also gained significant attention for energy harvesting applications. They can provide the optical and electrical properties of the host materials and the quantum effects exhibited by the nanoscale particles, like the localized surface plasmon resonance (LSPR) phenomenon. An important part of the research community in the field of plasmonics has been focused on costly metals like Au and Ag, with strong plasmonic response. However, a cost-effective alternative is Cu, which also presents an important plasmonic response in the visible spectrum, possesses attributes like abundance, non-toxicity, and recyclability. On top of that, Cu has shown promise in effectively transferring “hot carriers” to various metal oxide semiconductors, broadening its applicability.

The inclusion of such NPs in photoconversion devices is of interest in this thesis due to the potential of generating additional carriers through the LSPR effect upon exposure to light and transfer to the semiconductor. However, the fabrication of Cu metal nanoparticles interfacing with semiconductor metal oxides like Cu₂O and ZnO presents complex challenges such as particles aggregation and oxidation, limiting their plasmonic response and underlining the need for innovative synthesis techniques.

Overall, the main goal of this thesis is the growth of plasmonic Cu nanoparticles and metal oxide semiconductors, forming composites and multilayer heterostructures for optoelectronic applications. To ascertain the optimal placement of these nanoparticles within potential devices, various designs for Cu₂O and ZnO heterostructures were explored.

The manuscript is organized in five chapters:

In [Chapter 1](#) an overview of properties and the state of the art of metal oxides in photovoltaic applications is presented. Also, the phenomenon of LSPR is discussed and considered in the context of performance improvement of these devices. The main challenges for including copper nanoparticles in the devices forming composites or multilayers by different methods are mentioned.

[Chapter 2](#) provides a comprehensive overview of the basic principles of the sputtering method used for growing metal oxide and plasmonic composite layers, as well as the essential principles behind the structural, optical, chemical and electrical characterization techniques employed in our study.

In [Chapter 3](#), a simple method to synthesize Cu nanoparticles embedded in a Cu₂O matrix showing the localized surface plasmon effect is presented. Experimental conditions to obtain CuNPs-Cu₂O composites are discussed, as well as the dependence of their electrical, optical and structural properties on the growth parameters. FTO/ZnO/CuNPs-Cu₂O and FTO/ZnO/CuNPs-Cu₂O/Cu₂O devices are fabricated and their electrical characterization is presented (FTO: fluorine-doped tin oxide).

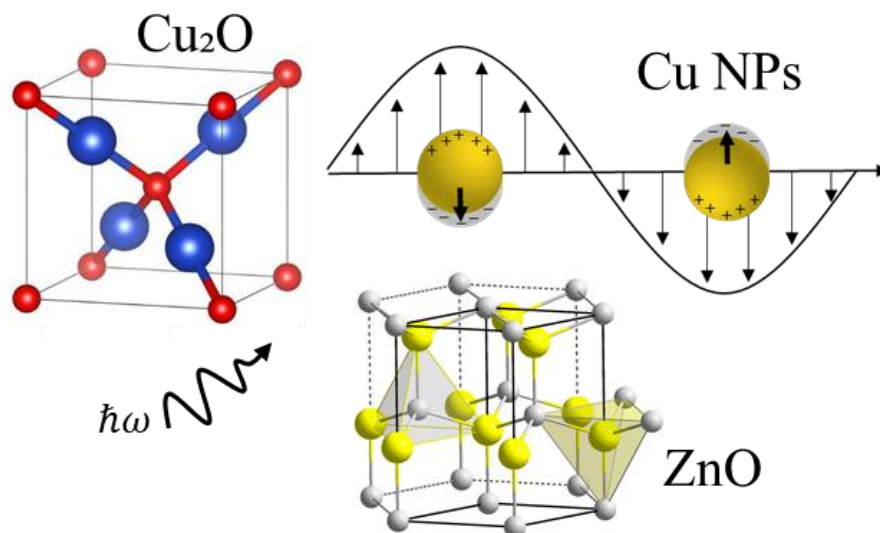
In [Chapter 4](#), the thermal annealing of plasmonic composites and plasmonic-based heterostructures, using a rapid thermal annealing (RTA) furnace, in oxygen-poor conditions to limit the oxidation of copper nanoparticles and harness the LSPR effect, is investigated. A comprehensive study of the microstructure, morphology, and optical properties of annealed composites is conducted, as well as J-V characterization and Impedance Spectroscopy measurements of annealed plasmonic devices in order to understand the underlying phenomena influencing their response.

In [Chapter 5](#), copper nanoparticles using a gas aggregation source (GAS) are synthesized and ZnO-CuNPs multilayer structures are constructed through sequential growth of ZnO thin films and Cu nanoparticles. Variations in nanoparticle density during deposition are analysed, both with and without holder rotation, and HRTEM and EELS analyses are performed to confirm the successful formation of the heterostructure. Ellipsometric spectroscopy is used to validate the presence of surface plasmon bands associated with Cu nanoparticles.

General [conclusions and perspectives](#) of this work are presented afterwards. Finally, an [Annexes](#) section is included with useful information in order to provide more details about the presented results.

CHAPTER 1

General Overview



Abstract

In this chapter an overview of the state of the art of metal oxides semiconductors applied to photovoltaic applications, particularly ZnO and Cu₂O, is presented. A summary of the main optical, structural and electrical properties of these materials will be discussed. Besides, the localized surface plasmon resonance phenomenon is described from a general point of view, focusing on its application in optoelectronics, particularly in solar cells. The main deposition methods used for the inclusion of metal plasmonic nanoparticles and principal challenges are also presented.

Contents

| | |
|---|----|
| CHAPTER 1 | 5 |
| General Overview | 5 |
| 1.1 Metal oxides semiconductors and devices..... | 9 |
| 1.1.1 Cu ₂ O basic properties..... | 10 |
| 1.1.2 ZnO basic properties. | 14 |
| 1.1.3 ZnO/Cu ₂ O based devices. | 16 |
| 1.2 Metal nanoparticles and plasmonic devices..... | 17 |
| 1.2.1 Localized surface plasmon resonance effect..... | 18 |
| 1.2.2 Tuning of the plasmonic response by controlling particles properties..... | 20 |
| 1.2.3 Plasmonic devices for optoelectronic applications. | 22 |

1.1 Metal oxides semiconductors and devices.

Metal oxide semiconductors (MOs) are non-toxic and Earth's crust abundant materials known for their unique and remarkable properties. One of their standout features is their carrier mobility of up to $10^2 \text{ cm}^2 \cdot \text{V}^{-1} \cdot \text{s}^{-1}$, which makes them highly desirable for electronic applications. MOs materials also exhibit excellent mechanical stress tolerance and are compatible with organic, dielectric and photoactive substances. Furthermore, they offer high optical transparency [1], making them suitable for optoelectronic devices. The production of high-quality electronic-grade MOs thin films can be accomplished using vapor-phase processes (thermal deposition, sputtering, pulsed-laser deposition, atomic layer deposition) and solution-phase processes (spin-coating, spray coating, printing) at near-ambient conditions [1]. This accessibility to high-quality thin films in convenient conditions expands their usability to a wide range of high-value and low-fabrication cost applications.

The use of MOs in renewable energy conversion devices, in particular solar cells, has been widely explored and already included in commercialized technologies as electrodes [2–5] and charge transport materials [6–8]. Since intrinsic MOs normally possess weak conductivity as a result of their relatively large bandgap, defect engineering and doping have enabled the development of a successful strategy to achieve very low resistivities and increase carrier concentration. Some examples are the outstanding transparent conductor oxides (TCOs) employed as electrodes materials, for example, indium tin oxide (ITO) [9,10], fluorine-doped tin oxide (FTO) [9,11], and aluminium-doped zinc oxide (AZO) [9,12,13]. The wide bandgaps of these layers are advantageous for maximizing the light transmission through them and the absorption of the material interfaced with them. Furthermore, the existence of MOs presenting either n-type or p-type conductivity opens up a range of possibilities in band engineering designs and development of functional all-oxides heterostructures. Some examples of widely studied n-type (electron transport) materials are TiO_2 [14,15], ZnO [16,17], SnO_2 [7,18] and In_2O_3 [19] while relevant p-type (hole transport) materials include Cu_2O [20,21], NiO [22,23] and SnO [24,25]. In Table 1.1 a summary of some properties of these MOs is presented.

Table 1.1 Summary of some MOs properties reported by different groups.

| Conductivity type | MO material | Bandgap (eV) | Carrier mobility ($\text{cm}^2 \cdot \text{V}^{-1} \cdot \text{s}^{-1}$) | Carrier concentration (cm^{-3}) | Resistivity ($\Omega \cdot \text{cm}$) | Ref. |
|-------------------|--------------------------------|--------------|--|--|--|--------------|
| n-type | TiO ₂ | 3 – 3.2 | $10^{-6} - 10^{-4}$ | -- | -- | [26–28] |
| | ZnO | ~ 3.37 | $10^0 - 10^2$ | $10^{18} - 10^{20}$ | $10^{-3} - 10^4$ | [6,26,29–32] |
| | SnO ₂ | ~ 3.7 | < 30 | $10^{19} - 10^{20}$ | $10^{-3} - 10^{-2}$ | [29] |
| | In ₂ O ₃ | ~ 3.7 | ~ 50 | $10^{17} - 10^{19}$ | 10^{-1} | [29,33] |
| p-type | Cu ₂ O | 2 – 2.7 | $10^{-1} - 10^2$ | $10^{12} - 10^{16}$ | $10^0 - 10^6$ | [8,29,34–39] |
| | NiO | 3.6 – 4.0 | 0.1 – 3.5 | $10^{15} - 10^{19}$ | $10^1 - 10^2$ | [40–42] |
| | SnO | 2.6– 3.2 | 0.26 – 18 | $10^{15} - 10^{19}$ | $10^{-1} - 10^2$ | [24,25,29] |

In this thesis, we are interested in studying ZnO and Cu₂O-based heterostructures due to the promising potential of these semiconductors in near transparent optoelectronic applications, particularly in solar cells, since absorption, carriers mobility and e-h concentration play key roles in getting better efficiencies. More detailed description of their structural, electronic and optical properties is presented in the following sections.

1.1.1 Cu₂O basic properties.

Copper I oxide (Cu₂O), also known as cuprite, is a stable copper oxide phase which exhibits a cubic crystal structure, and falls under the $\text{Pn}\bar{3}\text{m}$ space group. Its unit cell is characterized by two sub-lattices, shifted against each other by 1/4 of the space diagonal [43], containing a total of six atoms: four Cu cations compose a face-centered cubic sub-lattice and two O anions form a body-centered cubic sub-lattice. Each oxygen atom is tetrahedrally-coordinated with the four neighbouring copper atoms while each copper atom shows linear coordination with the two surrounding oxygen atoms (Figure 1.1a). The interatomic Cu–O, O–O, and Cu–Cu distances are 1.849 Å, 3.68 Å and 3.012 Å, respectively. The lattice parameter for bulk Cu₂O has been experimentally determined to be 4.269 Å [44,45]. It is worth to mention that some interplanar distances in the Cu₂O cubic structure, particularly that corresponding to the planes (111) close to 2.5 Å ($2\theta \sim 36^\circ$), are very close to the interplanar distances of the other copper oxide phases

(Cu_4O_3 and CuO) and techniques like Raman spectroscopy are required to support X-rays diffraction measurements (Figure 1.1 b, c).

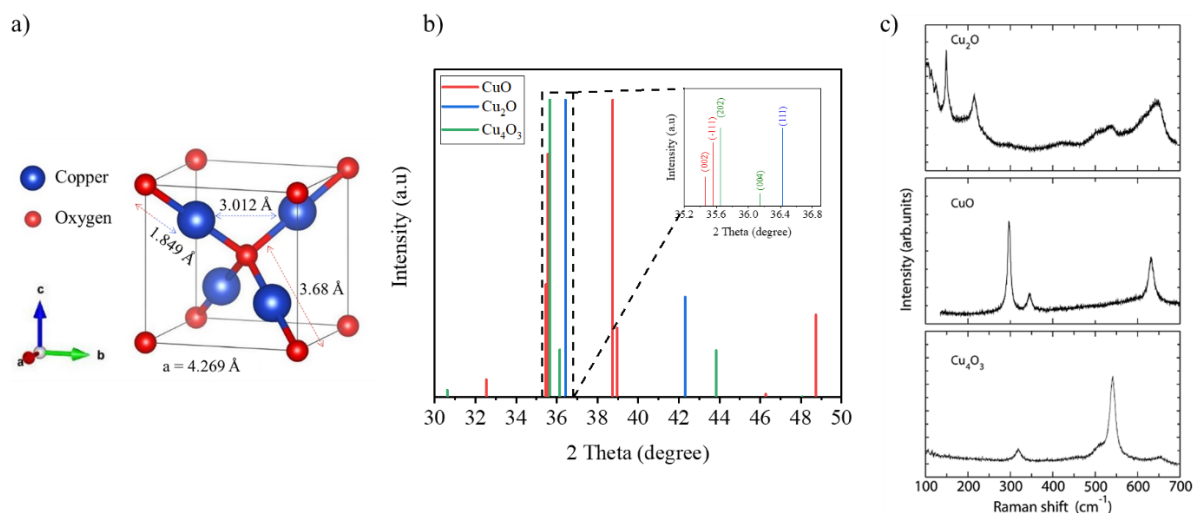


Figure 1.1: (a) Cubic crystal structure of Cu_2O or cuprite and interatomic distances between Cu atoms (blue spheres) and O atoms (red spheres) (modified from [46]). (b) X-rays diffraction maximum intensity positions reported for copper oxides phases where very close peaks around 36° are present, making difficult to distinct between the copper oxide phases. (c) Raman spectroscopy of the copper oxides, which better provides the differentiation of the different phases (modified from [47]).

Cu_2O presents a direct forbidden band gap between 1.97 eV and 2.1 eV and an optically-allowed bandgap ranging from 2.4 eV to 2.7 eV [36], according to theoretical calculation and experimental measurements. The Cu_2O band structure at the Γ – point of the Brillouin zone is shown in Figure 1.2. It can be noticed a valence band (VB) maximum ($\Gamma_{25'}$) which has a predominant Cu-d atomic orbital character and even parity. Also, two conduction band (CB) minima are present with s-like contribution from both O and Cu atoms: the Γ_1 with even parity and the $\Gamma_{12'}$ with odd parity. Therefore, optical transition ($\Gamma_{25'}$) \rightarrow (Γ_1) between the uppermost VB and the lowest CB is dipole-forbidden since they share the same parity. On the other hand, ($\Gamma_{25'}$) \rightarrow ($\Gamma_{12'}$) transition is allowed and corresponds to the absorption experimentally obtained above 2.4 eV [36,48].

Besides, it is well established its intrinsic p-type conductivity, associated to copper vacancies sites in the crystal structure. This has been corroborated by theoretical calculations and deep

transient spectroscopy [49]. According to Figure 1.3, the formation energies of these defects, including both, the simple V_{Cu} and the more intricate $V_{\text{Cu}}^{\text{split}}$ configuration (accounting for an interstitial Cu atom between two V_{Cu}), exhibit the lowest formation energies, whether in oxygen-rich or oxygen-poor conditions.

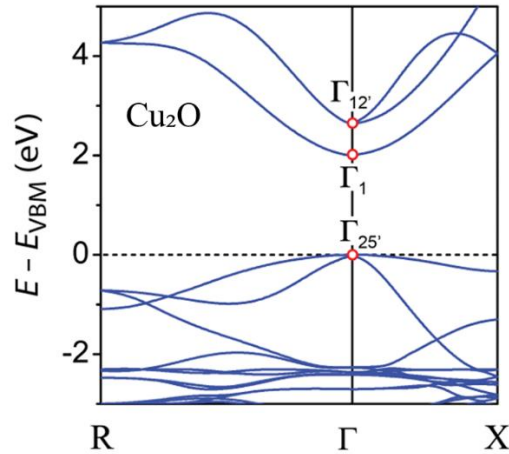


Figure 1.2: Cu_2O band structure at the Γ – point of the Brillouin zone (modified from [43]).

These formation energies are very close (1.15 and 1.14 eV) for both kinds of defects and at least 0.7 eV lower than other possible intrinsic acceptors like oxygen interstitials O_i in tetrahedral (O_i^{tet}) or octahedral (O_i^{oct}) coordination [44]. Therefore, the p-type conductivity in Cu_2O arises primarily from Cu vacancies. On the other hand, oxygen vacancies are present in neutral state (V_{O}) (in both oxygen-rich and oxygen-poor conditions) which do not contribute to the elimination of holes in Cu_2O , highlighting the difficulty of achieving n-type conduction in this material [36]. In that sense, it has been discussed the influence of other potential “hole killer” like copper interstitial (Cu_i), with a hole-eliminating positive charge state (Cu_i^+). However, this defect has large formation energy and no significant concentrations exist under equilibrium growth conditions [50].

Studies about possible extrinsic acceptors revealed that doping with sodium (Na) or nitrogen (N) results to be an effective approach to increase the hole concentration and decrease the resistivity of Cu_2O (in the case of N). In particular, molecular nitrogen (provided, for example, by a N_2 flow during the deposition) replaces copper or oxygen atoms, acting as shallow acceptors and increasing the hole concentration [36,44]. Hydrogen, on the contrary, has been

found to be an extrinsic defect that tends to form a $H - V_{Cu}$ complex with very low formation energy (0.17 eV [44]), capable to reduce the hole concentration in Cu_2O and eventually suppress the p-type conductivity [36].

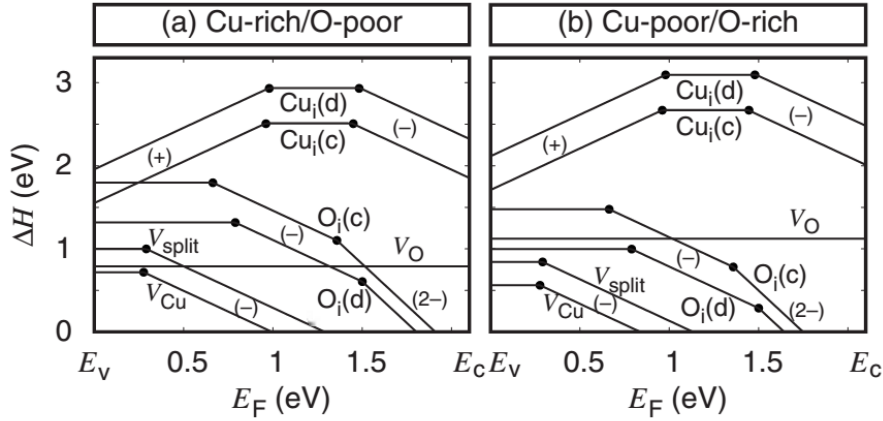


Figure 1.3: Formation energy of Cu_2O intrinsic defects in (a) Cu-rich/O-poor conditions and (b) Cu-poor/O-rich conditions [50].

Regarding the electrical properties of the Cu_2O material, electrical resistivities within the range $10^0 - 10^6 \Omega \cdot cm$ [36,37,39], carrier densities between $10^{12} - 10^{16} cm^{-3}$ [35,38] and mobilities from $10^{-1} - 10^2 cm^2 \cdot V^{-1} \cdot s^{-1}$ [36,38] have been reported depending on the preparation method. By electrodeposition method, varying temperature, pH and deposition potential, Cu_2O films with resistivities of $10^3 - 10^6 \Omega \cdot cm$, carrier density between $10^{12} cm^{-3}$ and $10^{14} cm^{-3}$ and mobility from 0.4 to $1.8 cm^2 \cdot V^{-1} \cdot s^{-1}$ were obtained [38,51]. Another group deposited Cu_2O using chemical bath deposition method at low temperature ($60^\circ C$) with resistivity values of $10^3 - 10^4 \Omega \cdot cm$ and mobility in the order of $10^1 - 10^2 cm^2 \cdot V^{-1} \cdot s^{-1}$ [52]. Better layer properties were found using pulsed laser deposition technique and $750^\circ C$ of substrate temperature, with a resulting resistivity of $16 \Omega \cdot cm$ and mobility of $30 cm^2 \cdot V^{-1} \cdot s^{-1}$ [53]. This is also the case for the reactive sputtering technique, which has proven to be an effective method for depositing Cu_2O thin films with good electrical quality without the need to use such high temperatures ($> 500^\circ C$). Resistivities of $490 \Omega \cdot cm$ at room temperature and $7.32 \Omega \cdot cm$ after post-annealing at $280^\circ C$ were obtained by Wang *et al.* [37]. More recently Qin *et al.* reported a resistivity of $145 \Omega \cdot cm$ ($350^\circ C$) with a hole mobility of $7.74 cm^2 \cdot V^{-1} \cdot s^{-1}$ and a carrier density of $5.5 \times 10^{15} cm^{-3}$ [54].

1.1.2 ZnO basic properties.

Zinc oxide (ZnO) is a widely studied, transparent, abundant and non-toxic semiconductor with very promising properties for multiple devices applications like emitting diodes [55], sensors [56], photodetectors [57,58] and solar cells [16,59]. This material predominantly adopts a hexagonal wurtzite-type crystal structure, characterized by lattice parameters values of $a = 3.25 \text{ \AA}$ and $c = 5.20 \text{ \AA}$. The structure can be described as two superimposed hexagonal-close-packed (hcp) Zn and O lattices where each Zn^{2+} (O^{2-}) atoms is tetrahedrally-coordinated with four O^{2-} (Zn^{2+}) (Figure 1.4). This arrangement gives rise to spontaneous polarization along the c-axis, resulting in a preferential growth along the [0001] for most of films and nanostructures [29,31].

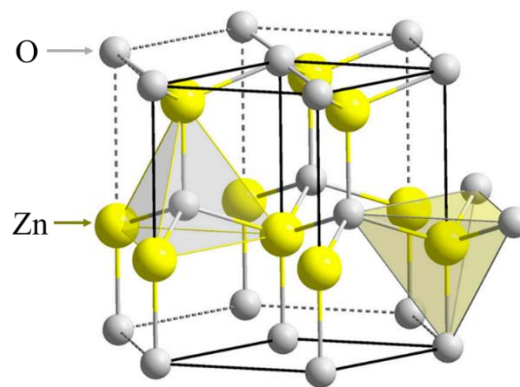


Figure 1.4: ZnO hexagonal wurtzite-type structure which present a spontaneous polarization in the c-axis (modified from [31]). The unit cell is enclosed by the solid dark lines.

Also, this material presents a direct band gap ($\sim 3.37 \text{ eV}$ [31]) and a large exciton binding energy of 60 meV . This attracts the attention from the community interested in applications involving UV/blue wavelength optoelectronics and exciton emission at room temperature [60,61]. The band structure, depicted in Figure 1.5a, shows the valence band maximum and conduction band minimum at the Γ -point of the Brillouin zone which arise mainly from occupied $2p$ states of O^{2-} and empty $4s$ states of Zn^{2+} , respectively [62].

ZnO usually exhibits n-type conductivity with high carrier mobilities and electron concentration up to $100 \text{ cm}^2 \cdot \text{V}^{-1} \cdot \text{s}^{-1}$ [31] and 10^{19} cm^{-3} [29], respectively. The defects responsible for the intrinsic n-type conductivity present in this material have been object of debate for several years and is not fully understood. Among the native defects identified are oxygen vacancies (V_{O}), zinc vacancies (V_{Zn}), oxygen interstitials (O_i), zinc interstitials (Zn_i),

oxygen (O_{Zn}) and zinc (Zn_O) antisites. In Figure 1.5b it can be seen the formation energy of the ZnO native defects in Zn-rich and O-rich conditions [63]. Many works associate the n-type conductivity to V_O due to their lower formation energy [64] while in more recent studies researchers argued that these are deep donors and therefore hardly responsible for the n-type conductivity [31]. Another consideration has been the Zn_i but, although it is a shallow donor (~ 0.05 eV) below the conduction band [46]), it presents very high formation energy [65]. On the other hand, O_i and V_{Zn} have been considered as acceptor defects. V_{Zn} are deep acceptors with low formation energy (the lowest under oxygen-rich conditions), considered as the main compensating centers in n-type ZnO. Additionally, it has been considered that O_i , O_{Zn} and Zn_O possess formation energies that are sufficiently high to prevent them from occurring in substantial concentrations within the material [31].

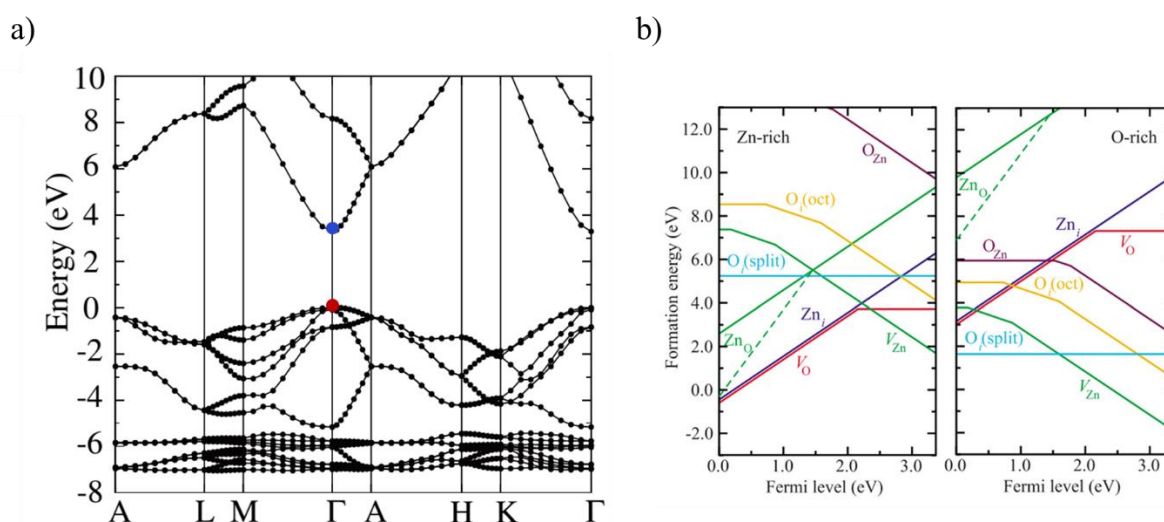


Figure 1.5: (a) Calculated band structure of ZnO where the valence-band maximum (VBM, red dot) is set to zero (modified from [65]). (b) Formation energy of ZnO native defects in Zn-rich and O-rich conditions [63].

Therefore, there is a tendency to claim that some impurities from the growth process could act like extrinsic donor defects. Special attention has been put on hydrogen, fluorine or group III impurities (In, Ga, B, Al) [31]. Interstitial hydrogen (H_i) and hydrogen substitutionally occupying oxygen sites (H_O) have been recognized as shallow donors within ZnO, characterized by low formation energies, implying their likely existence in significant quantities within the ZnO material [46]. Fluorine substituting oxygen atoms also acts as a

shallow donor with a low formation energy [31]. Finally, group III impurities use to be intentionally introduced, substituting Zn sites [31], enabling to reach electron concentration over 10^{21} cm^{-3} [29].

As in Cu_2O , the electrical properties of ZnO can be modified depending on the growth methods employed to obtain this material. Resistivities within the range $10^{-3} - 10^4 \text{ } \Omega \cdot \text{cm}$ can be reached, as shown in Table 1.1. Chemical routes like sol-gel, chemical vapor deposition and electrochemical deposition are employed to obtain both ZnO thin films and nanostructures, being the sol-gel method the most dominant [63]. A very low resistivity of $10^{-3} \text{ } \Omega \cdot \text{cm}$ was obtained by Chen and coauthors [66] for ZnO films grown by sol-gel method and UV post-treatment. Physical vapor deposition methods like pulsed laser deposition, magnetron sputtering (DC, RF, HiPIMS), atomic layer deposition and molecular beam epitaxy have been also widely used [31]. ZnO thin films with resistivity in the range of $10^{-2} - 10^4 \text{ } \Omega \cdot \text{cm}$ were obtained by de Melo *et al.* using DC reactive magnetron sputtering, changing the position of the substrate with respect to the target axis [32]. In this thesis the growth conditions described in [32] to obtain high conductivity ZnO films are used.

1.1.3 ZnO/ Cu_2O based devices.

As mentioned above, metal oxide semiconductors have been considered for the development of photovoltaic and optoelectronic devices due to their unique properties and low environmental impact. It has also been noticed that many of the MOs studied present n-type conductivity, which make difficult the design of all-oxide p-n heterostructures including a p-type semiconductor presenting a suitable bandgap and good electrical properties.

That is why Cu_2O has resulted to be an attractive candidate to play the role of absorber (p-type) due to its high hole mobility and large absorption coefficient ($10^4 - 10^5 \text{ cm}^{-1}$) [45]. Heterojunction architectures based on Cu_2O , combined with various n-type metal oxides like TiO_2 [67–69], Ga_2O_3 [70–72] and ZnO [73–75], have been the subject of extensive research.

A particular interest has been paid to p- Cu_2O /n-ZnO heterojunction, since ZnO has been identified as one of the most stable, efficient, and transparent conductive metal oxides available. Moreover, nanostructured ZnO configurations can be reached (nanorods, nanotubes,

nanowires), increasing the effective contact area and contributing to increase the charge separation. Also, the relative positions of the energy bands in ZnO and Cu₂O semiconductors play a crucial role in the separation of photogenerated electrons and holes, contributing to the device's performance [74]. Although Cu₂O presents a Shockley–Queisser theoretical power conversion efficiency (PCE) limit of ~20% in 1.5 A.M. conditions, PCE does not overcome the 8.4 % for the Cu₂O-based solar cells [34,45,76]. Therefore new approaches, including doping, surface modification, quantum dots and localized surface plasmon resonance exploitation have been considered [77–79].

In this thesis, our approach is focused on the incorporation of metal nanoparticles (NPs) presenting localized surface plasmon resonance in ZnO-Cu₂O based devices, in order to enhance the light absorption, electron-hole generation and charge collection.

1.2 Metal nanoparticles and plasmonic devices.

Since ancient times, the use of metal NPs for artistic and decorative purposes has been remarkable. The ability of NPs to change their coloration as a function of their size, for example, has caused increasing interest to the human kind. However, it was not until the early 20th century that the mechanism underlying this interaction with light was fully understood thanks to the work of Gustave Mie, who was the first to provide a theoretical basis for explaining the localized surface plasmon resonance (LSPR) phenomenon, observed in metal NPs, by solving Maxwell's equations.

Today, LSPR has transcended its historical context and has found diverse applications in scientific and technological fields. It allows light to be precisely manipulated and controlled at the nanometer scale, and researchers tailor the size, shape, composition and arrangement of NPs to customize their chemical, optical and electrical properties. This versatile control has opened the doors to a multitude of multidisciplinary fields, such as catalysis, optoelectronics, bio-detection and photovoltaics, among others. The path from the use of metallic NPs for mere artistic appeal to connecting their potential in cutting-edge technology exemplifies the remarkable evolution of our understanding and use of these nanoscale materials.

1.2.1 Localized surface plasmon resonance effect.

LSPR phenomenon occurs in metal NPs when the wavelength of the incident light is larger than the particle radius R . If the frequency of the electromagnetic field coincides with the metal plasmon frequency, conduction electrons oscillate collectively in resonance with the field (Figure 1.6a).

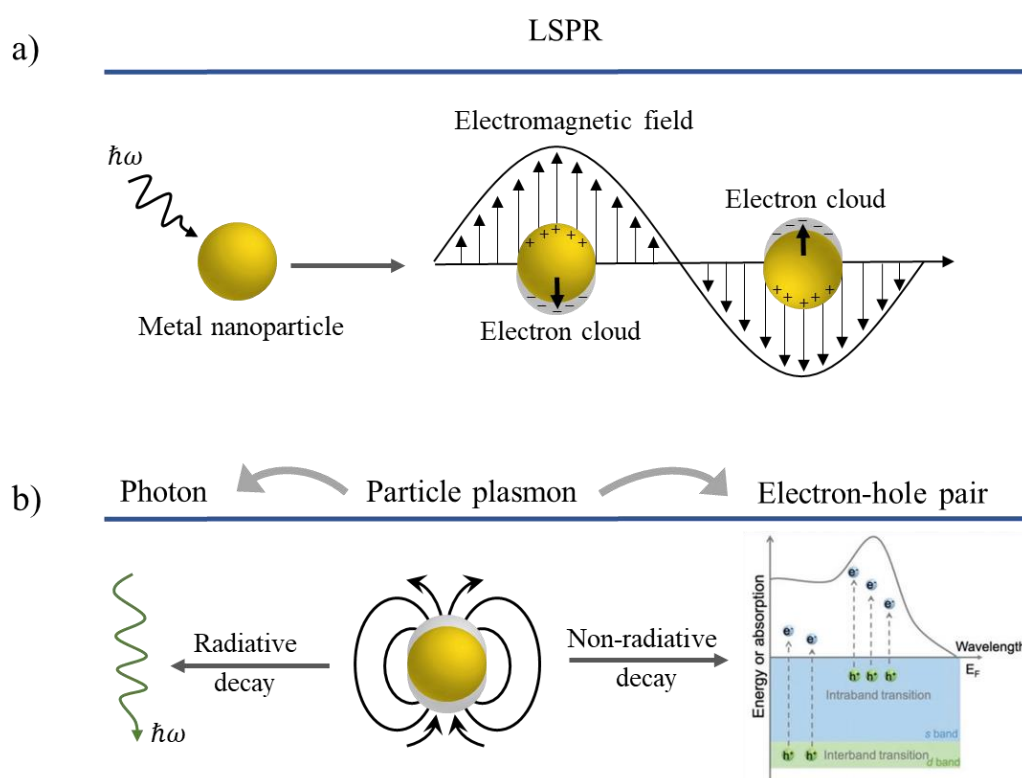


Figure 1.6: (a) A schematic representation illustrating the synchronized movement of free electrons within a spherical metallic nanoparticle when stimulated by an external, time-dependent electric field that matches the plasmon frequency (modified from [80]). In (b) a schematic of the radiative (left) and non-radiative (right) decay of LSPRs in metallic NPs is shown (modified from [81,82]).

This results in a selective absorption of the light with the plasmon frequency, enhancement of the electromagnetic field in the vicinity of the NPs [81], “hot carriers” generation, among other mechanisms explained in section 1.2.3.

The LSPR excitation can decay radiatively or non-radiatively (Figure 1.6b). The radiative decay accounts for light scattering, which is very advantageous in light trapping, for example,

while non-radiative decay is induced by electron-holes pairs excitations within the conduction band (intraband transition) and between the d band and sp conduction band (interband transition) [81].

Gustave Mie solved the Maxwell's equations for calculating the extinction (absorption + scattering) cross-section σ_{ext} of a spherical metal nanoparticle, with only dipole polarization contribution ($R/\lambda < 0.1$). The extinction cross-section will depend on its volume $V_0 = (4\pi/3)R^3$ and the dielectric function ε , including a real part ε_r and an imaginary part ε_i , the dielectric function of the surrounding medium ε_m (assumed frequency-independent over the spectral range of interest) [83], the speed of light c and its angular frequency ω :

$$\sigma_{\text{ext}} = 9 \frac{\omega}{c} \varepsilon_m^{3/2} V_0 \left[\frac{\varepsilon_i(\omega)}{(\varepsilon_r(\omega) + 2 \varepsilon_m)^2 + \varepsilon_i(\omega)^2} \right] \quad (1.1)$$

When $\varepsilon_r = -2 \varepsilon_m$ ($\varepsilon_m \neq 0$) the extinction cross-section reaches its maximum value and the resonant condition is fulfilled. This condition is only fulfilled by metals, since standard dielectrics and non-metals have typically $1 < \varepsilon_r < 50$. Additionally, to have the lowest possible losses, ε_i should be close to zero, which is seen only in some metals, or weakly dependent on ω [84,85]. From equation 1.1 it can be seen than the size of the particle, the dielectric function of the surrounding medium ε_m and ε_i have a direct influence on the extinction cross-section amplitude. The imaginary part of the dielectric function of the metal also influences the width and symmetry of the absorption band given by the term ε_i^2 . Meanwhile, the term $(\varepsilon_r(\omega) + 2 \varepsilon_m)^2$ influence in the position of the surface plasmon band [86].

In terms of plasmonic applications, it is important to choose a metal that can support a strong plasmon response at the desired resonance wavelength (strong enhancement of σ_{ext}). A quality factor (Q) accounting for the strength of the plasmon resonance, is given by [84]:

$$Q = \frac{\omega (d \varepsilon_r / d \omega)}{2 \varepsilon_i^2} \quad (1.2)$$

Figure 1.7 displays the quality factors of various metals when in contact with air. The shaded area on the graph represents materials with quality factors well-suited for plasmonic

applications. It can be seen that gold (Au), silver (Ag), and copper (Cu) are suitable metals for applications in the visible range. Although lithium also possesses an appropriate quality factor, its reactivity and challenging handling make it a seldom-considered option.

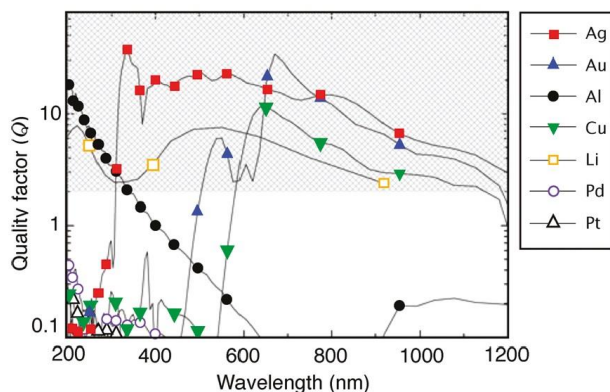


Figure 1.7: Quality factor of the localized surface plasmon resonance of different metals in air where the shadow region corresponds to the zone of interest for most applications [84].

1.2.2 Tuning of the plasmonic response by controlling particles properties.

The Mie equation is inadequate for accurately describing the optical characteristics of metal NPs when their diameter ($2R$) is equal to or exceeds 30 nm [85]. As the nanoparticle size increases, the charge separation within the nanostructure intensifies, resulting in a lower frequency for the collective oscillation of electrons. Consequently, this leads to a red-shift (through lower energies) of the surface plasmon band (SPB) (Figure 1.8a) [84].

Additionally, large sizes introduce the possibility of higher-order multipole effects. In the case of not spherical particles, the electron cloud is unevenly distributed inside the particles, provoking more than one oscillation mode, influencing the plasmonic response. For example, in Au nanorods (Figure 1.8b) two bands are present in the extension cross-section spectrum: a high energy band (transverse mode) associated to electron oscillations perpendicular to the major axis of the particle and a low energy band (longitudinal mode) associated to electron oscillations along the particles major axis appear. The separation between these bands increases with particles aspect ratio [87].

Another factor affecting the position and broadness of the LSPR band is particle aggregation. When particles are closely packed together, it generates electromagnetic coupling, resulting in the extinction spectrum comprising both the LSPR of individual particles and interactions between them. This phenomenon becomes significant when the distance between neighbouring particles is less than five times the particle's radius, leading to a noticeable red-shift and widening of the SPB. The red-shift caused by particle aggregation can often exceed that resulting from increasing the particle size. This effect involves the coexistence of the LSPR of individual particles and interactions between them, indicating strong coupling among the localized surface plasmons (LSPs) of these nanostructures upon excitation (Figure 1.8c) [88].

Another morphological features like sharpness and symmetry influences the plasmonic response [84]. Sharp features tend to increase charge separation and reduce the restoring force for the dipole oscillation. A reduction in resonance frequency or red-shift in wavelength is consequently observed. On the other hand, the number of SPB increases as the symmetry of a structure decreases. Finally, chemical composition could also induce plasmon peaks shift. For example, variation in the molar ratio of compound particles (Ag and Au) results in SPB shift [84].

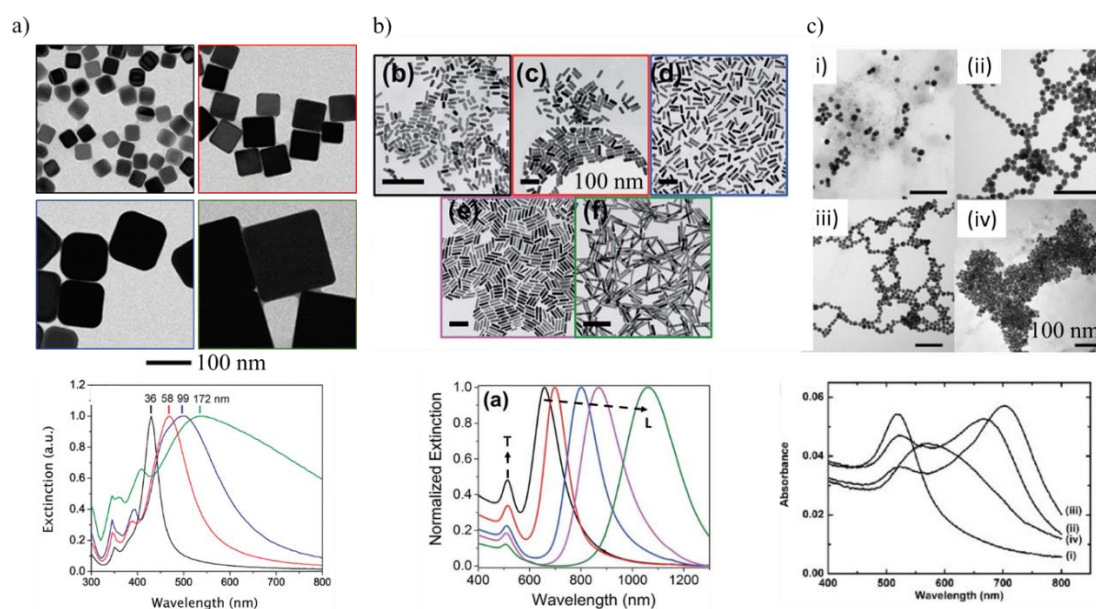


Figure 1.8: Evolution of the extinction spectra and absorbance of: a) Ag nanocubes with different sizes, b) Au nanorods with different aspect ratios in which the longitudinal (L) and

transverse (T) plasmon modes are pointed out and c) Au NPs with different assemblages. Images modified from [84], [87] and [88], respectively.

1.2.3 Plasmonic devices for optoelectronic applications.

Photodetectors and solar cells are known energy conversion devices where the incident light is absorbed by an active semiconductor layer generating electron-hole pairs that are collected by a closed circuit, generating a photocurrent (Figure 1.9a). The efficiency of these devices will depend, among other factors, on the ability to generate and collect more carriers.

The possibility to control the plasmonic response over the electromagnetic spectrum by tuning the size, shape and NPs distribution, allows to fabricate innovative devices for light trapping, manipulation and energy harvesting. Therefore, the integration of metal NPs in semiconductor based-heterostructures has been widely studied as an alternative to improve devices efficiency due to the mechanisms that take place as a result of the metal-semiconductor interaction.

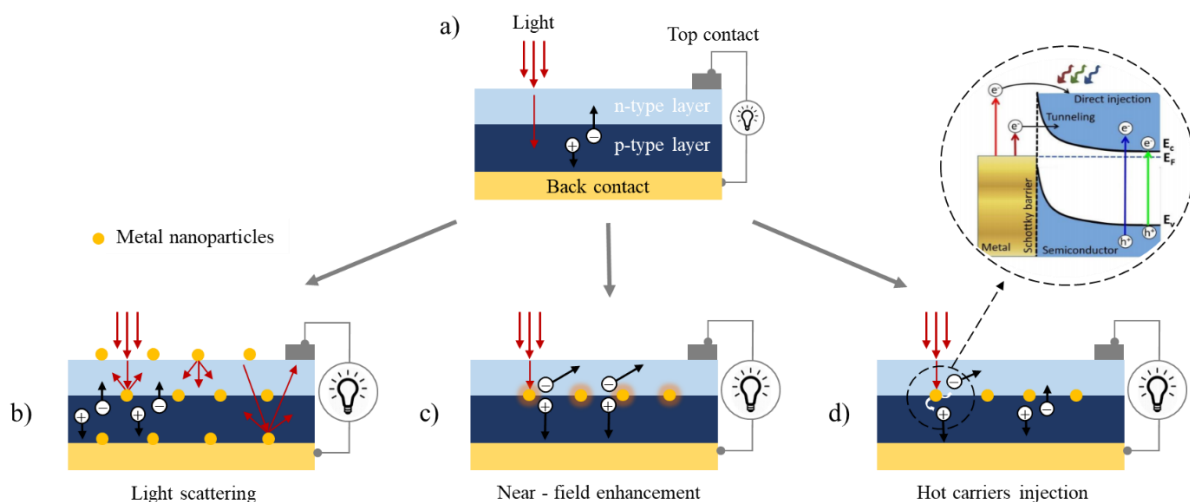


Figure 1.9: Schematic representation of (a) a classical p-n junction solar cell and the main mechanisms that takes place after inclusion of metal NPs in the heterostructure: (b) light scattering, (c) local electromagnetic field-enhancement and (d) hot carriers injection (modified from [89]). A band diagram showing the hot carriers transference from a plasmon nanoparticle through a semiconductor is shown in the enclosed area (modified from [90]).

Five main mechanisms have been mentioned in the literature: light scattering, near-field enhancement [81], plasmon induced carrier separation or hot carriers injection [81], heating effect [91] and dipole-dipole coupling [92]. Light scattering, near-field enhancement and hot carriers injection are the main mechanisms discussed in most of the publications related to solar cells and photo detection devices and these will be the main focus in the following discussions.

Particles with relative large dimensions (around 100 nm) have been reported to have a higher scattering cross-section than small NPs (around 10 nm). In solar cells, light trapping by backward and forward scattering could increase the effective optical path length of photons, allowing these photons to be absorbed by the active layers with the subsequent electron-hole pair generation (Figure 1.9b). The texturing of materials employed to avoid reflection losses, can be substituted by NPs at the surface, avoiding preparation processes that could induce recombination and defects in the dielectric [81]. On the other hand, the local or near – field enhancement effect in plasmonic solar cells is exploited to enhance photonic absorption close to the particle surface (Figure 1.9c). A spherical particle is able to induce a light intensity increase of up to 10^3 times close to the particle surface [82]. The concept behind near-field enhanced plasmonic solar cells centers on the transfer of energy from the plasmon's near-field to the active (or light-absorbing) layer of the solar cells. Consequently, this leads to an improvement in absorption efficiency, thereby increasing the probability of excitation and subsequently boosting the photocurrent [81]. Finally, plasmon-induced hot carriers transfer represents one mechanism explored for plasmonic energy conversion. When plasmonic metallic nanostructures come into close contact with semiconducting materials and LSPR excitation occurs, hot electrons emitted by non-radiative decay of the surface plasmons can be directly injected from the NPs into the semiconductor conduction band. This injection occurs by overcoming or tunnelling through the Schottky barrier that exists between the metallic NPs and the semiconductor material (Figure 1.9d).

Nowadays, the inclusion of plasmonic nanostructures has been applied to different solar cells families trying to take advantage of these different mechanisms. In the following Table 1.2 a few examples of some reported studies in the last decade about inclusion of metal NPs in solar cells is shown. Brief description of the plasmonic nanostructure, mechanisms involved and PCE enhancement is included.

It is worth to mention that, according to the consulted literature, Au NPs are preferably used to increase absorption and hot carriers injection while Ag particles are mostly used to enhance light scattering. This is because the scattering cross section of Ag is higher than its absorption cross section [93] while for Au NPs (< 100 nm) the opposite occurs [94].

Table 1.2 Some examples of studies where the solar cells efficiency was increased by inclusion of plasmonic NPs.

| Solar cell technology | Plasmonic nanostructure | Mechanism | PCE enhancement | Reference |
|---------------------------|-------------------------------------|--|-----------------|-----------|
| GaAs | PEDOT:PSS decorated with Au NSs | Near – field enhancement, scattering | 3.85 % | [95] |
| Perovskites | Au NSs @ spiro-OMeTAD (HTL) | Near – field enhancement | 1.48 % | [96] |
| Silicon | Ag-Al alloy NPs at top surface | Scattering | 4.22 % | [97] |
| DSSC | Ag NPs @ TiO ₂ | Scattering, hot carriers injection | 0.79 % | [98] |
| Thin films (metal oxides) | n-Al:ZnO/Ag NPs/p-Cu ₂ O | Near – field enhancement, hot carriers injection | 4.3 % | [99] |

*NSs (nanostars), NPs (NPs), DSSC (dye synthesized solar cell), HTL (hole transport layer).

On the other hand, although Cu NPs present strong enhanced light absorption in the visible range, scattering and near-field intensity, scarce reports about inclusion of them in solar cells were found. Most of the works related to the plasmonic effect exploitation using Cu NPs were related to other applications like biological imaging [100], surface-enhanced Raman scattering (SERS) [101], light wave guiding [102], sensors [103] and photodetectors [104], showing similar performance that Au and Ag NPs [105]. Therefore, the inclusion of Cu NPs in solar cells is still at an early stage. One of the main reasons to hinder the inclusion of Cu NPs in many applications, compared to Au and Ag, is their easy oxidation [82]. However, their excellent plasmonic properties, Earth's crust abundance and lower cost compared to the after mentioned metals, make it an interesting and worthy candidate for further research.

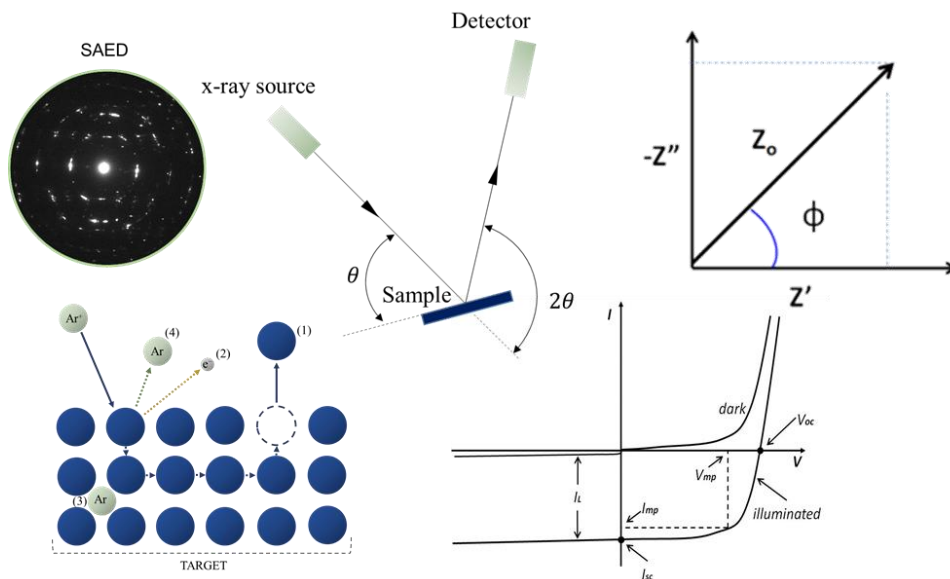
Cu-based nanostructures are typically synthesized using several primary techniques, including wet chemical method [106], electrochemical deposition [107], thermal decomposition [108], pulsed laser deposition [109], sputtering [82,110], among others. Among them, sputtering

method is a very promising technique since particles can be incorporated within different architectures, controlling the oxidation state and morphology [111].

In this thesis, we used the sputtering method using different routes to obtain Cu based plasmonic composites for all-oxide solar cells and optoelectronic applications.

CHAPTER 2

Synthesis and characterization methods



Abstract

This chapter provides a comprehensive overview of the synthesis and characterization methods employed for the study of plasmonic nanoparticles, composites, metal oxide thin films and devices. Deposition of metal oxides (ZnO, Cu₂O, CuO) and plasmonic CuNPs-Cu₂O composites was performed by DC Reactive Magnetron Sputtering while, for multilayers fabrication of Cu nanoparticles and ZnO, a Gas Aggregation Source (GAS) was integrated. Thermal treatment of CuNPs-Cu₂O composites was done using a Rapid Thermal Annealing (RTA) furnace. The crystalline structure of all the samples was studied by X-rays diffraction (XRD) and the optical characterization was performed using UV–Vis-NIR spectrophotometry and ellipsometric spectroscopy. To do compositional analysis and study the films morphology Scanning Electron Microscopy (SEM) and Transmission Electron Microscopy (TEM) were employed. Films resistivity was calculated after using the four-point probe method. Devices characterization was performed taking the J-V curves in dark and under 1 sun of light intensity (100 mW/cm²). Spectral Photocurrent (SP) and Impedance Spectroscopy (IS) also helped to understand the devices behavior.

Contents

| | |
|---|----|
| CHAPTER 2 | 27 |
| Synthesis and characterization methods | 27 |
| 2.1 Deposition methods and films preparation. | 31 |
| 2.1.1 Sputtering technique..... | 31 |
| 2.1.2 Gas Aggregation Source. | 36 |
| 2.1.3 Rapid Thermal Annealing system. | 38 |
| 2.2 Characterization of the films..... | 40 |
| 2.2.1 X- Rays Diffraction..... | 40 |
| 2.2.2 UV-Vis-NIR spectroscopy. | 42 |
| 2.2.3 Ellipsometric spectroscopy. | 45 |
| 2.2.4 Four-Point Probe method. | 47 |
| 2.2.5 Scanning Electron Microscopy. | 48 |
| 2.2.6 Transmission Electron Microscopy..... | 49 |
| 2.2.7 Current – Voltage characteristics | 52 |
| 2.2.8 Modulated Photocurrent Spectroscopy. | 55 |
| 2.2.9 Impedance spectroscopy. | 56 |

2.1 Deposition methods and films preparation.

2.1.1 Sputtering technique.

Generalities

Physical vapour deposition (PVD) involves a variety of in-vacuum methods to obtain thin films of metals and compounds. All of them are based on the physical generation of vapour from a source material (target), by different mechanisms, and its subsequent condensation as a layer on the desired surface. Sputtering is a widely used PVD technique employed on both laboratory and industrial scales. In this method, high-energy positive ions bombard the target ejecting atoms or molecules and propelling them towards the substrate by momentum transference.

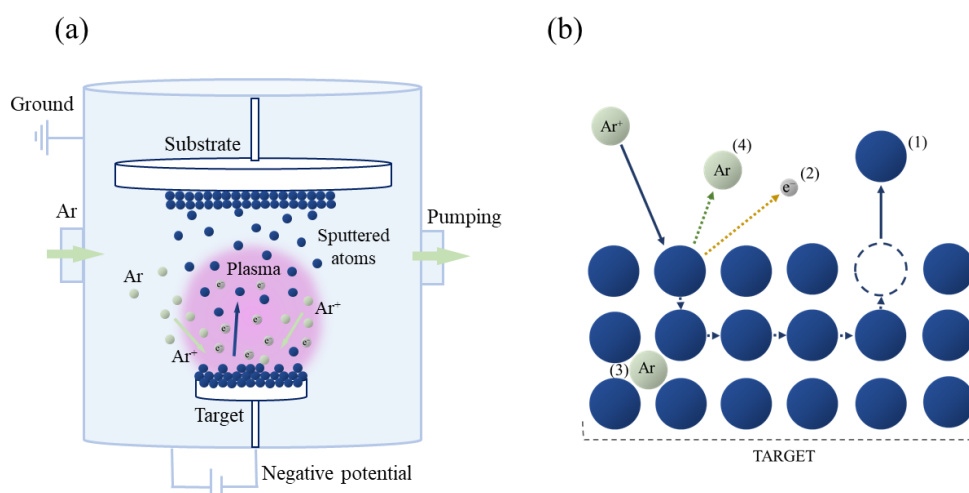


Figure 2.1: Graphical description of a typical sputtering process: (a) generation of plasma and deposition process inside a sputtering chamber; (b) processes taking place due to the ions-target interaction.

In a deposition chamber with a low-pressure rarefied atmosphere of an inert gas, typically argon (Ar), the walls of the chamber and the substrate are connected to the ground (anode), while a negative potential is applied to the target (cathode). This setup establishes an electrical discharge that ionizes the gas and generates a plasma. The potential difference between the cathode and wall causes the Ar^+ ions to be accelerated towards the target transferring momentum and causing material ejection (1). This material is then deposited on the substrate,

forming a film. Secondary electrons (SE) generation is also promoted by Ar^+ ions (2), contributing to keep the plasma discharge. Other processes like neutralization of Ar^+ ions by SE with subsequent reflection of Ar atoms (4), or Ar atoms implantation into the target (3) can take place [112,113]. Figure 2.1 depicts a schematic of a typical deposition and the processes occurring during the Ar^+ - target interaction.

In order to have the sputtering phenomenon, Ar^+ ions kinetic energy should be higher than a critical value (in the order of 15 - 30 eV) known as sputtering threshold [113]. Besides, the working pressure inside the chamber must be low enough [114]. To achieve this, a magnetron device is used to increase the mean free path of sputtered atoms towards the substrate. This ensures high-energy incident particles, a high deposition rate, and the possibility to obtain a dense morphology. Additionally, two important parameters should be considered in a sputtering process: the sputtering yield (Y) and the secondary electron emission coefficient of the target (γ). The sputtering yield is defined as the number of sputtered atoms per incident ion and depends on several factors, including the atomic masses of the incident ion and the target material, the energy of the ion, the surface binding energy of the target, and a dimensionless parameter that depends on the mass ratio of the incident ion and the target atom. On the other hand, the secondary emission coefficient (γ) is defined as the number of emitted SE per incident ion and depends principally on the material [115].

Direct current reactive magnetron sputtering

Up to this point, it has been discussed the basic diode configuration of the sputtering process. However, this configuration has its limitations, such as low gas ionization efficiency, resulting in a low deposition rate and poor film quality. Additionally, it requires operation at pressures higher than 1 Pa (10^{-2} mbar) to maintain the plasma. The magnetron configuration is an alternative in which the electrons that produce the plasma are confined near the target thanks to the presence of the electric (E) and magnetic (B) fields (Figure 2.2a) [114]. The magnetic field B generated by two concentric magnets of inverted polarities interacts with the electric field E established between the anode and the cathode. Both fields induce a Lorentz force in the region between the B field lines and the target surface, which drives the electrons to move in a torus-shape zone (Hall current) [115], causing an increase of the gas ionization probability.

This allows to work at lower pressure ($2 - 3 \times 10^{-3}$ mbar) and operating voltages (500 V compared to 2 - 3 kV in the basic configuration) and increase the ions flux density in this region of the target, promoting the material removal and the deposition rate [116]. Moreover, as the pressure is lower, sputtered particles experience fewer collisions as they drift towards the substrate and, thereby, impact on the film surface with a larger kinetic energy that can be used for diffusion on the surface and formation of a denser morphology.

A direct consequence of this process is the modification of the flat target surface with the appearance of an eroded zone (racetrack). As the deposition time increases, the effective area of this region increases, causing modifications in the values of working voltage and deposition rate. Racetrack can also affect the homogeneity of the film thickness, so the substrate is usually rotated [115].

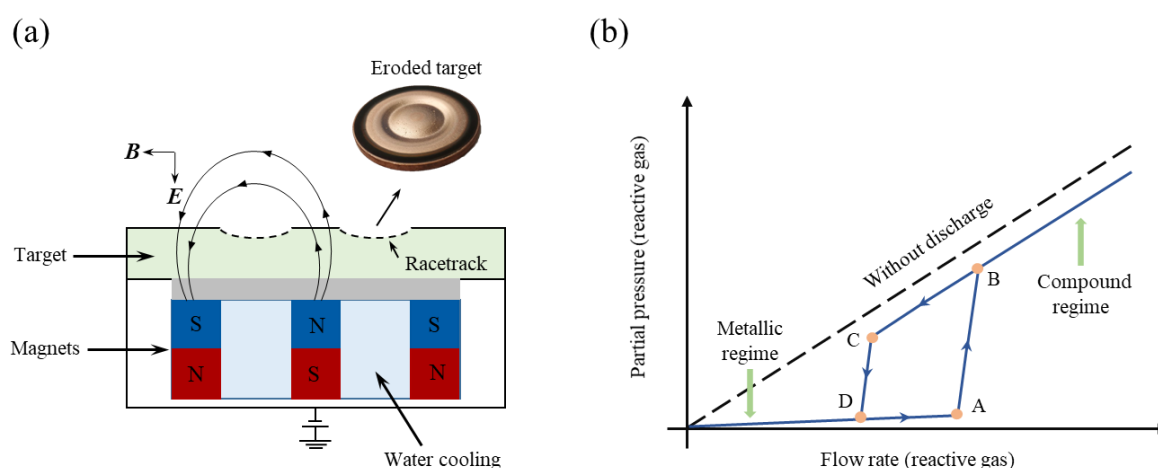


Figure 2.2: (a) Schematic of a planar magnetron configuration with two concentric magnets of equal intensity and opposite polarization. The higher impact of the Ar^+ ions in the electrons confinement zone generates a racetrack. (b) Typical hysteresis behavior of the partial pressure of a reactive gas as function of its flowrate, occurring during a high reactivity sputtering process.

The above description has been limited to the growth of metallic layers through the injection of an inert gas applying a continuous discharge (DC sputtering). Other gases capable of reacting with the metal atoms can also be introduced during the sputtering process to grow compounds such as oxides, nitrides, etc. Although these types of compounds can also be deposited using targets of the desired material, these are usually more expensive and fragile, and a radio frequency (RF) sputtering system is often required due to the insulating character of many

compounds [115]. In the reactive DC magnetron sputtering configuration, the reactive and inert gases are introduced, forming a mixture inside the chamber. Once injected, the reactive gas is able to react with any surface or species with which it comes into contact (walls, target, substrate, sputtered atoms) while the excess is extracted through the pumping system. The deposition rate will depend on the amount of gas introduced.

In many systems with high reactivity, the pressure responds in hysteresis manner to the introduced reactant gas flow. This behavior can be detailed in [Figure 2.2b](#) for a constant discharge current. When the gas is introduced into the chamber, most of it reacts with the chamber walls (Getter effect) being almost entirely consumed. A small poisoning of the target occurs and the contribution to the oxygen partial pressure is almost zero. The target remains in metallic mode and the sputtering efficiency is high (high deposition rates). This mode is known as the elemental or metallic regime (0-A). After a certain value of flowrate (A), runaway of the contamination of surfaces (target, walls) occurs. While the target adopts a more ceramic character, causing its sputtering rate to decrease, the etching rate of poisoning atoms by Ar^+ ions also decreases. In the meantime, the Getter effect by the target surface, walls and sputtered vapor decreases, causing a rise in the partial pressure of reactive gas that, in turn, increases the ceramic character of the target. Under such conditions, a small increase in the gas flow causes a considerable jump in the pressure inside the chamber (A-B). From state B onwards, the target is completely poisoned and the compound, or ceramic sputtering mode, is achieved. The deposition rate decreases as the sputtering yield of metals is higher compared to that of compounds, and the partial pressure increases at the same rate as in a non-discharge regime [117]. In other words, in this regime, the Getter effect becomes almost negligible. As the gas flow is decreased again, a target decontamination occurs and consequently a transition from D to B is observed, showing the hysteresis behavior. The system enters again in the metallic mode, but this transition is shifted towards lower values of the gas flowrate due to the greater thermodynamic stability and lower sputtering rate of oxides compared to metals. Hysteresis is an undesirable phenomenon in experimental reactive sputtering systems and can be diminished by controlling different variables such as the pumping speed, reactivity of the gas to the target material, size of the target, target material, target to substrate distance and discharge current [117,118].

Description of the sputtering system

In this thesis, thin films of metal oxides and composites were grown using a home-built magnetron sputtering system, whose components are described below:

Deposition chamber: The system consists of a 40-l chamber with three upwards equidistant magnetrons located at 7.5 cm from the chamber axis. The magnetrons can be moved 38 cm along the vertical direction, and the targets placed on them are parallel to the sample-holder (Figure 2.1a). The substrate holder consists of a 25 cm diameter metal disk coupled to a motor that allows it to rotate at different frequencies. No heating system is incorporated.

Power supply: An Advanced Energy MDX 500 DC power supply is used to establish the potential during the growth, with flexibility to set it via a voltage, current or power value. In our case, a constant current value was always defined. For substrates cleaning before deposition and ensuring of good adhesion to the substrate surface, an Advanced Energy Cesar[®] RF power generator is used.

Vacuum system: Two pumps, a primary and a turbomolecular, are connected to the deposition chamber. The primary one is a TRIVAC[®] B D 40 B oil-sealed rotary vane vacuum pump with a working speed of 40 m³/h, capable of reaching a pressure of 10⁻⁴ mbar. The turbomolecular is a water-cooled Alcatel Adixen ATP400 vacuum pump (6000 - 27000 rpm), which can establish a vacuum of 10⁻⁵ mbar in the chamber before deposition. The pressure is monitored by two gauges: (1) a PTR 90 N PENNINGVAC transmitter with measuring ranges of 10⁻³ - 1 mbar (Ar) and 3·10⁻³ – 0.3 mbar (Air, O₂); (2) a more accurate CERAVAC CTR 100N transmitter able to measure from 1.3 mbar to 1.3·10⁻⁴ mbar, insensitive to gas compositions and used to measure the pressure during deposition.

Gas monitoring system: The flow of gases entering the system is regulated using the Bronkhorst FlowView V1.23 software and a Bronkhorst High-Tech flowmeter. This setup enables the selection of the gas to be introduced (Ar, O₂, N₂) and the adjustment of its flowrate.

In a typical experiment four steps were followed:

1. The substrates were cleaned with acetone, ethanol and ultrasonic bath.

2. The samples were placed on the holder and then into the chamber, at 5 cm from the target. The position of the sample was fixed by measuring the distance respect to the center of the holder plate.
3. A primary vacuum was established ($\sim 5 \times 10^{-3}$ mbar) before turning on the turbomolecular pump. When a pressure between 10^{-5} and 10^{-4} mbar was reached, Ar and O₂ gases were introduced.
4. The RF generator was switched on for substrate cleaning. After 1 minute, the MDX generator was turned on (initiating the deposition) and then, the RF generator was turned off.

2.1.2 Gas Aggregation Source.

The sputtering system described in previous section is coupled to a NanoGen 50/Trio magnetron sputtered nanoparticles source (Figure 2.3). This complement allows to grow copper nanoparticles controlling their properties by changing experimental parameters like total pressure, target power, gases injection and magnetron position. The formation of nanoparticles and their growth occurs due to the condensation of a vapour of metal atoms sputtered under relative high pressure (0.1 - 0.9 mbar) in an atmosphere of argon or reactive gas mixture. This condensation process follows three main steps: metallic vapor supersaturation, nucleation, and subsequent cluster growth [119]. Clusters formation occurs in a limited space (aggregation zone) and spends a certain period of time (residence time) before be transported through a conical aperture towards the deposition chamber. The coupling of the nanoparticles source to the deposition chamber allows the synthesis of nanoparticles and thin layers separately, simultaneously, or sequentially, offering great flexibility to the system.

The schematic of the NanoGen system, as depicted in Figure 2.3, shows three concentric magnetrons with a diameter of 2.54 cm located inside a cylindrical chamber (~ 26 cm long). The chamber is connected to the main deposition chamber by a ~ 32 cm channel. The passage of nanoparticles from the source chamber to the channel occurs through a divergent conical funnel with a minimum aperture of ~ 3 mm. This is possible due to a pressure difference between the chambers (30 Pa – 40 Pa).

The pressure inside the source chamber (~ 40 Pa) can be defined by the pumping system of the deposition chamber. However, a differential pumping system is also connected to the source, allowing to control the pressure difference between chambers during the deposition and therefore the residence time. The pumping system consists of an Agilent IDP-7 Dry Scroll Vacuum pump with a base pressure of 4.0×10^{-2} mbar (7.2 m³/h) followed by a water-cooled Pfeiffer HiPace[®] 300 turbomolecular pump (918 m³/h for Ar gas). The pressure inside the aggregation chamber is sensed by a Leybold GmbH PENNINGVAC PTR90 gauge with a measuring range of $5 \cdot 10^{-9}$ – 1000 mbar.

The magnetrons current is fixed via a TDK-Lambda generator (630 V, 1.3 A) which allows to define the control mode by power, voltage or current [120]. The magnetrons system is coupled to a linear translation system which is controlled to define the distance between the target and the aperture (5 cm – 15 cm), controlling the aggregation length and therefore the time of the nanoparticles inside the source.

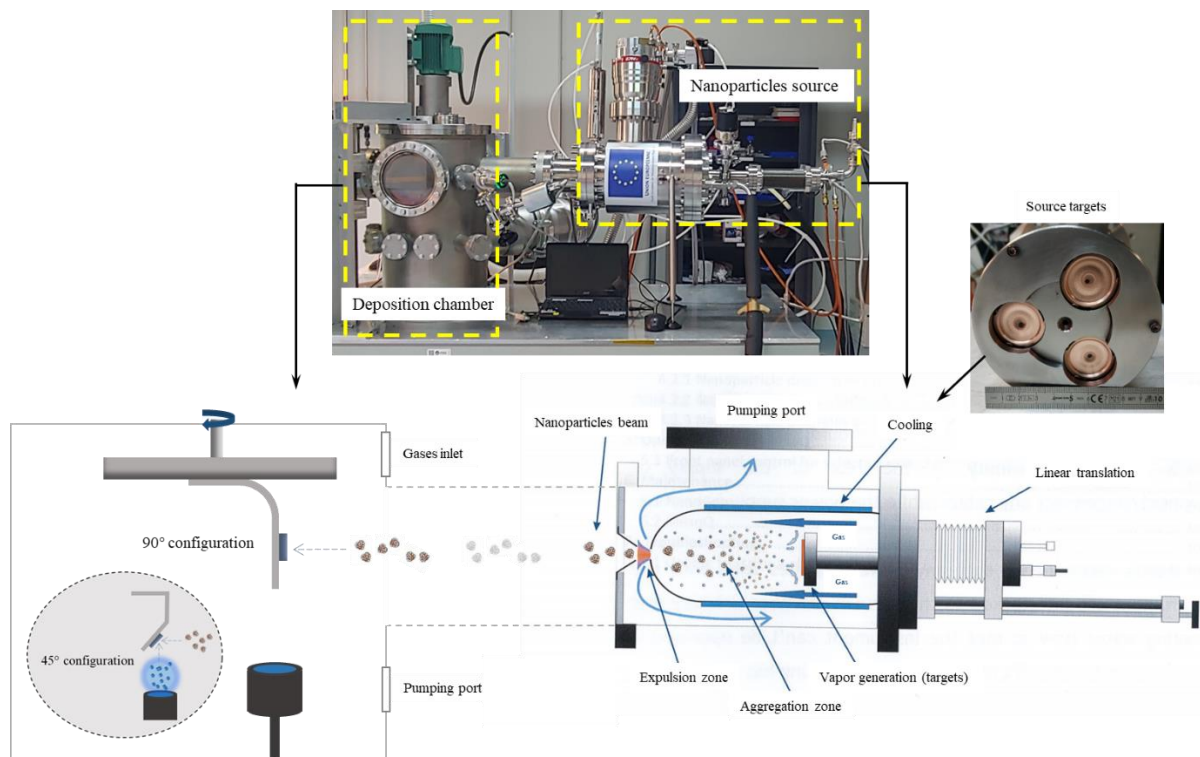


Figure 2.3: Picture of the sputtering system coupled to the NanoGen gas aggregation source (GAS). Below a schematic of the system, describing its parts and the nanoparticles deposition

process using a 90° configuration holder (for nanoparticles only) and a 45° configuration holder (for composites) (modified from [120]).

The cathode and walls of the aggregation chamber are cooled using water and liquid nitrogen, respectively. The low temperature of the liquid nitrogen allows to evacuate the heat generated during the condensation process, favouring the nucleation phenomena occurring inside the chamber. The injection of gas used during the formation of the nanoparticles (Ar) is done from the axis of the cathode. The gases inlet is monitored by a Mantis mass flow controller (MFC) and its corresponding MFC flowmeters.

In this thesis, the deposition of Cu nanoparticles on various substrates and materials (nickel grids, glass, and metal oxide films) was performed with the aim of controlling properties such as crystallinity, size, and density. Two different substrate holders were used: a 90° configuration holder for studying isolated nanoparticles and a 45° configuration holder for investigating multilayer or composite films. The parameters used in all the depositions is summarized in Table 2.1:

Table 2.1: Experimental parameters used for depositing Cu nanoparticles using the gas aggregation source.

| | |
|-----------------------------|---------------|
| Target - substrate distance | 50 cm - 60 cm |
| Generation current | 0.21 A |
| Working voltage | 390 V – 430 V |
| Ar flowrate | 160 sccm |

2.1.3 Rapid Thermal Annealing system.

An As-One 100 Rapid Thermal Annealing (RTA) furnace was used for all thermal annealing processes performed in this thesis. This system allows to perform a variety of annealing routines, reaching a wide range of temperatures (RT – 1250 °C, $\pm 2^\circ\text{C}$) with different ramps (until 200 °C/s) under atmospheric or vacuum conditions. The furnace is divided in two parts, the reactor with its associated circuits (Figure 2.4) and the control system.

The reactor consists of infrared halogen lamps inside a water-cooled stainless-steel chamber that transfer heat to the sample through a quartz window. The sample is placed on a silicon substrate supported by quartz pins. The temperature of the sample is then sensed by an optical pyrometer located below the silicon wafer and an ultra-fast digital PID controls the temperature [121]. The process is monitored from a computer via the AnnealSys Control Software (V5.0.3). An automatic macro-process was designed to ensure very low oxygen presence during annealing and study the composites films and devices with Cu nanoparticles while avoiding their oxidation.

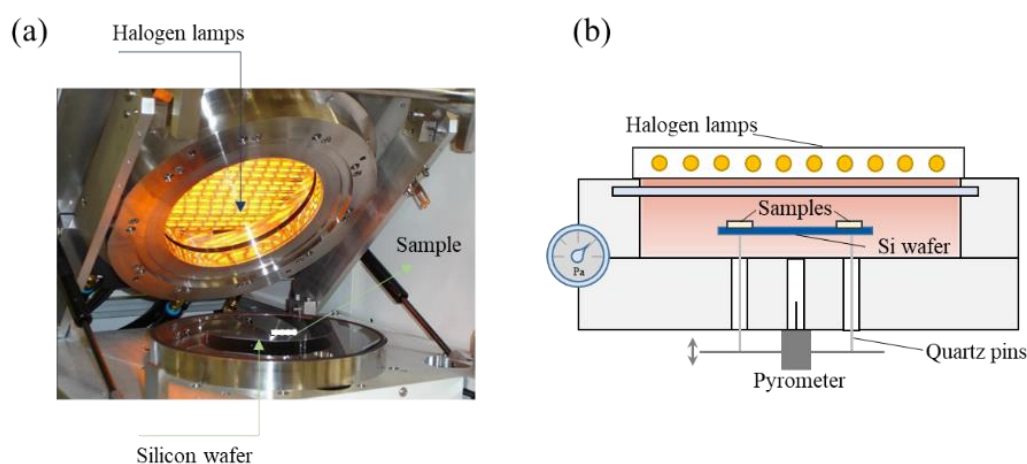


Figure 2.4: (a) Picture and (b) schematic of the annealing chamber of the As-One 100 Rapid Thermal Annealing (RTA) furnace (modified from [121]).

In a typical annealing process, an initial pumping is done and argon is injected until the atmospheric pressure is reached. Pumping and argon injection process is repeated 2 more times and nitrogen (α 1) is introduced (200 sccm) after pumping the argon again. The system is stabilized by decreasing the nitrogen flowrate (50 sccm) until the pressure is 352 Pa. The annealing starts increasing of temperature with a ramp of 15 °C/s until the set point is reached. Once this occurs the samples are treated during 1 hour in nitrogen environment. After 1 hour, the heating and nitrogen injection stop. Primary pumping is done until 200 Pa of pressure is reached. Argon is then purged until atmospheric pressure is achieved.

2.2 Characterization of the films.

2.2.1 X- Rays Diffraction.

X-ray diffraction is one of the most widely used basic methods to study the materials structure. The diffraction phenomenon occurs when an electromagnetic wave passes through a lattice whose spacing is of the same order as the wavelength of the incident radiation. In the case of a crystal, diffraction can be observed if the used wavelength is close to the interatomic distances (0.5-2.5 Å), corresponding to the X-rays spectrum. When X-rays are incident on a crystalline solid, they are scattered and interfere with each other constructively or destructively, resulting in the observation of diffraction peaks or intensity maxima in the first case if the Bragg's law is fulfilled:

$$2d_{hkl} \sin \theta_{hkl} = n\lambda \quad (2.1)$$

In this equation, n is an integer number, λ is the wavelength of the X-rays (the most commonly used wavelength is $\lambda = 1.5406 \text{ \AA}$, which corresponds to Cu $K\alpha$). In the Bragg-Brentano configuration, θ is the angle between the incident beam and the material surface, and d_{hkl} is the distance between planes with hkl Miller's indices, parallel to the surface (Figure 2.5a). Therefore, each crystalline structure has a unique diffraction pattern that describes its structural information and constitutes its "fingerprint".

There are several geometries for obtaining diffraction patterns. Bragg-Brentano, or θ - 2θ , configuration is the most commonly used (Figure 2.5b). In this configuration, the X-rays source is fixed while the sample rotates synchronically with the detector, at $\dot{\theta}$ and $2\dot{\theta}$ rates, respectively. With this geometry, only the planes parallel to the sample surface that fulfill the Bragg condition will be detected. In monocrystalline structures few peaks will appear since all the planes parallel to the surface belong to the same family. On the other hand, polycrystalline samples will show several peaks since many grains with different orientation conform the material.

A typical diffraction pattern corresponding to a polycrystalline Cu film, which present a cubic structure, is shown in the Figure 2.5c. Three peaks are observed corresponding to different planes family: $\{111\}$, $\{200\}$ and $\{220\}$, being the $\{200\}$ the most intense peak.

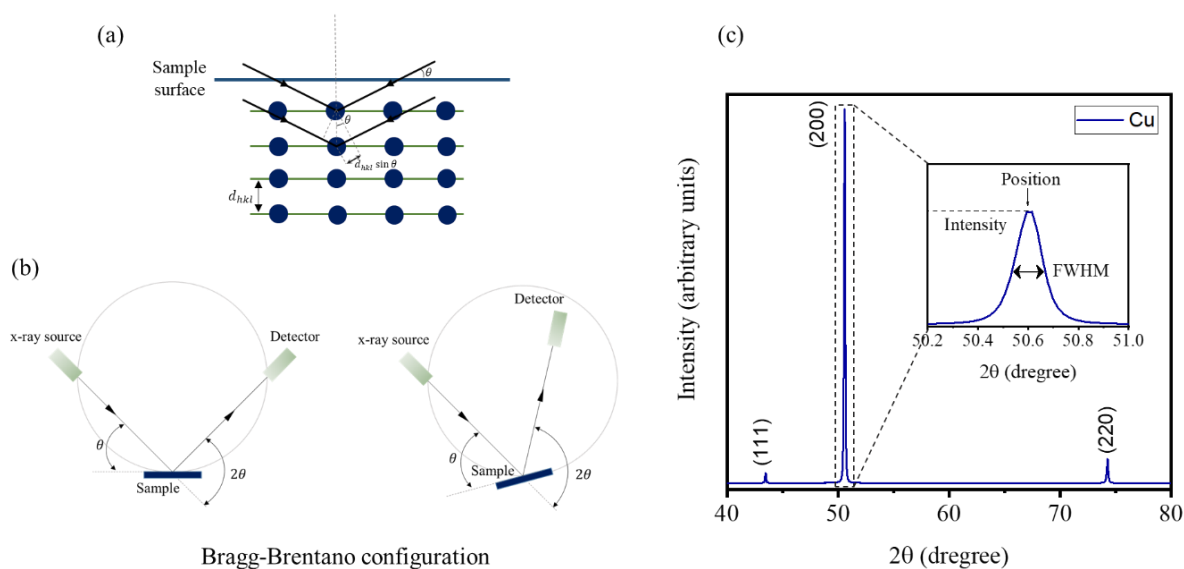


Figure 2.5: (a) Interaction of the X-rays with the atomic structure of a crystalline solid, (b) Bragg-Brentano configuration schematic showing how the patterns measurements are done and (c) typical pattern of Cu thin film with preferential orientation in the [100] direction. The parameters from which structural information is extracted (intensity, position and full width at the half maximum FWHM) are shown in the inset (modified from [122]).

Information about the crystalline structure of the material can be extracted by analysing the position, intensity and shape of the diffraction maxima or peaks in the pattern. The position of the peak (2θ) can give qualitative information about the phases present, the crystalline structure and the unit cell parameters. For example, interplanar distances can be directly determined using the Bragg's law equation. The intensity of the diffraction maxima indicates the preferential crystallographic orientation of the sample: the diffraction pattern showed in Figure 2.5c indicates that the measured Cu films have a strong preferential orientation perpendicular to the planes (200). On the other hand, the shape of the peaks, gives information about the microstructure of the material: defects, strains and length of coherent domains. In this thesis, to determine the average length of coherent domains, the diffraction peaks were adjusted to a Voigt function in order to determine the peaks parameters: intensity, position and full width at the half maximum (FWHM). With this last parameter and using the Scherrer formula it was possible to calculate the domains lengths of the hkl planes family:

$$L_{hkl} = \frac{k \lambda}{\beta \cos \theta} \quad (2.2)$$

In Scherrer equation the coherent domains length L_{hkl} depends on λ (the wavelength of radiation, 1.5406 Å in our case), β (the full width at half maximum (FWHM)), k (a constant that depends on the particles geometry and it's considered 0.829 in spherical particles) and θ [123,124].

In this thesis a diffractometer Bruker D8 Advanced in Bragg/Brentano configuration (Cu $K\alpha$ X-ray source, wavelength $\lambda = 0.15406$ nm) was employed to study the crystalline structure of the samples. The crystalline structure corresponding to each pattern was extracted using JCPDS database and DIFFRAC.EVA software provided by Bruker.

2.2.2 UV-Vis-NIR spectroscopy.

Optical properties of the thin films and plasmonic composites were studied by measuring transmittance and reflectance spectra using the UV-Vis-NIR spectroscopy technique. With this method, apart from the absorption coefficient, the bandgap and Urbach energy of the compounds were determined.

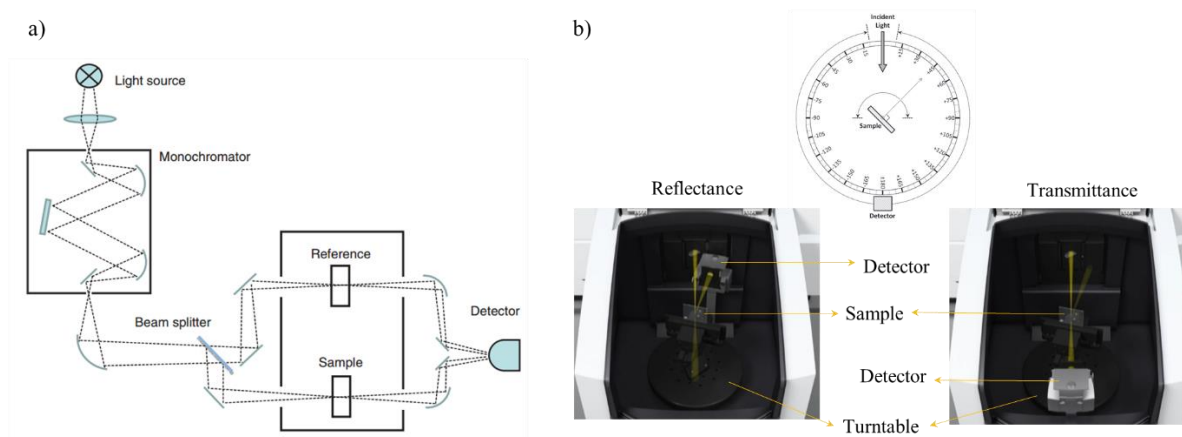


Figure 2.6: UV-Vis-NIR configurations used to obtain the transmittance and specular reflectance: (a) double beam [125] and (b) universal measurement accessory [126].

Two spectrometers with different configuration were used in this thesis: a double beam Cary 5000 UV-Vis-NIR spectrophotometer and a Cary 7000 UV-Vis-NIR Spectrophotometer with a Universal Measurement Accessory (UMA) (Figure 2.6). In both systems, a monochromatic light is focused on the sample, occurring different phenomena during this interaction:

reflectance (R), absorption (A), scattering (S) and transmission (T) of light. The sum of the fractions of these radiation intensities is equal to the incident light intensity ($R + T + S + A = 1$).

Transmittance and reflectance can be directly measured in both configurations. The intensity of transmitted T (reflected R) light is measured by a detector, which simultaneously receive a reference beam of the same monochromatic light and compare both intensities:

$$T(R) = I_{T(R)}/I_0 \quad (2.3)$$

where I_0 is the initial intensity of the light and $I_{T(R)}$ is the final intensity of the transmitted (reflected) light after interacting with the sample. That way, for each wavelength selected via a monochromator, a value of transmitted (reflected) radiation is obtained. Scattered light is not taken into account in this thesis since the films studied can be considered with relatively flat surfaces. An indication of this can be extracted from the reflectance spectrum if the reflectance does not decrease to zero for low wavelengths (high energies) [127].

In UMA configuration, the source and sample are fixed (defining the light incidence angle) and the detector is able to move almost 360° degrees around the sample (from 6° to 354°). By controlling the detector position (angle) respect to the incident beam, many measurements configuration are possible. In our case, transmittance and quasi-specular reflectance were measured selecting the following angles:

Table 2.2: Set angles used for transmittance and reflectance measurements in UMA.

| Measurement | Sample angle | Detector angle |
|---------------|--------------|----------------|
| Transmittance | 0° | 180° |
| Reflectance | 0° | 6° |

In practical terms, it is impossible to measure the film independently since it is always grown on a substrate. The substrate reflectance and transmittance must be taken into account to have accurate results. Considering the films facing the incident light, its transmittance results [128]:

$$T_{\text{film}} = T_{\text{meas}}/\sqrt{T_{\text{sub}}} \quad (2.4)$$

From T spectra, the absorption coefficient describing the amount of radiation absorbed by a material with thickness t at a specific wavelength, can be calculated according to the Beer-Lambert's law [127]:

$$T = e^{-\alpha t}, \quad \alpha = \frac{1}{t} \ln \left(\frac{1}{T} \right) \quad (2.5)$$

Considering films with some reflectance as product of metallic copper content and neglecting multiple reflections at the film/substrate interface, the expression becomes [129]:

$$\alpha = \frac{1}{t} \ln \left(\frac{1 - R}{T} \right) \quad (2.6)$$

The bandgap of the films can be calculated using the Tauc method, in which the absorption coefficient is related to the bandgap energy E_g by the following equation:

$$(\alpha h\nu)^n = C(h\nu - E_g) \quad (2.7)$$

where C and h are a proportionality constant and the Planck's constant, respectively, and ν is the light frequency. The exponent n depends on the nature of the bands transitions occurring in the material, being 2 for direct allowed transitions, $2/3$ for direct forbidden transitions and $1/2$ for indirect allowed transitions [130,131].

Plotting the left member as a function of $h\nu$ and fitting the linear section of the curve, the bandgap of the material will be its interception with the line $(\alpha h\nu)^n = 0$. In the Figure 2.7 a typical spectrum of transmittance/reflectance of Cu_2O is shown and its corresponding Tauc plot where the bandgap is estimated.

At energies below the bandgap, the absorption should be zero, however, interband states related to structural disorders and thermal fluctuation in the material originate a band tail in the absorption coefficient spectrum. The energy that quantifies the extent of such disorder can be determined from the Urbach rule, an empirical relationship that states that the absorption coefficient (α) as a function of photon energy ($h\nu$) near the bandgap follows an exponential dependence:

$$\alpha = \alpha_0 \exp \left(\frac{h\nu}{E_u} \right) \quad (2.8)$$

$$h\nu = E - E_0 \quad E_u = kT/\sigma$$

The constants E_0 , σ and α_0 depend on each material, in particular on its temperature in the last case [132,133]. By plotting the logarithm of the absorption coefficient as function of $h\nu$, the Urbach energy E_u will correspond to the inverse of the slope of the linear fit of the curve.

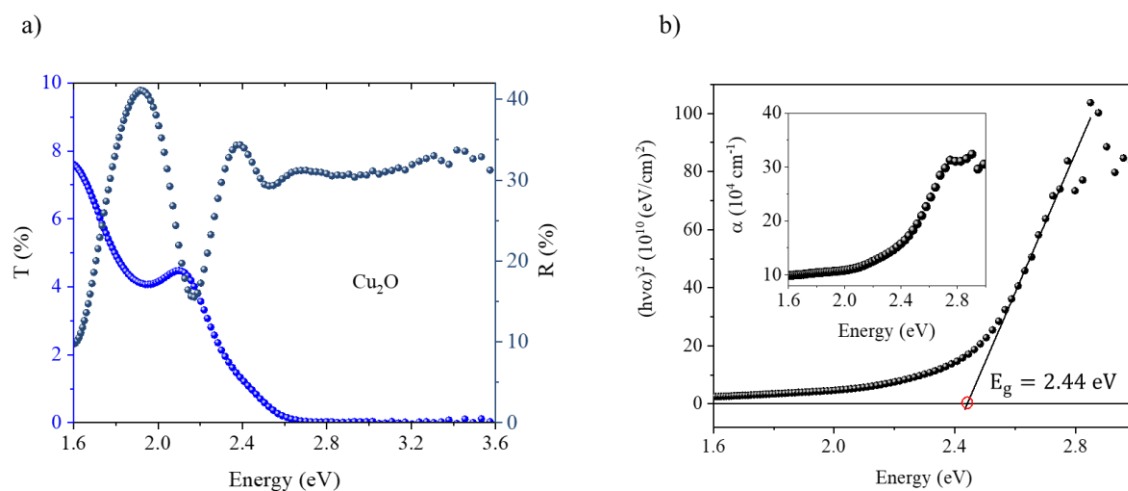


Figure 2.7: (a) Transmittance and reflectance spectra of a Cu_2O film grown by reactive magnetron sputtering. (b) Absorption coefficient (inset) and Tauc plot with the corresponding bandgap determination.

2.2.3 Ellipsometric spectroscopy.

Ellipsometry is an optical measurement technique used to determine smooth films thickness and other optical functions (refractive index, extinction coefficient, absorption coefficient, dielectric function). Its physical principle is based on the polarization change of a light beam when it is reflected from (or transmitted through) a layer. An ellipsometer consists of a light source (monochromatic or white), a polarization state generator, the sample, a polarization state detector and a light detector. Conventional spectroscopic ellipsometers use a white light source and include also a monochromator to select the wavelength of the incident beam (Figure 2.8).

In a typical measurement, the incident light is linearly polarized before reaching the sample with a certain angle (ϕ). The reflected beam has an elliptical polarization after its interaction with the sample since several interferences occur changing the ratio between the amplitudes

(Ψ) and the phase difference (Δ) of the electric field components (perpendicular (s) and parallel (p)).

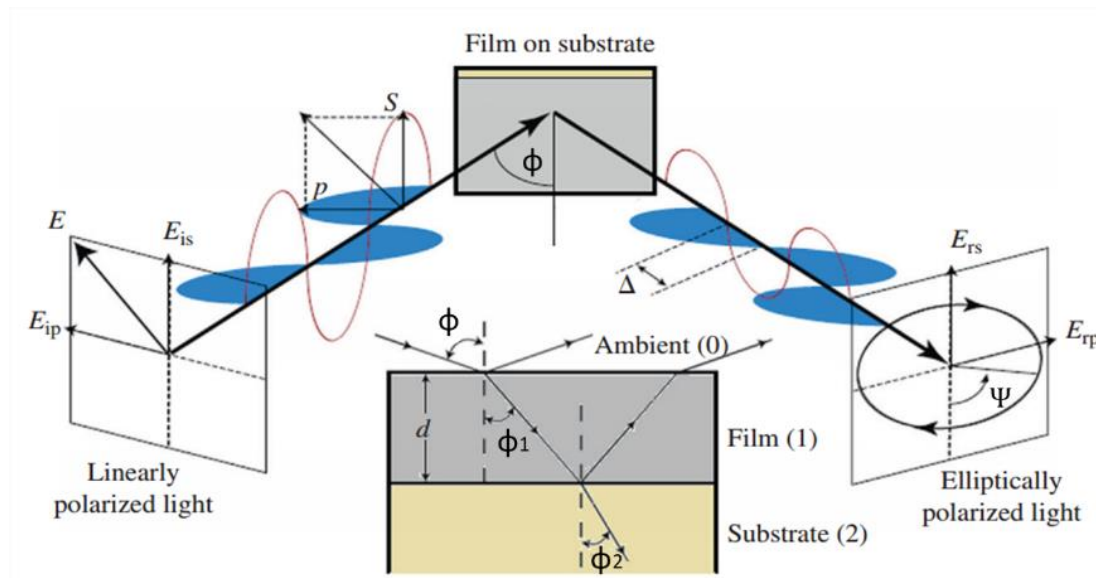


Figure 2.8: Schematic description of ellipsometric spectroscopy measurement (modified from [134]).

The ellipsometer detects these changes by directly measuring the luminosity flux intensity [134]:

$$I_s = \sin 2\Psi \sin \Delta \quad (2.9)$$

$$I_p = \sin 2\Psi \cos \Delta \quad (2.10)$$

The quantities I_s and I_p as function of the light wavelength do not directly reveal information about the material properties. To determine the thickness, optical constants, and phases volume ratio of the samples under investigation, it is necessary to employ physical models that take into account the specific characteristics of the system.

In homogeneous systems, the Lorentz oscillator is a versatile theoretical model used to describe the optical properties of semiconductors, insulators, and composites [135]. It serves as the foundation for several other methods including the Cauchy model (refractive index description), the Drude expression (free-electron metals modelling), the Forouhi-Bloomer model (complex dielectric response determination), the Tauc-Lorentz (bandgap energy and optical constants

determination) and Tanguy models (statistical description of electronic transitions around the bandgap) [136,137].

In heterogeneous systems, the effective medium approximation (EMA) includes various theories, such as the Lorentz-Lorentz, Maxwell Garnett, and Bruggeman models, to determine the effective dielectric constant of films composed of multiple materials. These models consider the mixing of individual constituents, with the host material often assumed to be air. The Lorentz-Lorentz theory addresses atomic-level mixing, while the Maxwell Garnett model applies when a minority phase is dispersed within a host material dominated by the largest constituent fraction. On the other hand, the Bruggeman model is employed when there is no clear majority fraction, treating both phases equally [135]. Moreover, the Bruggeman theory is commonly used to model surface roughness by treating it as a mixture of material and air, each occupying an equal volume fraction of 50%.

In this thesis, the ellipsometric spectroscopy was performed using a UVISSEL ellipsometer at different angles of incidence ϕ to minimize the mean square error. The models used for homogeneous thin films characterization were the Tauc-Lorentz (Cu_2O) and Tanguy (ZnO), while for composites ($\text{CuNPs-Cu}_2\text{O}$) a sum of two Lorentzian oscillators and a Tauc-Lorentz model were used. The Bruggeman model was applied to describe the surface roughness and multilayers compounds (ZnO-CuNPs).

2.2.4 Four-Point Probe method.

A very precise method to determine the resistivity of materials is the four-point probe technique. The method consists of four equidistant tips placed in a linear configuration on the sample surface (Figure 2.9). A current in the order of the μA (depending on the resistivity of the sample) is applied by the outer tips while the resulted voltage difference due to the current circulation is measured with the inner tips. With the current and its corresponding voltage value the sheet resistance can be calculated as $\rho_s = C (\Delta V/I)$ where C is a geometrical constant depending of the samples dimensions and the points separation [138]. If the thickness (t) of the film is known, the resistivity of the material is determined by $\rho = \rho_s * t$.

In this work, the resistivity of the samples was measured using a Four-Point probe system in a linear configuration via a Keithley 2700 Multimeter and a Keithley 237 Source Measure Unit.

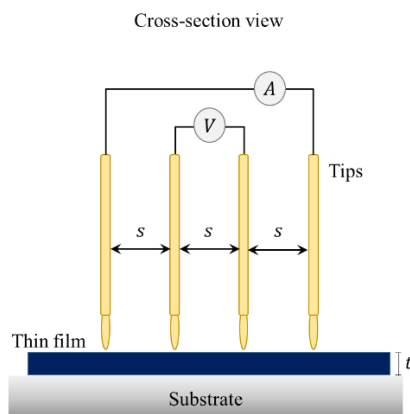


Figure 2.9: Four-point probe method using a linear configuration.

2.2.5 Scanning Electron Microscopy.

Surface micrographs and chemical composition of samples were obtained using Scanning Electron Microscopy (SEM). In a conventional SEM microscope, a high-energy electron beam is accelerated by a potential of a few kV and focused on a specific spot on the sample through magnetic lenses. A scanning system moves the spot across the sample surface, creating an image of a particular area. Various detectors capture signals resulting from the electron-sample interaction, including secondary electrons, backscattered electrons, characteristic X-rays, Auger electrons, among others (Figure 2.10).

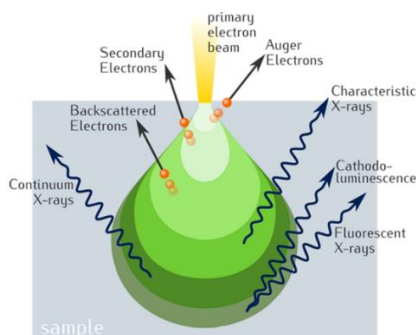


Figure 2.10: Schematic of the sample – electron beam interaction during scanning electron microscopy (modified from [139]).

Topographic images are generated by secondary electrons (SE) produced when incident electrons interact inelastically with atoms, transferring energy. The energy lost by incident electrons depends on the binding energy of the electron with the atom. Secondary electrons with low energy (3-5 eV) can only escape from a small region of a few nanometers, providing surface information [140]. The resolution of the micrograph is influenced by the accelerating voltage (energy of incident electrons) and the aperture, which controls the size and shape of the electron beam. Lower accelerating voltages reveal more surface details, while a smaller aperture size narrows the electron beam, resulting in improved resolution and finer details. On the other hand, a larger aperture allows a wider electron beam, sacrificing resolution but collecting a greater signal from the sample.

Chemical analysis, on the other hand, relies on the elastic interaction of primary electrons with the sample, particularly the emission of characteristic X-rays. When an incident electron collides with an inner shell electron, causing its removal, an outer shell electron falls into the lower energy state and emits an x-ray photon with a wavelength specific to the chemical element. Energy-dispersive spectroscopy (EDS) utilizes these characteristic X-rays to perform chemical analysis. The energy of the incident electron must be slightly higher (~ 2.6 times) than the energy required to remove the electron from the inner shells K, L, etc., (ionization energy) to efficiently emit X-rays during the analysis [141].

In this thesis, a ZEISS GeminiSEM 500 scanning electron microscope was used to obtain top-view micrographs using an Inlens secondary electron detector at low acceleration voltages (1 kV – 5 kV) and apertures (20 μm – 30 μm). The microscope is equipped with an Oxford Energy Dispersive X-ray spectrometer (EDS) detector allowing to perform the compositional analysis.

2.2.6 Transmission Electron Microscopy

Transmission electron microscopy (TEM) is a powerful technique used for atomic scale compositional and structural analysis. It involves the transmission of a focused beam of electrons through a thin specimen (< 100 nm), interacting by elastic scattering (which contributes to imaging) and inelastic scattering (which provides valuable spectroscopic information). This technique offers two main operation modes in order to study materials from different perspectives and gather specific information [142]:

Diffraction mode: In diffraction mode, crystalline structure is analysed. The back focal plane (BFP) of the objective lens collects electrons scattered in the same direction, projecting them onto a screen (Figure 2.11a). Single crystals show a spots array or a diffraction pattern representing (hkl) crystallographic planes. Polycrystalline and amorphous materials display rings, with amorphous patterns being broader. Selected-Area Electron Diffraction (SAED) technique focuses on a specific sample area using an aperture in the image plane (Figure 2.12). HRTEM micrographs produce also diffraction patterns through Fast Fourier Transformed (FFT) analysis.

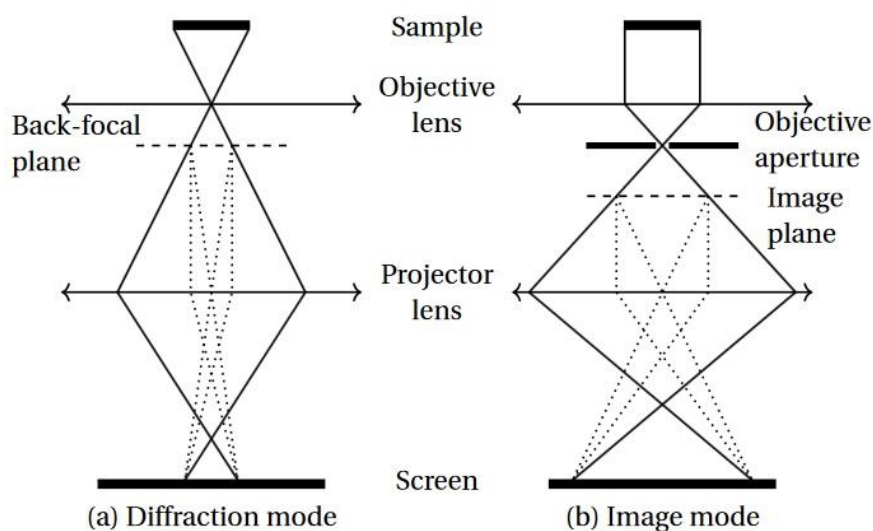


Figure 2.11: Schematic showing, in a simple representation, the TEM configuration for (a) diffraction and (b) imaging mode [46].

TEM image mode: This mode captures high-resolution images of the transmitted electron beam, providing details about sample morphology, structure, defects, and nanoscale features (Figure 2.11b). Bright-field imaging (BF) shows the overall structure by capturing directly transmitted electrons (brighter regions associated with lighter elements). Dark-field imaging (DF) blocks the transmitted beam, highlighting specific scattering regions, defects, and heavy elements (Figure 2.12). A specific diffraction spot or a range of diffraction spots can be selected to form the DF image. High-resolution imaging (HR) captures images with exceptional spatial resolution, revealing atom arrangement, lattice planes, defects, interfaces, and nanoscale features.

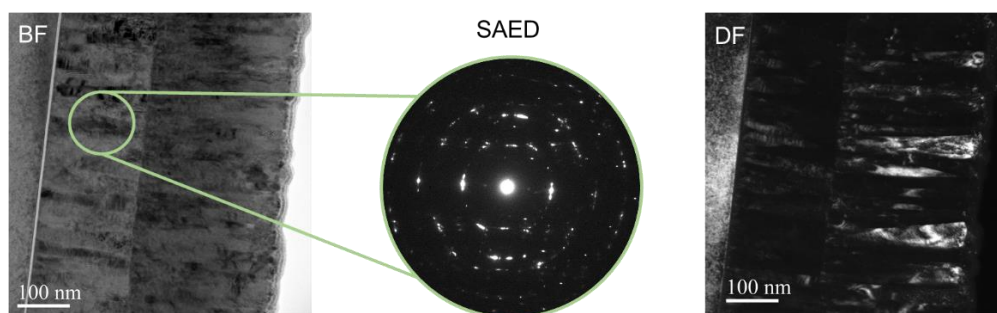


Figure 2.12: Examples of micrographs taken under diffraction and image modes. Bright and dark field micrographs of n-ZnO/p-Cu₂O junction and SAED corresponding to the ZnO film.

Other techniques are available within TEM to further understand the chemical composition and atomic structure of the material:

Scanning Transmission Electron Microscopy (STEM): STEM mode scans a focused electron beam across a sample for high-resolution imaging. It achieves atomic-scale resolution and enables elemental mapping with detectors like HAADF or EDS. High-angle annular dark field (HAADF) imaging collects high-angle scattered electrons for atomic number-based contrast, while EDS collects characteristic X-rays for analysis. STEM is valuable for nanomaterial imaging, interface examination and nanoparticle analysis, revealing structure, composition, and elemental distribution [142].

Electron Energy-Loss Spectroscopy (EELS): This technique reveals useful information regarding the chemical state, bonding, electronic structure, etc. through inelastic electron-sample interactions and is usually recorded at each pixel during STEM imaging. An EELS spectrum consists on a plot of incident electron energy versus energy loss (Figure 2.13). At energies close to zero a zero-loss peak appears corresponding to transmitted or elastically scattered electrons. At higher energies (< 50 eV), peaks corresponding to conduction to valence band transitions appear, giving information about the bandgap and defects states in semiconductors or insulators. Plasmons bands can also be found. From 50 eV onwards, the energy-loss falls considerably but some ionization edges can be observed. These peaks appear as result of ionization of electrons from the inner atomic shells (K, L, M, etc.) and a chemical element can be directly associated. According to atomic theory calculations, K-edges exhibit a triangular shape (saw tooth), while L, M, and higher-order edges can display either rounded profiles with a delayed maximum or sharp peaks right at the ionization edge (commonly

referred to as "white lines"). The analysis of this fine structure is known as energy-loss-near-edge spectroscopy (ELNES). In transition metals, white lines appear at L-edge energy (split in L_2 and L_3 by spin coupling) due to transitions from the core 2p states to unoccupied 3d states (above de Fermi level) [143,144]. The ratio of the white lines intensities is related to oxidation states, which is useful to identify the presence of metallic copper or copper oxides, for example.

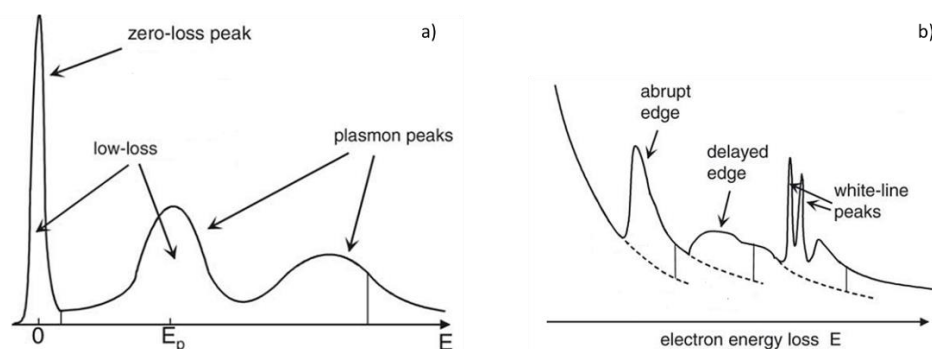


Figure 2.13: Schematic of a typical EELS spectrum: peaks appearing at (a) low loss and (b) high loss regions are shown (modified from [143]).

Energy-Filtered TEM (EFTEM): EFTEM combines imaging and spectroscopy by utilizing an energy filter to select and analyse specific energy-loss ranges in the electron beam. It allows to obtain elemental maps, electron energy-loss spectra, and perform chemical mapping of the sample [142].

Transmission electron microscopy (TEM) investigations were carried out using a JEM - ARM 200F Cold FEG TEM/STEM operating at 200 kV coupled with a GIF Quantum 965 ER. The samples were prepared using a focused ion beam with a dual-beam SEM-FIB FEI Helios NanoLab 600i. Using TEM mode, bright field and dark field images were collected. With HRTEM particles size were estimated and using STEM mode, energy loss near edge structure (ELNES) spectra at the O-K and Cu- $L_{2,3}$ edges as well as Cu and O composite composition maps were obtained.

2.2.7 Current – Voltage characteristics

Optoelectronic devices like solar cells, photodetectors, diodes, and lasers are based on p-n junctions. Measuring current as a function of applied voltage across the n-type and p-type sides

evaluates their energy conversion efficiency. This non-linear voltamperic characteristic is described by the diode equation:

$$I = I_s \left(e^{\frac{qV}{n k T}} - 1 \right) \quad (2.11)$$

Here, I_s represents the reverse dark saturation current, q is the electron charge, n is the diode ideality factor, k is the Boltzmann constant and T is the absolute temperature in Kelvin [145].

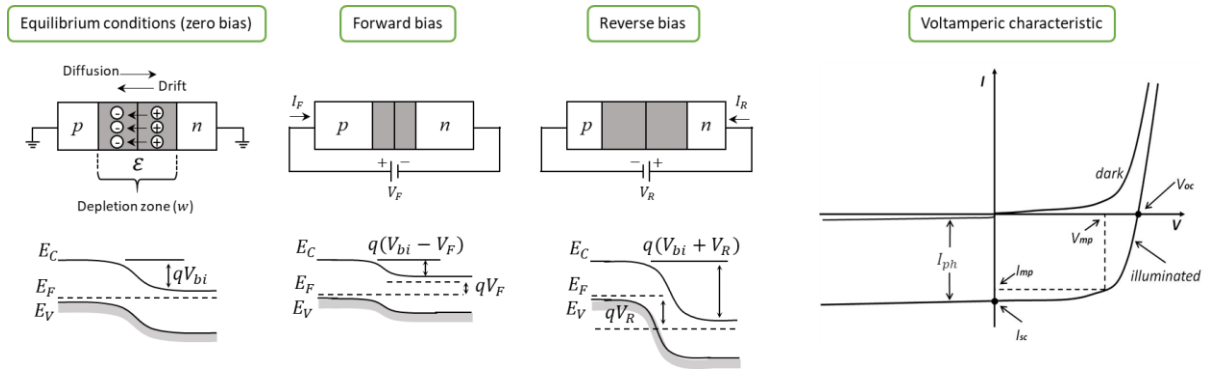


Figure 2.14: Schematic of a p-n junction and bands alignments under equilibrium, forward and backward conditions (modified from [43]). I-V characteristic curves indicating the principal parameters determining the efficiency of the device [146].

Under zero bias condition, free electrons and holes (majority carriers) diffuse across the p-n junction, leading to the accumulation of ionized donor and acceptor atoms near the junction (forming a depletion region). This generates a drift electric field \mathcal{E} , establishing a potential barrier (Figure 2.14). Equilibrium is achieved when the carrier diffusion current balances the drift current induced by the electric field, resulting in no net current flow. The built-in potential, determined by the concentration of acceptors and donors as well as the depletion region width, characterize this equilibrium state.

Applying a forward bias (higher voltage at the p-type terminal) reduces the drift potential ($V_{bi} - V_F$), resulting in a diffusion electron current from the n-side to the p-side of the junction. This current increases with higher bias (first quadrant in the voltamperic characteristic graph). In reverse bias, the potential barrier increases ($V_{bi} + V_R$), obstructing electron flow through the p-type material. However, a small and nearly constant current (I_s) emerges for reverse biases (third quadrant) (Figure 2.14) [145].

Under illumination, the p-n junction absorbs photons with energies equal to, or exceeding, the bandgap, creating electron-hole pairs. Electrons diffuse to the n-type conduction band while holes migrate to the p-type material due to the electric field ε . This shifts the diode curve towards negative currents in a quantity I_{ph} , leading to modifications in the diode equation [147]:

$$I = I_0 \left(e^{\frac{qV}{nkT}} - 1 \right) - I_{ph} \quad (2.12)$$

At zero bias (short circuit condition) the maximum negative current is reached ($I_{ph} = I_{sc}$). Short circuit current depends on the light intensity and photogenerated carriers (related to the absorption coefficient and bandgap) and the diffusion length of carriers. The diffusion length, which affects the efficiency of electron-hole pair collection in the depletion zone, depends on material properties (quality and defects), temperature, and doping level.

On the other hand, in open circuit conditions, where no current will flow through the device, a maximum voltage V_{oc} will appear due to the photogenerated charges accumulation at the n and p terminals. Therefore, V_{oc} will be mainly affected by the properties of the semiconductors and the transport mechanisms present in the p-n junction: bandgap, temperature, doping concentration and recombination mechanisms. V_{oc} is directly proportional to the bandgap and inversely proportional to temperature and recombination [147].

In non-ideal conditions, other parameters like shunt and series resistance must be considered. Shunt resistance refers to the resistance path running parallel to the intended current flow, caused by junction defects or structural imperfections. Higher shunt resistance reduces current leakage. Series resistance, inherent to electrical components, hinders current flow along the intended path. Lower series resistance allows for efficient current flow. Balancing these resistance factors is crucial for optimizing device performance [147].

The efficiency of a solar cell depends on the I_{ph} , V_{oc} and the fill factor (FF). The fill factor depends on the two first parameters and the maximum power ($V_m \times I_m$) reached in working conditions and gives an idea of how "square" the I-V curve of the device is, being its optimal value equal to one:

$$FF = \frac{I_{mp} \times V_{mp}}{I_{sc} \times V_{oc}} \quad (2.13)$$

Then, defining the efficiency as the ratio between the incident light power P_{light} and the generated power, results [147]:

$$\eta = \frac{I_{\text{SC}} \times V_{\text{OC}} \times \text{FF}}{P_{\text{light}}} \quad (2.14)$$

The I-V measurements in dark and under 1 sun of light intensity (100 mW/cm^2) were performed using a Keithley 2400 Source Meter Unit, a halogen lamp of 150 W and 24 V whose intensity was regulated by a DSC-Electronics Programmable DC Power Supply using a Calibrated Reference silicon solar cell from Radboud University Nijmegen.

2.2.8 Modulated Photocurrent Spectroscopy.

Modulated Photocurrent Spectroscopy is a characterization technique that provides valuable insights about spectral sensitivity and device performance across different wavelengths. It involves illuminating the device with light of varying wavelengths and recording the resulting photocurrent. Modulating the incident light at a specific frequency helps separate the photocurrent signal from noise, enhancing measurement accuracy.

Spectral response (SR) is the relationship between the device photocurrent and the incident light power at each wavelength. By plotting the photocurrent as a function of wavelength, information about the device absorption properties and spectral range of operation is provided [147].

Quantum efficiency (QE) measures the device effectiveness in converting incident photons into electrical charge carriers. It represents the ratio of charge carriers generated by absorbed photons to the total number of incident photons. Higher quantum efficiency indicates better conversion of light into electrical current. Factors influencing quantum efficiency include material properties, bandgap energy, absorption coefficient, and losses due to recombination and reflection. The quantum efficiency and spectral response are interconnected through the following expression [148]:

$$\text{SR} = \frac{q\lambda}{hc} \text{QE} \quad (2.15)$$

In this thesis spectral photocurrent was measured using a modulated photocurrent spectroscopy system equipped with a xenon lamp with a high stability regulated power system (300 W from

Lot-Oriel), a monochromator (Omni- λ 300i model with a 1200 g/mm grating) giving a monochromatic light in the 300-1100 nm wavelength range with a resolution of 0.1 nm, a Stanford Research current preamplifier (model SR570) and a lock-in amplifier (model SR850).

2.2.9 Impedance Spectroscopy.

Impedance Spectroscopy (IS) is a very useful technique to study the physical and chemical properties of photo and electro-active materials, interfaces and multilayer devices. The impedance measurements are based on the application of an alternating voltage V_{ac} , varying its frequency and measuring the alternating current I_{ac} response (Figure 2.15 a.1). The current response as function of the voltage frequency will give information of the relaxation processes that takes place such as electrical and ionic conduction, dipoles polarization, lattice distortions, etc. At small frequencies (Hz – MHz), slow processes like conduction and charge transference at interfaces (μs – s) can be studied, while for analysis of structural properties higher frequencies (MHz – GHz) are required [149]. The measurements can be done under different conditions like illumination, voltage bias or temperature.

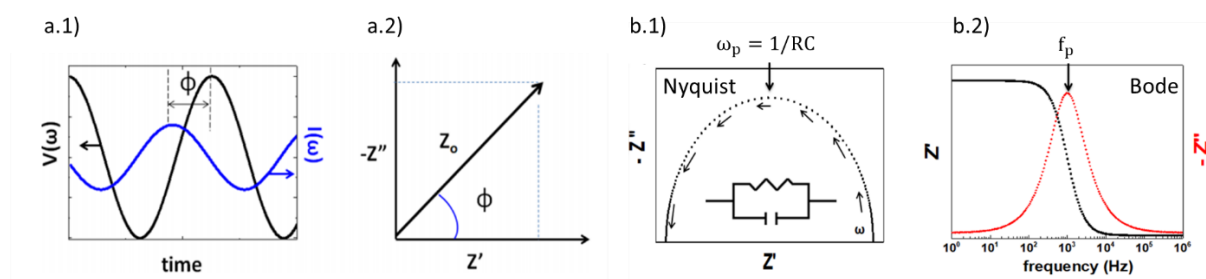


Figure 2.15: (a.1) Representation of the sinusoidal applied voltage and resultant current in the time scale; (a.2) complex impedance representation; (b.1) Nyquist and (b.2) Bode representations used for the fitting and interpretation of impedance measurements (modified from [149]).

In the time domain, the alternating voltage and current can be expressed as sinusoidal functions. The complex magnitude that relates both functions and physically represents the resistance of the sample, known as impedance $Z(t)$, is given by:

$$Z(t) = \frac{V(t)}{I(t)} = Z_0 e^{-i\phi} \quad (2.16)$$

where, $Z_0 = \frac{V_0}{I_0}$ is the ratio between the voltage and current signals amplitudes and ϕ is the phase difference between them (Figure 2.15 a.2).

Impedance can be written in terms of ideal circuit elements as Resistors (R), Capacitors (C) and Inductors (L). Typically, when a system is studied, an equivalent circuit is attributed taking into account real physical and chemical processes related to each circuit element. For example, resistors are dissipative elements that oppose to the current flow while capacitors describe charge accumulation that usually appears at the interfaces. Inductance, on the other hand, opposes changes in current flow by an electromagnetic force. RC elements are present in most of the solar cells systems describing charge transference or conductivity. The RC product represents the characteristic time constant of the corresponding relaxation process described.

Usually, several relaxation processes occur with a distribution of time scale, such as charge transference in non-uniform electrode surface, carrier transport in amorphous semiconductors, etc. In that case, a constant phase element (CPE) is included in the circuit, substituting the ideal capacitor element:

$$Z_{\text{CPE}} = \frac{1}{Q(i\omega)^n} \quad (2.17)$$

The dispersion parameter n determines the meaning of Q . When $n = 1$, $Q = C$ and when $n = 0$ then $Q = \frac{1}{R}$ [149].

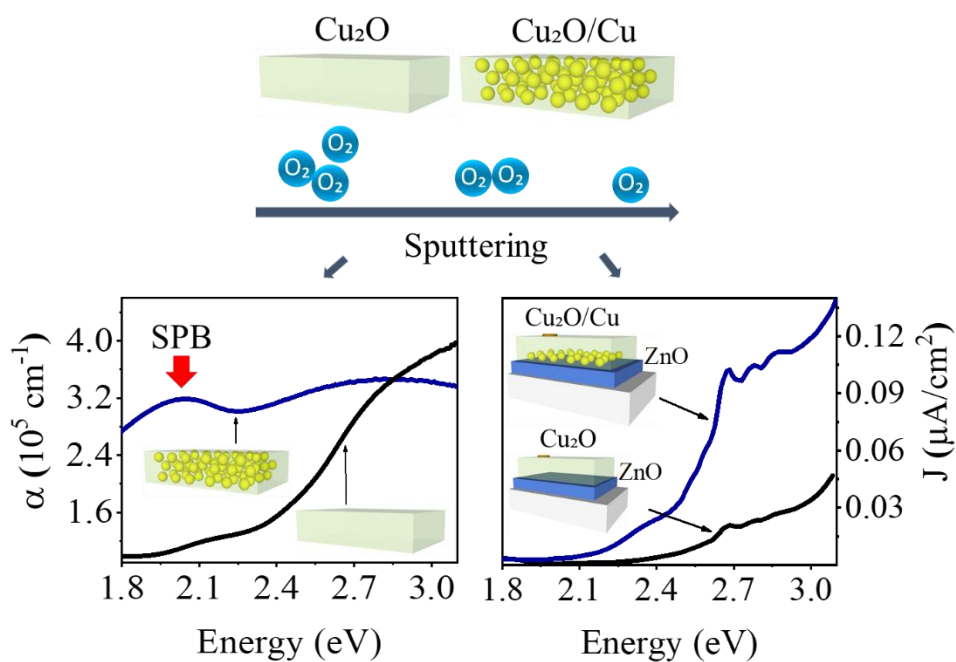
Two principal representation are used for IS interpretation: Nyquist and Bode plots (Figure 2.15 b.1 and b.2). The former is the representation of the complex impedance which is usually a semicircle for RC elements. When the semicircle is distorted indicates the presence of a CPE instead an ideal C element. From the Nyquist plot, the RC time constant τ ($RC = \tau$) can be calculated as $\omega_p \tau = 1$, where ω_p is the angular frequency at the maximum point of the semicircle and is related to the voltage signal frequency as $\omega_p = 2\pi f_p$. The number of semicircles indicates the number of relaxation processes and usually can appear overlapped. This kind of representation is mostly used when the graph is fitted in order to define how many time constants are in the system, extract the circuit elements values and do quantitative

analysis. The Bode plot, on the other hand, is a representation of any parameter (phase, impedance real part Z' , impedance imaginary part Z'') in the frequency domain. From Z'' (or ϕ) vs f graphs it is possible to directly determine time constants as carrier life time considering a conduction or transference process [149].

In this thesis, impedance measurements of solar devices were performed using a HIOKI IM3570 impedance analyser in a two-probe configuration (contacting FTO and gold device electrodes) under illumination, at zero bias, in a frequency range of 4 Hz – 5 MHz and 10 mV of V_{ac} . The same light source used for I-V measurements was incorporated in this set up.

CHAPTER 3

Reactively-sputtered plasmonic composites based on Cu nanoparticles and metal oxides semiconductors



Abstract

In this study plasmonic copper (Cu) nanoparticles were in-situ grown into a Cu₂O semiconductor matrix by using reactive magnetron sputtering and adjusting the amount of oxygen available during the synthesis. By varying only the oxygen flowrate (OFR) and employing a single Cu target, it was possible to observe the evolution in the simultaneous formation of metallic Cu and Cu₂O phases for oxygen-poor conditions. Such formation is accompanied by the development of the surface plasmon band (SPB) corresponding to Cu, as evidenced by optical measurements. Sample position with respect to the target axis was found to also have an influence in the crystallinity, optical absorption and electrical resistivity of the films. Devices based on the studied nanocomposites were characterized by J-V and spectral photocurrent measurements, showing an increase of the photocurrent density under light illumination as a result of the plasmonic particles incorporation and consequent hot carriers injection.

Contents

| | |
|--|----|
| CHAPTER 3 | 59 |
| Reactively-sputtered plasmonic composites based on Cu nanoparticles and metal oxides semiconductors | 59 |
| 3.1 Introduction | 63 |
| 3.2 Cu-O films deposition | 64 |
| 3.2.1 Characterization of CuNPs-Cu ₂ O composites: oxygen flowrate dependence. | 67 |
| 3.2.2 Characterization of CuNPs-Cu ₂ O composites: substrate position dependence. | 75 |
| 3.3 Devices fabrication | 82 |
| 3.3.1 Photocurrent enhancement with plasmonic particles incorporation. | 83 |
| 3.3.2 Performance enhancement of the nanocomposites. | 88 |
| Chapter conclusions | 89 |

3.1 Introduction

As mentioned in [Chapter 1](#), metal nanoparticles (NPs) have been extensively studied due to their promising optical properties [\[150\]](#). One of the most interesting features of metal NPs is their capability to exhibit the so-called localized surface plasmon resonance (LSPR), which refers to a coherent oscillation of the conduction band electrons in nanoobjects interacting with an external electro-magnetic field of the same frequency as the metal plasmon frequency [\[90,151,152\]](#). Plasmon modes and energies strongly depend on metal NPs parameters like size, shape, inter-particle distance and the refractive index of the surrounding media [\[85,88\]](#).

While metal NPs hosting the LSPR effect can be produced by various chemical or physical methods such as electrodeposition [\[153\]](#), sputtering [\[154\]](#), laser ablation and electron beam lithography [\[85\]](#), isolated metal NPs, among which Au, Ag, and Cu are known examples [\[84\]](#), tend to aggregate and are prone to oxidation. An interesting strategy to avoid these phenomena is to embed them into a proper matrix to better exploit their unique optical behavior and, at the same time, protect them from the surrounding environment. Interfacing semiconductor metal oxides (like ZnO, Cu₂O and TiO₂) and metal nanoparticles is of great interest for the enhancement of light harvesting in optoelectronic applications [\[154–158\]](#). Nevertheless, most of the studies on such systems involve expensive plasmonic metals (like Au and Ag), which makes Cu an interesting/inexpensive alternative to consider due to its abundance in the Earth's crust, non-toxicity and recyclability. Since copper is being already used in the microelectronic industry for interconnects, copper-based devices would be easy to implement. Furthermore, it has been demonstrated the effective transfer of “hot” charge carriers from this metal to various metal oxide semiconductors like ZnO [\[159\]](#), TiO₂ [\[160\]](#) and Cu₂O [\[161\]](#), under illumination as consequence of LSPR de-excitation. During the last decade, the number of studies using Cu₂O in various applications, e.g., photocatalysis [\[162–165\]](#), gas sensors [\[166–168\]](#) and solar cells [\[162,169–171\]](#), have increased due to its low cost, possibility of including it in large scale production as a result of the abundance of copper and oxygen, its absorption in the visible range of the electromagnetic spectrum and p-type conductivity. Moreover, this semiconductor can be obtained by multiple vacuum and non-vacuum methods such as electrochemical deposition, chemical oxidation, laser deposition, chemical vapor deposition, sputtering, among others [\[162\]](#).

Coupling metallic Cu NPs to Cu₂O and protecting the NPs from oxidation by the environment is challenging because it requires that Cu⁰ and Cu⁺ oxidation states coexist but are well separated spatially and, simultaneously, that Cu⁺ plays a protecting role for Cu⁰. Despite this can be achieved in nanoparticles forming core-shell heterostructures using physical or chemical approaches [106,109,110,153,172,173], the synthesis of composite films using a process compatible with the microelectronic industry would open new possibilities such as ease of implementation in future devices.

In this study we report on a single step route to synthesize nanocomposite films consisting in Cu NPs embedded in a Cu₂O matrix and showing the LSPR effect. This study tests the hypothesis that by carefully controlling the amount of oxygen available during the condensation of copper vapor to form a thin film, it is possible to restrict the oxidation to a fraction of the copper atoms landed on the growing film surface and to induce the segregation of remaining metallic copper atoms in order to form the sought architecture. For this, we resort to reactive sputtering deposition from a copper target in an argon-oxygen atmosphere. The influence of the elaboration parameters on the microstructure, optical and electrical properties of the synthesized films is investigated. Furthermore, J-V and spectral photocurrent measurements of CuNPs-Cu₂O nanocomposite-based devices, will test the possibility to increase the photocurrent by hot carriers injection.

3.2 Cu-O films deposition

In order to obtain, simultaneously, Cu₂O and Cu phases to form composites with plasmonic response, Cu-O films were grown on glass microscope slides using a Cu target facing the holder, at 5 cm of the sample. The position of the samples on the holder surface was measured with respect to the holder rotation axis. The argon flowrate was fixed at 50 sccm while the flowrate of the reactive O₂ gas (OFR) was changed. The substrate-holder was rotated at 3.5 Hz to ensure a good substrate covering. The base pressure into the chamber reached around 0.04 Pa and the total pressure during deposition was between 0.3 - 0.5 Pa, depending on the OFR, while a discharge current of 0.15 A was established. No intentional heating was applied and therefore deposition was accomplished close to room temperature. Surface activation was done by radiofrequency polarization (1 min) before each growth process to enable good adhesion of the

deposited film to the glass substrate. An example of the samples placement in the holder plate (at 2 cm of its axis) and resulting films changing the OFR, is shown in [Figure 3.1](#).

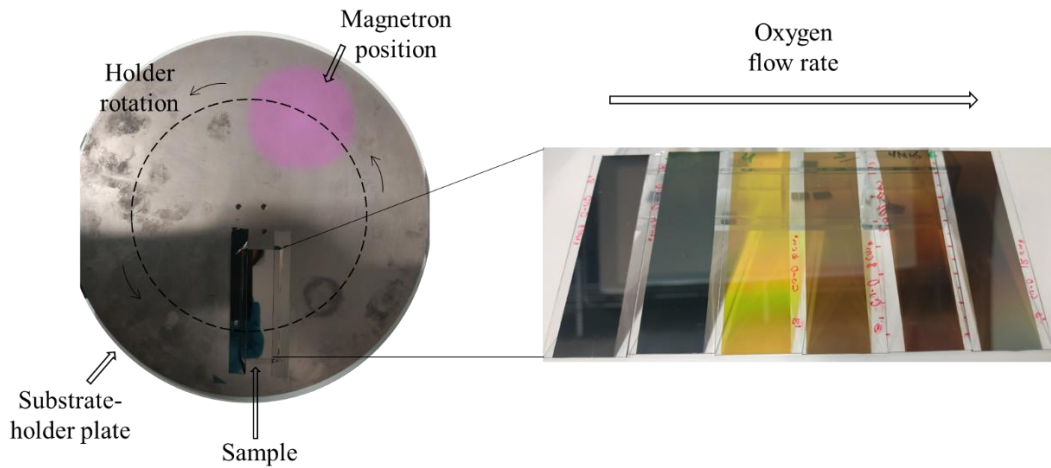


Figure 3.1: Substrate-holder plate and typical sample placement taking into account the position of the magnetron and the distance to the center of the holder (left). Picture of a set of Cu-O samples obtained in this thesis varying the oxygen flowrate (right).

Before starting with the deposition of the reactive Cu-O system, the curve of oxygen partial pressure as a function of the oxygen input flowrate was obtained at a working current of 0.15 A. This allowed us to evaluate if we were in stable deposition conditions. After injecting the argon gas (50 sccm), the OFR was progressively increased from 2 sccm to 20 sccm, noting the total pressure values (after stabilization) corresponding to each OFR.

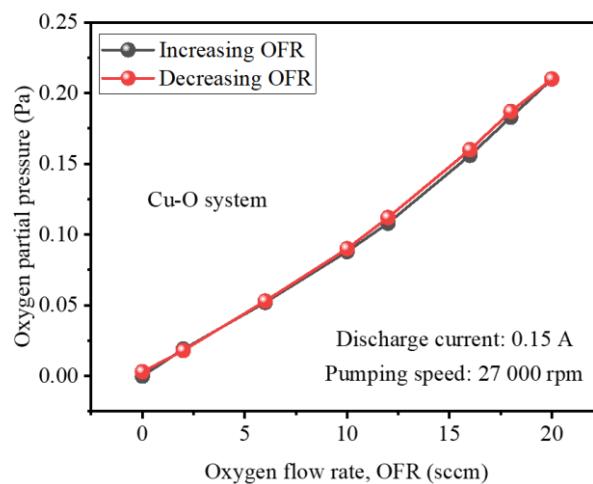
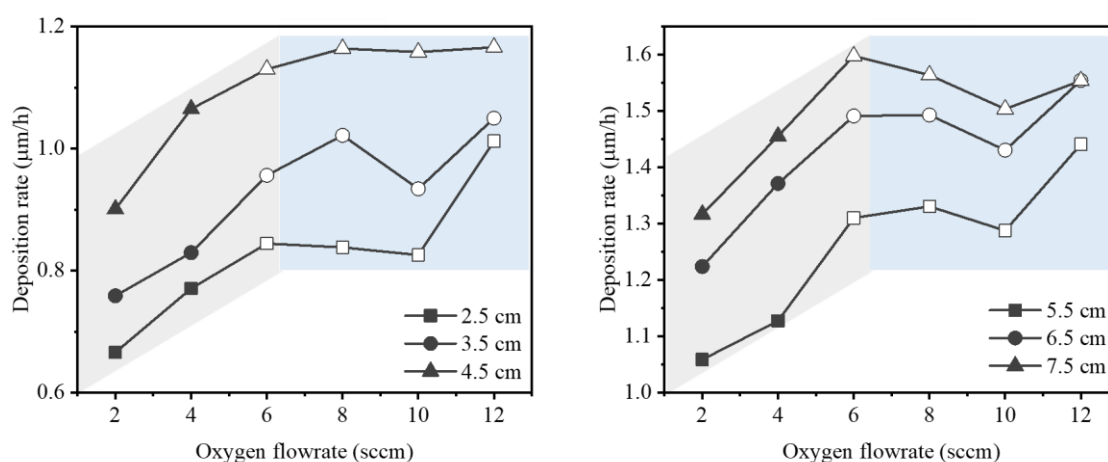


Figure 3.2: Plot of oxygen partial pressure versus oxygen flowrate (OFR) corresponding to a Cu-O system. No hysteresis is observed.

The oxygen partial pressure was then calculated by subtracting the argon pressure (corresponding to 0 sccm of OFR) from the total pressure. When 20 sccm of oxygen were injected, the OFR values were progressively decreased to 0 sccm. As is possible to see in [Figure 3.2](#), the curves (increasing and decreasing OFR) are very close in both cases, with no hysteresis loop. Therefore, deposition could be performed under stable conditions.

As Cu has different oxidation states (Cu_2O , Cu_4O_3 , CuO), it was necessary to select the appropriate OFR region to obtain the desired compounds (semiconductor or composite), by studying the deposition rate as function of the oxygen flowrate (OFR).



[Figure 3.3](#): Deposition rate versus oxygen flowrate for a Cu-O system for different sample positions. Two regions are observed: a first one with high variation on the deposition rate suggesting a possible mixture of Cu-Cu₂O phases in the coatings and, a second one, where the variation is lower indicating possible oxides thin films deposition.

Graphs in [Figure 3.3](#) show the deposition rate behavior for different OFR and sample positions with respect to the center of the holder plate. Two principal regions were identified. The first one (2 - 6 sccm) shows an increase in the deposition rate with each OFR change, possibly indicating a progressive variation in the composition of the layers. Cu-Cu₂O mixtures were expected in this region since low OFR should not allow the oxidation of most of the Cu atoms. Moreover, deposition rate of metallic Cu is lower due to the smaller molar volume of the metal compared to its corresponding oxides.

From 6 sccm – 12 sccm (second region) the deposition rates are relatively more stable, although some variations are observed. It may be indicative of the presence of different phases of oxides with similar but not equal deposition rates. In fact, Pierson *et al.* have shown that above a certain OFR, the deposition rate decreases due to more advanced oxidation of the target surface [174]. It is interesting to note that, although the behavior is similar for all samples, the deposition rate varies between positions, indicating a possible variation in the films properties along the holder radius. This crude analysis needs to be further complemented by structural and chemical investigations and to relate it to the optoelectronic properties.

3.2.1 Characterization of CuNPs-Cu₂O composites: oxygen flowrate dependence.

Structural analysis

XRD measurements allowed to analyze the different phases obtained when the OFR is increased. A mixture of Cu and Cu₂O was found for samples synthesized using 2 and 4 sccm of OFR, labelled as samples 2 and 4, respectively. In contrast, the x-ray diffractograms of samples synthesized using 5 and 6 sccm of OFR, respectively labelled as samples 5 and 6, indicate the presence of Cu₂O as a single phase (Figure 3.4 and Annex 1). A mixture of Cu₂O, Cu₄O₃ and CuO was obtained for higher OFR (8, 10 and 12 sccm) (Annex 1). In the following we restrain our study to samples 2, 4 and 5, of higher interest for our purpose.

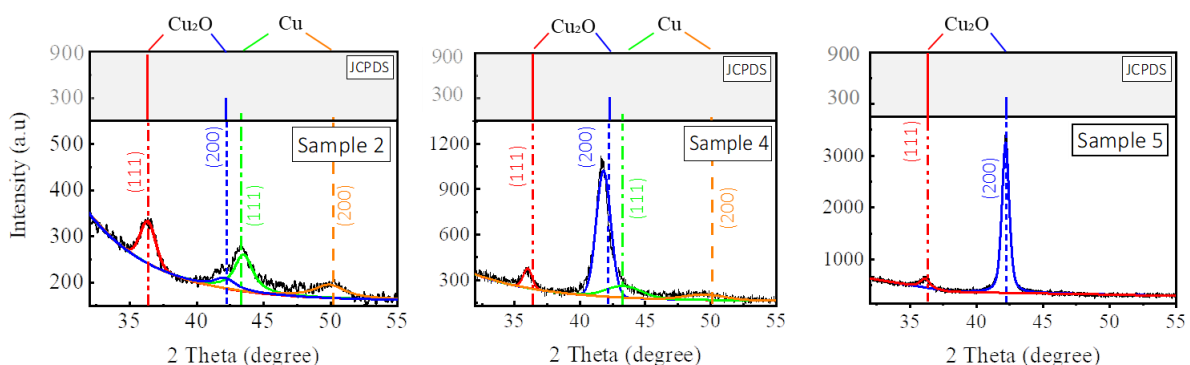


Figure 3.4: X-ray diffractograms of samples grown at 2 sccm, 4 sccm and 5 sccm of O₂ (samples 2, 4 and 5 respectively) with the corresponding fitting of the Cu and Cu₂O peaks to a Voigt function.

The two cubic phases, Cu and Cu₂O, in sample 2, coexist with a [111] preferential orientation (JCPDS 00-004-0836 and JCPDS 04-007-9767, respectively) although weaker (200) peaks are also observed. Increasing the OFR to 4 sccm is accompanied by a noticeable change in the preferential orientation of the Cu₂O phase: the (200) peak becomes much more intense. This behavior becomes even more remarkable as the OFR is further increased to 5 sccm, since only the signal of the Cu₂O phase is observed. A possible explanation for this behavior may be pointed to the surface energy of the (111) and (200) crystallographic planes: the surface energy of the (200) planes is higher than that of (111) [175]. In another study related to the manipulation of growth orientation of reactively sputter-deposited Cu₂O films, Wang *et al.* have obtained the (111) or (200) orientation at high and low sputtering pressure, respectively [175]. As increasing the sputtering pressure lowers the kinetic energy of adatoms, the authors proposed that the growth of (100) requires more energetic adatoms. An increasing research interest related to reactive sputter deposition of oxides is the influence of film bombardment by energetic oxygen ions on the film structure. There are indications in the literature that sputtered oxygen atoms can capture a secondary electron to form O⁻ ions that are accelerated to gain a kinetic energy equivalent to the difference between the plasma potential and the target voltage [176,177], i.e., several hundreds of eV. Within this mechanism, the ion-metal flux ratio (J_{O^-}/J_{Cu}) incident to the sample increases with the OFR and more energetic oxygen ions impact on the surface (Figure 3.5a), transferring more energy to the growing film and easing the formation of (200) planes [178].

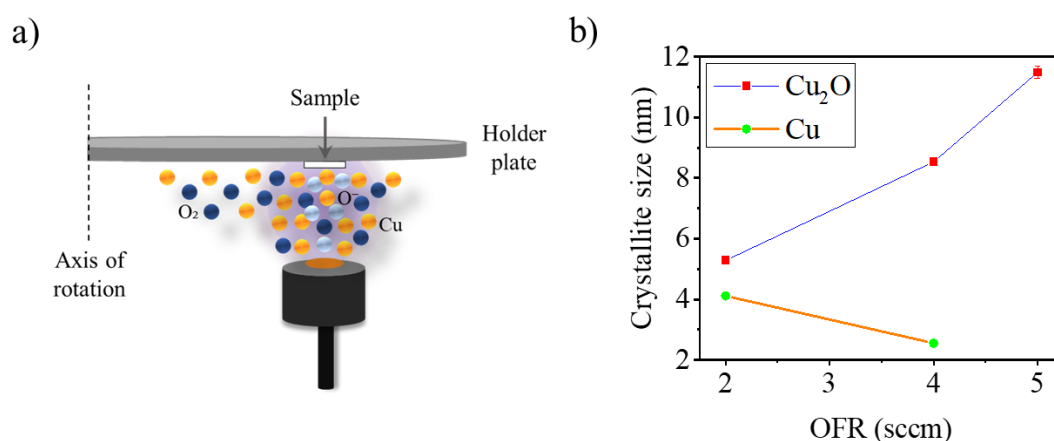


Figure 3.5: (a) Schematic representation of sample positioning and the energetic oxygen ions incidence (light blue particles) which is increased when the OFR increases, leading to higher

energy transfer for (200) planes formation. Dark blue and orange particles represent oxygen molecules and copper atoms, respectively. (b) Evolution of the average size of crystallites of the [111] and [200] oriented domains of Cu and Cu₂O, with the OFR. The colors of the two curves represent those of the XRD peaks used for calculation.

In addition to the influence of the OFR on the crystalline orientation, it was possible to notice a change in the length of coherent domains of both Cu₂O and Cu phases. [Figure 3.5b](#) shows the evolution with OFR of the average size of the coherent domains along [111] and [100] directions of Cu and Cu₂O, respectively, calculated by fitting the corresponding peaks to a Voigt function and applying the Scherrer formula. It can be seen an increase in the Cu₂O crystallite size when the OFR increases, while the Cu domains become smaller due to the incremented oxidation. It is worth to mention that the contribution to the peaks shape given by lattice strains is not considered in this estimation and, therefore, this calculation gives us an overestimated idea of the sizes of coherent domains.

From the above discussion, it can be considered that the oxygen concentration in the samples mainly influences the Cu oxidation states, and therefore, the fraction and nature of phases obtained for different OFR. The energetic oxygen ions, on the other hand, have a more important role in the crystallite orientation.

Optical properties and optical modelling

The incorporation of Cu nanoparticles also has an impact on the optical properties of the grown layers, as evidenced in the absorption spectra extracted from transmittance and reflectance measurements. In [Figure 3.6a](#) a distinctive band centered around 2 eV is observed in samples 2 and 4, while it is absent in the spectrum of sample 5. According to the literature [[179,180](#)], this band can be associated to the surface plasmon band (SPB) of metallic Cu nanoparticles. The position and height of the band, as well as the bandwidth, are related to the shape, size, size distribution, surface state, surface coverage, and surrounding environment of the given nanoparticles [[85](#)]. Moreover, due to the interparticle coupling, the proximity of these nanostructures can induce red-shift and broadening of the SPB [[88](#)]. In sample 2, the SPB is broader and red-shifted, compared to sample 4. Then, it is expected to exhibit in that case a higher proximity of the Cu domains with a larger size. The latter was already confirmed by

XRD (Figure 3.5b). Additionally, the presence of only one SPB in both cases suggests the presence of rounded structures [84]. The absence of any band that could imply the presence of a plasmonic effect in sample 5 is in agreement with the XRD results, where only Cu_2O phase was observed for this condition. For higher OFR, where there is no presence of Cu, there is neither any absorption peak close to the reported plasmon band of Cu (see Annexes, Figure A2).

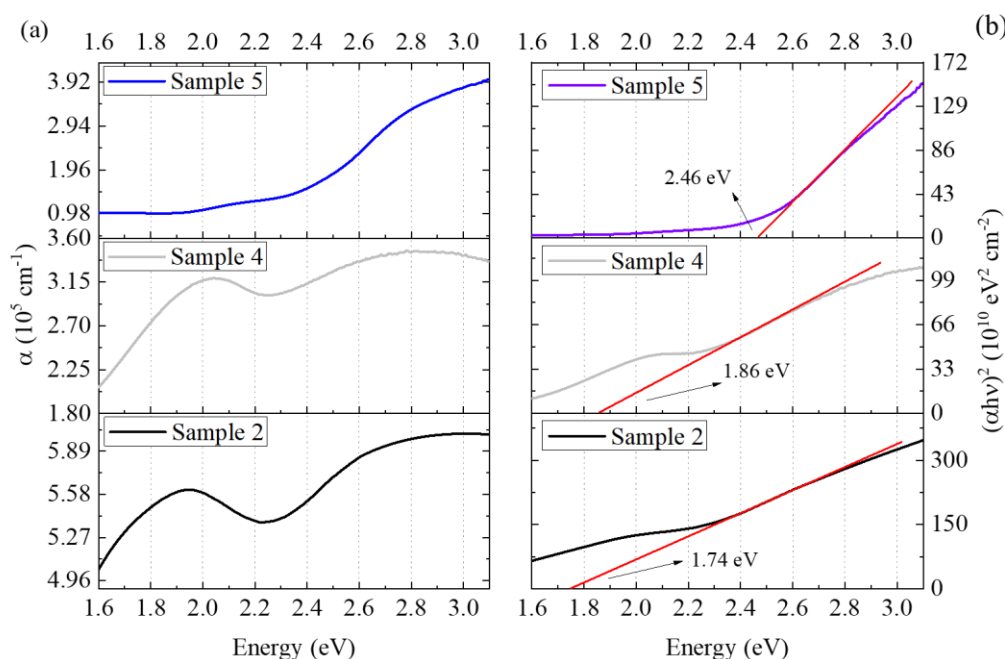


Figure 3.6: (a) Absorption coefficient curves and (b) respective Tauc plots for samples 2, 4 and 5. Surface plasmon bands (SPBs) are observed for samples 2 (around 1.9 eV) and sample 4 (close to 2 eV). For sample 5, no SPB is observed. The bandgap increases as the OFR is higher.

The bandgap values were estimated using the Tauc plot method, assuming that direct allowed transitions take place in these films (Figure 3.6b). Sample 5 shows a bandgap value around 2.46 eV, close to the value reported for Cu_2O material [36,44]. In Sample 2 and sample 4 the values obtained (1.74 eV and 1.86 eV, respectively) cannot be considered as representing the Cu_2O matrix bandgap since the presence of the nanoparticles induces absorption related to interband transitions in metallic copper in this region and can overlap with the signal from the Cu_2O matrix. Furthermore, the higher the polycrystalline character of the layer (as in the case of sample 2), the higher the density of grain boundaries, which increases the disorder in the

crystalline structure [178]. This disorder is expected to increase the density of localized states close to the CB and VB, and therefore decrease the bandgap value [37,181].

Spectroscopic ellipsometry was used to obtain more information about the Cu nanoparticles. The models used for the fitting of the experimental data (Tauc-Lorentz for sample 5 and a sum of two Lorentzian oscillators and a Tauc-Lorentz model for samples 2 and 4) are shown in Figure 3.7a (Sample 5) and Figure 3.7b (Samples 2 and 4) (fits in Annexes, Figure A3). The imaginary parts of the effective dielectric functions for samples 2 and 4 (Figure 3.7d), estimated from the modelling, show plasmonic modes at 1.48 eV (Sample 2), 1.26 eV (Sample 4) and 1.86 eV (Sample 4). In all cases, a wide peak is observed above 2 eV, which is associated to the interband transitions in the Cu₂O matrix and Cu NPs. Real part of the dielectric function (Figure 3.7c) in sample 2 has negative values below 2 eV that, together with the presence of the plasmonic peak in the imaginary part of the dielectric function, suggests a hybrid behavior: metallic (due to the Cu nanoparticles in contact or forming chains) and Cu nanoparticles with plasmonic effect.

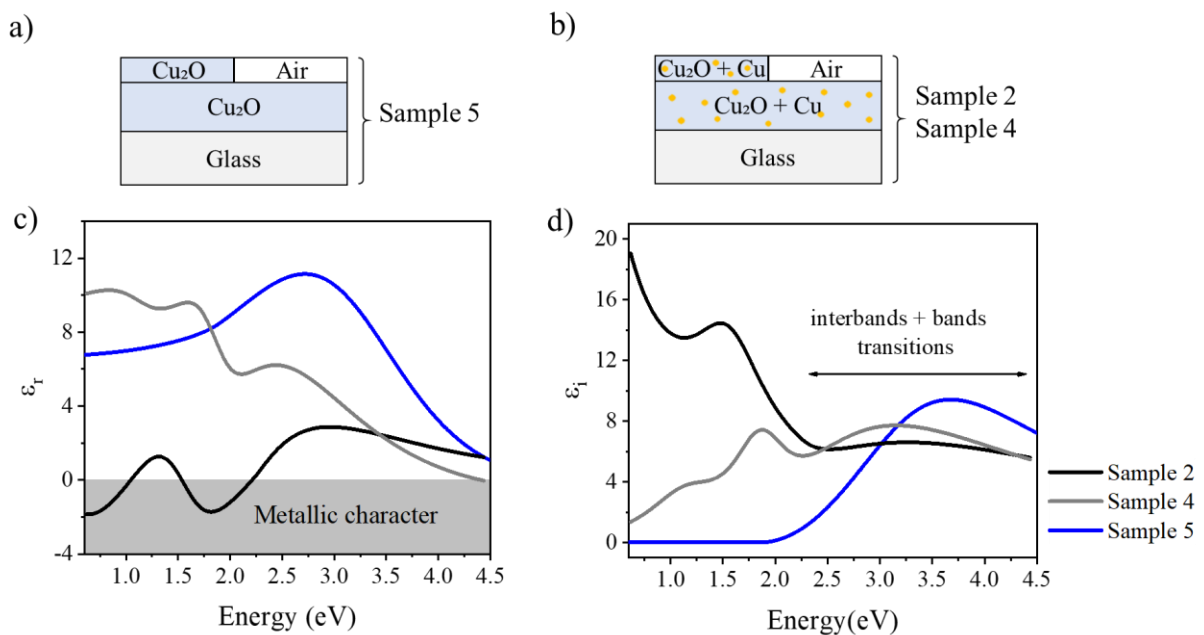


Figure 3.7: Physical models used for fitting ellipsometric measurements: (a) Tauc-Lorentz and a (b) sum of two Lorentzian oscillators and a Tauc-Lorentz model. (c) Real and (d) imaginary parts of the effective dielectric function for samples 2, 4 and 5.

Moreover, even though this is beyond the scope of the present study, it is worth noting that this sample exhibits epsilon near zero features in the 0.8 to 2.1 eV range that could be of value for various applications [182–184]. In the case of sample 4, the real part of the function is positive, indicating the LSPR of the particles embedded in dielectric Cu₂O.

Electrical behavior

Resistivity measurements of samples 2, 4 and 5 are shown in Figure 3.8. Low resistivities closer to the value reported for bulk copper, around 10^{-6} $\Omega\cdot\text{cm}$ [185], correspond to the sample where the presence of this metal is higher (lower OFR: 2 sccm). Then, a progressive increase in resistivity is observed as the formation of Cu₂O increases, until reaching the resistivity reported for this material, in the range from 10 to 10^5 $\Omega\cdot\text{cm}$ [35]. Considering this, it is reasonable to think that the main contribution to the resistivity is the formation of more Cu₂O or less Cu phase.

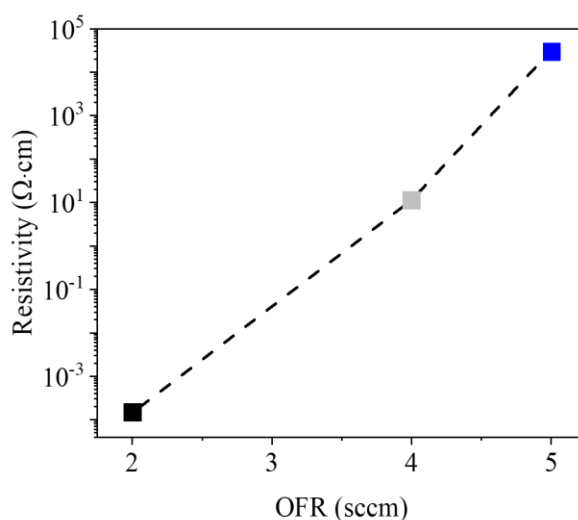


Figure 3.8: Resistivities of samples 2 (black square), sample 4 (grey square) and sample 5 (blue square) as function their corresponding OFR.

Analyzing the two lower OFR, we can consider other factors as well, like more isolated copper particles unable to share conduction electrons through the material and smaller grain size in sample 4 that causes an increase in the scattering by grain boundaries. The average size of coherence domains estimated from XRD indicates that when the OFR increases to 4 sccm, the length of Cu₂O domains becomes larger but that of Cu domains decreases. In addition,

following the assumption that the Cu nanoparticles are more separated in sample 4, it is expected that the resistivity becomes higher for this OFR.

Revealing the innermost structure of the composite films

The interpretation of these results is supported by the TEM analysis of samples 2 and 4, shown in Figure 3.9. The bright and dark field micrographs (Figure 3.9 (a, b, f, g)) and selected area electron diffraction patterns (SAED) (Figure 3.9 (d, i)) show two main differences between sample 4 and sample 2: in sample 4 the crystalline orientation is less random and a columnar growth microstructure is observed, in agreement with the XRD measurements that indicated a more pronounced preferred orientation for this sample. HRTEM micrographs (Figure 3.9 (c, h)) reveal a decrease in the size of Cu grains when the OFR increases, (7.29 ± 2.92) nm in sample 2 and (4.10 ± 0.68) nm in sample 4. This is again consistent with the behavior observed for the coherent domain size calculations (Figure 3.5b).

Figure 3.9 (e, j) shows the High Angle Annular Dark Field (HAADF)-STEM micrographs taken for the EELS analysis of samples 2 and 4 and the generated composition maps of Cu, O and the Cu-O mixture, corresponding to the yellow enclosed region. In the analyses of these maps, it is needed to consider the fact that information is obtained from the FIB lamella thickness that exceeds by far the size of crystallites. Hence a superposition of signals from many crystallites is observed. This could affect mostly the study of the Cu phase separately from the Cu₂O. However, it was possible to extract useful information.

In the mixed composition map of sample 2, the bright green area of the map represents a high copper concentration, while orange zones indicate a higher compensation between Cu and O. This can be seen in ELNES measurements at O-K and Cu-L_{2,3} edges in two different regions (red and blue squares located in the green and orange regions, respectively). In the green region (red spectrum in the ELNES graph) a very weak O-K edge is observed around 531.9 eV and the Cu-L₃ at 937.9 eV and Cu-L₂ at 957.9 eV edges are rather flat, indicative of the presence of metallic copper [32,186]. The orange area (blue spectrum), instead, shows a more defined O-K edge peak at 532.4 eV as well as a more pronounced Cu-L₃ edge at 937.4 eV, which differentiate the oxidation state Cu⁺¹ from Cu⁰ according to the literature [187].

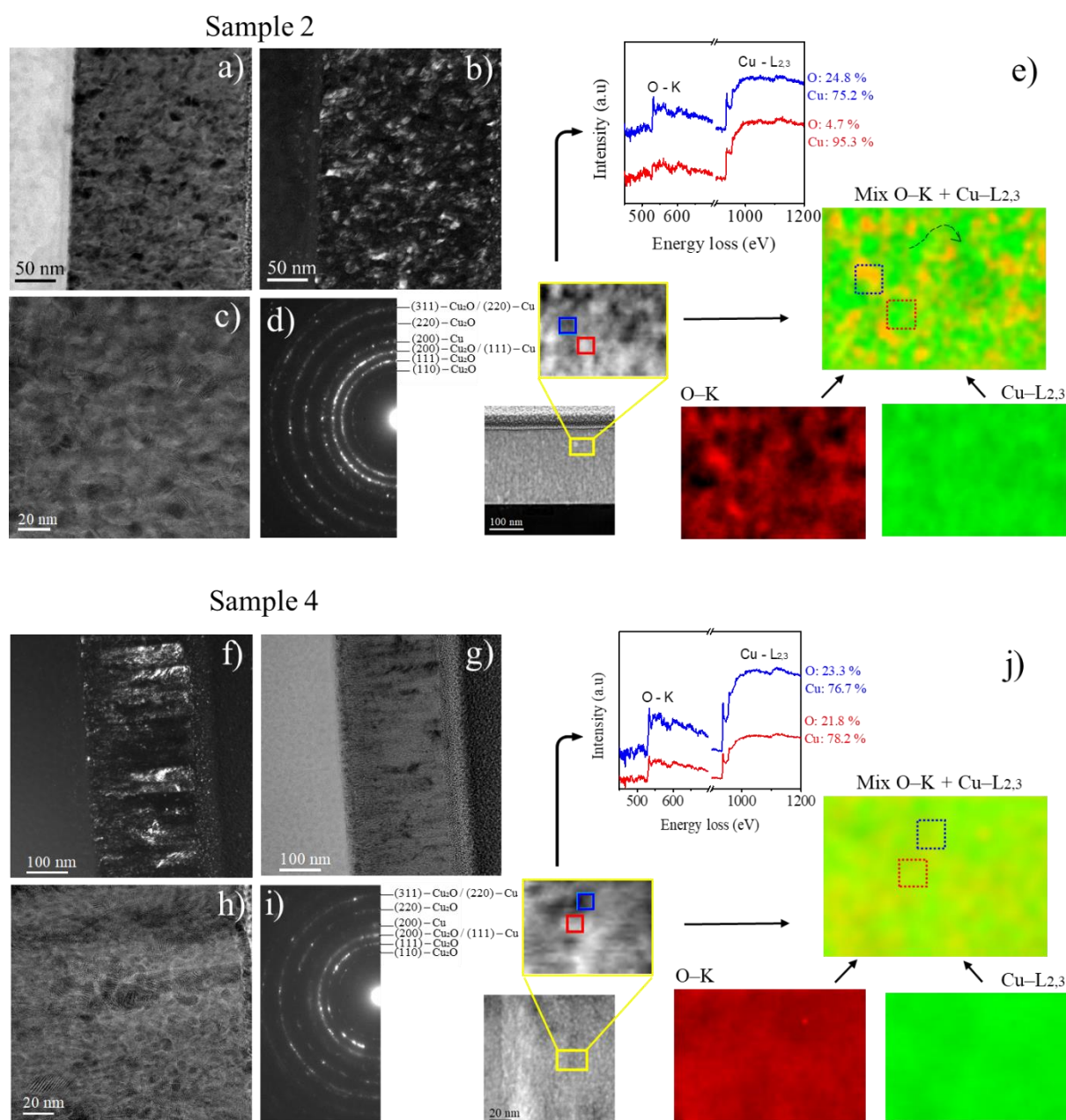


Figure 3.9: TEM analysis of samples 2 and 4: (a, b, f, g) bright and dark field micrographs where it can be seen the remarked nanocrystalline nature of the sample 2 while a columnar growth is observed for sample 4; (d, i) selected area electron diffraction patterns; (c, h) HRTEM images showing lower particles sizes in sample 4; (e, j) high angle annular dark field (HAADF)-STEM micrographs and energy loss near edge structure (ELNES) spectra at O-K and Cu-L_{2,3} edges corresponding to the blue and red square areas in a selected zone of the HAADF micrograph (yellow rectangle). Composition maps of copper (green), oxygen (red)

and mixture of both (orange). Dashed arrow in the mixed elemental map of sample 2 (e) shows the connection between copper domains.

A closer look at the map, tends to confirm the connection of copper domains into the copper oxide matrix in sample 2 (black dashed arrow). In sample 4, the ELNES spectra are similar and in line with the presence of Cu^{+1} in the two areas, and the different regions are not as easy to distinguish as in the previous case. However, it is possible to notice some green regions corresponding to the lower oxygen concentration, which suggest more isolated particles in sample 4, as suspected above when analyzing the resistivity and optical data. Based on the present study, it is interesting to note that the proposed elaboration process is versatile. Effectively, it enables, by varying a single parameter (the oxygen content in the gas phase), to elaborate pure Cu_2O films, CuNPs- Cu_2O nanocomposite films with embedded Cu plasmonic nanoparticles or CuNPs- Cu_2O nanocomposite films with embedded Cu plasmonic nanoparticles and percolating conductive Cu paths.

3.2.2 Characterization of CuNPs- Cu_2O composites: substrate position dependence.

The above study showed a one-step route to obtain CuNPs- Cu_2O composites varying the OFR of the sputtering process, corresponding to samples placed in the target axis. In addition, this section will discuss the dependency between the films properties and the position of the samples with respect to the holder rotation axis. (Figure 3.10a).

In section 3.2 it was observed a change in the deposition rate respect to the position at which the films were grown (Figure 3.10b), showing a decrease while we move away from the target axis. Deposition rate depends on the sputtering rate, proportional to the product $J(\text{Ar}^+)Y^1$ and, therefore, depends on the electrical parameters.

It also depends on the dispersion of the sputtered metal vapor and, consequently, for a given material, it is essentially a function of the distance between the target and the substrate, and, more generally, of the sample location relative to the target [188]. In our case, the electrical

¹ $J(\text{Ar}^+)$ is the argon ions flux and is proportional to the current discharge. Y increases linearly with the polarization voltage [50].

parameters are considered almost constant for the different OFR (same current discharge, working voltage between 390 V and 400 V) and only the distance from the substrate holder was varied contrary to the most common variation along the target axis [189–192].

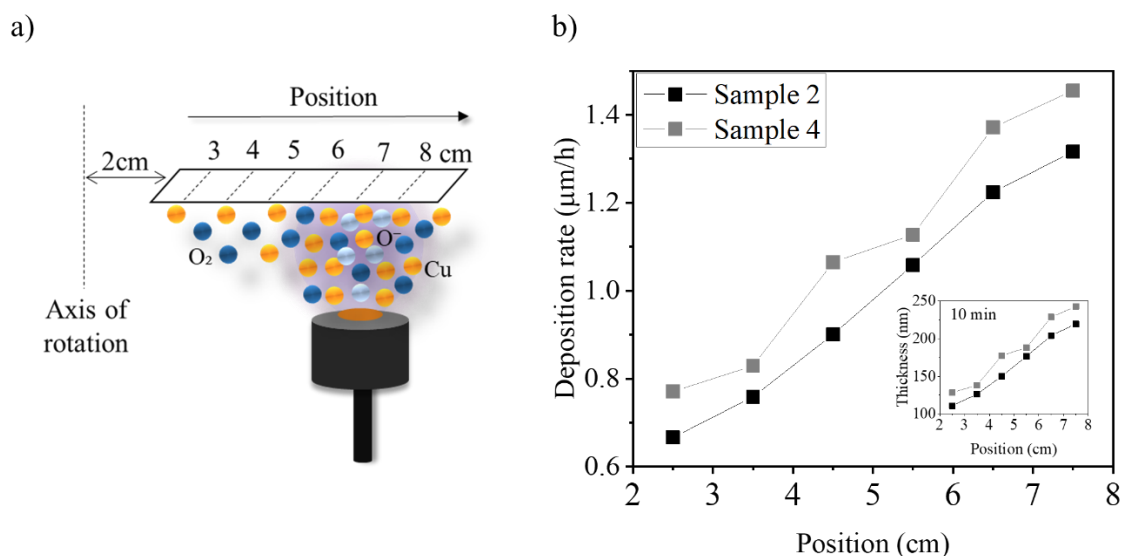


Figure 3.10: (a) Schematic of the sample positioning with respect to the axis of rotation of the holder plate. (b) Deposition rates and thicknesses of films grown at 2 sccm and 4 sccm of OFR, during 10 minutes, as function of the sample position.

Structural analysis

In the employed configuration, the density of sputtered atoms and the momentum transference by those and the accelerated oxygen ions close to the center of the holder, is expected to be lower [193]. This could have a direct influence on the crystalline structure of the films, as shown by X-ray diffraction analysis (Figure 3.11).

Diffraction peaks corresponding to Cu_2O and Cu cubic phases are observed independently of the sample position, suggesting the formation of CuNPs- Cu_2O composites in all the cases. Therefore, the change in thickness is primarily related to the dispersion of the metallic vapor, more than to a molar volume change associated to a change of phases. In Figure 3.12 it is possible to see the position dependence of the atomic composition (a) and the O/Cu ratio (b)

as measured by EDS. As we move towards the target axis (7.5 cm), the oxygen atomic % and the O/Cu ratio decrease, for sample 2 and sample 4.

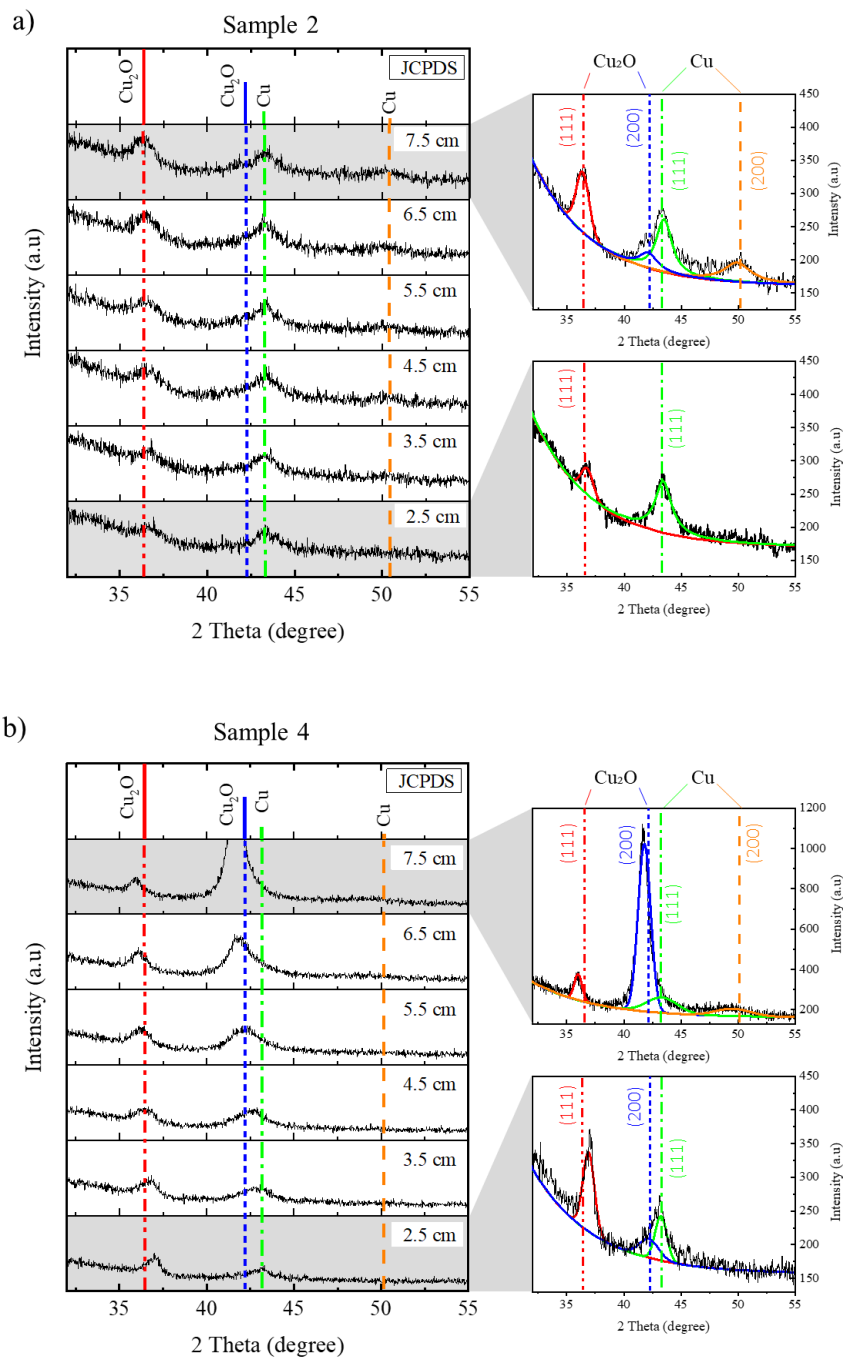


Figure 3.11: X-ray diffractograms for different OFR (2 sccm and 4 sccm) changing the position of the samples, measured with respect to the center of the sample holder. Cu and Cu_2O peaks fit to a Voigt function for two selected positions (2.5cm and 7.5 cm).

This is expected as XRD evidences the presence of metallic Cu additionally to the Cu_2O phase for both OFR under these conditions, and it is explained by the fact that, in front of the target axis, the deposition rate is higher and, therefore, the flux of incident Cu atoms is higher for the same oxygen availability. Hence, there is not enough oxygen available to oxidize all the copper atoms present on the film surface. Insets of Figure 3.12b evidence an overall decrease of the O/Cu ratio with the deposition rate, supporting this hypothesis.

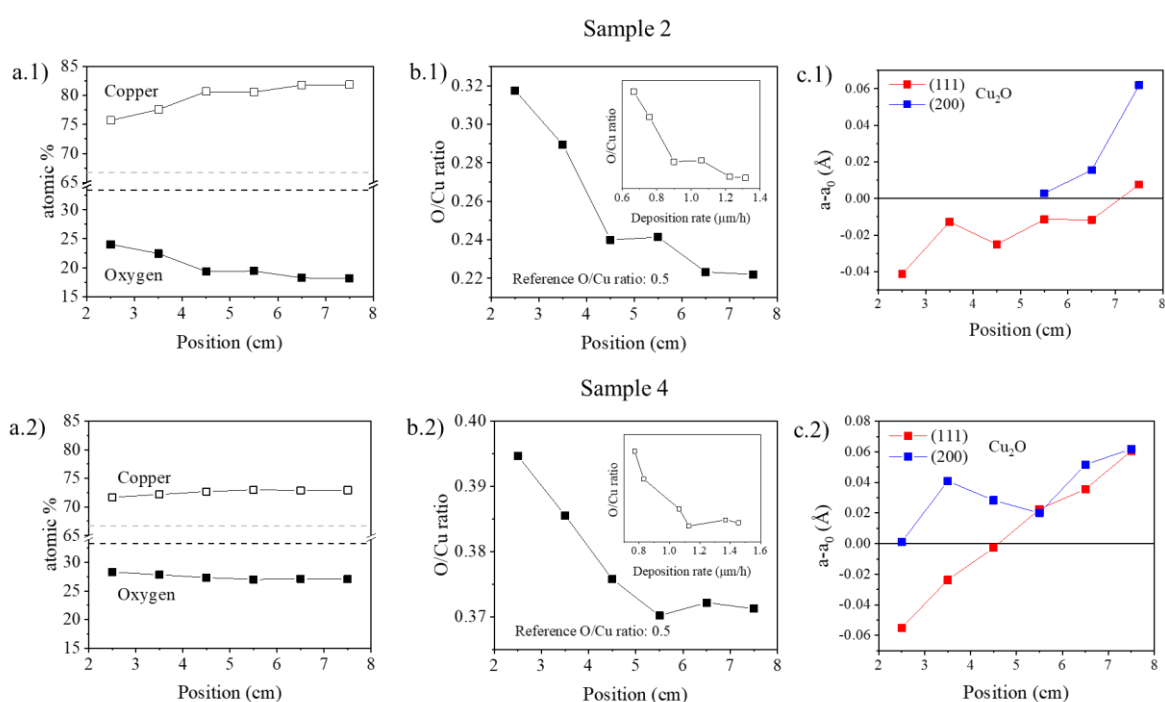


Figure 3.12: (a.1, a.2) Dependence of the atomic composition and (b.1, b.2) O/Cu ratio for samples 2 and sample 4 with the position respect the center of the holder plate. The dependence of the O/Cu ratio with deposition rate is also shown ((b.1, b.2) inset). (c1, c.2) Lattice parameter shift calculated from Cu_2O (111) and (200) peaks.

Moreover, an evolution in the preferential orientation of the films is observed. Following the same analysis than in the previous section 3.2.1, we can consider a possible influence of the impinging oxygen ions on the films orientation. Away from the target axis, the energy transference by oxygen ions is lower and might favour the formation of the most stable lattice configuration with lower surface energy: (111) planes of both Cu and Cu_2O [175]. Therefore, as we get closer to the target, the increasing energy transmitted by impingement of oxygen ions will have an influence principally in the formation of (200) planes of Cu_2O and Cu. In general,

at this position, and nearby, the incoming species, energetic oxygen ions or Cu atoms, have enough energy to contribute to the growth of more ordered structures despite the expected presence of a larger amount of metallic copper. In fact, since the sputtered particles present different thermalization degrees depending on the distance between the sample and the target, it is expected that there is a lower thermalization degree close to the target axis and, therefore, incoming species with a higher kinetic energy on average. That explains also the low crystallinity of the films far from the target axis due to the low mobility of adatoms.

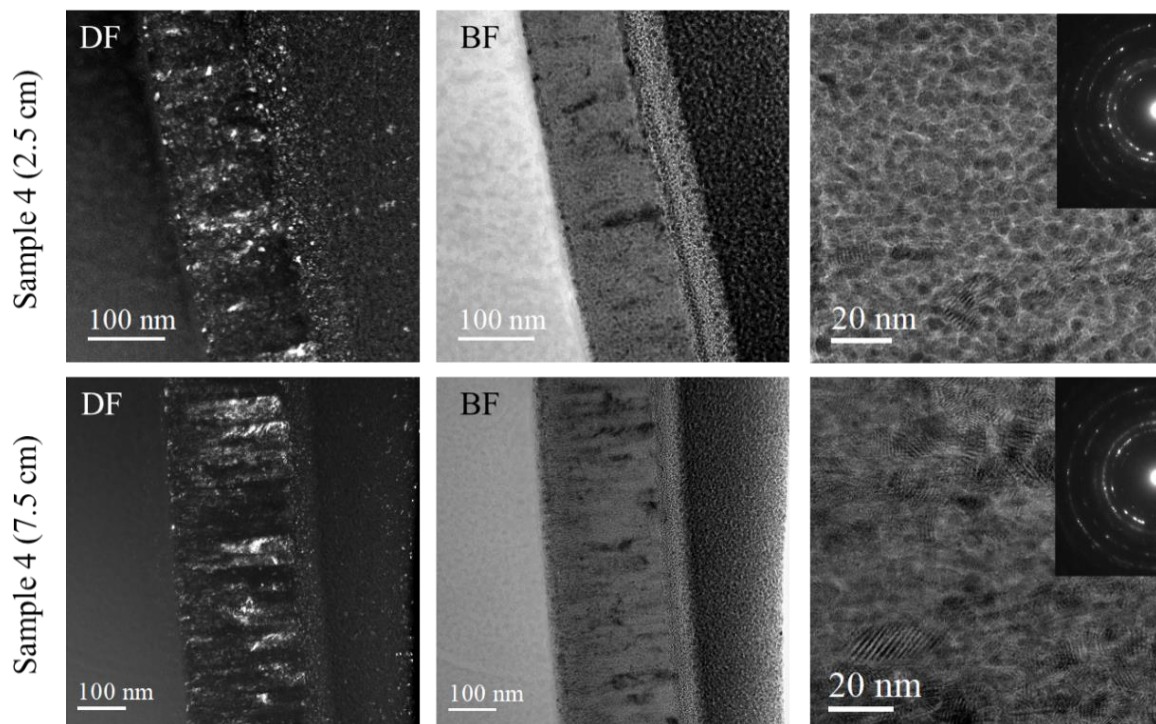


Figure 3.13: TEM analysis of sample 4 at two different positions (2.5 cm and 7.5 cm): dark and bright field micrographs where it can be seen the nanocrystalline nature at 2.5 cm and columnar growth at 7.5 cm; HRTEM images showing smaller particles sizes at 2.5 cm; SAED patterns showing a more oriented structure at 7.5 cm.

This analysis is also supported by TEM and HRTEM micrographs of sample 4 at the two more distant positions (2.5 cm and 7.5 cm) (Figure 3.13). The DF and BF images show the nanocrystalline nature at 2.5 cm and a columnar growth microstructure at 7.5 cm. SAED also indicates the more oriented crystalline structure obtained close to the target axis. Additionally,

it can be noticed in [Figure 3.11](#) a progressive shift of the (200) and (111) peaks of Cu_2O , from the reference peak position (for 2.5 cm) towards lower angles (for 7.5 cm). This shift has been observed in others works and is related to multiple causes like the presence of different phases, non-stoichiometry, local strains caused by the bombardment of atoms or ion during the growth process and thermal stress by annealing [44]. In our case, we believe that the most plausible explanation lies in the alteration of the film stoichiometry and the coexistence of a secondary phase (metallic Cu) within the host material (Cu_2O), which could also introduce strain into the lattice of the Cu_2O matrix [194,195].

In [Figure 3.12c](#) is possible to see the position dependence with the lattice parameter shift ($a - a_0$) of the Cu_2O phase extracted from the position of the (111) and (200) peaks of Cu_2O . Among the possible origins mentioned above, the change noticed in the lattice parameter might be associated to the presence of non-stoichiometric $\text{Cu}_{2+\delta}\text{O}_{1-\delta}$ and, therefore, the presence of point defects that cause contraction and expansion of the lattice far and close to the target, respectively. Korzhavyi *et al.* calculated the enthalpy of formation of different point defects in Cu_2O as a function of the oxygen atomic fraction [196]. At lower oxygen contents (mixture of Cu and Cu_2O) defects like oxygen vacancies (V_O), copper antisites (Cu_O) and copper in the tetrahedral and octahedral interstitial positions ($\text{Cu}_{\text{i}4}$, $\text{Cu}_{\text{i}6}$) were found.

Optical properties and optical modelling

The optical properties of the films as a function of their positioning showed no relevant changes in terms of matrix bandgap or shape and positioning of the SPB, according to ellipsometric measurements ([Figure 3.14](#)). The models used to analyse the position far from the target axis (2.5 cm) were the same as for 7.5 cm: a sum of two Lorentzian oscillators and a Tauc-Lorentz model. The real part of the dielectric function in sample 2 is lower than for sample 4 for both positions, indicating stronger metallic character, as previously discussed. This character is more marked at 7.5 cm, where more metallic atoms reach the substrate and not enough oxygen is available to form the compound. The hybrid behavior observed at 7.5 cm for sample 2 is reduced at 2.5 cm since most of the ϵ_r values are positive (less Cu nanoparticles in contact due to a higher oxidation). The imaginary part of the dielectric function shows the plasmonic modes corresponding to the Cu nanoparticles at 2.5 cm and 7.5 cm, for both OFR.

The absorption coefficients calculated from modelling of ellipsometric spectroscopy data show that, varying the position for both OFR, there are no noticeable changes associated to interband transitions in the Cu_2O matrix and Cu NPs. However, the SPB of the Cu NPs below 2.5 eV is lower as the films were grown farther from the target. Furthermore, in the case of sample 2, the position of the SPB slight blue shifted (from 1.82 eV to 1.9 eV). This decrease in the value of α can be associated to a lower presence of plasmonic nanoparticles at 2.5 cm with lower particle sizes (see HRTEM in Figure 3.13), related to the higher O/Cu ratio at this position.

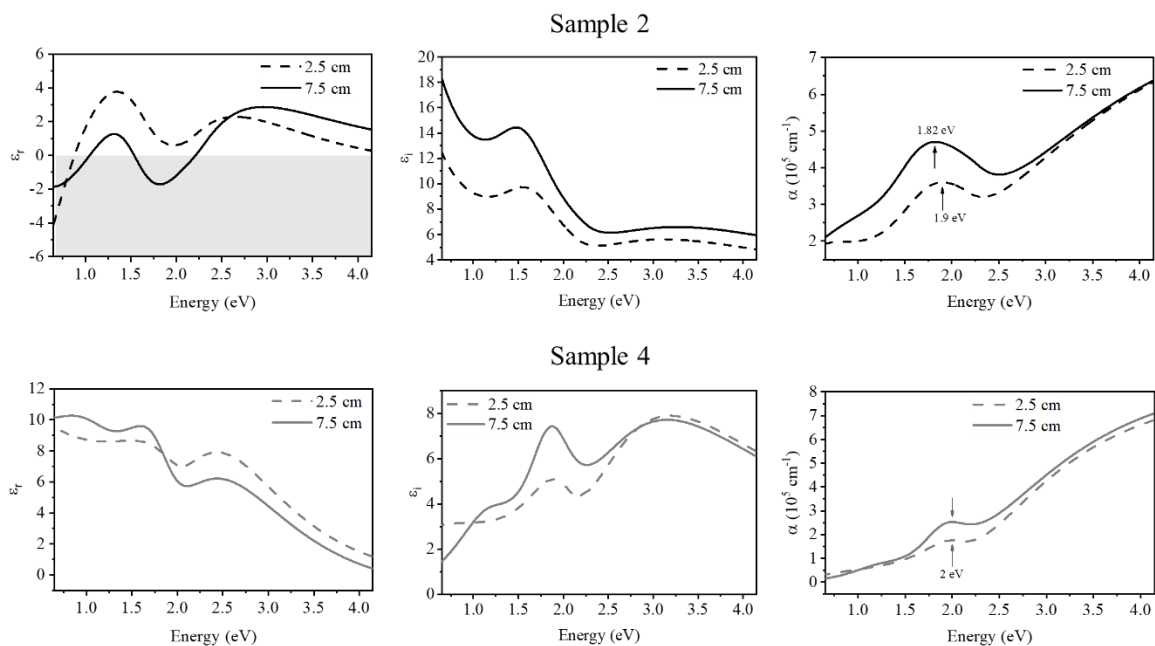


Figure 3.14: Real and imaginary parts of the dielectric functions and absorption coefficients of sample 2 and sample 4 at 2.5 cm and 7.5 cm, calculated by ellipsometric spectroscopy.

Electrical behavior

Resistivity values show a similar behavior for both OFR when we move lengthwise (Figure 3.15). The inhomogeneity in resistivity with the position respect to the center of the holder could be explained by the O/Cu ratio, evolution in the grains size, non-stoichiometry [193,197] and can increase due to internal strains or large quantity of dislocations [198].

We think that the changes in resistivity values is likely related to the oxygen content during the growth. Far from the target axis (region 1, Figure 3.15), the O/Cu ratio is higher and the copper that reach this region of the sample holder is more propitious to oxidize with the oxygen

availability. This leads to an increase in resistivity. As we move closer to the target axis the resistivity decreases in agreement with the diminution of the O/Cu ratio (more metallic Cu) (region 2). However, above the target, an increase in resistivity is again observed (region 3). We have considered two possible hypotheses to explain this behavior: the presence of donor point defects and the [100] preferential orientation.

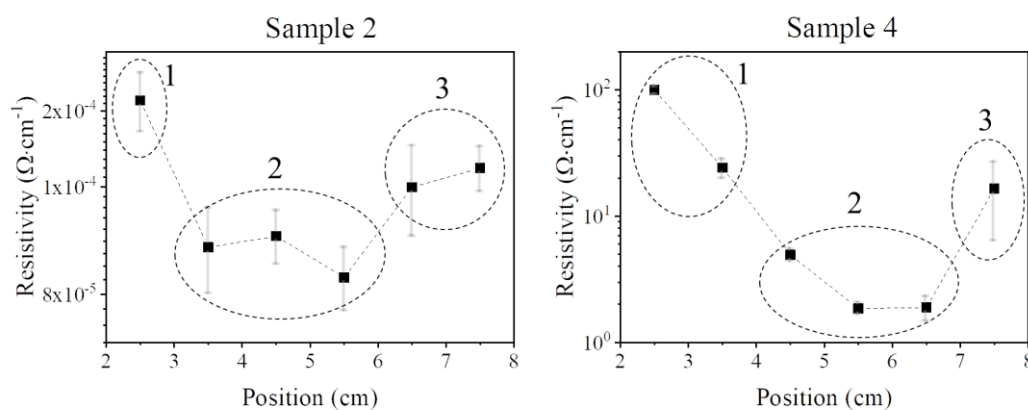


Figure 3.15: Resistivity behavior of films grown at 2 sccm and 4 sccm of OFR varying the position. Three regions in the graph are enclosed to facilitate the explanation provided in the text, regarding changes in resistivity.

As mentioned above, facing the target, there is some probability that point defects appear and produce the expansion of the crystal lattice in the growth direction. Some of these defects are donor defects or “hole killers” (for example Cu_i) [50,199,200] and, although it is reported that their concentration is not enough to change the intrinsic n-type conductivity of Cu_2O , a self-compensation process could happen in such a way that the resistivity increases [201]. On the other hand, the higher energy transference close to the target might also produce, as it was said previously, a favorable [100] growth direction which, as reported in others works, is less favorable for conductivity compared to [111] direction [202].

3.3 Devices fabrication

Three configurations of devices were fabricated in order to evaluate the impact of plasmonic Cu NPs in the current generation of optoelectronic devices. The first one was a reference cell consisting of a ZnO (~100 nm) / Cu_2O (~200 nm) p-n junction (labeled Dev_6sccm). In a

second device, the Cu_2O layer is replaced by a composite of Cu_2O and plasmonic Cu NPs obtained at 4 sccm of oxygen flowrate, at 7.5 cm of the holder axis (~ 200 nm and labeled Dev_4sccm). The last configuration includes a very thin interlayer of the same composite (~ 10 nm) between the ZnO n-type material and the Cu_2O p-type material (labeled Dev_4sccm/6sccm).

In all the cases, the ZnO layer was deposited on a previously cleaned FTO substrate by Reactive Magnetron Sputtering, using a Zn target (99.995 % of purity, Kurt J. Lesker Company) and 8 sccm of OFR. The distance of the target surface to the holder plate was 5 cm and the sample was placed at 3 cm from the center of the holder axis to achieve the better conductivity [32]. The argon flowrate was fixed at 50 sccm, reaching a working pressure of 0.4 Pa, and the applied current was 0.07 A.

Same procedure as described in section 3.2 was applied to deposit the Cu-O layers (Cu_2O and CuNPs- Cu_2O composites). In the case of the last configuration, a two-step route was followed: a very thin layer (10 nm) was first deposited using 4 sccm of OFR and then the OFR was increased to 6 sccm until the layer reached 200 nm of thickness. Finally, an Au back contact was deposited by magnetron sputtering, using an Au target (99.99 % of purity, Neyco Company), located at 5 cm from the holder plate, where the sample was located in the target axis. The current applied was 0.06 A and the working pressure was 0.5 Pa.

3.3.1 Photocurrent enhancement with plasmonic particles incorporation.

The three configurations of devices fabricated in order to evaluate the impact of incorporating the studied composites films with plasmonic NPs are represented in Figure 3.16.

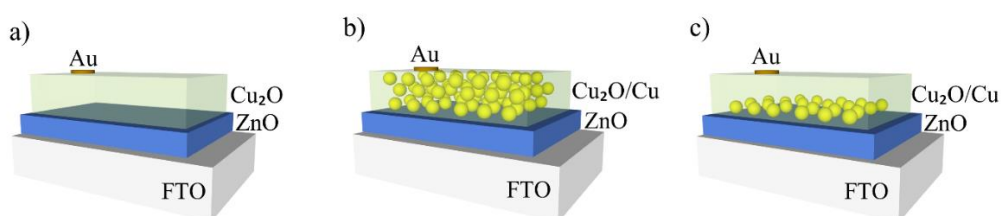


Figure 3.16: Schemes of the three devices fabricated without and with plasmonic composites (grown at 4 sccm): (a) Dev_6sccm, (b) Dev_4sccm and (c) Dev_4sccm/6sccm.

Current density – voltage (J-V) measurements under dark and illuminated conditions (1 sun or 100 mW/cm²) are shown in Figure 3.17 (a, b, c). In all the cases, a rectifying behavior typical of a p – n junction is observed. Upon illumination, all of them showed an increase in current density at 0 V, indicating the occurrence of a typical carrier collection process, which is higher for devices in which plasmonic nanodomains were incorporated. Although this was an expected result, it is interesting to notice that, by decreasing the thickness of the layer composed by plasmonic nanodomains (Dev_4sccm/6sccm), responsible for the injection of extra carriers, the J_{sc} is almost 4.5 times higher than in the reference device and 2 times higher than in Dev_4sccm (Figure 3.17d).

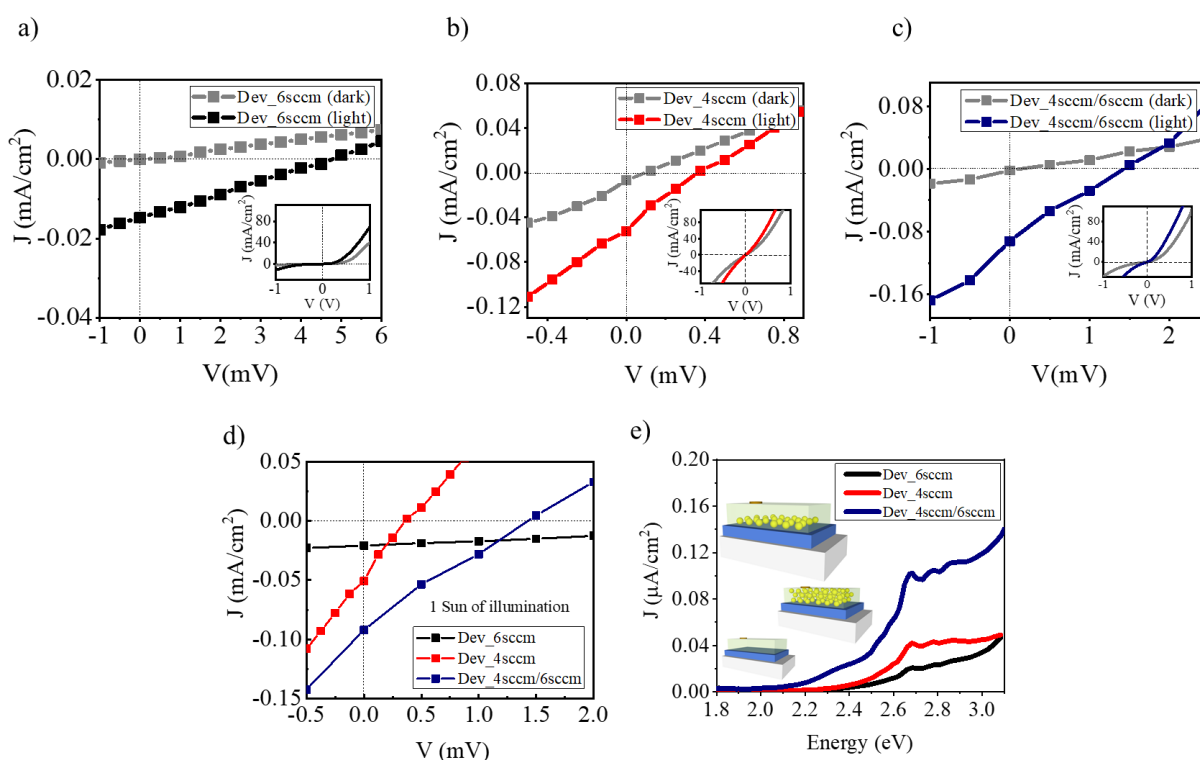


Figure 3.17: (a-d) Current density vs voltage measurements in dark and at 1 sun of illumination. (e) Modulated photocurrent spectroscopy.

J_{sc} is proportional to the minority carrier diffusion length and the absorption coefficient of the material [203]. In nanostructured films with many grain boundaries, like the studied plasmonic composites, a relatively high defect density is expected, which could decrease the carrier diffusion length. Then, although the generation rate should be increased in Dev_4sccm due to a higher absorption coefficient and more carriers injection induced by the plasmonic effect, low values of carrier diffusion length avoid significant increase in the current density. That

explains why Dev_4sccm/6sccm, an intermediate architecture between the other two configurations, is associated to an improvement in the charge generation and limited decrease of the diffusion length, allowing to collect more photogenerated carriers than the reference device. This configuration could also be favored by the strong local field enhancement [204] around the metal nanoparticles, allowing photocarriers being generated and separated close to the collection junction area [151,205] (Figure 3.18 (a-c)).

The above interpretation can be supported by analyzing the values of V_{oc} , which inversely depends on the saturation current J_0 [206]:

$$V_{oc} = \frac{kT}{q} \ln \left(\frac{J_{sc}}{J_0} + 1 \right) \quad (3.1)$$

where k is the Boltzmann constant, T the temperature and q the electron charge. The reverse saturation density current J_0 gives a measure of the recombination in the device related to the diffusion lengths. If J_0 increases more quickly than J_{sc} , then a lower value of V_{oc} is obtained.

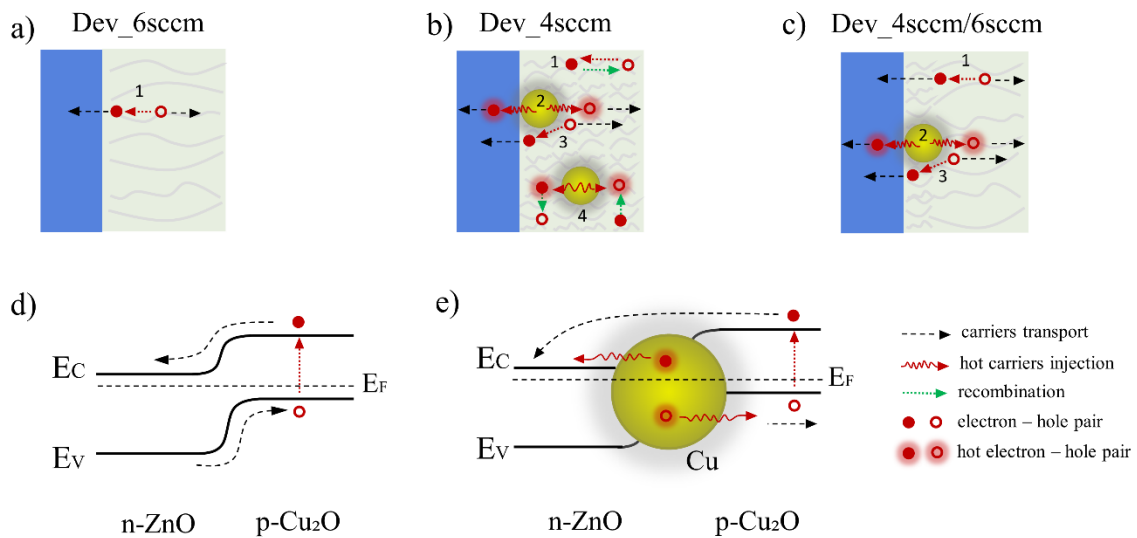


Figure 3.18: (a-c) Schematic of the processes related to the photocurrent generation in the different devices, under illumination: (1) electron – hole pair generation and recombination; (2) hot carriers injection from plasmonic NPs; (3) carrier separation by strong local field enhancement around the metal NPs; (4) annihilation of injected hot carriers by recombination. (d, e) Corresponding band alignments between n – ZnO, p – Cu₂O and CuNPs.

Modulated photocurrent measurements support the fact that plasmonic particles induce a positive effect on the generation of hot carriers (Figure 3.18e), particularly in Dev_4sccm/6sccm. The photocurrent response in this case, shows a broad band between 2 eV and 2.5 eV approximately, which is not seen in the other two configurations. This band likely comes from the injection of hot carriers (hot holes) into Cu₂O after photons with energies greater than 2 eV excite the metal NP. Effectively, according to calculations done by Tagliabue *et al.* [207], for energies above 2 eV, highly-energetic hot holes far below the Cu Fermi level are produced with high probability of being injected in the p-type material, while hot electrons with much lower energy are located just above the Cu Fermi level (Figure 3.18e). The collection of injected hot holes into the Cu₂O matrix in Dev_4sccm could be then limited by the low mean free path of hot holes [207] and a high density of recombination centers. In Dev_4sccm/6sccm, hot holes, after being transferred to the thin Cu₂O matrix, are immediately transported to the interfaced Cu₂O layer of lower density of defects, and subsequently collected (Figure 3.18 (b, c)). On the other hand, it is worth mentioning that from these measurements, it seems that the bandgap of the Cu₂O matrix vaguely changes for any of the devices, staying around 2.4 eV. This supports the hypothesis that the values obtained in the Tauc plot for samples 2 and 4 (Figure 3.6) are affected by the interband transitions occurring in the Cu nanoparticles.

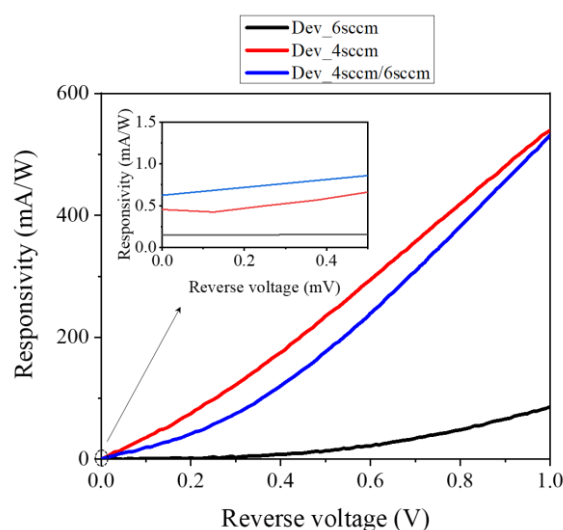


Figure 3.19: Responsivities as function of the reverse voltage calculated from the J-V measurements of the three fabricated devices: Dev_6sccm, Dev_4sccm and Dev_4sccm/6sccm.

The responsivities of the devices (Figure 3.19) were also calculated using the formula $R = \frac{J}{P}$, where J is the photocurrent density calculated by subtracting the dark current density from the current density under illumination with a power density (P) of 100 mW/cm². The photocurrent and responsivity values of the devices studied are comparable or even higher than recently studied photodetectors and solar devices where metal NPs are included (Table 3.1).

Table 3.1: Figures of merit of ZnO, Cu₂O and plasmonic NPs-based photodetectors and solar devices.

| Heterostructure | Photocurrent | Responsivity | Detection Range | Ref. |
|--|---|--------------------------------------|------------------|-----------|
| Au NPs/Cu ₂ O ¹ | ~1.32 μ A/cm ² (0 V) | ~22 μ A/W (0V) | 532 nm (VIS) | [208] |
| Al:ZnO/Ag NPs/Cu ₂ O ² | 21.41 mA/cm ² (0 V) | -- | VIS | [99] |
| ZnO NRs/Au NPs ² | 15.8 μ A/cm ² (0 V) 74 μ A/cm ² (0 V, 450°C) | -- | VIS | [209] |
| ZnO/CdMoO ₄ /Au NPs ³ | ~289.1 nA (5 V) | 321 mA/W (5 V) | 350 nm (UV) | [210] |
| ZnO/Cu NPs ⁴ | 950 mA/cm ² (-6 V) | 100 mA/W (-6 V) | 400-800 nm (VIS) | [159] |
| ZnO NRs/Au NPs/Al ₂ O ₃ ⁵ | ~160 nA (0 V) | 6.8 mA/W (0 V) | 365 nm (UV) | [58] |
| ZnO NWs/Au NPs ⁶ | -- | 510 mA/W (0 V) | 940 nm (NIR) | [211] |
| ZnO NRs/Al NPs ⁷ | ~1 μ A (5 V) | 0.4 mA/W (5 V) | 325 nm (UV) | [212] |
| ZnO NRs/Cu NPs ⁷ | ~0.1 mA (5 V) | 46 mA/W (5 V) | 325 nm (UV) | [212] |
| ZnO/CuNPs-Cu ₂ O ² | 52.4 μ A/cm ² (0 V) 188.9 mA/cm ² (1 V) | 0.45 mA/W (0 V) 539.6 mA/W (-1 V) | VIS | this work |
| ZnO/CuNPs-Cu ₂ O/Cu ₂ O ² | 92.1 μ A/cm ² (0 V) 151.2 mA/cm ² (1 V) | 0.62 mA/W (0 V) 531.3 mA/W (-1 V) | VIS | this work |

Power densities of the light sources: ¹ 60 mW/cm², ² 100 mW/cm², ³ 0.15 mW/cm², ⁴ 7 W/cm², ⁵ 0.6 W/cm², ⁶ 0.35 mW/cm², ⁷ 2.17 W/cm².

It is worth to notice that many of the configurations reported include nanostructured scaffolds like nanorods (NRs) / nanowires (NWs), which allow to increase the effective area for the charge photogeneration and separation and may positively impact the photoconversion. On the other hand, it can be seen that the use of Au/Ag expensive metals in these designs is predominant, making the Cu based configurations an interesting choice. Many other studies have included plasmonic nano-objects in photocatalysis devices [213,214] and sensors [215]

showing the promising potential of all-oxides heterostructures with plasmonic NPs like presented in this work.

3.3.2 Performance enhancement of the nanocomposites.

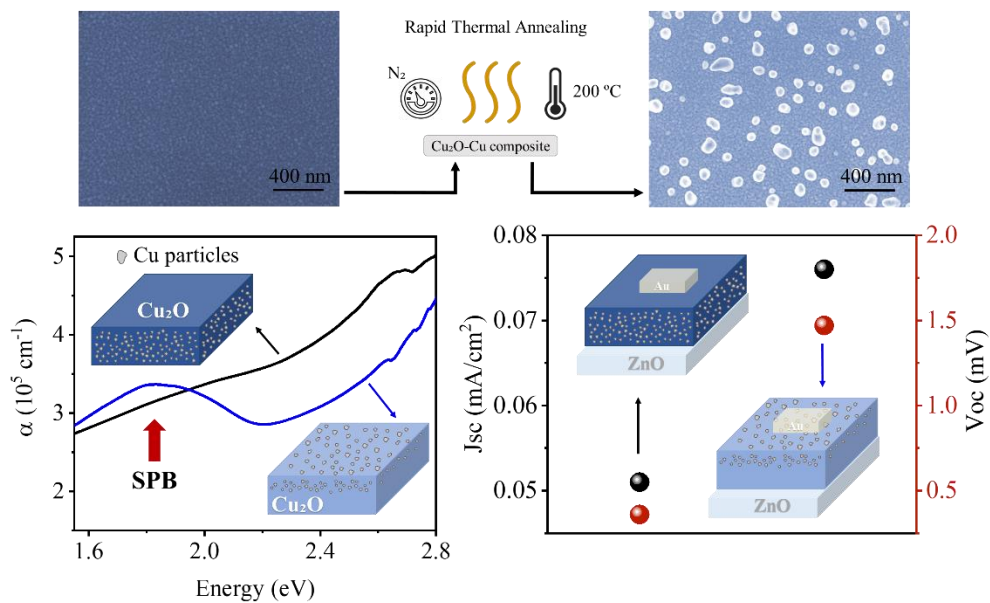
Some considerations about possibilities of improving the performance of the composites grown using an OFR of 4 sccm worth to be discussed. The low crystallinity of the matrix in nanoparticle-incorporated composites grown by sputtering has also been seen in previous works, and is associated to local strains and impurities interfering with the crystal growth [194]. Post-annealing could decrease the density of such defects and improve the matrix crystallinity, favoring the enhancement of the diffusion length. Yet, as seen in other studies, this would likely be accompanied by a segregation of metal to the surface and agglomeration of nanoparticles [216]. A careful control of the annealing atmosphere would also need to be considered because annealing in an oxidative atmosphere would lead to uncontrolled decay in the density of acceptor states in the matrix and particle oxidation. Another way to try improving the performance could be through fine tuning of the oxygen concentration during synthesis. Especially, according to the spectral photocurrent results, the proximity of the SPB to the absorption band of Cu_2O plays an important role in the enhancement of the photocurrent. This proximity depends on particle size, itself affected by the OFR. Within the tested conditions, the optimal OFR is likely between 4 sccm and 5 sccm, but the difference in the position of the SPB should not be noticeable using the same experimental conditions. Increasing the flux of sputtered metallic atoms, through an increase of the discharge current applied to the copper target, could widen the working window for OFRs leading to transition from percolated to isolated copper NPs in Cu_2O . Therefore, it could give more freedom to precisely adjust the size of particles.

Chapter conclusions

In this study, we proposed a single-step route to synthesize plasmonic copper nanodomains embedded in a p-type semiconducting Cu_2O matrix that trigger enhanced photoconversion when inserted at the interface of n-ZnO/p- Cu_2O heterojunctions. The enhancement finds its origin in hot carriers injection and collection following deexcitation of localized surface plasmon resonance (LSPR) at plasmonic Cu nanodomains. The single-step route proposed is based on the control of oxygen partial pressure or oxygen flowrate during reactive sputtering of copper, a method that can be easily scaled up and is compatible with the microelectronic industry.

CHAPTER 4

Influence of thermal annealing on the properties of CuNPs-Cu₂O composites and photoconversion devices.



Abstract

In this chapter, plasmonic composites based on Cu nanoparticles (NPs) and Cu₂O semiconductor (CuNPs-Cu₂O) are further studied in order to better exploit the plasmon effect in optoelectronic applications. Particularly, the study is focused on the evolution of the composites and particles properties when these are exposed to thermal treatment at relatively low temperatures. To this purpose a rapid thermal annealing (RTA) furnace was used, under nitrogen atmosphere and oxygen-poor conditions. At temperatures higher than 150 °C it was possible to see a copper segregation through the surface, increase in the crystal preferential orientation of the host material and improvement of the plasmon response. Same plasmonic devices studied in Chapter 3 were thermally-treated at 200 °C and characterized by SEM, HRTEM, J-V and Impedance Spectroscopy. The distribution and presence of plasmonic nanoparticles inside the devices was modified with annealing, while a further increase in the photocurrent as result of the plasmonic effect was observed compared with not annealed devices.

Contents

| | |
|---|-----|
| CHAPTER 4 | 91 |
| Influence of thermal annealing on the properties of CuNPs-Cu₂O composites and photoconversion devices | 91 |
| 4.1 Introduction..... | 95 |
| 4.2 Study of the influence of thermal annealing on the properties of CuNPs-Cu ₂ O composites and related devices. | 96 |
| 4.2.1 CuNPs-Cu ₂ O films growth and annealing. | 96 |
| 4.2.2 Characterization of CuNPs-Cu ₂ O composites annealed in oxygen-poor conditions. | 97 |
| 4.2.3 Influence of the thermal annealing on plasmonic devices performance. | 102 |
| Chapter conclusions..... | 113 |

4.1 Introduction

ZnO/Cu₂O thin film heterojunction has been studied by different groups [35,74,217,218] as a stable combination of low cost and non-toxic n-type and p-type semiconductors, respectively, which band alignment contributes to the separation of photogenerated electron and holes, a key aspect in solar cells and others optoelectronic devices. Although Cu₂O-based solar cells have a Shockley-Queisser theoretical power conversion efficiency (PCE) limit of 20 %, there are still many experimental issues to overcome the 8.4 % [219–221]. Among the remaining problems related to the low PCE reached so far are the interfacial recombination [76], the small grain size of Cu₂O films [74], the mobility and carrier concentration equilibrium [222], among others. Thermal annealing has been considered as a possible path to improve the properties of the Cu₂O-based heterostructures, influencing the crystallinity, carrier mobility, optical properties, defects passivation and devices performance [34,223–226].

Besides, modifications in the n-ZnO/p-Cu₂O heterostructures in order to improve their response include the incorporation of nanoparticles into the architecture and consequent exploitation of nanoscale effects like quantum confinement [77,227] and localized surface plasmon resonance (LSPR) [79,159,228]. Regarding the LSPR effect, it was previously mentioned that the junction between a plasmonic metal and a semiconductor allows to take advantage of extra carrier injection processes, which consist in the transference of hot electrons from the metal, excited with the light at the plasmon frequency, through the semiconductor conduction band. Photogeneration enhancement in optoelectronic devices like photodetectors and solar cells has been demonstrated using these configurations [99,208,209,212].

In Chapter 3, CuNPs-Cu₂O nanocomposites were in-situ obtained by reactive magnetron sputtering, following a one-step process in which plasmonic copper nanoparticles were formed inside the semiconductor matrix by controlling the oxygen feeding inside the deposition chamber. At low oxygen flowrates (2 sccm and 4 sccm) it was possible to oxidize just a fraction of copper atoms deposited on the evolving film surface, prompting the separation of Cu₂O and Cu phases. The response of CuNPs-Cu₂O nanocomposites-based devices under illuminated conditions have shown an increase in the photocurrent due to the extra carriers injection as a result of the LSPR effect. Furthermore, it was found that growing a thin composite layer close

to the ZnO interface (n-ZnO/CuNPs-Cu₂O/p-Cu₂O) makes more efficient the charge separation process, increasing the short-circuit current density (J_{sc}) by a factor of 4.5 with respect to the reference device (ZnO/Cu₂O). However, despite the increase in photocurrent as a result of the plasmonic particles, the open circuit voltage V_{oc} remained low. It was related to defects states and recombination centers induced by the metal nanoparticles.

In this chapter, thermal annealing of plasmonic composites (CuNPs-Cu₂O) and plasmonic based-heterostructures is studied using a rapid thermal annealing (RTA) furnace in oxygen-poor conditions, trying to limit the oxidation of the copper nanoparticles and take advantage of the LSPR effect. This has been found to be an alternative to improve the crystalline quality of the host material (Cu₂O), increase the grain size and passivate defects, increasing the V_{oc} . Additionally, a segregation and coalescence of Cu nanoparticles with temperature is observed, playing a role in the final response of the modified architectures. Microstructure, morphology and optical properties of annealed composites are studied. Furthermore, J-V characterization and Impedance Spectroscopy measurements helped to understand the phenomena influencing the response of annealed plasmonic devices.

4.2 Study of the influence of thermal annealing on the properties of CuNPs-Cu₂O composites and related devices.

4.2.1 CuNPs-Cu₂O films growth and annealing.

CuNPs-Cu₂O composites were grown on glass slides and Si substrates by reactive DC magnetron sputtering following the same procedure detailed in [Chapters 2 and 3](#). The substrates were placed on the circular holder plate at 7.5 cm from its rotation axis, facing the copper target surface, being the target-to-substrate holder distance equal to 5 cm. Two targets were used for the films study, a new one, with a nearly flat surface, and a used one, presenting a racetrack. After evacuating the chamber (reaching a vacuum of 10^{-3} Pa), argon (50 sccm) and oxygen (4 sccm) gases were introduced and a discharge current of 0.15 A was established on the copper target. Surface activation by radio frequency (RF) polarization (1 min) was applied and the plate was rotating during the whole process (RF and deposition) at 3.5 Hz.

The resulted CuNPs-Cu₂O composites were taken out of the sputtering chamber and introduced in an As-One 100 Rapid Thermal Annealing (RTA) furnace for thermal treatment. Fixing a heating ramp of 15 °C/s and the macro described in [Chapter 2](#), the samples were annealed during 1 hour at different temperatures (150 °C, 200 °C, 250 °C and 300 °C). Under these conditions the composites were treated in oxygen-poor atmosphere to avoid or limit the oxidation of the copper particles present inside the composite.

4.2.2 Characterization of CuNPs-Cu₂O composites annealed in oxygen-poor conditions.

Temperature dependence

Crystalline structure and morphology of CuNPs-Cu₂O composites (grown at 7.5 cm from the holder axis, using a new target), before and after annealing at different temperatures (150 °C, 200 °C, 250 °C and 300 °C), were analysed by X-rays diffraction (XRD) and scanning electron microscopy (SEM) ([Figure 4.1](#)).

As depicted in [Figure 4.1b](#), XRD indicates the presence of peaks corresponding to the cubic phases of Cu₂O and Cu (JCPDS 00-004-0836 and JCPDS 04-007-9767, respectively), whose intensity was clearly influenced by the thermal treatment, especially the (200) peak of Cu₂O. This suggests a strong rearrangement of the crystal lattice and the development of the {100} high energy family planes, favouring the formation of larger domains of Cu₂O, oriented in this direction ([Figure 4.1c](#)). On the other hand, the temperature increase has also an effect on the [111] orientation of the Cu domains, present in the composites, accompanied by an increase in the crystallite size up to 50 nm, approximately.

According to the SEM micrographs ([Figure 4.1 \(a.1 - a.5\)](#)) these results can be related to the formation of larger Cu particles at the film surface due to the diffusion and coalescence of this metal upon annealing. It can be observed that when a temperature of 150 °C is applied, grains or particles of 90 nm of lateral length, on average, appear on the sample surface. The density of these particles increases as the temperature increases to 200 °C, although the average size does not vary considerably ([Figure 4.1d](#)).

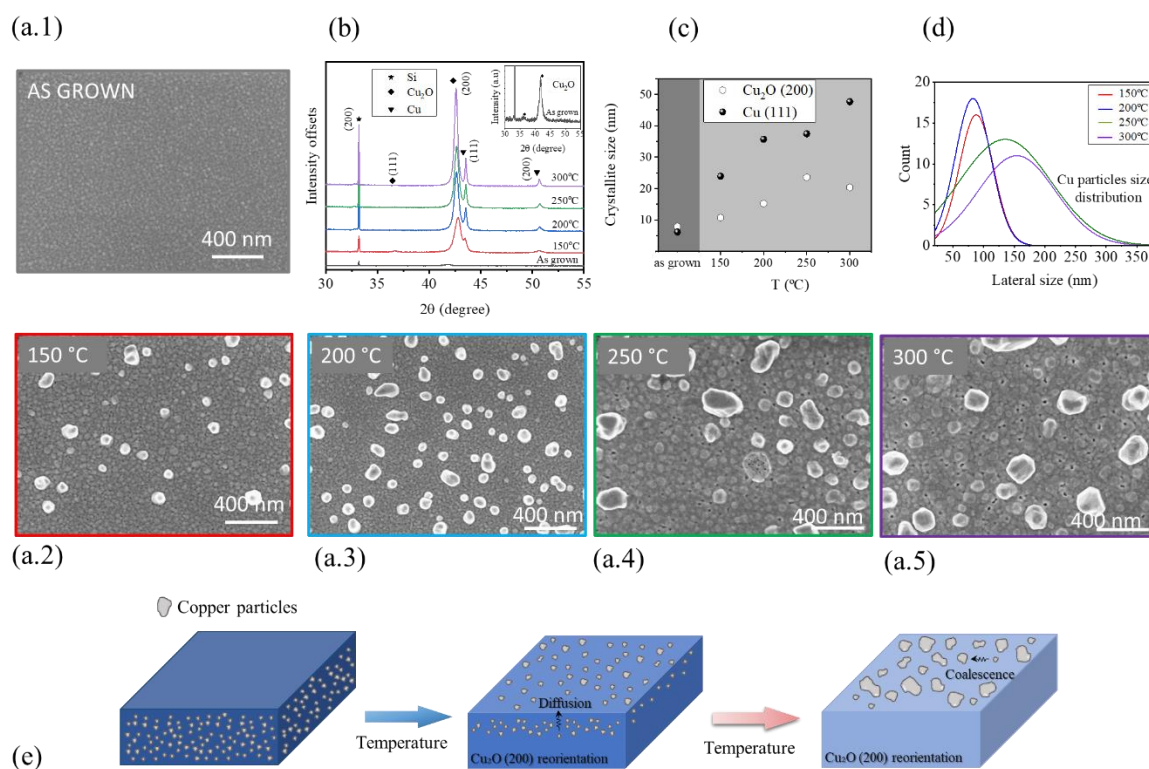


Figure 4.1: (a.1-a.5) Scanning electron microscopy of CuNPs-Cu₂O composites before and after annealing at 4 different temperatures for 1 hour (150 °C, 200 °C, 250 °C and 300 °C). (b) Diffraction patterns of the samples before and after treatment. (c) Coherent domains and (d) particles sizes extracted from XRD (using the Scherrer formula) and SEM images, respectively. (e) Schematic of the segregation and coalescence of the Cu particles into the composite with the thermal treatment.

This suggests the progressive occurrence of diffusion of copper atoms to the composite surface and nucleation and growth of additional particles (see proposed schematic in Figure 4.1e). At 250 °C and above, there is a jump in particle size at the surface, while particles density decreases. This suggests a saturation in the diffusion of particles to the surface and the coalescence of particles already present on it, forming larger grains and decreasing the density. From 300 °C onwards, the increase in the grain size and decrease in the density of particles is no longer observed. A decrease in the number of smaller particles and appearance of micropores in the film are evidenced instead.

Figure 4.2a shows the absorption coefficient plot obtained from UV-Vis-NIR spectroscopy measurements. After applying thermal treatment, the band corresponding to the plasmonic

response of the Cu nanodomains within the composite (around 2 eV [173,179]) considerably increases and shifts towards lower energies associated to higher plasmonic particles size (Figure 4.2b). At the same time, the FWHM of the surface plasmon bands (SPBs) decreases indicating a possible decrease in the size distribution or higher homogeneity, as well as the formation of more rounded structures [84] (inset of Figure 4.2b).

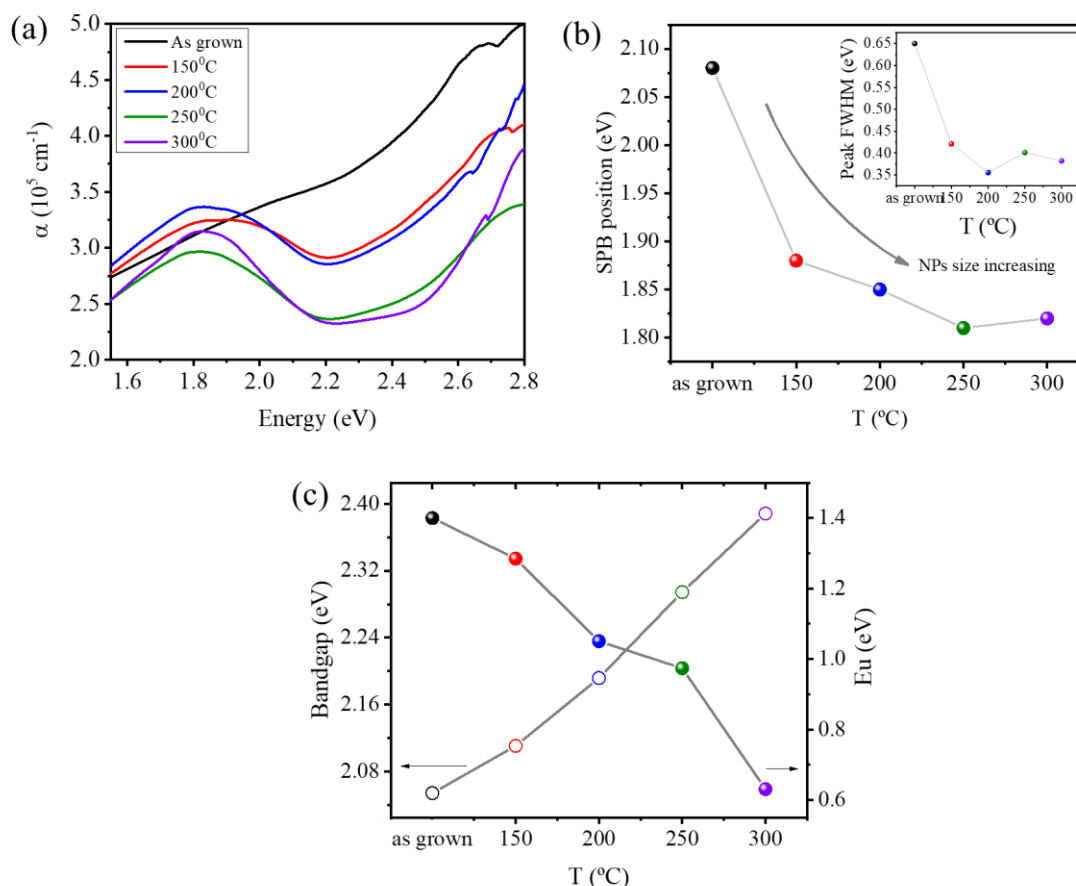


Figure 4.2: (a) Absorption coefficient; (b) surface plasmon band (SPB) position and (inset) FWHM of the SPB taken from a Gaussian fit; (c) bandgap and Urbach energy obtained from UV-Vis-NIR spectroscopy measurements.

The Cu_2O bandgap, estimated using the Tauc method and considering allowed direct transitions, exhibits an increase from 2.04 eV (for the untreated sample) to 2.4 eV (for the sample treated at 300 °C) (Figure 4.2c). As discussed in Chapter 3, these values below 2.4 eV (reported for Cu_2O [36,44]) should not be merely attributed to the semiconductor bandgap since other effects like interband transitions occurring in the copper particles and defect states localized near the

Cu_2O conduction and valence bands can contribute by overlapping. Regarding the last, the Urbach energy has been calculated in order to evaluate the modification of the degree of disorder in the crystalline structure of Cu_2O (Figure 4.2c). The results show how the increase in temperature decreases the amplitude of the Urbach tail and consequently the density of defect states, in agreement with the bandgap evolution. It can be associated to the increase in the size of the coherent domains of Cu_2O , reported in Figure 4.1c, and lower density of structural defects.

Target consumption and sample position dependence

The structural and optical properties discussed above can be affected or modified depending on the target surface profile. The angular distribution of the sputtered atoms and accelerated oxygen ions from the vicinity of the target surface changes depending on its racetrack depth. We have discussed how this can affect the momentum transference and mobility of adatoms to form high energy crystalline planes. A simplified schematic of the emitted atoms distribution is shown in Figure 4.3 (on top) and, according to it, we can expect that in samples grown facing the target, more Cu atoms impinge the surface if the target has a planar surface (new target).

In this figure, SEM micrographs showing the surface morphology of samples grown at 7.5 cm, and annealed at 200 °C, are also presented. It can be seen the presence of bigger Cu particles when the sputtered target is new or nearly flat. To understand this, it is necessary to consider the balance between the flux of sputtered particles impinging on the growing film and the flux of oxygen molecules from the reactive gas mixture. A new target exhibits a lower surface area, in particular in the region corresponding to the racetrack, leading to a higher current density for a fixed value of the discharge current. Therefore, for a given partial pressure of oxygen in the gas mixture, the target surface will be less oxidized than in the case of a used (eroded) target. Consequently, given the fact that a higher amount of metallic copper atoms is expected to be found in the films deposited with a new target, after annealing at 200 °C, more big Cu particles will appear. On the other hand, coherent domain size calculations showed close values of crystallite sizes (~ 35 nm) while SPB resulted at the same position in the two cases (1.84 eV, approximately). The main difference lies then in the SPB intensity, which is higher when more incidence of copper atoms occurs perpendicular to the substrate (new target). This may

be related to higher homogeneity in particle size, which promotes higher LSPR excitation at the same energy [229].

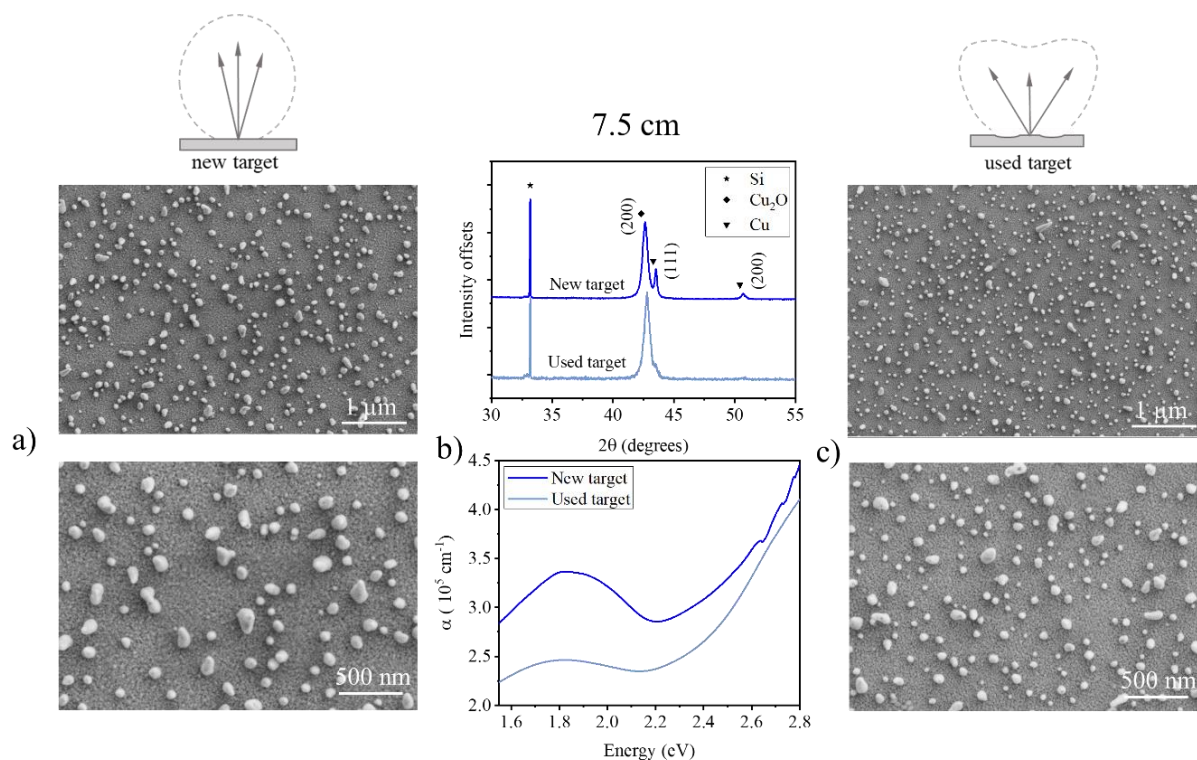


Figure 4.3: SEM micrographs of samples grown at 7.5 cm, using the (a) new and (c) the eroded target, and annealed at the same temperature (200 °C). On top of the micrographs a schematic representing the influence of the target surface profile on the sputtered atoms dispersion is shown. What is schematically emitted from the center (represented by arrows) results from the distributed emissions at the racetrack. (b) Corresponding XRD patterns and absorption coefficient.

From the above analysis, we can be tempted to infer that, using an eroded target, the higher incidence of copper atoms as well as the higher plasmonic response, would likely correspond to a position shifted out of the target axis. Hence, just as particle size homogeneity could be associated with SPB intensity when the target is changed, the positioning of the sample may also play a role. It is important, thus, to consider the positioning of the sample depending of the target consumption in order to obtain the best composite properties.

4.2.3 Influence of the thermal annealing on plasmonic devices performance.

In [Chapter 3](#), it was demonstrated the photocurrent enhancement in n-ZnO/p-Cu₂O based devices after inclusion of plasmonic Cu nanoparticles. Limitations in the photogeneration was associated to the density of defects in the composites and the more suitable configuration resulted to be the one with the particles close to the p-n junction zone. As described in previous section, the thermal treatment of the CuNPs-Cu₂O composites has three principal consequences: the supposed decrease in the density of defect states in the host material, the diffusion of Cu atoms through the Cu₂O matrix and the coalescence of Cu particles associated to improvement of the plasmonic response. Therefore, annealing at relatively low temperatures may be an interesting path through the performance improvement of the presented devices.

Devices preparation

The CuNPs-Cu₂O-based devices studied in [Chapter 3](#) (composites grown at 7.5 cm, using an eroded target) were divided into two pieces, with the second one following an annealing process (200 °C, 1 hour) under the conditions described above ([section 4.2.1](#)). This temperature was selected since the size of particles starts to increase considerably for higher temperature values, decreasing the homogeneity on the surface and shifting the SPB peak towards lower energies. Regarding this last fact, it has been discussed in the previous chapter that the proximity of the SPB to the Cu₂O bandgap value has a positive impact on the photocurrent. Moreover, at this temperature high preferential orientation and no porosity was observed for Cu₂O, according to results obtained in [section 4.2.2](#). After annealing, Au contacts were deposited by sputtering applying a 0.06 A current under 0.5 Pa of Ar working pressure. The distance between the Au target (99.99% of purity, Neyco Company) and the substrate-holder was 5 cm.

The annealed devices were labelled as Dev_4sccmTT (corresponding to the annealed n-ZnO/CuNPs-Cu₂O heterostructure) and Dev_4sccm/6sccmTT (corresponding to the annealed n-ZnO/CuNPs-Cu₂O/p-Cu₂O heterostructure).

Devices morphology and in-depth chemical composition.

Scanning and transmission electron microscopy of annealed devices were performed in order to better understand the resulted morphology by surface and in-depth chemical analysis. SEM micrographs (Figure 4.4, insets) showed the expected appearance of Cu NPs at the device surface. It can be noticed that, for Dev_4sccm/6sccmTT, only a few Cu particles were formed at the surface, associated to lower Cu content in this configuration.

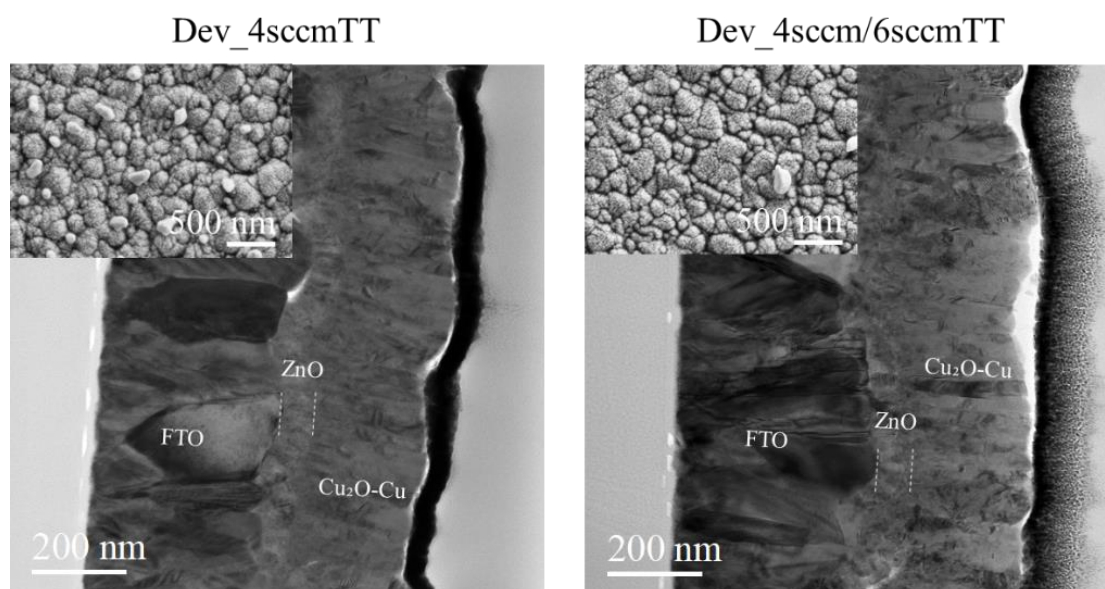


Figure 4.4: TEM and SEM (inset) micrographs corresponding to devices Dev_4sccmTT and Dev_4sccm/6sccmTT after being annealed at 200 °C. The layers conforming the devices are indicated.

Figure 4.4 also presents the bright field micrographs taken from TEM analysis, indicating the three different layers forming the devices: FTO, ZnO and Cu-O, with a thickness of around 380 nm, 70 nm and 250 nm, respectively. It can be noted that the roughness and large grain sizes of the conductive oxide layer (FTO) had an influence on the final roughness of the composite layer. This is supported by SEM micrographs, where a different morphology is observed compared to the films on glass (Figure 4.3). It can be noticed that the particles appearing at the device surface, according to SEM, are not visible in the cross-section view (TEM micrographs). Since the TEM analysis was done after cleaning the samples surface with ethanol and ultrasonic bath, due to undesired samples contamination, we suspect that the particles were completely removed.

In order to investigate about the in-depth presence of metallic copper, STEM analysis was done in a selected area including the ZnO and Cu-O layers. In Figure 4.5 it can be seen the High Angle Annular Dark Field (HAADF)-STEM micrographs taken for the EELS analysis of Dev_4sccmTT and Dev_4sccm/6sccmTT.

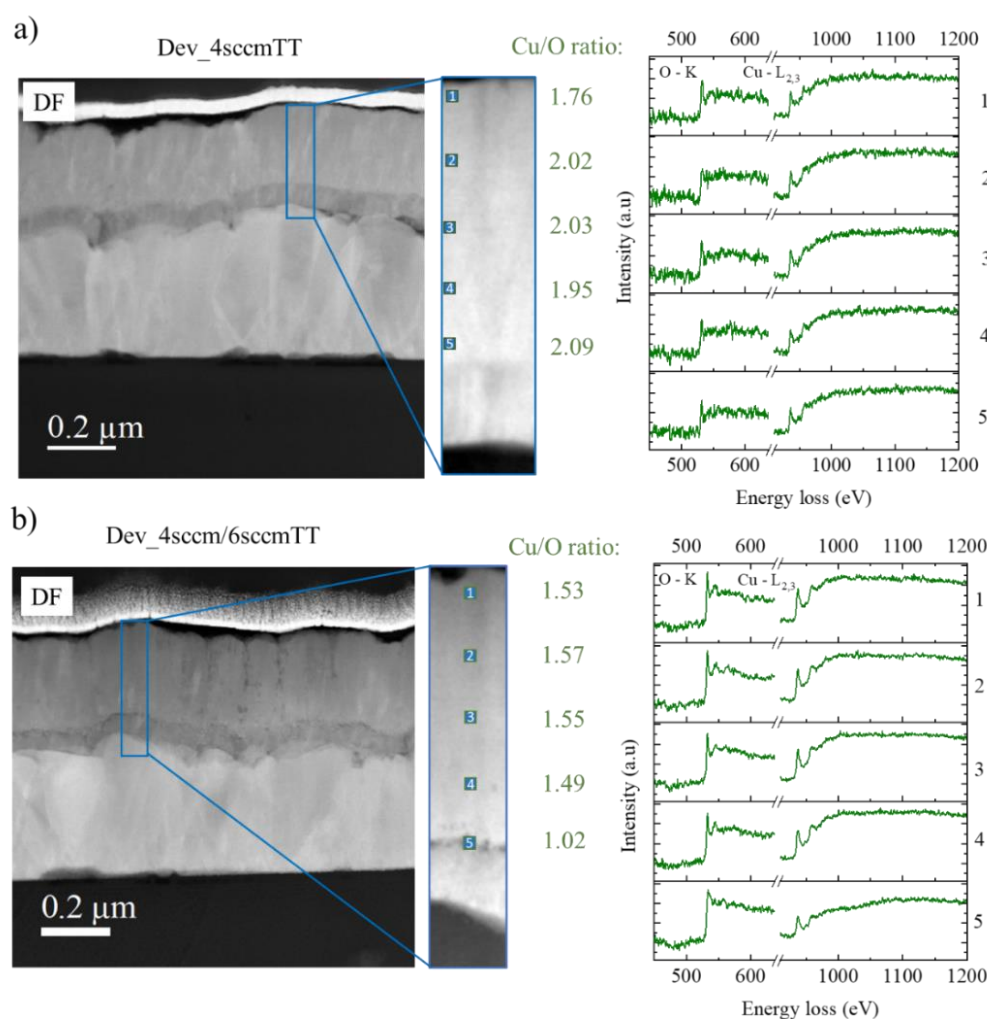


Figure 4.5: High angle annular dark field (HAADF)-STEM micrographs and energy loss near edge structure (ELNES) spectra at O-K and Cu-L_{2,3} edges corresponding to the selected area of the HAADF micrograph (rectangle) of Dev_4sccmTT and Dev_4sccm/6sccmTT.

The estimation of the atomic contents from ELNES measurements at O-K and Cu-L_{2,3} edges, corresponding to the selected regions, indicates that the Cu/O ratio barely varies in depth inside the Cu-O layer for both devices. In Dev_4sccm/6sccmTT the atomic content of Cu (~60 %) is lower compared to Dev_4sccmTT (~67 %) and the theoretical value of this element in Cu₂O (66.7 %). This agrees with the lower Cu % of the initial CuNPs-Cu₂O/p-Cu₂O bilayer, and

suspected Cu migration towards the surface. The ELNES spectra reveal the presence of Cu-L₃ and Cu-L₂ edges at 937.9 eV and 957.9 eV, respectively, indicating the Cu¹⁺ oxidation state within Cu₂O for both devices [32,186]. Nevertheless, detection of the Cu⁰ oxidation state remained elusive.

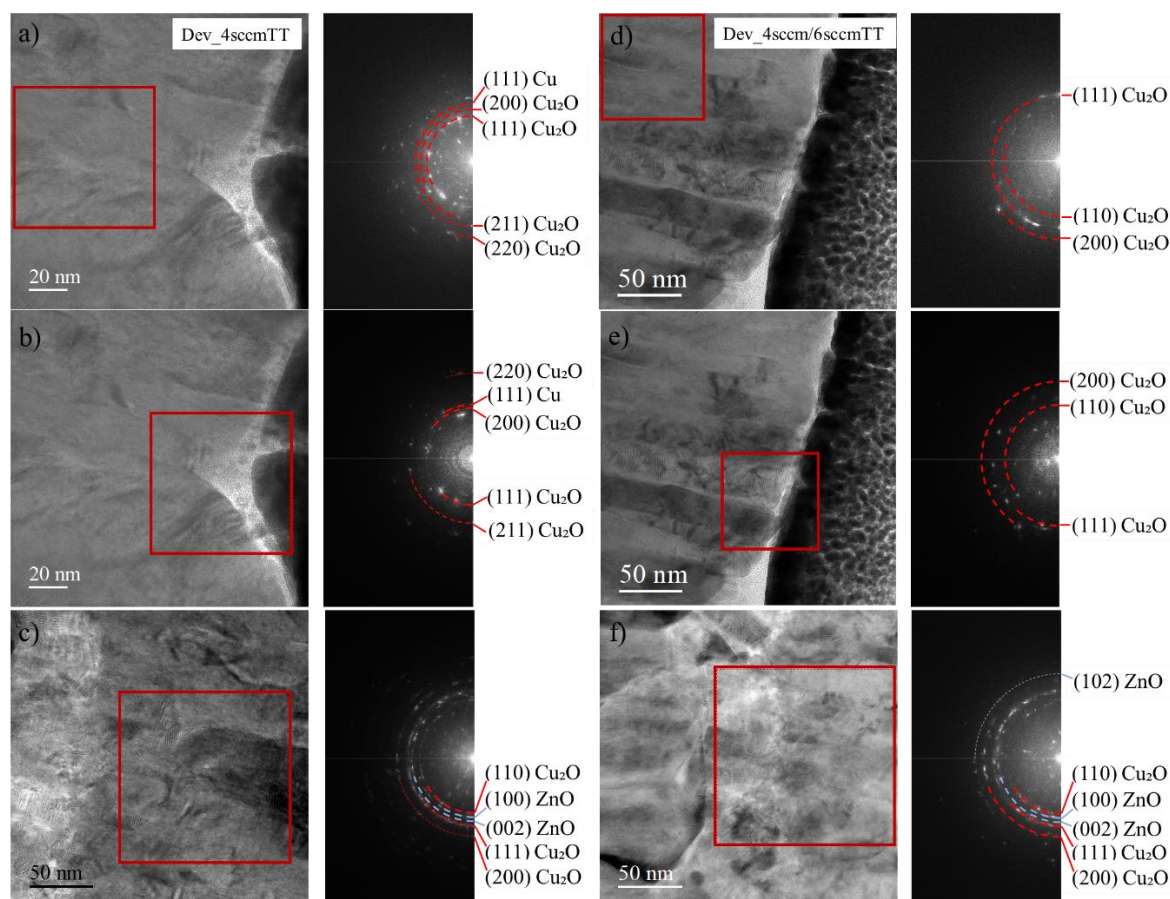


Figure 4.6: HRTEM micrographs and corresponding FFT of Dev_4sccmTT and Dev_4sccm/6sccmTT. The squares enclose the area where the FFT was applied.

The metallic copper phase was, nevertheless, distinguished through the Fast Fourier Transformed (FFT) analysis (Figure 4.6). In Dev_4sccmTT three different zones were analyzed: close to the surface of the Cu-O layer (a), at the center (b) and next to the junction ZnO/Cu-O (c). A diffraction ring corresponding to (111) Cu planes was detected close to the surface, supporting the hypothesis of copper diffusion through the matrix and segregation at the surface. Same analysis was done for Dev_4sccm/6sccmTT and no diffraction signal was found for the metallic copper.

Summarizing, these results suggest that the architecture of annealed devices was changed with respect to the as grown ones. Metal nanoparticles resulted to be present in both devices close to the contact area, being their density much lower in Dev_4sccm/6sccmTT.

Electrical characterization: current density vs voltage measurements.

Figure 4.7 shows the J-V characterization of the devices in dark and illuminated conditions. In dark conditions (a) a rectifying behavior for all devices is observed. Dev_4sccmTT presents higher reverse saturation current than Dev_4sccm/6sccm and Dev_4sccm/6sccmTT, according to the semi-log plot of $|J|$ vs V (Figure 4.7a, inset). The progressive increase in the current under the action of the reverse bias, which must be small and constant for devices with a diode behavior (saturation current), could be associated to hot carriers photogenerated by the plasmonic effect, induced by Cu nanoparticles. The hot carriers energy allows the path of these through the energy barrier of both semiconductors, generating a current, whatever the polarity of the applied potential is. It is suspected then, that the current in reverse bias is higher in devices with higher amount of plasmonic Cu nanoparticles (Dev_4sccm and Dev_4sccmTT). The small increase in the current for Dev_4sccm/6sccmTT suggests lower hot carriers transference, compared to the others configurations.

From J-V curves measured under illumination conditions (b) it is seen that Dev_4sccmTT presents the higher J_{sc} . We proved in section 4.2.2 that the annealing process improves the plasmon response of the particles. Additionally, it is suspected that the segregation of nanoparticles close to the Au contact could induce an effect similar to the effect we observed when the nanoparticles were close to the p-n junction, allowing a more efficient collection of hot carriers and an increase in J_{sc} (Figure 4.8 (b, c)). Another effect likely influencing the photocurrent enhancement in this configuration is the scattering by the big Cu particles at the device surface, increasing the effective optical path length of photons inside the Cu_2O layer and, consequently, the light absorption of it, with the subsequent electron-hole pairs generation.

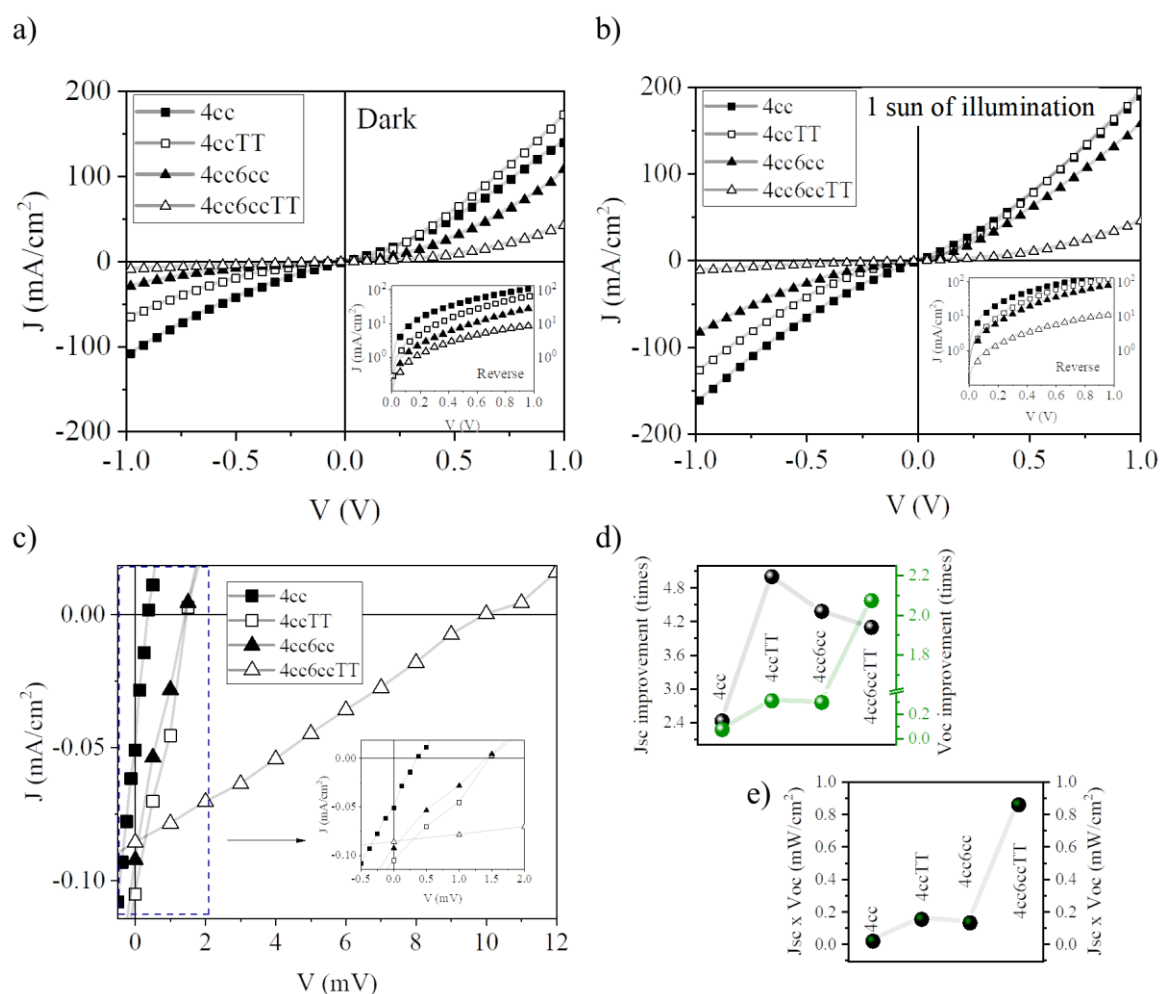


Figure 4.7: Measurements of current density as a function of voltage in (a) dark and (b) illumination conditions for devices before (Chapter 3) and after annealing at 200 °C. (c) Zoom of the J-V curves in illumination. (d) Analysis of the short circuit current density (J_{sc}) and open circuit voltage (V_{oc}) improvement with respect to a reference device n-ZnO/p-Cu₂O (Chapter 3) with $J_{sc} = 0.021$ mA/cm² and $V_{oc} = 4.8$ mV. (e) $J_{sc} \times V_{oc}$ product plot in order to find the best parameter combination. Devices are labelled as: Dev_4sccm (4cc), Dev_4sccmTT (4ccTT), Dev_4sccm/6sccm (4cc6cc) and Dev_4sccm/6sccmTT (4cc6ccTT).

However, the high saturation current of Dev_4sccmTT suggests remaining lattice defects and recombination phenomena limiting the V_{oc} that inversely depends on the saturation current. Even so, an increase in V_{oc} with respect to the non-annealed configuration (Dev_4sccm) is observed. A priori, we associate this improvement to defects passivation in the Cu₂O matrix. Within this hypothesis, the defect passivation and higher ordering of the crystalline structure

as result of the thermal annealing have a direct impact in the V_{oc} , improved in treated samples compared to the non-annealed devices.

An increase in the open circuit voltage (V_{oc}) by almost an order of magnitude is observed in Dev_4sccm/6sccmTT, compared with the other designs. This sample presented the lower saturation current J_0 , which explain the increase in the V_{oc} , according to [equation 3.1](#).

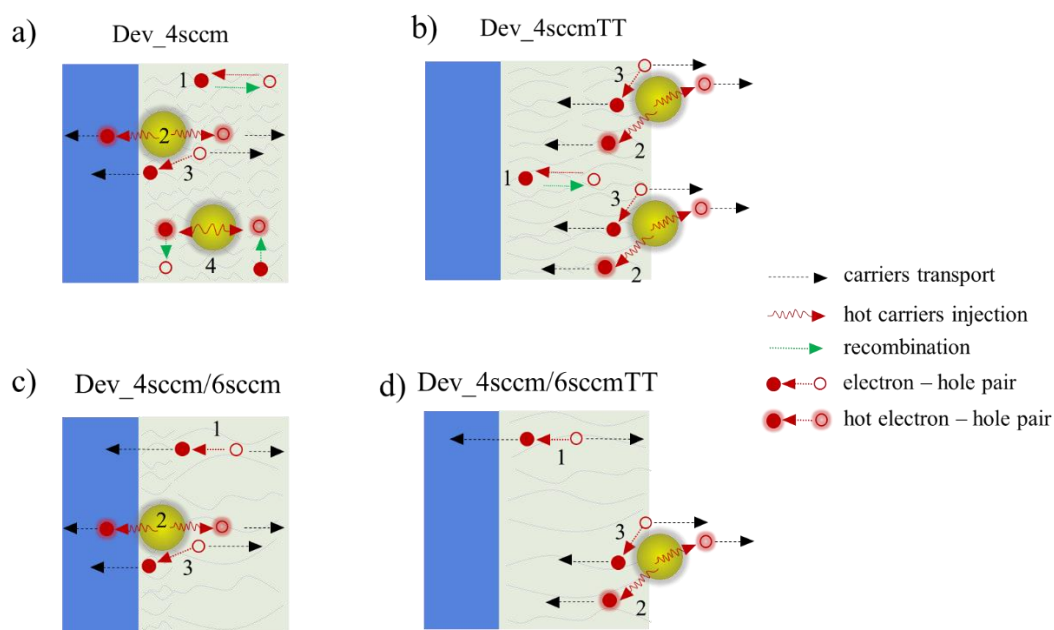


Figure 4.8: Proposed schematic of the transference, injection and recombination of carriers in (a) Dev_4sccm, (b) Dev_4sccmTT, (c) Dev_4sccm/6sccm and (d) Dev_4sccm/6sccmTT. Analogous to [Figure 3.18](#), the processes related to the photocurrent generation are represented: (1) electron – hole pair generation and recombination; (2) hot carriers injection from plasmonic NPs; (3) carrier separation by strong local field enhancement around the metal NPs; (4) annihilation of injected hot carriers by recombination.

As a summary, the graphs of J_{sc} and V_{oc} improvement with respect to the reference device n-ZnO/p-Cu₂O (Dev_6sccm) presented in [Chapter 3](#), as well as the $J_{sc} \times V_{oc}$ product, proportional to the efficiency of the devices ([equation 2.14](#)), are shown in [Figure 4.7 \(d, e\)](#). The J_{sc} value of Dev_4sccmTT grew 5 times respect to the reference sample and the V_{oc} reached a value close to the bilayer configuration (Dev_4sccm/6sccm). A best efficiency is expected for Dev_4sccm/6sccmTT ([e](#)) principally associated to less defects in the heterostructure, although J_{sc} did not present an improvement. The last can be explained by the

lower contribution to J_{sc} of only a few plasmonic particles close to the back contact in the case of the Dev_4sccm/6sccmTT compared to Dev_4sccm/6sccm.

Electrical characterization: Impedance Spectroscopy measurements.

Figure 4.9 (b, c) shows the Nyquist diagrams obtained from Impedance Spectroscopy (IS) measurements, under illumination, at zero bias. In many works it is usual to perform the measurements under open circuit or operational conditions (applying a bias $V_{bi} = V_{oc}$ or $0 \leq V_{bi} \leq V_{oc}$, respectively) [230,231]. In our case the values of V_{oc} were below the minimum permitted by the impedance analyser (10 mV). However, the J-V curves allowed to carry out the measurements at zero bias, in compliance with the linearity principle and ensuring low noise signal [232].

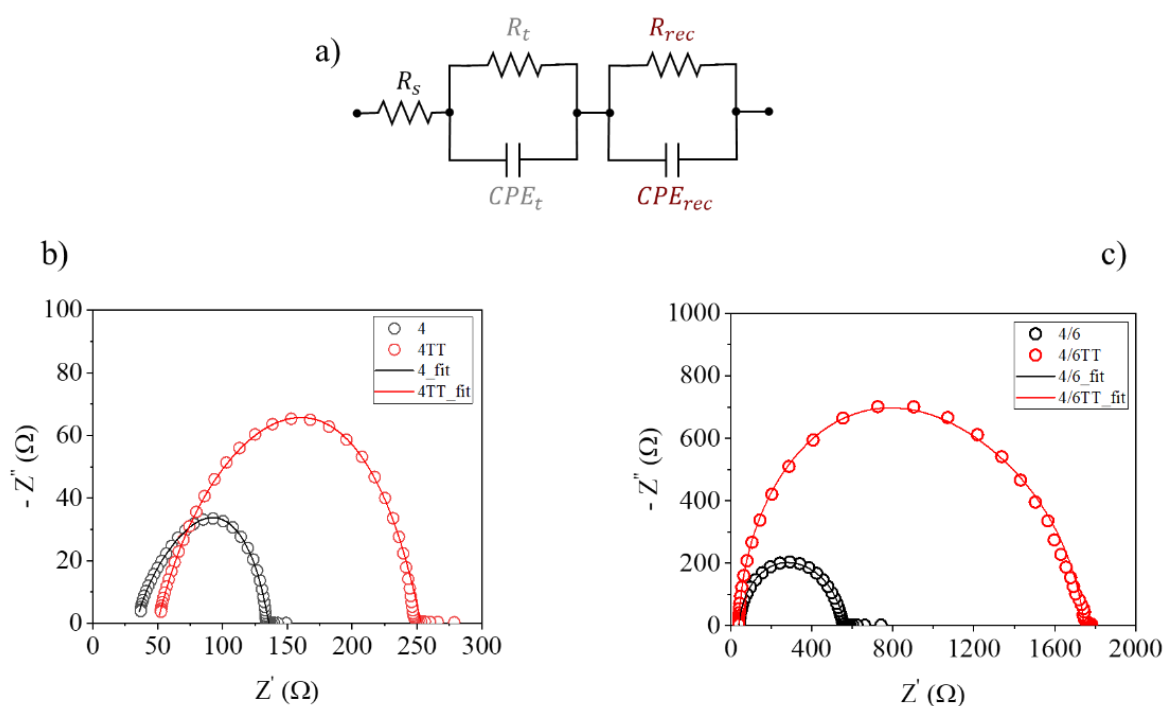


Figure 4.9: Results of Impedance Spectroscopy measurements at 1 sun of illumination and zero bias. (b, c) Nyquist diagrams of as grown devices and treated at 200°C. (a) Equivalent circuit used for data fitting. The devices were labelled in the graphs legend as: Dev_4sccm (4), Dev_4sccmTT (4TT), Dev_4sccm/6sccm (4/6) and Dev_4sccm/6sccmTT (4/6TT).

The Nyquist plots showed depressed semicircles characteristic of R – CPE based circuit. The tails appearing at lower frequencies have been observed in other studies and are associated to contacts effect [233]. Considering ohmic contacts (with a resistance R_s) and the electrical transport and recombination as R – CPE elements distributed in series, the equivalent circuit depicted in Figure 4.9a was proposed to model the impedance spectra. R – CPE elements were considered in series since the transport and recombination have different relaxation times, being two sequential processes [149].

Transport resistance R_t , accounting for the carrier transport or charge transference, recombination resistance R_{rec} , which is inversely proportional to the recombination current and directly proportional to generation rate in the device, and constant phase elements CPE, accounting for the capacitance per unit area due to charge accumulation, have been the components defined in the equivalent circuit [234]. The results of the data fitting using the EIS Spectrum Analyser software are included in Table 4.1.

R_s shows similar values for all devices, which is expectable since we have same contact materials. R_t and R_{rec} are higher in Dev_4sccm/6sccm and Dev_4sccm/6sccmTT than in Dev_4sccm and Dev_4sccmTT. Likewise, higher values of both resistances correspond to samples thermally treated, except for R_t in Dev_4sccmTT. The dispersion parameter n is close to 1 in most of the cases, indicating a near capacitive behavior of the CPE elements. The analysis of the values of Q will not be presented in this work since it is not completely understood and requires further study.

Table 4.1: Parameters calculated from data fitting using the EIS Spectrum Analyser software and considering the equivalent circuit from Figure 4.9a.

| Sample | R_s (Ω) | R_t (Ω) | Q_t (CPE _t) | n_t (CPE _t) | R_{rec} (Ω) | Q_{rec} (CPE _{rec}) | n_{rec} (CPE _{rec}) |
|-------------------|--------------------|--------------------|---------------------------|---------------------------|------------------------|---------------------------------|---------------------------------|
| Dev_4sccm | 33.3 | 68.4 | $3.3 \cdot 10^{-6}$ | 0.64 | 34.2 | $1.9 \cdot 10^{-7}$ | 0.99 |
| Dev_4sccmTT | 49.9 | 41.7 | $6.3 \cdot 10^{-7}$ | 0.99 | 161.5 | $2.9 \cdot 10^{-6}$ | 0.67 |
| Dev_4sccm/6sccm | 40.3 | 260.8 | $3.9 \cdot 10^{-7}$ | 0.85 | 257.5 | $4.7 \cdot 10^{-8}$ | 0.95 |
| Dev_4sccm/6sccmTT | 38.9 | 705.1 | $3.2 \cdot 10^{-7}$ | 0.86 | 1001.8 | $1.7 \cdot 10^{-8}$ | 1 |

Interestingly, we found an almost direct correlation between the behavior of R_{rec} ($1/R_t$) and the V_{oc} (J_{sc}) values (Figure 4.10) giving an idea of the mechanisms influencing the cell

parameters. Since R_{rec} is inversely proportional to the recombination current, it is related to defects and disorder in the crystalline structure, which directly influences the V_{oc} (a).

On the other hand, the higher carrier transport and charge transference, associated to $1/R_t$, corresponds to devices with higher J_{sc} while lower values of $(1/R_t)$ are related to lower J_{sc} (b). According to this analysis, Dev_4sccm should present a higher J_{sc} than Dev_4sccm/6sccm and Dev_4sccm/6sccmTT and this does not occur. We associated this low J_{sc} to the high defects density in this sample, which should decrease the carrier diffusion length considerably, counteracting the high values of charge transference, consequently decreasing the J_{sc} .

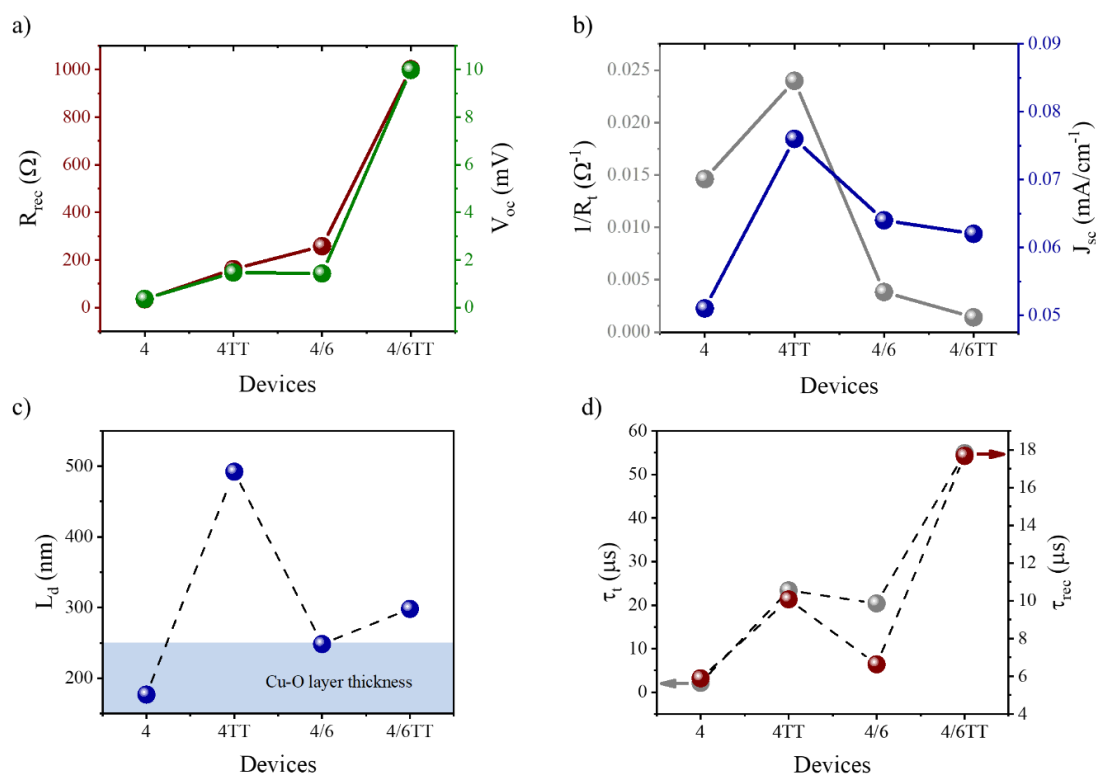


Figure 4.10: (a, b) Relation between R_{rec} ($1/R_t$) and the V_{oc} (J_{sc}) values for the different devices. (c) Carrier diffusion length L_d calculated from R_{rec} and R_t values. (d) Transit time τ_t and lifetime τ_{rec} obtained from the fitting parameters.

The carrier diffusion length L_d can be estimated from R_{rec} and R_t considering that $L_d = d\sqrt{R_{\text{rec}}/R_t}$, where d is the Cu-O layer thickness taken from TEM analysis (250 nm) [234,235]. In Figure 4.10c it can be seen that, in fact, the estimated diffusion length of Dev_4sccm is lower than the layer thickness.

The relaxation times (Figure 4.10d) corresponding to the transport/transference (transit time τ_t) and recombination/generation (carrier lifetime τ_{rec}) processes were calculated from the frequency f_p at the peaks maximum of the Bode plots ($\tau = 1/2\pi f_p$) (see Annex 4). A clear relation with the V_{oc} is observed.

Lower τ_t suggests faster injection of carriers or higher conductivity of carriers prior to collection. It is expected that samples with lower conductivity present higher τ_t , which is the case for thermally-treated devices. Dev_4sccmTT and Dev_4sccm/6sccm show close values of τ_t , which could be related to the presence of particles close to the carriers separation/collection zone. On the other hand, in agreement with the results reported in Chapter 3, the carrier lifetime τ_{rec} of Dev_4sccm is shorter than that of Dev_4sccm/6sccm and therefore the V_{oc} is lower in the first case. The photocarriers in Dev_4sccmTT have longer τ_{rec} , likely to the passivation of defects, resulting in higher V_{oc} than Dev_4sccm/6sccm. Finally, as expected from previous analysis, the higher carrier lifetime corresponds to Dev_4sccm/6sccmTT in agreement with the higher V_{oc} obtained for this device.

It is noticeable that the carrier lifetime is very low in general and below the transit time. This talks about the density of defects and recombination that takes place in all the devices, resulting in low V_{oc} . This should stimulate another study in order to take advantage of the photocurrent improvement that have been demonstrated with the inclusion of plasmonic nanoparticles.

Chapter conclusions

In this chapter we have reported on the thermal treatment of CuNPs-Cu₂O plasmonic composites using a Rapid Thermal Annealing (RTA) furnace, in oxygen-poor conditions. It was shown by X-rays diffraction the increase in the preferential orientation of the Cu₂O matrix and of the size of crystallites of the copper particles when the temperature was augmented from 150 °C to 300 °C. Scanning microscopy showed that a segregation of metallic copper and coalescence of metallic nanoparticles at the composite surface occur when the samples are heated. The treated samples showed an enhanced LSPR response compared to non-annealed composites, with the maximum response occurring at 200 °C. This improvement was accompanied by better ordering of the crystalline structure in the Cu₂O matrix, as indicated by lower Urbach energy values with increasing temperature, suggesting a reduced density of defect states. It was also found a dependency of structural and optical properties (SPB intensity) of the composites thermally treated, on the consumption of the target. This study concluded that, in used targets, the optimal plasmonic response should occur for films grown at positions shifted out of the target axis.

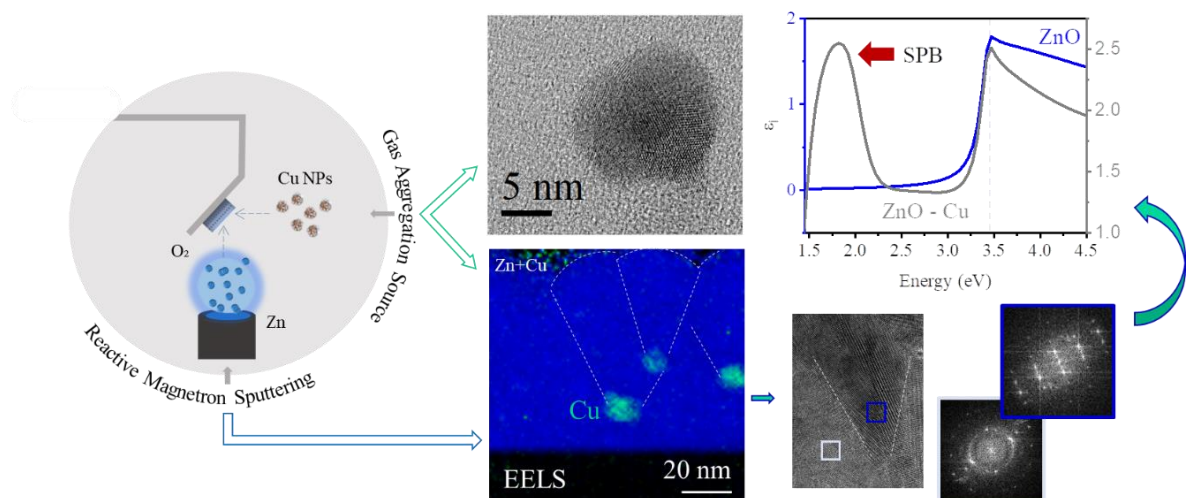
Furthermore, the two device configurations, studied in previous work (Chapter 3) and based on CuNPs-Cu₂O plasmonic composites, were thermally-treated at 200 °C under the same oxygen-poor conditions. In order to understand the architecture of the annealed devices and the localization of plasmonic copper nanoparticles, surface and in-depth study of the chemical composition was done using SEM, HRTEM and STEM analysis. Copper nanoparticles were observed on the device surface in both cases. Additionally, Cu presence close to surface of the p-type layer (close to the back contact) was evidenced for Dev_4sccmTT, with higher presence of copper particles before annealing. Meanwhile, the bilayer configuration Dev_4sccm/6sccmTT showed no traces of metallic phase in the Cu₂O layer with annealing.

Finally, electrical characterization of treated devices was done by means of J-V and Impedance Spectroscopy measurements. Higher density current in reverse bias suggested higher hot carriers injection, corresponding to Dev_4sccmTT. Besides, this device showed the highest J_{sc} , 5 times the value of the n-ZnO/p-Cu₂O reference device. This was associated with three possible causes: an enhancement of the LSPR response due to thermal annealing, favoured extra carrier collection due to the presence of particles near the back contact and light scattering

promoting the generation of electron-hole pairs in the Cu_2O layer. On the other hand, the higher value of V_{oc} was reached by Dev_4sccm/6sccmTT. Impedance modelling was used to find the possible physical mechanisms behind these results. A nearly direct relation between recombination and transport resistances with the values of V_{oc} and J_{sc} , respectively, was found. These results suggested a correlation between elevated J_{sc} values and the existence of more plasmonic copper nanoparticles close to the Au contact and p-n junction, coupled with minimal defects and recombination associated to higher V_{oc} .

CHAPTER 5

Synthesis of Cu NPs via a Gas Aggregation Source and fabrication of ZnO-CuNPs composites exhibiting LSPR



Abstract

This chapter focuses on the synthesis of Cu nanoparticles (NPs) using a gas aggregation source (GAS) and the subsequent fabrication of ZnO-CuNPs multilayer structures with plasmonic response. The GAS, coupled to a reactive sputtering deposition chamber, enables the growth of particles with control over size, composition and structure. The study explores the evolution of the nanoparticles density and size as a function of the deposition time, with and without holder rotation. The second aspect of this research delves into the fabrication of ZnO-CuNPs composites. These structures are designed as a ZnO + CuNPs sequence to integrate the synthesized nanoparticles into a ZnO matrix, aiming to exploit the properties of both materials, including the localized surface plasmon resonance effect (LSPR) of metal nanoparticles. HRTEM probed the obtaining of the multilayer configuration where Cu particles act as nucleation points for the ZnO structure, improving the crystallinity of the matrix. Finally, ellipsometric spectroscopy corroborates the surface plasmon band (SPB) corresponding to Cu NPs, resulting this approach a promise for potential optoelectronics applications.

Contents

| | |
|---|-----|
| CHAPTER 5 | 107 |
| Synthesis of Cu NPs via a Gas Aggregation Source and fabrication of ZnO-CuNPs composites exhibiting LSPR | 107 |
| 5.1 Introduction..... | 119 |
| 5.2 Copper nanoparticles by GAS | 120 |
| 5.3 ZnO-CuNPs multilayers composites by GAS..... | 124 |
| 5.3.1 ZnO-CuNPs multilayers deposition. | 124 |
| 5.3.2 Structural and morphological properties of ZnO-CuNPs multilayers..... | 126 |
| 5.3.3 Optical response of ZnO-CuNPs multilayers..... | 128 |
| 5.4 Studies in progress | 130 |
| 5.4.1 Electrical response of ZnO-CuNPs based devices. | 130 |
| Chapter conclusions | 132 |

5.1 Introduction

In [Chapter 3](#), we successfully synthesized CuNPs-Cu₂O plasmonic composites through reactive magnetron sputtering. This achievement was accomplished by exclusively regulating the oxygen flowrate (OFR) and ensuring oxidation occurred only for a fraction of the copper atoms deposited onto the growing film surface. However, applying this method to other metal oxide matrices such as CuO or ZnO has proven to be more challenging.

For CuO, which contains copper ions in their higher Cu oxidation state (Cu⁺²), reducing the OFR leads to the formation of less oxidized phases like Cu₂O or Cu₄O₃. This adjustment prevents the occurrence of remaining metallic copper without the presence of these aforementioned phases. On the other hand, we have explored during this thesis the possibility of incorporating metallic Cu into a ZnO matrix during the same deposition process ([Annex 5](#)). Zn and Cu targets were placed at different distances with respect to the sample holder (5 cm and 15 – 23 cm, respectively) and two OFR were used (6 sccm and 8 sccm). The results showed in all cases a resulting nearly amorphous ZnO and not clear copper plasmonic response.

A possible alternative to accomplish the fabrication of this challenging structures is the incorporation of previously sensitized particles using a gas aggregation source (GAS). The flexibility given by a system composed of a GAS coupled to a typical sputtering deposition chamber enables the independent, simultaneous, or sequential synthesis of metal nanoparticles and thin layers. This facility allows to design and study different composite structures, combining interesting properties and providing new functionalities. Additionally, the GAS allows to better control the density of particles and eventually the size by controlling the residence time. This last case remains as a future prospect. Control over the particles density and interconnection results important to avoid metallic behavior into the composite and better exploit the localized surface plasmon resonance (LSPR) for a potential application.

The main objective of this work is, therefore, to synthesize Cu NPs using a gas aggregation source and create ZnO-CuNPs multilayer structures with plasmonic properties via a sequential growth and ZnO thin films and Cu NPs. The study shows how the density of nanoparticles changes over deposition time, with and without holder rotation. HRTEM and EELS analyses are performed after the fabrication of the designed configuration in order to confirm the

successful formation of the heterostructure, while ellipsometric spectroscopy was performed to validate the presence of surface plasmon bands associated with Cu nanoparticles.

5.2 Copper nanoparticles by GAS

This study is dedicated to explore different experimental conditions to obtain Cu nanoparticles using the gas aggregation source (GAS) and analyse their morphology, size distribution, density, and chemical composition.

To carry out this investigation, we started maintaining constant the position of the Cu target in the GAS with respect to the sample holder (50 cm), located into the sputtering chamber (connected to the aggregation zone). At this position, the distance from the target to the aperture is of 5 cm. Using the 90 ° configuration holder, facing the source aperture, a glass substrate was used to deposit Cu nanoparticles during 1 minute, with the growth parameters presented in Chapter 2 (section 2.1.2).

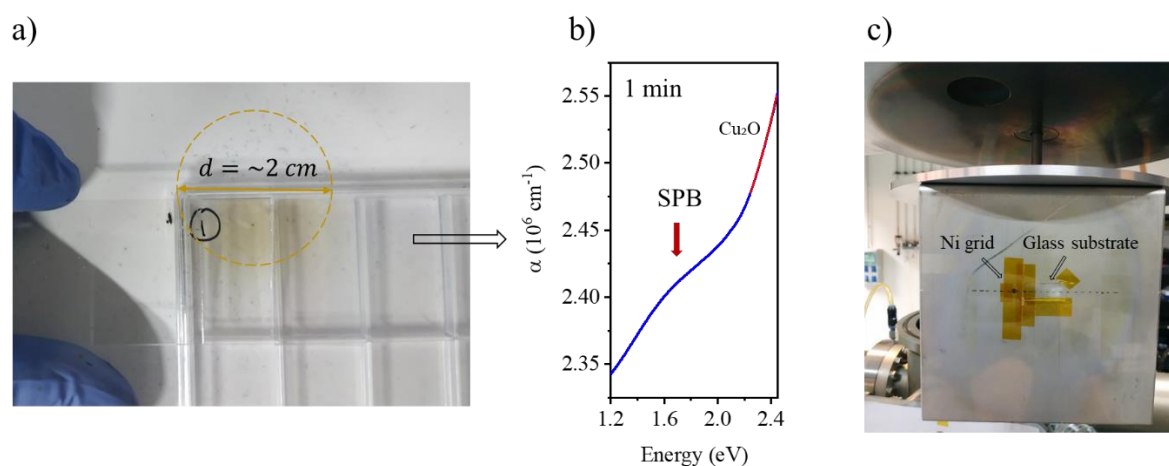


Figure 5.1: (a) Image of the approximate incidence area measured from depositing Cu particles during 1 min on a glass substrate using the 90 ° configuration holder, in order to define the center of the particles beam. (b) Absorption coefficient of the particles layer deposited during 1 min where the surface plasmon band (SPB) was identified as well as the absorption band of Cu_2O . (c) Image of typical samples positioning in the rest of the experiments. The dashed line indicates the vertical position of the source aperture.

A circular area of ~ 2 cm of diameter was observed after deposition (Figure 5.1a). The optical measurements of this layer suggested the presence of not completely oxidized particles layer, since a band around ~ 1.65 eV was observed in the absorption coefficient spectrum, in addition to the Cu_2O absorption band (~ 2.2 eV). The lower energy band was attributed to the surface plasmon band (SPB) of Cu nanoparticles. After defining the nanoparticles incidence area, glass substrates and nickel grids, used for the rest of the study, were placed facing the aperture on the higher incidence position, expecting the higher capture of nanoparticles (Figure 5.1c).

It is worth to comment that the mentioned calibration step is important to contribute to the repeatability of the depositions. The vertical position at which the samples should be placed was defined thanks to this analysis (dashed lines in Figure 5.1c). The horizontal one, instead, remained more difficult to control due to undesirable movements of the holder plate when the deposition chamber is closed.

Considering this, two set of samples were studied: one trying to maintain the holder fixed, facing the particles flux, and another rotating the holder plate at 3.5 Hz. Since the higher particles incidence occurs on a relatively small circular area, the rotation contributes to the repeatability and homogeneity of the depositions, avoiding variable results due to different x-positioning (along the dashed line) of the samples on the sample holder. In both cases, the working pressure difference between the aggregation zone and the deposition chamber was ~ 38 Pa and only the turbomolecular pumping, corresponding to the sputtering deposition chamber, was running. Meanwhile, the differential pump of the GAS was kept off. At these conditions, three deposition times were analysed for both sets of samples: 10, 20 and 30 seconds.

In Figure 5.2, SEM micrographs of the above-mentioned samples are shown. The first conclusion is that no differential pumping was needed to successfully obtain the nanoparticles on the grids. The pressure difference achieved was good enough for this purpose. The diameter distributions of the nanoparticles were estimated from the micrographs using Image J software and considering the nanoparticles with circular shape. An increase in the particles density is observed when the time is increased in both set of samples. Since fewer nanoparticles per unit time arrive on the substrate in the rotated set, the corresponding increase is less abrupt. Regarding the particles lateral size, or diameter, two maxima in the size distribution are observed. Additionally, as expected, time does not seem to have an influence on the most likely

sizes of these two distributions since it should depend mainly on the residence time into the GAS. However, no precise analysis can be done due to the low definition of some micrographs and we preferred to report the values supported by HRTEM.

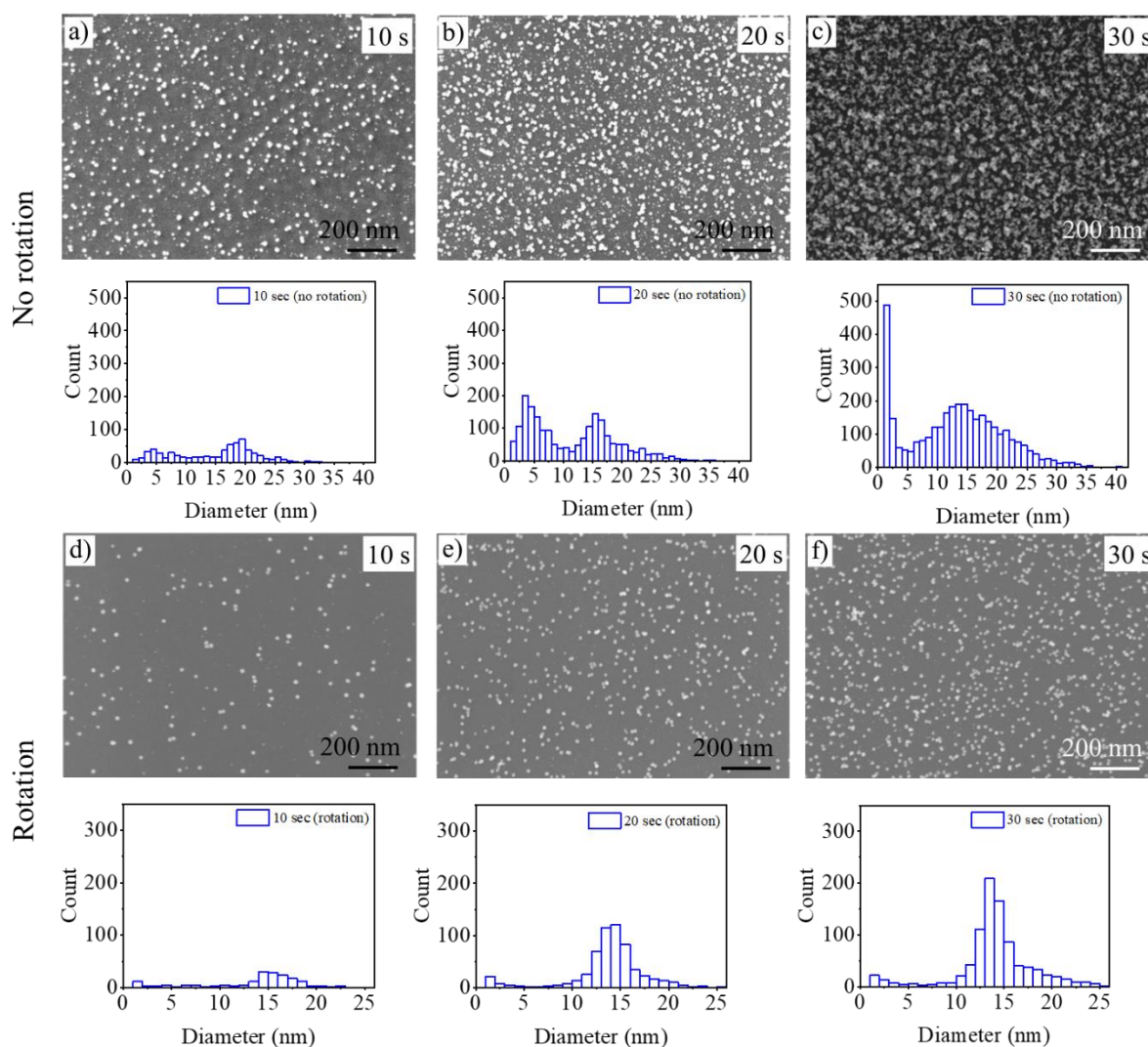


Figure 5.2: SEM micrographs corresponding to Cu nanoparticles deposited on nickel grids varying the deposition time (10 s, 20 s and 30 s). The first set of samples (a-c) was obtained without rotating the sample holder while, in the second set (d-f), it was rotated at 3.5 Hz. Corresponding size distribution histograms created considering a bin size of 1 nm are shown.

Transmission electron microscopy (TEM) was performed in order to better understand the morphology of the particles, surface distribution and structure (Figure 5.3). As no noticeable differences were observed between the samples, the one grown for 20 seconds, without rotation, was selected for analysis. The diameter distribution of the nanoparticles was estimated from

the bright field micrograph depicted in Figure 5.3a. The results showed sizes between 1 nm and 26 nm approximately while two predominant mean diameters, (2.46 ± 0.28) nm and (11.48 ± 0.29) nm, are observed from the histogram, in agreement with the previous SEM analysis considering the differences in the technique resolution. Based on these results and supported by HRTEM micrographs (Figure 5.3c, d), a possibility is that these lateral sizes characterize both independent particles and agglomerates of several of them, respectively.

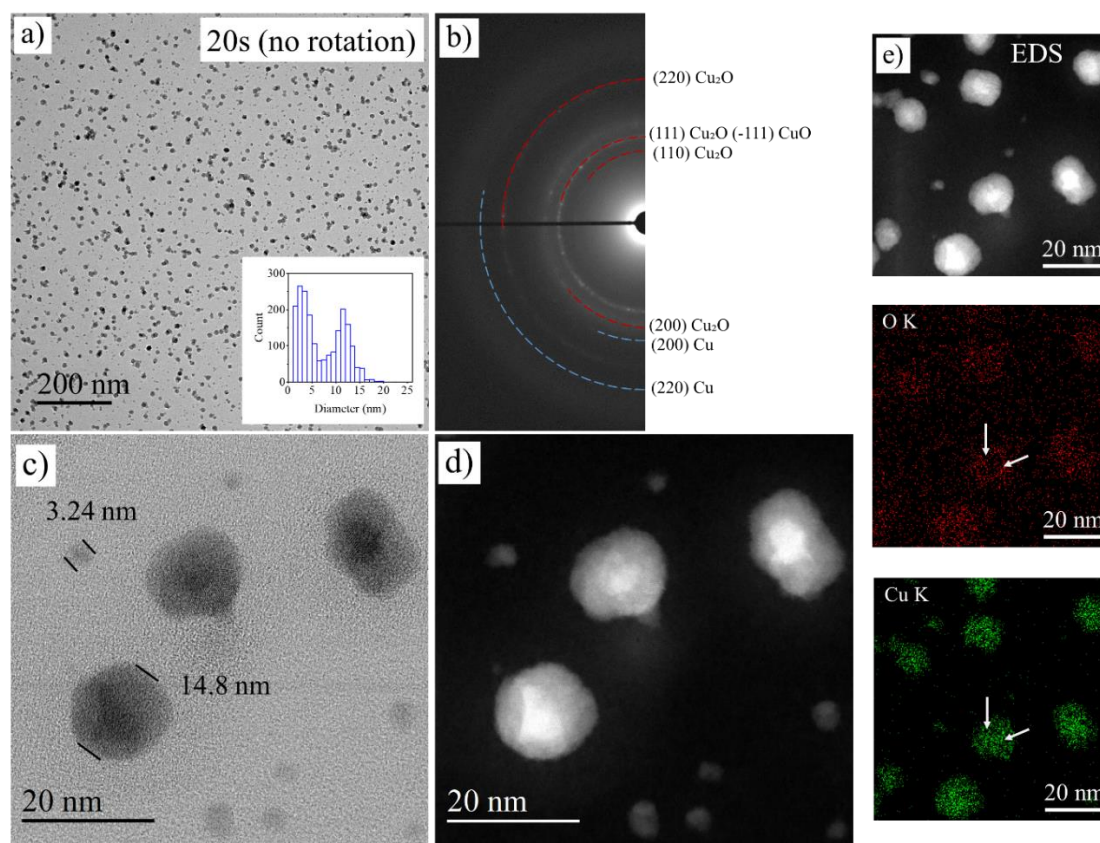


Figure 5.3: (a) Bright field (BF) micrograph and (b) corresponding selected area electron diffraction (SAED) pattern of nanoparticles deposited on a nickel grid, during 20 seconds, without rotating the substrate holder. HRTEM micrographs taken in (c) bright (BF) and (d) dark field (DF). (e) Composition maps corresponding to EDS analysis. White arrows indicate less oxygen in the core of a selected particle.

On the other hand, according to the SAED pattern (Figure 5.3b), these particles are principally formed by Cu_2O , deposited on the substrate with different preferential orientations: [110], [111] and [100], being the diffraction of the (111) and (200) planes the most intense. Additionally, (200) and (220) planes of the Cu phase with very low intensity can be noticed.

The diffraction of ($\bar{1}11$) planes corresponding to CuO are also likely present due to the proximity of this peak to the (111) peak of Cu₂O. The same occurs with the (111) and (200) planes of Cu and Cu₂O, respectively. The appearance of copper oxides is expected considering the small size of the particles and their imminent oxidation once they come into contact with the ambient atmosphere when removed from the deposition chamber.

Finally, the dark field micrograph in [Figure 5.3d](#) shows a bright region in the center of the clusters, indicating higher density. According to EDS analysis ([Figure 5.3 e](#)), some particles seem to have a lower atomic content of oxygen at the particles core compared with their surfaces, suggesting a progressive oxidation of the particles from the surface to the core after contacting with the atmosphere. It is worth to notice that, with the presented analysis, we cannot conclude if we are in presence of polycrystalline particles of ~ 15 nm of lateral size or agglomerates of small particles (monocrystallines or polycrystallines).

5.3 ZnO-CuNPs multilayers composites by GAS

5.3.1 ZnO-CuNPs multilayers deposition.

In this section, fabrication of ZnO-CuNPs composites is studied. Cu nanoparticles with previously known size distribution and density are incorporated inside a ZnO matrix. For this kind of experiments, a 45 ° tilted holder was used, allowing to deposit ZnO and Cu nanoparticles simultaneously or sequentially (see [section 2.1.2, Chapter 2](#)). Simultaneous growth could result in very packed Cu nanoparticles inside the matrix, due to the low deposition rate of ZnO (~ 4 nm/min), which could affect the individual plasmonic behavior. Besides this, to obtain a thin layer of 100 nm of composite, the continuous working of the GAS could be difficult, considering the need of a constant circulation of liquid nitrogen and progressive particles deposition on the aperture perimeter that we think could affect the dynamics of the particles flux.

Therefore, a sequential configuration was considered a suitable choice to obtain independent nanoparticles distributed inside the ZnO matrix. The schematic in [Figure 5.4](#) shows the steps followed to obtain a ZnO-CuNPs multilayer composite of approximately 100 nm. In the first

step, a ZnO film of approximately 20 nm (5 min) would be grown followed by 1 min of Cu nanoparticles generation (step 2). This sequence is repeated 4 times and a last film of ZnO completes the structure. In total, 5 layers of ZnO and 4 layers of Cu nanoparticles are expected.

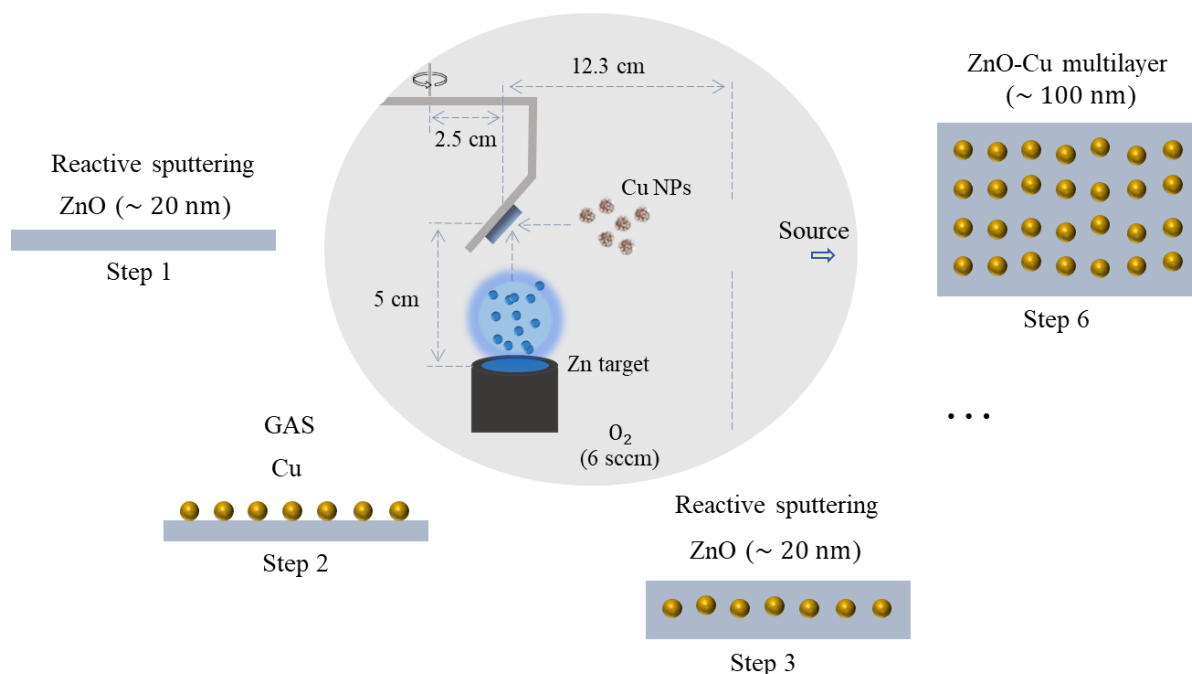


Figure 5.4: Schematic of the deposition steps followed to obtain a ZnO-CuNPs multilayer film and the system configuration using a 45 ° sample holder.

The deposition was carried out rotating the sample holder at 3.5 Hz. The ZnO layer was grown using a Zn target (99.995 % of purity, Kurt J. Lesker Company) placed at 5 cm of the sample position. The center of the sample was fixed at 2.5 cm of the rotating axis, to ensure high conductivity of the ZnO film [32]. This resulted in a distance of ~ 55 cm between the sample and the GAS target. Finally, the O₂ and Ar flowrates in the deposition chamber were 6 sccm and 50 sccm, respectively, reaching a working pressure of 0.4 Pa. The applied current was 0.07 A. The GAS experimental parameters were the same as mentioned in Chapter 2 and in previous section: 0.21 A of applied current, 160 sccm of Ar flowrate and 5 cm between the target and the source aperture. The working pressure difference between the deposition chamber and the source resulted between 29 Pa and 36 Pa during the whole process. Each Cu NPs layer was deposited during 1 min.

5.3.2 Structural and morphological properties of ZnO-CuNPs multilayers.

High resolution microscopy was used to analyse the microstructural properties of the synthesized multilayers (Figure 5.5). A columnar morphology with conical shape is observed in the film (a, b). An interesting observation is that these conical grains start at different heights inside the sample (c).

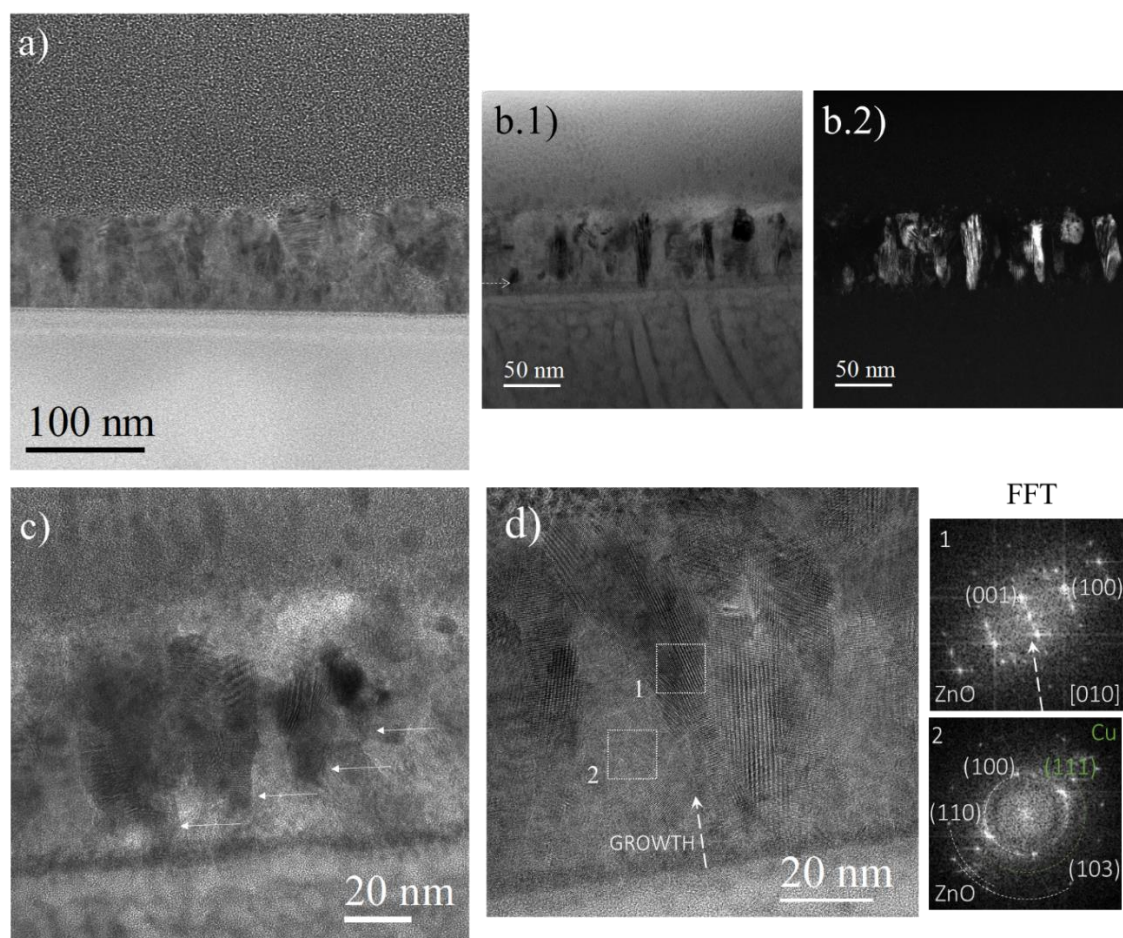


Figure 5.5: (a, b.1 and b.2) TEM micrographs corresponding to a ZnO-CuNPs multilayer film, including BF and DF micrographs. In HRTEM micrographs (c, d) the white arrows in (c) show the growth of ZnO grains starting from different heights. FFT analysis in (d) shows the preferred orientation of ZnO conical grains and the polycrystalline nature of the film outside these grains.

It can be noticed that all the particles layers are not distinguished a priori, except for the first layer (b.1, see white arrow). However, the distances between the apexes of the conical grains

are in relatively good agreement with the positions at which the particles should be deposited (every 20 nm approximately) (c).

This result suggests that Cu nanoparticles can ease the nucleation of crystalline ZnO. At the first ZnO deposition stages (a few nanometers) the film shows a nanocrystalline, nearly amorphous, structure, as it can be seen in Figure 5.5d, square 1. However, with the incorporation of the metal nanoparticles the growth of highly oriented ZnO grains in the [001] direction is promoted, enabling higher ordering in the thin film from very low thickness (Figure 5.5d, square 2).

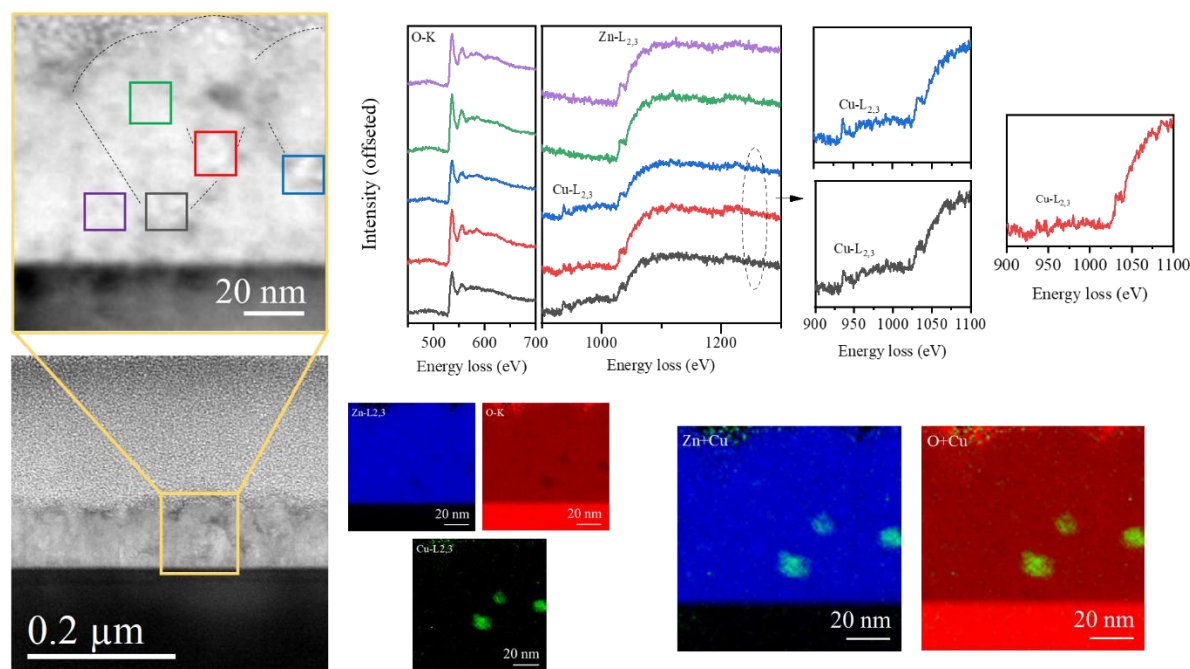


Figure 5.6: TEM analysis of the ZnO-CuNPs multilayer film: high angle annular dark field (HAADF)-STEM micrographs at two different magnifications (left); energy loss near edge structure (ELNES) spectra at O-K and Cu-L_{2,3} edges corresponding to the squares in the zoomed HAADF micrograph and composition maps of copper (green), oxygen (red), zinc (blue) and mixture of Zn + Cu and O + Cu.

Nanoparticles identification at different heights was possible through EELS analysis using the STEM mode (Figure 5.6). In a region of 100 nm x 100 nm a composition map was elaborated based on the atomic contents of Zn, O and Cu elements, estimated from EELS analysis. A homogeneous distribution of Zn and O is observed throughout the layer, additionally to well-defined Cu regions coinciding with the apexes of the ZnO grains. ELNES spectra including

these Cu-rich zones and outside areas, demonstrate the presence of Cu-L_{2,3} edges where the particles are positioned. These edges seem to correspond to Cu⁰ oxidation state of Cu according to the literature [187], although it is difficult to confirm due to the low intensity of these peaks.

5.3.3 Optical response of ZnO-CuNPs multilayers.

Ellipsometric spectroscopy helped to understand the optical response of the ZnO-CuNPs composites and, in particular, corroborate if the grown nanoparticles exhibit the LSPR effect. The measurements were performed at 2 incidence angles: 60° and 70°.

As the ZnO-CuNPs multilayer composite is a heterogeneous system consisting on two phases, the effective medium approximation was employed, which allows to determine the optical response of the system using the dielectric constant and the volume fraction of the ZnO matrix and the Cu nanoparticles. The system was considered like a stack of five ZnO and four ZnO + Cu layers (Figure 5.7b). The effective medium model used to reveal the optical response of the individual ZnO + Cu layers was the Bruggeman model, which is described by the following equation:

$$V_{\text{Cu}} \frac{\epsilon_{\text{ZnO}} - \epsilon_{\text{eff}}}{\epsilon_{\text{ZnO}} + 2 \epsilon_{\text{eff}}} + (1 - V_{\text{Cu}}) \frac{\epsilon_{\text{Cu}} - \epsilon_{\text{eff}}}{\epsilon_{\text{Cu}} + 2 \epsilon_{\text{eff}}} = 0 \quad (5.1)$$

where ϵ_{Cu} and ϵ_{ZnO} are the dielectric constants of Cu and ZnO, respectively, ϵ_{eff} is the effective dielectric constant of the medium and V_{Cu} and $(1 - V_{\text{Cu}})$ are the volume fractions of Cu and ZnO, respectively [134].

The ellipsometry data was then fitted (Annex 6), setting the dielectric functions of ZnO and Cu particles and adjusting the thicknesses of the ZnO and ZnO + Cu layers, as well as the volume fraction in the second case. The dielectric constant of ZnO was determined through a Tanguy model [136,137], considering a homogeneous system: ZnO on a Si substrate (Figure 5.7a) while the dielectric function of Cu was based on literature data [236]. All ZnO layers were assumed to have the same thickness as well as the thicknesses and volume fractions of the ZnO + Cu layers. This way, the effective dielectric function of the ZnO-CuNPs multilayer composite was determined.

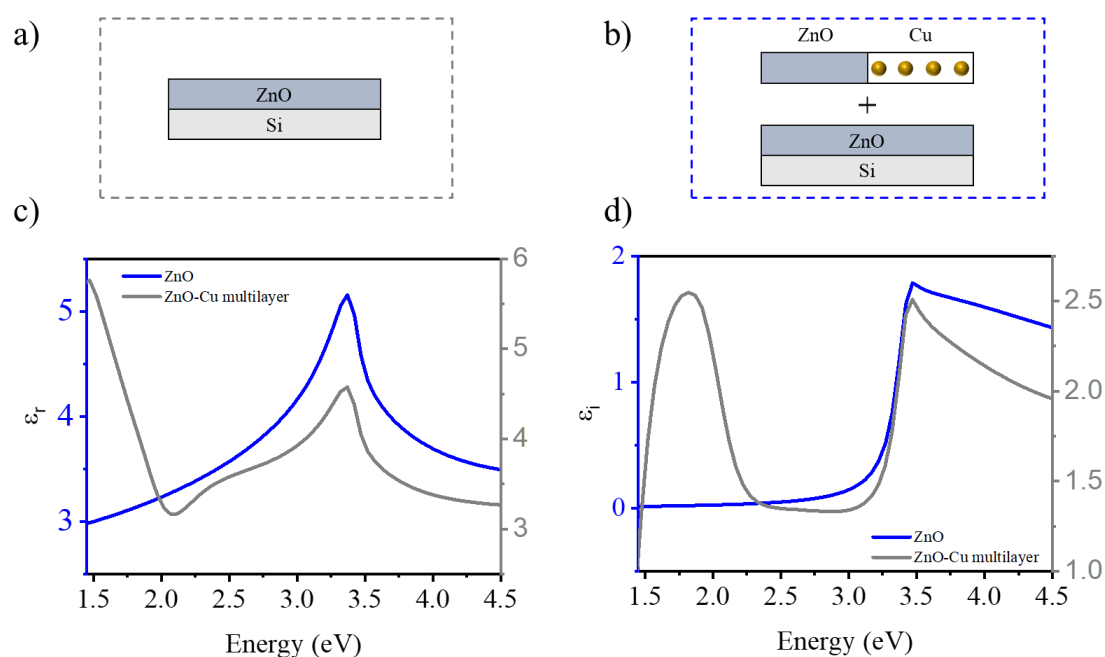


Figure 5.7: Models used to fit the ellipsometry data corresponding to (a) ZnO films and (b) ZnO-CuNPs multilayers where the deposition time of Cu nanoparticles was 1 min. (c) Real and (d) imaginary parts of the effective dielectric function calculated from ellipsometric spectroscopy measurements and the modelling.

Figure 5.7 (c, d) shows the real (ϵ_r) and imaginary (ϵ_i) parts of the dielectric function of the ZnO-CuNPs composite and a reference ZnO layer. The values of ϵ_i in the studied spectral range shows the LSPR band corresponding to Cu nanoparticles, at 1.82 eV (681 nm). Between 2.37 eV and 3 eV it can be seen a band attributed to interband transitions of Cu [237] or Cu₂O, considering a partial oxidation of the particles shell before reaching the sample. Beyond that, the spectra are dominated by the contribution of ZnO, showing an excitonic peak at 3.47 eV, considered within the values reported in literature [238]. The positive values of ϵ_r in the whole spectral range suggest not connected Cu nanoparticles embedded in the ZnO matrix in agreement with the information provided by the composition mapping (Figure 5.6).

5.4 Studies in progress

5.4.1 Electrical response of ZnO-CuNPs based devices.

In [Chapter 3](#), spectral photocurrent measurements of plasmonic devices were presented and discussed. It was suspected that, if the whole plasmon band has an energy higher than the bandgap energy of the matrix, the generation of hot carriers by plasmonic effect would be better exploited and the photocurrent would increase. To achieve this effect, we have considered two possibilities. The first one was to decrease the size of the nanoparticles until the SPB is sufficiently shifted beyond the gap value of the semiconductor. In the case of the composites studied, it could be observed that the particle sizes are very small and it would be very difficult to decrease the size of these particles until the gap energy value of Cu₂O is exceeded. Another alternative is to shift the gap of the absorber semiconductor to lower energies close to typical Cu SPB values. This is somewhat more achievable since there are a variety of absorber semiconductors whose gap is close to or below 2 eV, for example CuO (1.44 eV – 1.56 eV) [[36](#)]. Additionally, the bandgap of this semiconductor is close to the optimal value calculated for photovoltaic applications (1.1 eV – 1.5 eV) [[239,240](#)].

As a first approach to continue with the elaboration and study of devices based on ZnO-CuNPs composites, a junction between a CuO film (200 nm) and ZnO-CuNPs multilayer (100 nm) was fabricated. On a commercial indium tin oxide (ITO) substrate the composite was grown under the same conditions that the sample analysed in [section 5.3](#). CuO was grown using the same experimental conditions than Cu₂O (see [Chapter 3](#)) but using a higher OFR (20 sccm).

The I-V measurements were done using the same system than in previous chapters, under dark and 1 sun of illumination ([Figure 5.8](#)). Since we presented short circuit problems to successfully deposit a back contact, specifically a gold contact, the measurements were performed contacting the gold probes or needles of the system directly on the ITO and the CuO materials, respectively.

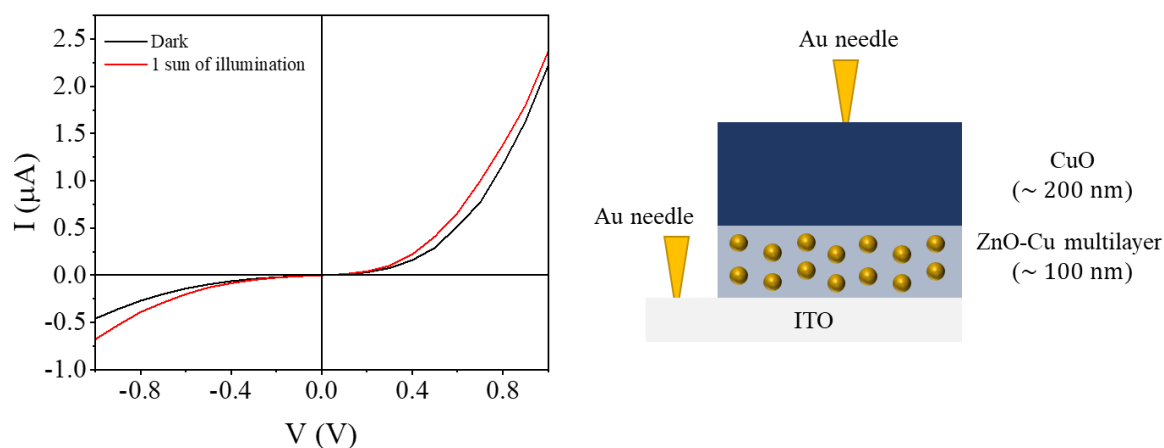


Figure 5.8: Current vs voltage measurements performed on a ITO/ZnO-CuNPs/CuO device contacting, through gold needles, the ITO front contact and the CuO layer. At the right a schematic of the device and the measurement is shown.

As a result, a very low current value was detected and not significant analysis of the device parameters was possible at this stage. However, this measurement revealed that the system shows the rectifying behavior of a p-n junction considering ohmic contacts between the needles and the ITO and CuO [241]. It's worth noting that this phenomenon could also be influenced by the formation of a Schottky junction between ZnO and the Cu nanoparticles. This could occur if the work function of the Cu particles exceeds that of ZnO, which is possible depending on various factors such as interface properties, defect density, and morphology [242]. In our study, this has not been tested thus far. In any case, the system was able to detect a subtle increase in the photocurrent with illumination in reverse and forward bias, likely attributed to hot electrons injection from metal nanoparticles to the ZnO semiconductor (photocurrent increase in reverse bias) and absorption of CuO material with a subsequent electron-hole pair separation at the p-n junction.

Chapter conclusions

In this chapter a gas aggregation source (GAS) was used for the successful synthesis of copper nanoparticles, a fundamental step in the creation of ZnO-CuNPs multilayer structures with plasmonic properties. The research studied how the density of nanoparticles changed over deposition time, both with and without the rotation of the sample holder. It was shown that the particles density increased with deposition time in both cases, with a more gradual rise in the rotated set due to reduced nanoparticle arrival rates. Besides, particle lateral size remained unaffected by deposition time, exhibiting bimodal distributions with peaks around 2.5 nm and 11.5 nm across all samples. This investigation provided insights into the control and manipulation of nanoparticle distribution within the future multilayer structure.

ZnO-CuNPs multilayer structures with plasmonic characteristics were obtained through a sequential growth process, involving the alternate deposition of ZnO thin films, via a reactive magnetron sputtering route, and copper nanoparticles using the GAS. High-resolution transmission electron microscopy (HRTEM) and electron energy loss spectroscopy (EELS) analyses were conducted after the fabrication of the designed configuration. These analyses served to confirm the successful formation of the heterostructure and provided valuable information about its structural and compositional characteristics. It was possible to identify nanoparticles at various heights of the film coinciding with the apexes of well-oriented ZnO grains. This observation suggested that Cu nanoparticles may serve as potential nucleation sites, promoting enhanced ordering within the thin film matrix, even at very low thickness levels. On the other hand, ellipsometric spectroscopy was used to validate the presence of the surface plasmon band around 1.5 eV, associated with copper nanoparticles within the multilayer structure. This spectroscopic technique allowed for the assessment of the plasmonic properties and their correlation with the fabricated configuration.

In conclusion, this chapter has shown the successful synthesis of copper nanoparticles and the creation of ZnO-CuNPs multilayer structures with plasmonic properties. It has provided valuable insights into the deposition process, nanoparticle density control, and structural characterization of the heterostructure, ultimately contributing to the understanding and potential applications of plasmonic materials in optoelectronic devices.

Conclusions and Perspectives

The main aim of this thesis was focused on investigate the growth of plasmonic Cu nanoparticles and semiconductor metal oxides (Cu_2O and ZnO) to create composites and multi-layered heterostructures tailored for optoelectronic applications, especially solar cells and photodetectors. Throughout this research, diverse designs for Cu_2O and ZnO heterostructures were systematically investigated, enabling a comprehensive understanding of the most effective nanoparticle integration strategies within potential devices.

In a first approach, plasmonic copper nanoparticles embedded in a p-type semiconducting Cu_2O matrix were achieved using reactive magnetron sputtering via a single-step route. By controlling the oxygen flowrate during the copper target sputtering process, the oxidation of copper atoms landing on the growing film surface was restricted, resulting in a CuNPs- Cu_2O composite layer. Two oxygen flowrates (2 sccm and 4 sccm) lead to be suitable to obtain the composite films under the fixed experimental conditions (0.15 A of discharge current, 5 cm of target - holder distance and 50 sccm of Ar flowrate).

When the composite was deposited orthogonal to the target axis and 4 sccm of OFR, a [100] columnar growth of the Cu_2O matrix and low Cu particles interconnectivity was observed by microstructural analysis. In this case, the NPs size where estimated to be around 4 nm. On the other hand, when the OFR was the lowest, a nanocrystalline matrix with connected and bigger

copper nanodomains (around 7 nm) was achieved. Resistivities in the order of $10 \Omega \cdot \text{cm}$ 10^{-4} and $10 \Omega \cdot \text{cm}$ for 2 sccm and 4 sccm of OFR, respectively, supported the higher presence of metallic and networked Cu particles in the first case. Interestingly, LSPR response was present in both Cu-based composites, with a single SPB close to 2 eV but slightly red-shifted for 2 sccm, mainly attributed to higher particles sizes. Ellipsometric measurements corroborated the hybrid behavior of the sample grown at lower OFR (metallic + plasmonic) and the plasmonic nature of the sample grown at 4 sccm.

The influence of the sample position respect to the Cu target axis on the film properties was also analysed. At the longer distance sample – target axis, for both OFR, the ordered growth of the Cu_2O matrix with a [100] preferential orientation decreased, which was associated to less energetic oxygen ions impinging the growing film surface. Besides, lower particles sizes, attributed to higher O/Cu ratio, and weaker LSPR response was observed at this position. The resistivity of the composites showed also a dependence with sample position. It reached higher values far from the target axis and decreased as the sample approached to it. This behavior was associated also to the O/Cu atoms ratio landing at the film surface. An increase in the resistivity is again perceived facing the target, attributed to the columnar growth of the matrix in the [100] direction or “hole killers” defects.

Two semi-transparent composites-based heterojunctions were fabricated by reactive magnetron sputtering: n-ZnO/CuNPs- Cu_2O and n-ZnO/CuNPs- Cu_2O /p- Cu_2O . The heterojunctions showed a rectifying behavior according to macroscopic electrical measurements. Also, it was demonstrated that CuNPs- Cu_2O composites triggered enhanced photoconversion when inserted at the interface of n-ZnO/p- Cu_2O heterojunctions. We associated this enhancement to hot carriers injection and collection, following deexcitation of LSPR at plasmonic Cu nanodomains, and near-field enhancement.

CuNPs- Cu_2O composites grown using an OFR of 4 sccm were treated at different temperatures (150 °C, 200 °C, 250 °C and 300 °C) in oxygen-poor conditions to avoid NPs oxidation. With the increase in temperature an improvement in the [100] preferential orientation of the Cu_2O matrix as well as a segregation and coalescence of metallic Cu at the composite surface was observed. The mean lateral sizes of the particles were from 90 nm to 150 nm, approximately, as the temperature increased. An improvement in the LSPR response was evidenced for the

treated samples respect to non-annealed composites, reaching a maximum value at 200 °C. Better ordering of the crystalline structure of the Cu₂O matrix was evidenced by Urbach energy calculations showing lower values as the temperature increased, indicating lower density of defects states. Additionally, a connection was observed between the structural and optical properties (SPB intensity) of thermally treated composites and the consumption of the target. The study illustrated that, in the case of eroded targets, the most effective plasmonic response was achieved when films were placed offset from to the target axis.

Equivalent n-ZnO/CuNPs-Cu₂O and n-ZnO/CuNPs-Cu₂O/p-Cu₂O semi-transparent devices were thermally-treated at 200 °C under the same oxygen-poor conditions. n-ZnO/p-Cu₂O heterostructures presenting Cu particles at the surface (n-ZnO/p-Cu₂O/CuNPs), interfacing with the Au back contact, were obtained in both cases. Electrical measurements (J-V) showed a short circuit current density five-fold higher than the value achieved for a reference n-ZnO/p-Cu₂O device when the thermal modified device presented higher amount of Cu NPs at the surface (n-ZnO/CuNPs-Cu₂O annealed device). This result was associated to three potential factors including the enhancement of the LSPR response induced by annealing, improved ease of extra carrier collection due to the proximity of Cu particles to the back contact, and the enhancement of light scattering, improving absorption and the generation of electron-hole pairs in the Cu₂O layer. Impedance measurements and modeling were performed indicating a close connection between higher J_{sc} values and the presence of plasmonic Cu NPs inducing more charge transfer. Meanwhile a link between minimizing defects and recombination with reaching higher V_{oc} was established. Finally, it was shown that plasmonic particles positioned closer to the back contact, after annealing, showed improved photocurrent generation compared to particles situated nearer the p-n junction.

Another approach explored in this thesis was the inclusion of Cu nanoparticles in the n-type ZnO matrix using a gas aggregation source coupled to the sputtering deposition chamber for particles generation and thin film/particles deposition, respectively. The first part of the study provided insights into the control of nanoparticles density, both with and without the rotation of the sample holder. It was observed than particle lateral size remained unaffected by deposition time or rotation, exhibiting two size distributions maxima around 2.5 nm and 11.5 nm in all the cases.

ZnO-CuNPs multilayer structures with plasmonic properties were successfully deposited via a sequential growth mechanism. HRTEM and EELS analysis confirmed the formation of the heterostructure consisting of nanoparticles positioned at different heights within the film, located at the apexes of well-oriented cone-shaped ZnO grains. This observation suggested that Cu nanoparticles could act as potential nucleation sites, facilitating enhanced ordering within the ZnO matrix, even at minimal thickness levels. In addition, ellipsometric spectroscopy confirmed the existence of a SPB around 1.5 eV, linked to the Cu NPs present in the multilayer structure.

The results presented in this thesis constitute a significant contribution to the search for innovative methods to obtain Cu-based plasmonic heterostructures that can be applied on an industrial scale with minimal complexity. Furthermore, they enhance our comprehension of the mechanisms taking place in plasmonic devices like solar cells, shedding light on the primary challenges involved in enhancing their efficiency.

Perspectives:

Based on the knowledge gained in this thesis, many avenues remain to be explored in the field of plasmonic optoelectronic applications, particularly solar cells. Below, we highlight some of the studies that could be of interest:

- In [Chapter 3](#), we fabricated a device where the CuNPs-Cu₂O composite was grown between the n-ZnO and the p-Cu₂O layers (n-ZnO/CuNPs-Cu₂O/p-Cu₂O). The thickness of this layer was expected to be around 10 nm according to the deposition rate of the composite. Its J_{sc} resulted almost 4.5 fold the J_{sc} of the reference device (n-ZnO/p-Cu₂O) and 2 fold the J_{sc} of the n-ZnO/CuNPs-Cu₂O device. Although the photocurrent was expected to be higher for the device with higher amount of plasmonic nanoparticles (n-ZnO/CuNPs-Cu₂O), high defect density and low carrier diffusion length avoided significant increase in the current density, explaining better results for n-ZnO/CuNPs-Cu₂O/p-Cu₂O configuration. An interesting study to carry out could be to change the interlayer thickness in order to find an equilibrium between increasing the amount of nanoparticles (inducing extra carrier injection) and minimizing defects density.

- Considering the photocurrent enhancement that metal nanoparticles induced when they are close to the p-n junction, the growth of Cu nanoparticles at the n-ZnO/p-Cu₂O interface instead of a layer of CuNPs-Cu₂O composite by DC magnetron sputtering results another interesting approach. The growth of nano-island is expected owing to the Volmer-Weber growth mode, as reported in previous works [159]. By controlling the deposition time of the Cu deposition, a variation in the nanoparticles sizes is expected as well as different devices performances.
- Considering the discussion presented in the last section of [Chapter 3](#), to favor the photocurrent enhancement by approaching the SPB to the Cu₂O absorption band (decreasing the particles sizes), some experiments could be performed increasing the discharge current applied to the copper target. With this study the working window for OFR could be widen giving more freedom to precisely adjust the size of particles.
- Cu nanoparticles deposited on a Ni-grid by the GAS were quite oxidized when put them in contact with ambient conditions. An interesting study results the deposition of two ZnO thin layers, for example around 10 nm, before and after depositing the nanoparticles, in order to study the oxidation at the particles surface in real deposition conditions. The thickness of the Cu₂O (or CuO) shell formed at the particles surface could be measured by HRTEM allowing, in addition, to establish a minimum size at which metallic copper is not fully oxidized in the ZnO matrix.
- The ZnO-CuNPs multilayer heterostructure was obtained depositing nanoparticles with sizes around 3 nm and 12 nm. A variation of nanoparticles sizes can be studied by increasing the aggregation path. Moreover, other configurations could be explored like Cu₂O-Cu and CuO-Cu multilayers as well as Cu nanoparticles on the TCO surface, at the p-n heterojunction or at the device surface. In the last case, the study about controlling the particles sizes could be useful to avoid complete oxidation of Cu nanoparticles when interacting with atmosphere.
- Independent layers containing Cu nanoparticles like CuNPs-Cu₂O composites, ZnO-CuNPs multilayers, CuNPs on ZnO thin film and CuNPs on Cu₂O or CuO thin films could be studied by impedance measurements and spectral photocurrent. This study could provide more information about the contribution of each layer to the device performance and consider it in new configurations.

- It is known that nanostructured materials, like ZnO nanorods or nanotubes, decorated with metal nanoparticles and/or p-type materials is a widely studied alternative to increase the absorption and charge collection in a potential device. A challenge in this field is the infiltration of the elongated structures to take advantage of the entire surface. We already grew ZnO nanorods and successfully infiltrated them with a thin layer of Cu₂O or CuO by atomic layer deposition (ALD) ([Annex 7](#)) since an improvement in the junction properties was demonstrated by de Melo *et al.* using this approach [35]. Our purpose is to continue this study by subsequently incorporating a layer of Cu nanoparticles or Cu-based composites in order to compare the performance of devices based on these nanostructures and the previous studied.

Annexes

1. XRD patterns of Cu-O layers grown at different OFR (6, 8, 10 and 12 sccm) are shown in Figure A1.

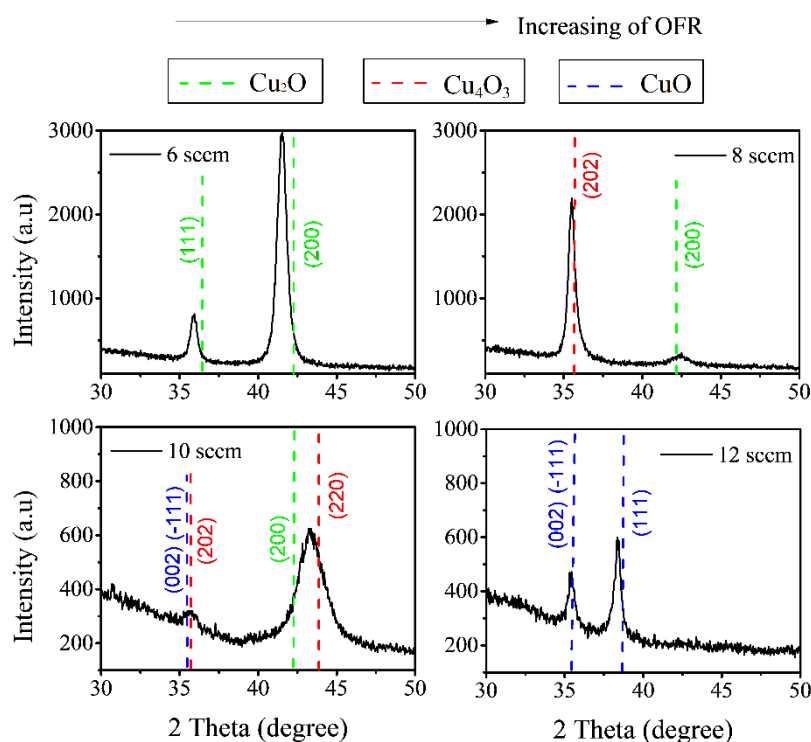


Figure A1. XRD patterns of samples grown at 6 sccm, 8 sccm, 10 sccm and 12 sccm. With the increasing of the OFR different phases of copper oxides appear, since the less oxidation state (Cu_2O) to the higher one (CuO). The metastable phase Cu_4O_3 can be seen as well. The evolution is in agreement with the reported results in literature [36].

2. In Figure A2 it can be seen the absorption coefficient of Cu-O layers grown at 6, 8, 10 and 12 sccm.

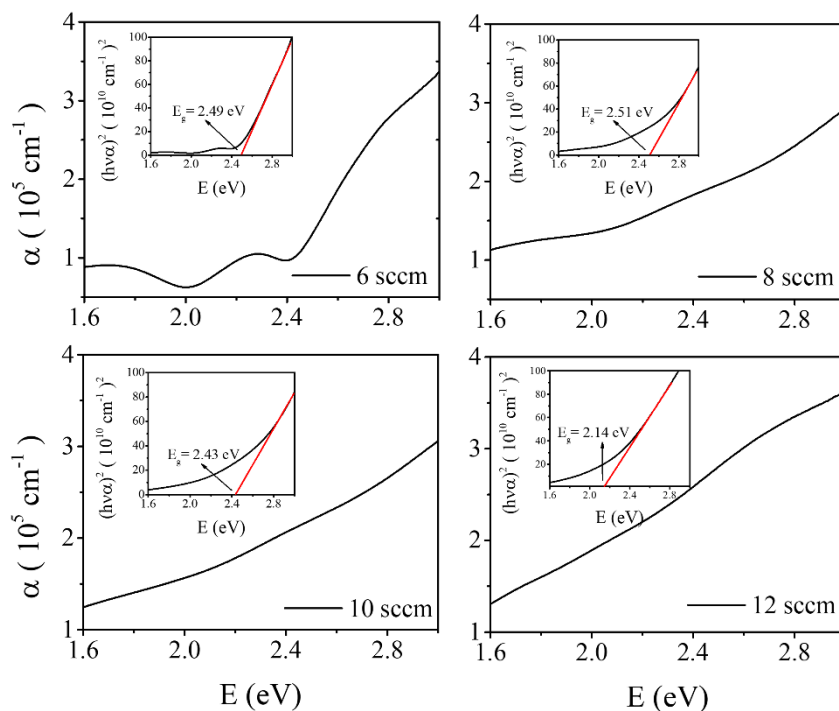


Figure A2. Absorption coefficients for samples 6, 8, 10 and 12. SPBs are not observed. The peaks below 2.4 eV in sample 6 appear as a consequence of the light interference in transmittance measurements.

3. Ellipsometric spectroscopy measurements of CuNPs-Cu₂O composites and Cu₂O films.

Ellipsometric measurements were made at 3 angles of incidence 50°, 60° and 70°. There were measured 2 parameters, I_s and I_c , which depend on the ellipsometry angles. The model used for sample 5 (Tauc Lorentz) is composed of a Cu₂O layer on a glass substrate with a roughness layer (50% layer - 50% air), while in the model used for samples 2 and 4 (a sum of two Lorentzian oscillators and a Tauc-Lorentz model) the Cu₂O layer includes small metal nanoparticles inside, as it was showed in Figure 3 (a, b). The measurements and fit of the data are shown in Figure S3.

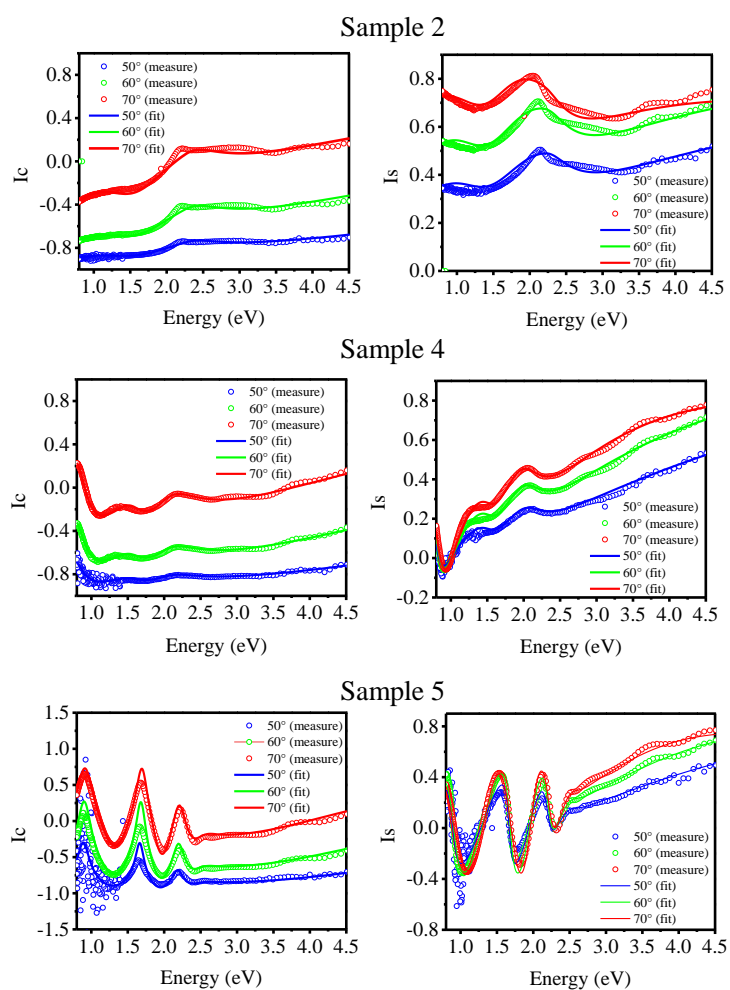


Figure A3. Ellipsometric measurements for the three samples studied and their respective fit using the selected models.

The calculated thickness of the Cu_2O and $\text{Cu}_2\text{O} + \text{Cu}$ layers, as well as the roughness layers are shown in table A3.

Table A3: Calculated thickness of the films and their corresponding roughness layers.

| Sample | Cu_2O and $\text{Cu}_2\text{O} + \text{Cu}$ layers thickness | Roughness layers thickness |
|--------|---|-------------------------------|
| 2 | 199 nm | 5 nm |
| 4 | 245 nm | 1 nm |
| 5 | 275 nm | 6.25 nm |

4. Bode plots and deconvolution corresponding to impedance measurements and modelling of Dev_4sccm, Dev_4sccmTT, Dev_4sccm/6sccm and Dev_4sccm/6sccmTT using the equivalent circuit presented in Chapter 4. The EIS Spectrum Analyser software was used.

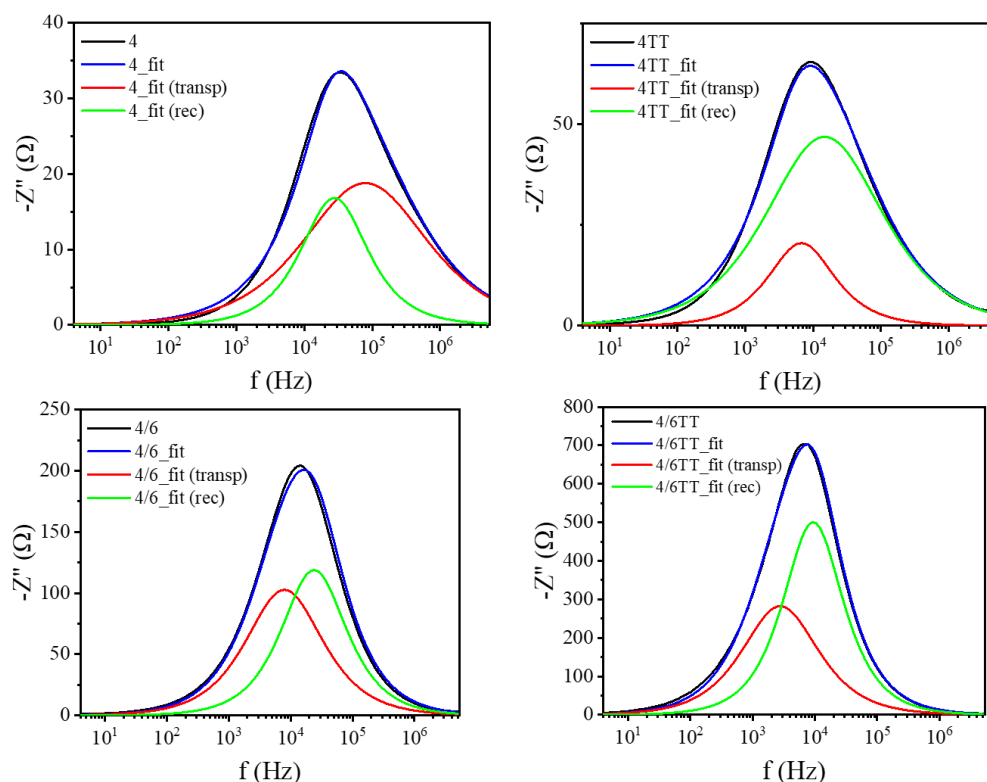


Figure A4. Bode plots and corresponding fit and deconvolution considering the equivalent circuit presented in Chapter 4. The time constants (carrier lifetime τ_{rec} and transit time τ_t) were determined from the frequency (f_p) of maximum of de peaks green and red, respectively, using the equation $\tau = 1/2\pi f_p$. In the legend, the devices were named as: 4 (Dev_4sccm), 4TT (Dev_4sccmTT), 4/6 (Dev_4sccm/6sccm) and 4/6TT (Dev_4sccm/6sccmTT).

5. Zn-O-Cu films were grown on Si substrate by reactive magnetron sputtering using two OFR (6 sccm and 8 sccm). The Ar flowrate was 50 sccm and the applied discharge currents corresponding to the Zn and Cu targets were 0.07 A and 0.15 A, respectively. X-rays diffraction patterns and absorption coefficients of the samples are shown in Figure A5 and Figure A6, respectively.

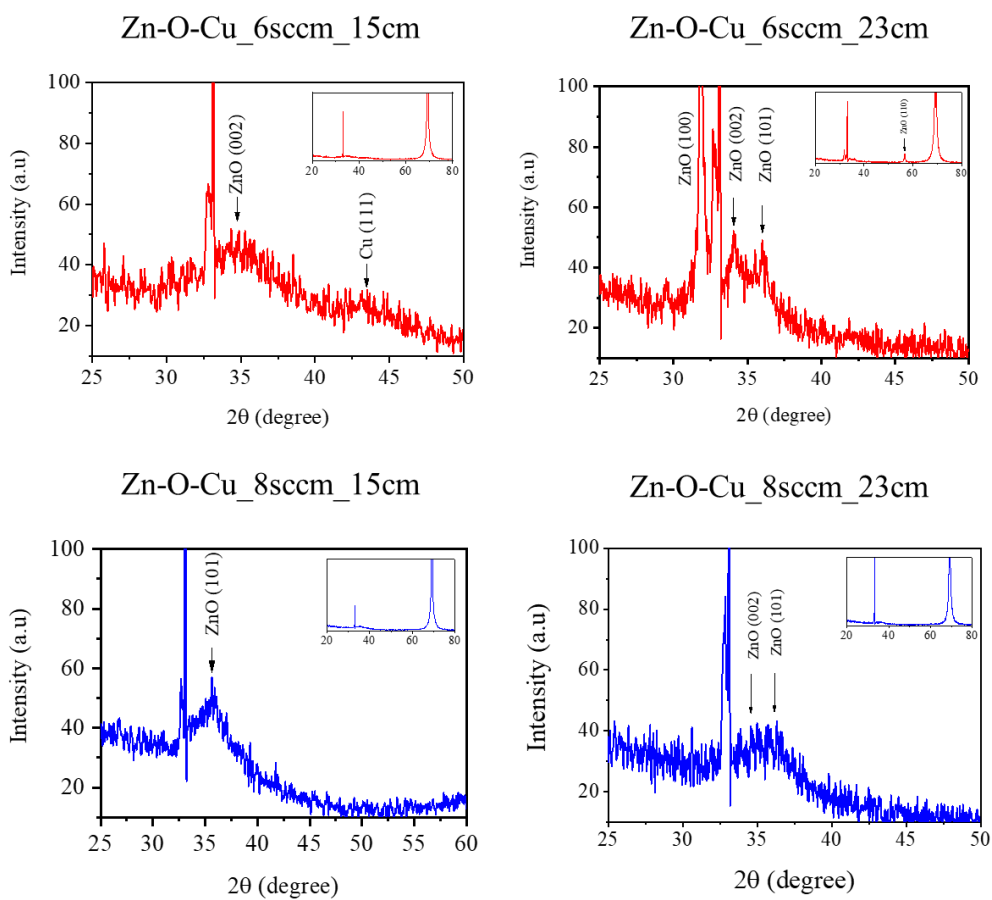


Figure A5. X-rays analysis of Zn-O-Cu layers grown at different oxygen flowrates (6 sccm and 8 sccm) and two copper target distances (15 cm and 23 cm).

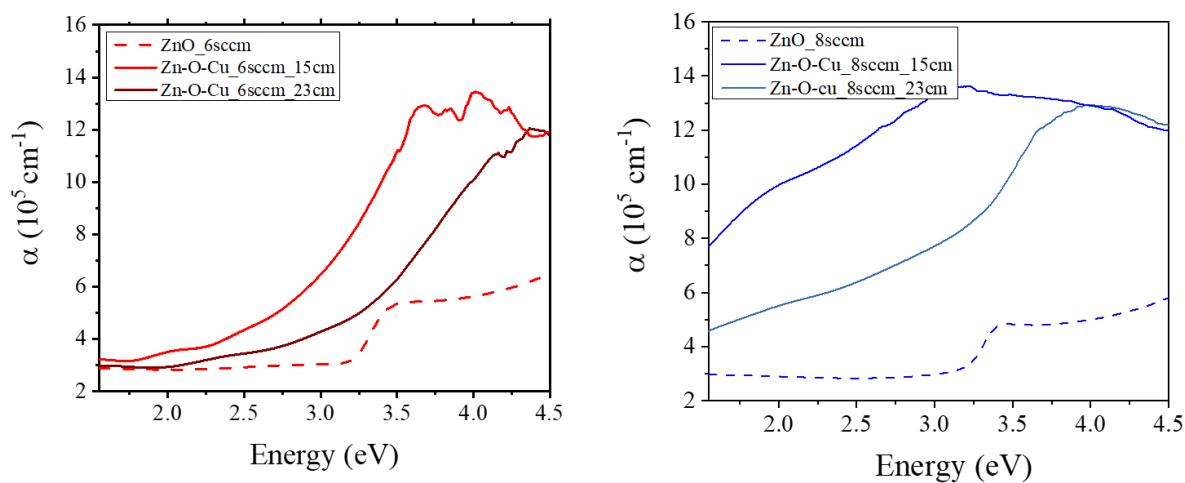


Figure A6. Absorption coefficient of Zn-O-Cu layers grown at different oxygen flowrates (6 sccm and 8 sccm) and two copper target distances (15 cm and 23 cm).

6. Ellipsometric spectroscopy measurements of ZnO and ZnO-CuNPs multilayer films. The measurements were performed at 2 incidence angles: 60° and 70°.

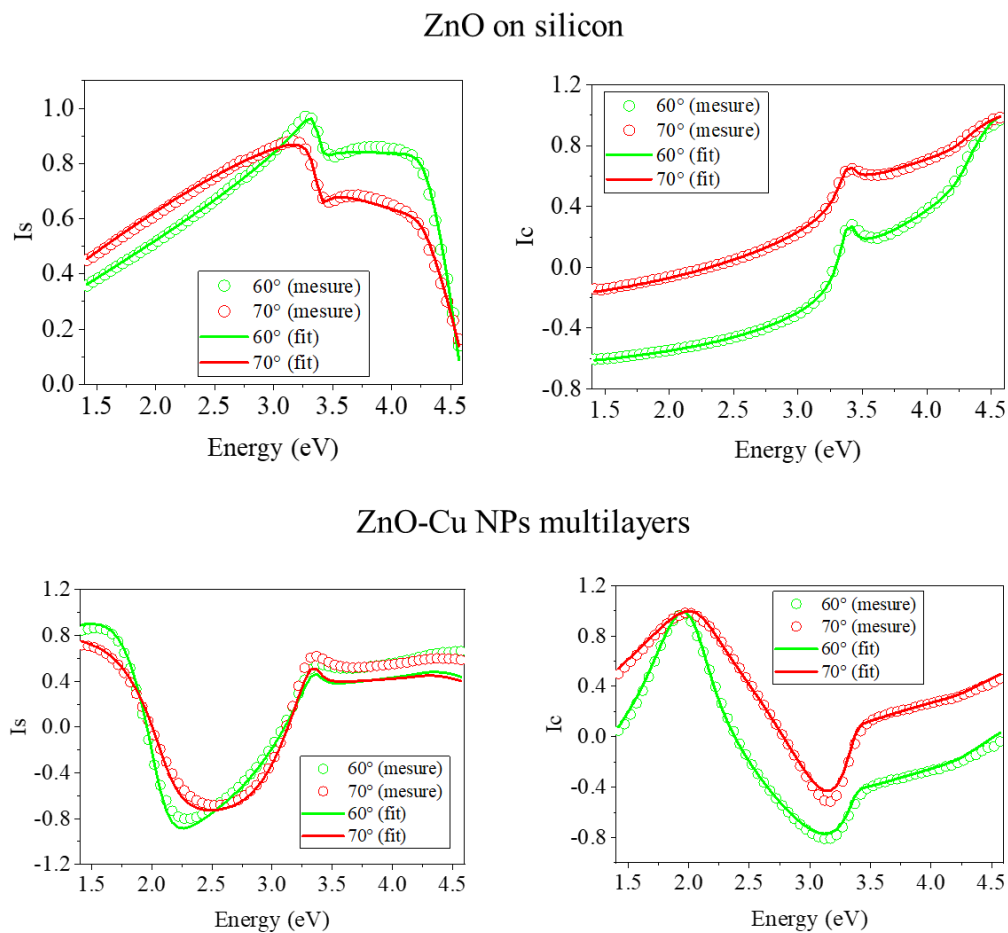


Figure A6. Ellipsometric measurements for the two samples studied and their respective fit using the models described in section 5.3.3 of Chapter 5.

In the case of the ZnO-CuNPs multilayer system, it was considered like a stack of five ZnO and four ZnO + Cu layers. The optical response of the individual ZnO + Cu layers was modelled by the Bruggeman model, while the dielectric constant of ZnO was determined through a Tanguy model.

7. ZnO nanorods (NRs) infiltration with Cu_2O and CuO by atomic layer deposition (ALD) technique.

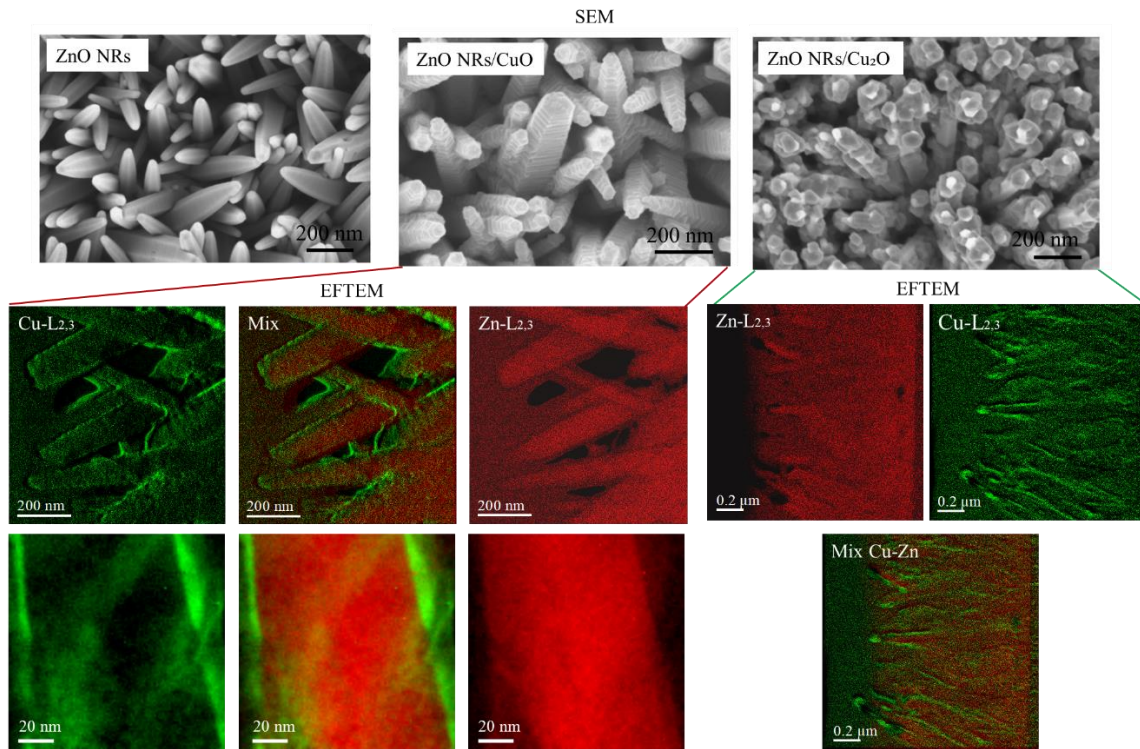


Figure A7.1. Scanning electron microscopy of ZnO nanorods covered by CuO and Cu_2O layers using the ALD technique. Energy-Filtered TEM corresponding to ZnO NRs/ CuO and ZnONRs/ Cu_2O samples.

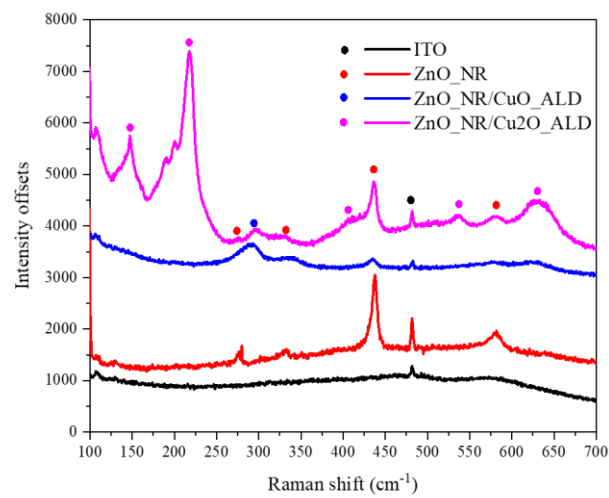


Figure A7.2: Raman spectroscopy measurements of ITO substrate, ZnO nanorods (NRs), ZnO NRs/CuO and ZnONRs/Cu₂O samples where it can be seen the successful infiltration of ZnO with both Cu₂O and CuO materials.

References

- [1] X. Yu, T.J. Marks, A. Facchetti, Metal oxides for optoelectronic applications, *Nature Mater.* 15 (2016) 383–396. <https://doi.org/10.1038/nmat4599>.
- [2] H. Park, Y.-J. Lee, J. Park, Y. Kim, J. Yi, Y. Lee, S. Kim, C.-K. Park, K.-J. Lim, Front and back TCO research review of a-Si/c-Si heterojunction with intrinsic thin layer (HIT) solar cell, *Transactions on Electrical and Electronic Materials.* 19 (2018) 165–172. <https://doi-org.bases-doc.univ-lorraine.fr/10.1007/s42341-018-0026-8>.
- [3] U. Ahmed, M. Alizadeh, N. Abd Rahim, S. Shahabuddin, M.S. Ahmed, A. Pandey, A comprehensive review on counter electrodes for dye sensitized solar cells: a special focus on Pt-TCO free counter electrodes, *Solar Energy.* 174 (2018) 1097–1125. <https://doi.org/10.1016/j.solener.2018.10.010>.
- [4] Z. Sun, X. Chen, Y. He, J. Li, J. Wang, H. Yan, Y. Zhang, Toward Efficiency Limits of Crystalline Silicon Solar Cells: Recent Progress in High-Efficiency Silicon Heterojunction Solar Cells, *Advanced Energy Materials.* 12 (2022) 2200015. <https://doi.org/10.1002/aenm.202200015>.
- [5] S. Calnan, A.N. Tiwari, High mobility transparent conducting oxides for thin film solar cells, *Thin Solid Films.* 518 (2010) 1839–1849. <https://doi.org/10.1016/j.tsf.2009.09.044>.
- [6] M. Ahmed, A. Bakry, E.R. Shaaban, Impact of composition on microstructural, electrical and optical properties of ZnO thin films incorporation by In₂O₃ for solar cells, *International Journal of Energy Research.* 46 (2022) 12963–12973. <https://doi.org/10.1002/er.8074>.
- [7] L. Xiong, Y. Guo, J. Wen, H. Liu, G. Yang, P. Qin, G. Fang, Review on the application of SnO₂ in perovskite solar cells, *Advanced Functional Materials.* 28 (2018) 1802757. <https://doi.org/10.1002/adfm.201802757>.
- [8] A. Lakshmanan, Z.C. Alex, S. Meher, Cu₂O thin films grown by magnetron sputtering as solar cell absorber layers, *Materials Science in Semiconductor Processing.* 148 (2022) 106818. <https://doi.org/10.1016/j.mssp.2022.106818>.
- [9] A.D. Adewoyin, M.A. Olopade, M.A.C. Chendo, A comparative study of the effect of transparent conducting oxides on the performance of Cu₂ZnSnS₄ thin film solar cell, *J Comput Electron.* 17 (2018) 361–372. <https://doi.org/10.1007/s10825-017-1106-4>.

- [10] A.J. Bett, K.M. Winkler, M. Bivour, L. Cojocaru, Ö.Ş. Kabakli, P.S.C. Schulze, G. Siefer, L. Tutsch, M. Hermle, S.W. Glunz, J.C. Goldschmidt, Semi-Transparent Perovskite Solar Cells with ITO Directly Sputtered on Spiro-OMeTAD for Tandem Applications, *ACS Appl. Mater. Interfaces*. 11 (2019) 45796–45804. <https://doi.org/10.1021/acsami.9b17241>.
- [11] C. Sima, C. Grigoriu, S. Antohe, Comparison of the dye-sensitized solar cells performances based on transparent conductive ITO and FTO, *Thin Solid Films*. 519 (2010) 595–597. <https://doi.org/10.1016/j.tsf.2010.07.002>.
- [12] O. Sánchez-Sobrado, M.J. Mendes, T. Mateus, J. Costa, D. Nunes, H. Aguas, E. Fortunato, R. Martins, Photonic-structured TCO front contacts yielding optical and electrically enhanced thin-film solar cells, *Solar Energy*. 196 (2020) 92–98. <https://doi.org/10.1016/j.solener.2019.11.051>.
- [13] A. Sharmin, S. Tabassum, M.S. Bashar, Z.H. Mahmood, Depositions and characterization of sol–gel processed Al-doped ZnO (AZO) as transparent conducting oxide (TCO) for solar cell application, *J Theor Appl Phys*. 13 (2019) 123–132. <https://doi.org/10.1007/s40094-019-0329-0>.
- [14] X. Hou, K. Aitola, P.D. Lund, TiO₂ nanotubes for dye-sensitized solar cells—A review, *Energy Science & Engineering*. 9 (2021) 921–937. <https://doi.org/10.1002/ese3.831>.
- [15] W. Hu, S. Yang, S. Yang, Surface Modification of TiO₂ for Perovskite Solar Cells, *TRECHEM*. 2 (2020) 148–162. <https://doi.org/10.1016/j.trechm.2019.11.002>.
- [16] A. Wibowo, M. Agung Marsudi, M. Ikhlasul Amal, M. Bagas Ananda, R. Stephanie, H. Ardy, L. Jaya Diguna, ZnO nanostructured materials for emerging solar cell applications, *RSC Advances*. 10 (2020) 42838–42859. <https://doi.org/10.1039/D0RA07689A>.
- [17] J. Han, H. Kwon, E. Kim, D.-W. Kim, H. Jung Son, D. Ha Kim, Interfacial engineering of a ZnO electron transporting layer using self-assembled monolayers for high performance and stable perovskite solar cells, *Journal of Materials Chemistry A*. 8 (2020) 2105–2113. <https://doi.org/10.1039/C9TA12750J>.
- [18] K. Deng, Q. Chen, L. Li, Modification Engineering in SnO₂ Electron Transport Layer toward Perovskite Solar Cells: Efficiency and Stability, *Advanced Functional Materials*. 30 (2020) 2004209. <https://doi.org/10.1002/adfm.202004209>.
- [19] Kamlesh, D. Suthar, Himanshu, M.S. Dhaka, Physical properties of thermal annealing induced In₂O₃ thin films for sensing layer applications, *Materials Today: Proceedings*. (2023). <https://doi.org/10.1016/j.matpr.2023.06.392>.

- [20] Y. Yang, M. Pritzker, Y. Li, Electrodeposited p-type Cu₂O thin films at high pH for all-oxide solar cells with improved performance, *Thin Solid Films*. 676 (2019) 42–53. <https://doi.org/10.1016/j.tsf.2019.02.014>.
- [21] I.V. Bagal, N.R. Chodankar, M.A. Hassan, A. Waseem, M.A. Johar, D.-H. Kim, S.-W. Ryu, Cu₂O as an emerging photocathode for solar water splitting - A status review, *International Journal of Hydrogen Energy*. 44 (2019) 21351–21378. <https://doi.org/10.1016/j.ijhydene.2019.06.184>.
- [22] P.K. Sharma, M.K. Singh, G.D. Sharma, A. Agrawal, NiO nanoparticles: Facile route synthesis, characterization and potential towards third generation solar cell, *Materials Today: Proceedings*. 43 (2021) 3061–3065. <https://doi.org/10.1016/j.matpr.2021.01.400>.
- [23] J.H. Park, J. Seo, S. Park, S.S. Shin, Y.C. Kim, N.J. Jeon, H.-W. Shin, T.K. Ahn, J.H. Noh, S.C. Yoon, C.S. Hwang, S.I. Seok, Efficient CH₃NH₃PbI₃ Perovskite Solar Cells Employing Nanostructured p-Type NiO Electrode Formed by a Pulsed Laser Deposition, *Advanced Materials*. 27 (2015) 4013–4019. <https://doi.org/10.1002/adma.201500523>.
- [24] L. Pan, P. Liu, S. Ullah, J. Wang, P. Yang, L. Liu, S.-E. Yang, H. Guo, T. Xia, Y. Chen, Investigation of p-type SnO films served as a potential hole-transporting material for highly efficient perovskite solar cells, *J. Phys. D: Appl. Phys.* 53 (2020) 485103. <https://doi.org/10.1088/1361-6463/abae33>.
- [25] K.J. Saji, Y.P. Venkata Subbaiah, K. Tian, A. Tiwari, P-type SnO thin films and SnO/ZnO heterostructures for all-oxide electronic and optoelectronic device applications, *Thin Solid Films*. 605 (2016) 193–201. <https://doi.org/10.1016/j.tsf.2015.09.026>.
- [26] X. Sun, C. Wang, D. Su, G. Wang, Y. Zhong, Application of photocatalytic materials in sensors, *Advanced Materials Technologies*. 5 (2020) 1900993. <https://doi.org/10.1002/admt.201900993>.
- [27] T.T. Nguyen, M. Patel, J. Kim, All-inorganic metal oxide transparent solar cells, *Solar Energy Materials and Solar Cells*. 217 (2020) 110708. <https://doi.org/10.1016/j.solmat.2020.110708>.
- [28] S.S. Shin, S.J. Lee, S.I. Seok, Metal Oxide Charge Transport Layers for Efficient and Stable Perovskite Solar Cells, *Advanced Functional Materials*. 29 (2019) 1900455. <https://doi.org/10.1002/adfm.201900455>.
- [29] H. He, 2 - Metal oxide semiconductors and conductors, in: Z. Cui, G. Korotcenkov (Eds.), *Solution Processed Metal Oxide Thin Films for Electronic Applications*, Elsevier, 2020: pp. 7–30. <https://doi.org/10.1016/B978-0-12-814930-0.00002-5>.

- [30] V.K. Arepalli, W.-J. Lee, Y.-D. Chung, J. Kim, Growth and device properties of ALD deposited ZnO films for CIGS solar cells, *Materials Science in Semiconductor Processing*. 121 (2021) 105406. <https://doi.org/10.1016/j.mssp.2020.105406>.
- [31] M.A. Borysiewicz, ZnO as a Functional Material, a Review, *Crystals*. 9 (2019) 505. <https://doi.org/10.3390/cryst9100505>.
- [32] C. de Melo, M. Jullien, J. Ghanbaja, F. Montaigne, J.-F. Pierson, F. Soldera, F. Rigoni, N. Almqvist, A. Vomiero, F. Mücklich, Local structure and point-defect-dependent area-selective atomic layer deposition approach for facile synthesis of p-Cu₂O/n-ZnO segmented nanojunctions, *ACS Applied Materials & Interfaces*. 10 (2018) 37671–37678. <https://doi.org/10.1021/acsami.8b12584>.
- [33] N. Fellahi, M. Addou, A. Kachouane, M.E. Jouad, Z. Sofiani, Optical properties of undoped and tin-doped nanostructured In₂O₃ thin films deposited by spray pyrolysis, *Eur. Phys. J. Appl. Phys.* 74 (2016) 24611. <https://doi.org/10.1051/epjap/2015150383>.
- [34] K. Bergum, H.N. Riise, S. Gorantla, P.F. Lindberg, I.J.T. Jensen, A.E. Gunnæs, A. Galeckas, S. Diplas, B.G. Svensson, E. Monakhov, Improving carrier transport in Cu₂O thin films by rapid thermal annealing, *J. Phys.: Condens. Matter*. 30 (2018) 075702. <https://doi.org/10.1088/1361-648X/aaa5f4>.
- [35] C. de Melo, M. Jullien, Y. Battie, A. En Naciri, J. Ghanbaja, F. Montaigne, J.-F. Pierson, F. Rigoni, N. Almqvist, A. Vomiero, S. Migot, F. Mücklich, D. Horwat, Semi-Transparent p-Cu₂O/n-ZnO Nanoscale-Film Heterojunctions for Photodetection and Photovoltaic Applications, *ACS Appl. Nano Mater.* 2 (2019) 4358–4366. <https://doi.org/10.1021/acsanm.9b00808>.
- [36] Y. Wang, J.F. Pierson, Binary copper oxides as photovoltaic absorbers: recent progress in materials and applications, *J. Phys. D: Appl. Phys.* 54 (2021) 263002. <https://doi.org/10.1088/1361-6463/abf165>.
- [37] Y. Wang, P. Miska, D. Pilloud, D. Horwat, F. Mücklich, J.F. Pierson, Transmittance enhancement and optical band gap widening of Cu₂O thin films after air annealing, *Journal of Applied Physics*. 115 (2014) 073505. <https://doi.org/10.1063/1.4865957>.
- [38] K. Mizuno, M. Izaki, K. Murase, T. Shinagawa, M. Chigane, M. Inaba, A. Tasaka, Y. Awakura, Structural and electrical characterizations of electrodeposited p-type semiconductor Cu₂O films, *Journal of The Electrochemical Society*. 152 (2005) C179. <https://doi.org/10.1149/1.1862478>.
- [39] A. Ogwu, T. Darma, E. Bouquerel, Electrical resistivity of copper oxide thin films prepared by reactive magnetron sputtering, *Journal of Achievements in Materials and*

- Manufacturing Engineering. 24 (2007) 172–177.
http://jamme.acmsse.h2.pl/papers_vol24_1/24121.pdf.
- [40] H. Sun, S.-C. Chen, P.-J. Chen, S.-L. Ou, C.-Y. Liu, Y.-Q. Xin, p-type conductive NiO_x: Cu thin films with high carrier mobility deposited by ion beam assisted deposition, *Ceramics International*. 44 (2018) 3291–3296.
<https://doi.org/10.1016/j.ceramint.2017.11.103>.
- [41] M.I. Pintor-Monroy, B.L. Murillo-Borjas, M. Catalano, M.A. Quevedo-López, Controlling Carrier Type and Concentration in NiO Films To Enable in Situ PN Homojunctions, *ACS Appl. Mater. Interfaces*. 11 (2019) 27048–27056.
<https://doi.org/10.1021/acsami.9b04380>.
- [42] H.-L. Chen, Y.-M. Lu, W.-S. Hwang, Characterization of sputtered NiO thin films, *Surface and Coatings Technology*. 198 (2005) 138–142.
<https://doi.org/10.1016/j.surfcoat.2004.10.032>.
- [43] F. Schweiner, Theory of excitons in cuprous oxide, PhD Thesis, 2017.
<https://doi.org/10.18419/opus-9483>.
- [44] B.K. Meyer, A. Polity, D. Reppin, M. Becker, P. Hering, P.J. Klar, T. Sander, C. Reindl, J. Benz, M. Eickhoff, C. Heiliger, M. Heinemann, J. Bläsing, A. Krost, S. Shokovets, C. Müller, C. Ronning, Binary copper oxide semiconductors: From materials towards devices, *Physica Status Solidi (b)*. 249 (2012) 1487–1509.
<https://onlinelibrary.wiley.com/doi/abs/10.1002/pssb.201248128> (accessed July 3, 2023).
- [45] A. Lakshmanan, Z.C. Alex, S. Meher, Recent advances in cuprous oxide thin film based photovoltaics, *Materials Today Sustainability*. 20 (2022) 100244.
<https://doi.org/10.1016/j.mtsust.2022.100244>.
- [46] C. de M. Sánchez, Selective growth of Cu₂O and metallic Cu by atomic layer deposition on ZnO and their application in optoelectronics, Phd Thesis, Université de Lorraine; Universität des Saarlandes, 2019. <https://hal.univ-lorraine.fr/tel-02998178> (accessed September 25, 2023).
- [47] Y. Wang, Controllable growth, microstructure and electronic structure of copper oxide thin films, Phd Thesis, Université de Lorraine, 2015. <https://hal.univ-lorraine.fr/tel-01754623v1> (accessed September 20, 2023).
- [48] S. Lany, Band-structure calculations for the 3d transition metal oxides in GW, *Phys. Rev. B*. 87 (2013) 085112. <https://doi.org/10.1103/PhysRevB.87.085112>.

- [49] A. Soon, X.-Y. Cui, B. Delley, S.-H. Wei, C. Stampfl, Native defect-induced multifarious magnetism in nonstoichiometric cuprous oxide: First-principles study of bulk and surface properties of $\text{Cu}_{2-\delta}\text{O}$, *Phys. Rev. B.* 79 (2009) 035205. <https://doi.org/10.1103/PhysRevB.79.035205>.
- [50] H. Raebiger, S. Lany, A. Zunger, Origins of the p -type nature and cation deficiency in Cu_2O and related materials, *Phys. Rev. B.* 76 (2007) 045209. <https://doi.org/10.1103/PhysRevB.76.045209>.
- [51] D. Dai, P.-Y. Huang, T.-Y. Wu, C.-H. Shih, L. Chang, Epitaxial electrodeposition of Cu_2O on Ag substrates in sulfate baths, *Journal of Crystal Growth.* 603 (2023) 126983. <https://doi.org/10.1016/j.jcrysro.2022.126983>.
- [52] G. Altindemir, C. Gumus, Cu_2O thin films prepared by using four different copper salts at a low temperature: An investigation of their physical properties, *Materials Science in Semiconductor Processing.* 107 (2020) 104805. <https://doi.org/10.1016/j.mssp.2019.104805>.
- [53] C.V. Kartha, J.-L. Rehspringer, D. Muller, S. Roques, J. Bartringer, G. Ferblantier, A. Slaoui, T. Fix, Insights into Cu_2O thin film absorber via pulsed laser deposition, *Ceramics International.* 48 (2022) 15274–15281. <https://doi.org/10.1016/j.ceramint.2022.02.061>.
- [54] C. Qin, X. Chen, R. Liang, N. Jiang, Z. Zheng, Z. Ye, L. Zhu, Fabricating High-Quality Cu_2O Photocathode by Magnetron Sputtering: Insight into Defect States and Charge Carrier Collection in Cu_2O , *ACS Appl. Energy Mater.* 5 (2022) 14410–14422. <https://doi.org/10.1021/acsaem.2c02974>.
- [55] F. Rahman, Zinc oxide light-emitting diodes: a review, *Optical Engineering.* 58 (2019) 010901–010901. <https://doi.org/10.1117/1.OE.58.1.010901>.
- [56] Y. Kang, F. Yu, L. Zhang, W. Wang, L. Chen, Y. Li, Review of ZnO-based nanomaterials in gas sensors, *Solid State Ionics.* 360 (2021) 115544. <https://doi.org/10.1016/j.ssi.2020.115544>.
- [57] W. Ouyang, J. Chen, Z. Shi, X. Fang, Self-powered UV photodetectors based on ZnO nanomaterials, *Applied Physics Reviews.* 8 (2021). <https://doi.org/10.1063/5.0058482>.
- [58] F. Cao, X. Ji, Enhanced self-powered UV sensing performance of $\text{ZnO}/\text{Au}/\text{Al}_2\text{O}_3$ photodetector with the decoration of Au nanoparticles, *J Mater Sci: Mater Electron.* 31 (2020) 2657–2665. <https://doi.org/10.1007/s10854-019-02805-9>.

- [59] J. Luo, Y. Wang, Q. Zhang, Progress in perovskite solar cells based on ZnO nanostructures, *Solar Energy*. 163 (2018) 289–306. <https://doi.org/10.1016/j.solener.2018.01.035>.
- [60] S. Ghosh, R. Su, J. Zhao, A. Fieramosca, J. Wu, T. Li, Q. Zhang, F. Li, Z. Chen, T. Liew, Microcavity exciton polaritons at room temperature, *Photonics Insights*. 1 (2022) R04–R04. <https://doi.org/10.3788/PI.2022.R04>.
- [61] B. Nikoobakht, J. Lee, A. Agrawal, S. Wight, M. Shur, ZnO fin optical cavities, *The Journal of Physical Chemistry C*. 126 (2022) 10515–10523. <https://doi.org/10.1021/acs.jpcc.2c02068>.
- [62] C. Klingshirn, ZnO: From basics towards applications, *Physica Status Solidi (b)*. 244 (2007) 3027–3073. <https://doi.org/10.1002/pssb.200743072>.
- [63] I. Ayoub, V. Kumar, R. Abolhassani, R. Sehgal, V. Sharma, R. Sehgal, H.C. Swart, Y.K. Mishra, Advances in ZnO: Manipulation of defects for enhancing their technological potentials, *Nanotechnology Reviews*. 11 (2022) 575–619. <https://doi.org/10.1515/ntrev-2022-0035>.
- [64] D.C. Look, J.W. Hemsky, J. Sizelove, Residual native shallow donor in ZnO, *Physical Review Letters*. 82 (1999) 2552. <https://doi.org/10.1103/PhysRevLett.82.2552>.
- [65] A. Janotti, C.G. Van de Walle, Fundamentals of zinc oxide as a semiconductor, *Reports on Progress in Physics*. 72 (2009) 126501. <https://doi.org/10.1088/0034-4885/72/12/126501>.
- [66] Z. Chen, J. Wang, H. Wu, J. Yang, Y. Wang, J. Zhang, Q. Bao, M. Wang, Z. Ma, W. Tress, Z. Tang, A Transparent Electrode Based on Solution-Processed ZnO for Organic Optoelectronic Devices, *Nat Commun*. 13 (2022) 4387. <https://doi.org/10.1038/s41467-022-32010-y>.
- [67] A. Mathur, P.P. Singh, S. Upadhyay, N. Yadav, K. Singh, D. Singh, B. Singh, Role of absorber and buffer layer thickness on Cu₂O/TiO₂ heterojunction solar cells, *Solar Energy*. 233 (2022) 287–291. <https://doi.org/10.1016/j.solener.2022.01.047>.
- [68] M. Pavan, S. Rühle, A. Ginsburg, D.A. Keller, H.-N. Barad, P.M. Sberna, D. Nunes, R. Martins, A.Y. Anderson, A. Zaban, TiO₂/Cu₂O all-oxide heterojunction solar cells produced by spray pyrolysis, *Solar Energy Materials and Solar Cells*. 132 (2015) 549–556. <https://doi.org/10.1016/j.solmat.2014.10.005>.
- [69] P. Sawicka-Chudy, M. Sibiński, R. Pawełek, G. Wisz, B. Cieniek, P. Potera, P. Szczepan, S. Adamiak, M. Cholewa, Ł. Głowa, Characteristics of TiO₂, Cu₂O, and TiO₂/Cu₂O thin

- films for application in PV devices, *AIP Advances*. 9 (2019). <https://doi.org/10.1063/1.5093037>.
- [70] D. Chua, S.B. Kim, R. Gordon, Enhancement of the open circuit voltage of Cu₂O/Ga₂O₃ heterojunction solar cells through the mitigation of interfacial recombination, *AIP Advances*. 9 (2019). <https://doi.org/10.1063/1.5096283>.
- [71] T. Minami, Y. Nishi, T. Miyata, Heterojunction solar cell with 6% efficiency based on an n-type aluminum–gallium–oxide thin film and p-type sodium-doped Cu₂O sheet, *Applied Physics Express*. 8 (2015) 022301. <https://doi.org/10.7567/APEX.8.022301>.
- [72] A.K. Saikumar, S.D. Nehate, K.B. Sundaram, A review of recent developments in aluminum gallium oxide thin films and devices, *Critical Reviews in Solid State and Materials Sciences*. 47 (2022) 538–569. <https://doi.org/10.1080/10408436.2021.1922357>.
- [73] T. Miyata, H. Tokunaga, K. Watanabe, N. Ikenaga, T. Minami, Photovoltaic properties of low-damage magnetron-sputtered n-type ZnO thin film/p-type Cu₂O sheet heterojunction solar cells, *Thin Solid Films*. 697 (2020) 137825. <https://doi.org/10.1016/j.tsf.2020.137825>.
- [74] Z. Zang, Efficiency enhancement of ZnO/Cu₂O solar cells with well oriented and micrometer grain sized Cu₂O films, *Applied Physics Letters*. 112 (2018) 042106. <https://doi.org/10.1063/1.5017002>.
- [75] T. Özdal, M. Kılıç, H. Kavak, Impact of improvements in ZnO thin film solution process on ZnO/Cu₂O solar cell performance, *Superlattices and Microstructures*. 156 (2021) 106948. <https://doi.org/10.1016/j.spmi.2021.106948>.
- [76] A. J, N. Nayak, T. Sahoo, Tailoring the optical and electrical behavior of Cu₂O/ZnO heterojunction by varying the Zn²⁺ ion concentration for solar-cell applications, *Micro and Nanostructures*. 174 (2023) 207488. <https://doi.org/10.1016/j.micrna.2022.207488>.
- [77] J. Pan, C. Zhao, B. Wang, Z. Dong, Z. Jiang, J. Wang, C. Song, Y. Zheng, C. Li, The transparent device of CdS quantum dots modified Cu₂O/ZnO orderly nano array p-n junction towards the enhanced photovoltaic conversion, *Journal of Alloys and Compounds*. 827 (2020) 154267. <https://doi.org/10.1016/j.jallcom.2020.154267>.
- [78] T. Minami, Y. Nishi, T. Miyata, Cu₂O-based solar cells using oxide semiconductors, *J. Semicond*. 37 (2016) 014002. <https://doi.org/10.1088/1674-4926/37/1/014002>.
- [79] I.-H. Yoo, S.S. Kalanur, K. Eom, B. Ahn, I.S. Cho, H.K. Yu, H. Jeon, H. Seo, Plasmon-enhanced ZnO nanorod/Au NPs/Cu₂O structure solar cells: Effects and limitations,

- Korean J. Chem. Eng. 34 (2017) 3200–3207. <https://doi.org/10.1007/s11814-017-0222-y>.
- [80] M.A. Fuller, I. Köper, Biomedical applications of polyelectrolyte coated spherical gold nanoparticles, *Nano Convergence*. 6 (2019) 11. <https://doi.org/10.1186/s40580-019-0183-4>.
- [81] K. Ueno, T. Oshikiri, Q. Sun, X. Shi, H. Misawa, Solid-State Plasmonic Solar Cells, *Chem. Rev.* 118 (2018) 2955–2993. <https://doi.org/10.1021/acs.chemrev.7b00235>.
- [82] Y. Xin, K. Yu, L. Zhang, Y. Yang, H. Yuan, H. Li, L. Wang, J. Zeng, Copper-based plasmonic catalysis: recent advances and future perspectives, *Advanced Materials*. 33 (2021) 2008145. <https://doi.org/10.1002/adma.202008145>.
- [83] M.M. Alvarez, J.T. Khoury, T.G. Schaaff, M.N. Shafigullin, I. Vezmar, R.L. Whetten, Optical Absorption Spectra of Nanocrystal Gold Molecules, *J. Phys. Chem. B*. 101 (1997) 3706–3712. <https://doi.org/10.1021/jp962922n>.
- [84] M. Rycenga, C.M. Cobley, J. Zeng, W. Li, C.H. Moran, Q. Zhang, D. Qin, Y. Xia, Controlling the Synthesis and Assembly of Silver Nanostructures for Plasmonic Applications, *Chem. Rev.* 111 (2011) 3669–3712. <https://doi.org/10.1021/cr100275d>.
- [85] E. Hutter, J.H. Fendler, Exploitation of Localized Surface Plasmon Resonance, *Advanced Materials*. 16 (2004) 1685–1706. <https://doi.org/10.1002/adma.200400271>.
- [86] P.K. Jain, X. Huang, I.H. El-Sayed, M.A. El-Sayed, Review of Some Interesting Surface Plasmon Resonance-enhanced Properties of Noble Metal Nanoparticles and Their Applications to Biosystems, *Plasmonics*. 2 (2007) 107–118. <https://doi.org/10.1007/s11468-007-9031-1>.
- [87] J.G. Hinman, A.J. Stork, J.A. Varnell, A.A. Gewirth, C.J. Murphy, Seed mediated growth of gold nanorods: towards nanorod matryoshkas, *Faraday Discussions*. 191 (2016) 9–33. <https://doi.org/10.1039/C6FD00145A>.
- [88] S. Lin, M. Li, E. Dujardin, C. Girard, S. Mann, One-Dimensional Plasmon Coupling by Facile Self-Assembly of Gold Nanoparticles into Branched Chain Networks, *Advanced Materials*. 17 (2005) 2553–2559. <https://onlinelibrary.wiley.com/doi/abs/10.1002/adma.200500828> (accessed July 3, 2023).
- [89] P. Mandal, Application of Plasmonics in Solar Cell Efficiency Improvement: a Brief Review on Recent Progress, *Plasmonics*. 17 (2022) 1247–1267. <https://doi.org/10.1007/s11468-022-01616-9>.

- [90] S.V. Boriskina, H. Ghasemi, G. Chen, Plasmonic materials for energy: From physics to applications, *Materials Today*. 16 (2013) 375–386. <https://doi.org/10.1016/j.mattod.2013.09.003>.
- [91] E.G. Graham, C.M. Macneill, N.H. Levi-Polyachenko, Review of metal, carbon and polymer nanoparticles for infrared photothermal therapy, *Nano LIFE*. 03 (2013) 1330002. <https://doi.org/10.1142/S1793984413300021>.
- [92] A. Ali, F. El-Mellouhi, A. Mitra, B. Aïssa, Research Progress of Plasmonic Nanostructure-Enhanced Photovoltaic Solar Cells, *Nanomaterials*. 12 (2022) 788. <https://doi.org/10.3390/nano12050788>.
- [93] M.A. Alkhalayfeh, A.A. Aziz, M.Z. Pakhuruddin, An overview of enhanced polymer solar cells with embedded plasmonic nanoparticles, *Renewable and Sustainable Energy Reviews*. 141 (2021) 110726. <https://doi.org/10.1016/j.rser.2021.110726>.
- [94] H. Gao, J. Meng, J. Sun, J. Deng, Enhanced performance of polymer solar cells based on P₃HT: PCBM via incorporating Au nanoparticles prepared by the micellar method, *J Mater Sci: Mater Electron*. 31 (2020) 10760–10767. <https://doi.org/10.1007/s10854-020-03626-x>.
- [95] S.-Q. Zhu, B. Bian, Y.-F. Zhu, J. Yang, D. Zhang, L. Feng, Enhancement in power conversion efficiency of GaAs solar cells by utilizing gold nanostar film for light-trapping, *Frontiers in Chemistry*. 7 (2019) 137. <https://doi.org/10.3389/fchem.2019.00137>.
- [96] R.T. Ginting, S. Kaur, D.-K. Lim, J.-M. Kim, J.H. Lee, S.H. Lee, J.-W. Kang, Plasmonic effect of gold nanostars in highly efficient organic and perovskite solar cells, *ACS Applied Materials & Interfaces*. 9 (2017) 36111–36118. <https://doi.org/10.1021/acsami.7b11084>.
- [97] P.K. Parashar, V.K. Komarala, Engineered optical properties of silver-aluminum alloy nanoparticles embedded in SiON matrix for maximizing light confinement in plasmonic silicon solar cells, *Scientific Reports*. 7 (2017) 12520. <https://doi.org/10.1038/s41598-017-12826-1>.
- [98] S. Saravanan, R. Kato, M. Balamurugan, S. Kaushik, T. Soga, Efficiency improvement in dye sensitized solar cells by the plasmonic effect of green synthesized silver nanoparticles, *Journal of Science: Advanced Materials and Devices*. 2 (2017) 418–424. <https://doi.org/10.1016/j.jsamd.2017.10.004>.
- [99] G. Kaur, K.L. Yadav, A. Mitra, Localized surface plasmon induced enhancement of electron-hole generation with silver metal island at n-Al:ZnO/p-Cu₂O heterojunction, *Applied Physics Letters*. 107 (2015) 053901. <https://doi.org/10.1063/1.4928373>.

- [100] G. Deka, C.-K. Sun, K. Fujita, S.-W. Chu, Nonlinear plasmonic imaging techniques and their biological applications, *6* (2017) 31–49. <https://doi.org/10.1515/nanoph-2015-0149>.
- [101] X. Ren, E. Cao, W. Lin, Y. Song, W. Liang, J. Wang, Recent advances in surface plasmon-driven catalytic reactions, *RSC Advances*. *7* (2017) 31189–31203. <https://doi.org/10.1039/C7RA05346K>.
- [102] D.Y. Fedyanin, D.I. Yakubovsky, R.V. Kirtaev, V.S. Volkov, Ultralow-loss CMOS copper plasmonic waveguides, *Nano Letters*. *16* (2016) 362–366. <https://doi.org/10.1021/acs.nanolett.5b03942>.
- [103] Y.V. Stebunov, D.I. Yakubovsky, D.Yu. Fedyanin, A.V. Arsenin, V.S. Volkov, Superior Sensitivity of Copper-Based Plasmonic Biosensors, *Langmuir*. *34* (2018) 4681–4687. <https://doi.org/10.1021/acs.langmuir.8b00276>.
- [104] D.-D. Wang, C.-W. Ge, G.-A. Wu, Z.-P. Li, J.-Z. Wang, T.-F. Zhang, Y.-Q. Yu, L.-B. Luo, A sensitive red light nano-photodetector propelled by plasmonic copper nanoparticles, *J. Mater. Chem. C*. *5* (2017) 1328–1335. <https://doi.org/10.1039/C6TC05117K>.
- [105] G. Barbillon, Latest Advances in Nanoplasmonics and Use of New Tools for Plasmonic Characterization, MDPI - Multidisciplinary Digital Publishing Institute, Basel, 2022. <https://doi.org/10.3390/photronics9020112>.
- [106] S.B. Kalidindi, U. Sanyal, B.R. Jagirdar, Nanostructured Cu and Cu@Cu₂O core shell catalysts for hydrogen generation from ammonia–borane, *Phys. Chem. Chem. Phys.* *10* (2008) 5870–5874. <https://doi.org/10.1039/B805726E>.
- [107] F. Parveen, B. Sannakki, M.V. Mandke, H.M. Pathan, Copper nanoparticles: Synthesis methods and its light harvesting performance, *Solar Energy Materials and Solar Cells*. *144* (2016) 371–382. <https://doi.org/10.1016/j.solmat.2015.08.033>.
- [108] M. Salavati-Niasari, F. Davar, N. Mir, Synthesis and characterization of metallic copper nanoparticles via thermal decomposition, *Polyhedron*. *27* (2008) 3514–3518. <https://doi.org/10.1016/j.poly.2008.08.020>.
- [109] H. Yin, Y. Zhao, X. Xu, J. Chen, X. Wang, J. Yu, J. Wang, W. Wu, Realization of Tunable Localized Surface Plasmon Resonance of Cu@Cu₂O Core–Shell Nanoparticles by the Pulse Laser Deposition Method, *ACS Omega*. *4* (2019) 14404–14410. <https://doi.org/10.1021/acsomega.9b01253>.

- [110] T. Ghodselahi, M.A. Vesaghi, A. Shafiekhani, Study of surface plasmon resonance of Cu@Cu₂O core-shell nanoparticles by Mie theory, *J. Phys. D: Appl. Phys.* 42 (2008) 015308. <https://doi.org/10.1088/0022-3727/42/1/015308>.
- [111] R. Werner, T. Höche, S. Mayr, Synthesis of shape, size and structure controlled nanocrystals by pre-seeded inert gas condensation, *CrystEngComm*. 13 (2011) 3046–3050. <https://doi.org/10.1039/C1CE00002K>.
- [112] K. Strijckmans, R. Schelfhout, D. Depla, Tutorial: Hysteresis during the reactive magnetron sputtering process, *Journal of Applied Physics*. 124 (2018). <https://doi.org/10.1063/1.5042084>.
- [113] K. Wasa, Sputtering phenomena, *Handbook of Sputtering Technology*. (2012) 41–75.
- [114] S. Swann, Magnetron sputtering, *Physics in Technology*. 19 (1988) 67. <https://doi.org/10.1088/0305-4624/19/2/304>.
- [115] J.T. Gudmundsson, D. Lundin, Introduction to magnetron sputtering, *High Power Impulse Magnetron Sputtering*. (2020) 1–48. <https://doi.org/10.1016/B978-0-12-812454-3.00006-1>.
- [116] P.J. Kelly, R.D. Arnell, Magnetron sputtering: a review of recent developments and applications, *Vacuum*. 56 (2000) 159–172. [https://doi.org/10.1016/S0042-207X\(99\)00189-X](https://doi.org/10.1016/S0042-207X(99)00189-X).
- [117] S. Berg, T. Nyberg, Fundamental understanding and modeling of reactive sputtering processes, *Thin Solid Films*. 476 (2005) 215–230. <https://doi.org/10.1016/j.tsf.2004.10.051>.
- [118] I. Safi, Recent aspects concerning DC reactive magnetron sputtering of thin films: a review, *Surface and Coatings Technology*. 127 (2000) 203–218. [https://doi.org/10.1016/S0257-8972\(00\)00566-1](https://doi.org/10.1016/S0257-8972(00)00566-1).
- [119] W. Chamorro-Coral, A. Caillard, P. Brault, P. Andreazza, C. Coutanceau, S. Baranton, The role of oxygen on the growth of palladium clusters synthesized by gas aggregation source, *Plasma Processes and Polymers*. 16 (2019) e1900006. <https://doi.org/10.1002/ppap.201900006>.
- [120] Nanogen 50/Trio - MesoQ operation manual V1.7 - 011012.
- [121] AnnealSys, ASOne100 User Manual.
- [122] A. Borroto, Synthesis, structure and properties of zirconium-based binary alloy thin films, Université de Lorraine; Universität des Saarlandes, 2019. <https://hal.univ-lorraine.fr/tel-03876259> (accessed July 3, 2023).

- [123] B.D. Cullity, *Elements of X-ray Diffraction*, Addison-Wesley Publishing, 1956.
- [124] V. Pecharsky, P. Zavalij, *Fundamentals of Powder Diffraction and Structural characterization of Materials* Springer ScienceBusiness Media, Second Edition, Springer, 2009.
- [125] C. Würth, M. Grabolle, J. Pauli, M. Spieles, U. Resch-Genger, Relative and absolute determination of fluorescence quantum yields of transparent samples, *Nature Protocols*. 8 (2013) 1535–1550. <https://doi.org/10.1038/nprot.2013.087>.
- [126] Cary 7000 Universal Measurement Spectrophotometer (UMS) Video | Agilent. <https://www.agilent.com/en/product/molecular-spectroscopy/uv-vis-uv-vis-nir-spectroscopy/uv-vis-uv-vis-nir-systems/cary-7000-universal-measurement-spectrophotometer-ums/cary-7000-ums-video> (accessed July 3, 2023).
- [127] O. Stenzel, *The Physics of Thin Film Optical Spectra*, Springer, 2005.
- [128] M. Mickan, *Deposition of Al-doped ZnO films by high power impulse magnetron sputtering*, Université de Lorraine; Université de Linköping (Suède), 2017. 10.3384/diss.diva-142925.
- [129] R. Raciti, R. Bahariqushchi, C. Summonte, A. Aydinli, A. Terrasi, S. Mirabella, Optical bandgap of semiconductor nanostructures: Methods for experimental data analysis, *Journal of Applied Physics*. 121 (2017) 234304. <https://doi.org/10.1063/1.4986436>.
- [130] M. Amroun, M. Khadraoui, R. Miloua, Z. Kebbab, K. Sahraoui, Investigation on the structural, optical and electrical properties of mixed SnS₂—CdS thin films, *Optik*. 131 (2017) 152–164. <https://doi.org/10.1016/j.ijleo.2016.11.005>.
- [131] V. Agekyan, Spectroscopic properties of semiconductor crystals with direct forbidden energy gap, *Physica Status Solidi (a)*. 43 (1977) 11–42. <https://doi.org/10.1002/pssa.2210430102>.
- [132] R.C. Rai, Analysis of the Urbach tails in absorption spectra of undoped ZnO thin films, *Journal of Applied Physics*. 113 (2013) 153508. <https://doi.org/10.1063/1.4801900>.
- [133] A E Rakhshani, Study of Urbach tail, bandgap energy and grain-boundary characteristics in CdS by modulated photocurrent spectroscopy, *Journal of Physics: Condensed Matter*. 12 (2000) 4391. <https://doi.org/10.1088/0953-8984/12/19/309>.
- [134] A. Mahmood, A. Nasar, C. Mircea, N. Bensaada Laidani, J. De Hosson, *Handbook of modern coating technologies: Advanced characterization methods*, in: *Handbook of Modern Coating Technologies: Advanced Characterization Methods*, 2021.
- [135] H. Tompkins, E.A. Irene, *Handbook of ellipsometry*, William Andrew, 2005.

- [136] M.-B. Bouzourâa, Y. Battie, S. Dalmaso, M.-A. Zaibi, M. Oueslati, A.E. Naciri, Comparative study of ZnO optical dispersion laws, Superlattices and Microstructures. 104 (2017) 24–36. <https://doi.org/10.1016/j.spmi.2017.01.044>.
- [137] C. Tanguy, Optical dispersion by Wannier excitons, Physical Review Letters. 75 (1995) 4090. <https://doi.org/10.1103/PhysRevLett.75.4090>.
- [138] F. Smits, Measurement of sheet resistivities with the four-point probe, Bell System Technical Journal. 37 (1958) 711–718. <https://doi.org/10.1002/j.1538-7305.1958.tb03883.x>.
- [139] Scanning electron microscope, Wikipedia. (2023). https://en.wikipedia.org/w/index.php?title=Scanning_electron_microscope&oldid=1158184325 (accessed July 3, 2023).
- [140] W. Zhou, R. Apkarian, Z.L. Wang, D. Joy, Fundamentals of scanning electron microscopy (SEM), Scanning Microscopy for Nanotechnology: Techniques and Applications. (2007) 1–40.
- [141] C. Campos, M. Vasconcellos, J. Trincavelli, S. Segui, Analytical expression for K-and L-shell cross sections of neutral atoms near ionization threshold by electron impact, Journal of Physics B: Atomic, Molecular and Optical Physics. 40 (2007) 3835. <https://doi.org/10.1088/0953-4075/40/19/004>.
- [142] D.B.W.C.B. Carter, Transmission Electron Microscopy A Textbook for Materials Science, springer publication, 2009.
- [143] R. Egerton, M. Malac, EELS in the TEM, Journal of Electron Spectroscopy and Related Phenomena. 143 (2005) 43–50. <https://doi.org/10.1016/j.elspec.2003.12.009>.
- [144] F. Hofer, F.-P. Schmidt, W. Grogger, G. Kothleitner, Fundamentals of electron energy-loss spectroscopy, in: IOP Publishing, 2016: p. 012007. <https://doi.org/10.1088/1757-899X/109/1/012007>.
- [145] S.M. Sze, Semiconductor devices: physics and technology, John wiley & sons, 2008.
- [146] P.S. Priambodo, D. Sukoco, W. Purnomo, H. Sudiby, D. Hartanto, P.S. Priambodo, D. Sukoco, W. Purnomo, H. Sudiby, D. Hartanto, Electric Energy Management and Engineering in Solar Cell System, Solar Cells - Research and Application Perspectives. (2013). <https://doi.org/10.5772/52572>.
- [147] S.M. Sze, K.K. Ng, Physics of semiconductor devices, John wiley & sons, 2007.

- [148] Basic Characteristics and Characterization of Solar Cells, in: Materials Concepts for Solar Cells, WORLD SCIENTIFIC (EUROPE), 2017: pp. 3–43. https://doi.org/10.1142/9781786344496_0001.
- [149] E. Von Hauff, Impedance spectroscopy for emerging photovoltaics, *The Journal of Physical Chemistry C*. 123 (2019) 11329–11346. <https://doi.org/10.1021/acs.jpcc.9b00892>.
- [150] J. Prakash, R.A. Harris, H.C. Swart, Embedded plasmonic nanostructures: synthesis, fundamental aspects and their surface enhanced Raman scattering applications, *International Reviews in Physical Chemistry*. 35 (2016) 353–398. <https://doi.org/10.1080/0144235X.2016.1187006>.
- [151] M.A. Green, S. Pillai, Harnessing plasmonics for solar cells, *Nature Photon*. 6 (2012) 130–132. <https://doi.org/10.1038/nphoton.2012.30>.
- [152] A. Pescaglini, A. Martín, D. Cammi, G. Juska, C. Ronning, E. Pelucchi, D. Iacopino, Hot-Electron Injection in Au Nanorod–ZnO Nanowire Hybrid Device for Near-Infrared Photodetection, *Nano Lett*. 14 (2014) 6202–6209. <https://doi.org/10.1021/nl5024854>.
- [153] M. Huang, Y. Zhang, C. Du, S. Peng, D. Shi, Plasmon Peak Sensitivity Investigation of Individual Cu and Cu@Cu₂O Core–Shell Nanoparticle Sensors, *Plasmonics*. 11 (2016) 1197–1200. <https://doi.org/10.1007/s11468-015-0161-6>.
- [154] S. Kunwar, S. Pandit, J.-H. Jeong, J. Lee, Improved Photoresponse of UV Photodetectors by the Incorporation of Plasmonic Nanoparticles on GaN Through the Resonant Coupling of Localized Surface Plasmon Resonance, *Nano-Micro Lett*. 12 (2020) 91. <https://doi.org/10.1007/s40820-020-00437-x>.
- [155] N. Zhou, V. López-Puente, Q. Wang, L. Polavarapu, I. Pastoriza-Santos, Q.-H. Xu, Plasmon-enhanced light harvesting: applications in enhanced photocatalysis, photodynamic therapy and photovoltaics, *RSC Advances*. 5 (2015) 29076–29097. <https://doi.org/10.1039/C5RA01819F>.
- [156] G.-Y. Yao, Z.-Y. Zhao, Q.-L. Liu, X.-D. Dong, Q.-M. Zhao, Theoretical calculations for localized surface plasmon resonance effects of Cu/TiO₂ nanosphere: Generation, modulation, and application in photocatalysis, *Solar Energy Materials and Solar Cells*. 208 (2020) 110385. <https://doi.org/10.1016/j.solmat.2019.110385>.
- [157] K. Nakayama, K. Tanabe, H.A. Atwater, Plasmonic nanoparticle enhanced light absorption in GaAs solar cells, *Applied Physics Letters*. 93 (2008) 121904. <https://doi.org/10.1063/1.2988288>.

- [158] H. Tang, C.-J. Chen, Z. Huang, J. Bright, G. Meng, R.-S. Liu, N. Wu, Plasmonic hot electrons for sensing, photodetection, and solar energy applications: A perspective, *The Journal of Chemical Physics*. 152 (2020) 220901. <https://doi.org/10.1063/5.0005334>.
- [159] C. de Melo, M. Jullien, Y. Battie, A. En Naciri, J. Ghanbaja, F. Montaigne, J.-F. Pierson, F. Rigoni, N. Almqvist, A. Vomiero, S. Migot, F. Mücklich, D. Horwat, Tunable Localized Surface Plasmon Resonance and Broadband Visible Photoresponse of Cu Nanoparticles/ZnO Surfaces, *ACS Appl. Mater. Interfaces*. 10 (2018) 40958–40965. <https://doi.org/10.1021/acsami.8b17194>.
- [160] J. Nie, A.O.T. Patrocínio, S. Hamid, F. Sieland, J. Sann, S. Xia, D.W. Bahnemann, J. Schneider, New insights into the plasmonic enhancement for photocatalytic H₂ production by Cu–TiO₂ upon visible light illumination, *Phys. Chem. Chem. Phys.* 20 (2018) 5264–5273. <https://doi.org/10.1039/C7CP07762A>.
- [161] J. Pal, A.K. Sasmal, M. Ganguly, T. Pal, Surface Plasmon Effect of Cu and Presence of n–p Heterojunction in Oxide Nanocomposites for Visible Light Photocatalysis, *J. Phys. Chem. C*. 119 (2015) 3780–3790. <https://doi.org/10.1021/jp5114812>.
- [162] R. Wick, S.D. Tilley, Photovoltaic and Photoelectrochemical Solar Energy Conversion with Cu₂O, *J. Phys. Chem. C*. 119 (2015) 26243–26257. <https://doi.org/10.1021/acs.jpcc.5b08397>.
- [163] M.A. Shoeib, O.E. Abdelsalam, M.G. Khafagi, R.E. Hammam, Synthesis of Cu₂O nanocrystallites and their adsorption and photocatalysis behavior, *Advanced Powder Technology*. 23 (2012) 298–304. <https://doi.org/10.1016/j.appt.2011.04.001>.
- [164] V. Scuderi, G. Amiard, S. Boninelli, S. Scalse, M. Miritello, P.M. Sberna, G. Impellizzeri, V. Privitera, Photocatalytic activity of CuO and Cu₂O nanowires, *Materials Science in Semiconductor Processing*. 42 (2016) 89–93. <https://doi.org/10.1016/j.mssp.2015.08.008>.
- [165] A. Kusior, M. Synowiec, K. Zakrzewska, M. Radecka, Surface-Controlled Photocatalysis and Chemical Sensing of TiO₂, α-Fe₂O₃, and Cu₂O Nanocrystals, *Crystals*. 9 (2019) 163. <https://doi.org/10.3390/cryst9030163>.
- [166] K. Henzler, A. Heilemann, J. Kneer, P. Guttmann, H. Jia, E. Bartsch, Y. Lu, S. Palzer, Investigation of reactions between trace gases and functional CuO nanospheres and octahedrons using NEXAFS-TXM imaging, *Sci Rep*. 5 (2015) 17729. <https://doi.org/10.1038/srep17729>.
- [167] N. Wang, W. Tao, X. Gong, L. Zhao, T. Wang, L. Zhao, F. Liu, X. Liu, P. Sun, G. Lu, Highly sensitive and selective NO₂ gas sensor fabricated from Cu₂O-CuO microflowers,

- Sensors and Actuators B: Chemical. 362 (2022) 131803. <https://doi.org/10.1016/j.snb.2022.131803>.
- [168] J.H. Bang, A. Mirzaei, M.S. Choi, S. Han, H.Y. Lee, S.S. Kim, H.W. Kim, Decoration of multi-walled carbon nanotubes with CuO/Cu₂O nanoparticles for selective sensing of H₂S gas, *Sensors and Actuators B: Chemical*. 344 (2021) 130176. <https://doi.org/10.1016/j.snb.2021.130176>.
- [169] L.-C. Chen, Review of preparation and optoelectronic characteristics of Cu₂O-based solar cells with nanostructure, *Materials Science in Semiconductor Processing*. 16 (2013) 1172–1185. <https://doi.org/10.1016/j.mssp.2012.12.028>.
- [170] L. Lin, L. Jiang, P. Li, B. Fan, Y. Qiu, A modeled perovskite solar cell structure with a Cu₂O hole-transporting layer enabling over 20% efficiency by low-cost low-temperature processing, *Journal of Physics and Chemistry of Solids*. 124 (2019) 205–211. <https://doi.org/10.1016/j.jpcs.2018.09.024>.
- [171] S. Shibasaki, Y. Honishi, N. Nakagawa, M. Yamazaki, Y. Mizuno, Y. Nishida, K. Sugimoto, K. Yamamoto, Highly transparent Cu₂O absorbing layer for thin film solar cells, *Applied Physics Letters*. 119 (2021) 242102. <https://doi.org/10.1063/5.0072310>.
- [172] R. Hajimammadov, A. Bykov, A. Popov, K.L. Juhasz, G.S. Lorite, M. Mohl, A. Kukovecz, M. Huuhtanen, K. Kordas, Random networks of core-shell-like Cu-Cu₂O/CuO nanowires as surface plasmon resonance-enhanced sensors, *Sci Rep*. 8 (2018) 4708. <https://doi.org/10.1038/s41598-018-23119-6>.
- [173] T. Ghodselahi, M.A. Vesaghi, Localized Surface Plasmon Resonance of Cu@Cu₂O core-shell nanoparticles: Absorption, Scattering and Luminescence, *Physica B: Condensed Matter*. 406 (2011) 2678–2683. <https://doi.org/10.1016/j.physb.2011.03.082>.
- [174] J. Pierson, D. Wiederkehr, A. Billard, Reactive magnetron sputtering of copper, silver, and gold, *Thin Solid Films*. 478 (2005) 196–205. <https://doi.org/10.1016/j.tsf.2004.10.043>.
- [175] Y. Wang, J. Ghanbaja, F. Soldera, P. Boulet, D. Horwat, F. Mücklich, J.F. Pierson, Controlling the preferred orientation in sputter-deposited Cu₂O thin films: Influence of the initial growth stage and homoepitaxial growth mechanism, *Acta Materialia*. 76 (2014) 207–212. <https://doi.org/10.1016/j.actamat.2014.05.008>.
- [176] K. Ellmer, T. Welzel, Reactive magnetron sputtering of transparent conductive oxide thin films: Role of energetic particle (ion) bombardment, *Journal of Materials Research*. 27 (2012) 765–779. <https://doi.org/10.1557/jmr.2011.428>.

- [177] W. Chamorro, D. Horwat, P. Pigeat, P. Miska, S. Migot, F. Soldera, P. Boulet, F. Mücklich, Near-room temperature single-domain epitaxy of reactively sputtered ZnO films, *J. Phys. D: Appl. Phys.* 46 (2013) 235107. <https://doi.org/10.1088/0022-3727/46/23/235107>.
- [178] S. Han, A.J. Flewitt, Control of grain orientation and its impact on carrier mobility in reactively sputtered Cu₂O thin films, *Thin Solid Films*. 704 (2020) 138000. <https://doi.org/10.1016/j.tsf.2020.138000>.
- [179] G. Celep, E. Cottancin, J. Lermé, M. Pellarin, L. Arnaud, J.R. Huntzinger, J.L. Vialle, M. Broyer, B. Palpant, O. Boisron, P. Mélinon, Optical properties of copper clusters embedded in alumina: An experimental and theoretical study of size dependence, *Phys. Rev. B*. 70 (2004) 165409. <https://doi.org/10.1103/PhysRevB.70.165409>.
- [180] T. Ghodselahe, M.A. Vesaghi, A. Shafiekhani, A. Baghizadeh, M. Lameii, XPS study of the Cu@Cu₂O core-shell nanoparticles, *Applied Surface Science*. 255 (2008) 2730–2734. <https://doi.org/10.1016/j.apsusc.2008.08.110>.
- [181] B. Rajesh Kumar, B. Hymavathi, T. Subba Rao, Structural and Optical Properties of Nanostructured Cu₂O Thin Films for Optoelectronic Devices, *Materials Today: Proceedings*. 4 (2017) 3903–3910. <https://doi.org/10.1016/j.matpr.2017.02.289>.
- [182] R. Maas, J. Parsons, N. Engheta, A. Polman, Experimental realization of an epsilon-near-zero metamaterial at visible wavelengths, *Nature Photon.* 7 (2013) 907–912. <https://doi.org/10.1038/nphoton.2013.256>.
- [183] D.C. Adams, S. Inampudi, T. Ribaud, D. Slocum, S. Vangala, N.A. Kuhta, W.D. Goodhue, V.A. Podolskiy, D. Wasserman, Funneling Light through a Subwavelength Aperture with Epsilon-Near-Zero Materials, *Phys. Rev. Lett.* 107 (2011) 133901. <https://doi.org/10.1103/PhysRevLett.107.133901>.
- [184] N. Kinsey, C. DeVault, A. Boltasseva, V.M. Shalae, Near-zero-index materials for photonics, *Nat Rev Mater*. 4 (2019) 742–760. <https://doi.org/10.1038/s41578-019-0133-0>.
- [185] D. Gall, Electron mean free path in elemental metals, *Journal of Applied Physics*. 119 (2016) 085101. <https://doi.org/10.1063/1.4942216>.
- [186] Y. Wang, S. Lany, J. Ghanbaja, Y. Fagot-Revurat, Y.P. Chen, F. Soldera, D. Horwat, F. Mücklich, J.F. Pierson, Electronic structures of Cu₂O, Cu₄O₃, and CuO: A joint experimental and theoretical study, *Phys. Rev. B*. 94 (2016) 245418. <https://doi.org/10.1103/PhysRevB.94.245418>.

- [187] R.D. Leapman, L.A. Grunes, P.L. Fejes, Study of the $L_{2,3}$ edges in the 3d transition metals and their oxides by electron-energy-loss spectroscopy with comparisons to theory, *Phys. Rev. B.* 26 (1982) 614–635. <https://doi.org/10.1103/PhysRevB.26.614>.
- [188] A. Billard, F. Perry, Pulvérisation cathodique magnétron, *Techniques de l'ingénieur. Matériaux Métalliques.* (2005). <http://pascal-francis.inist.fr/vibad/index.php?action=getRecordDetail&idt=21784860>.
- [189] L. Meng, T. Ren, C. Li, The control of the diameter of the nanorods prepared by dc reactive magnetron sputtering and the applications for DSSC, *Applied Surface Science.* 256 (2010) 3676–3682. <https://doi.org/10.1016/j.apsusc.2009.12.169>.
- [190] J. Musil, S. Kadlec, Reactive sputtering of TiN films at large substrate to target distances, *Vacuum.* 40 (1990) 435–444. [https://doi.org/10.1016/0042-207X\(90\)90241-P](https://doi.org/10.1016/0042-207X(90)90241-P).
- [191] W. Gao, Z. Li, ZnO thin films produced by magnetron sputtering, *Ceramics International.* 30 (2004) 1155–1159. <https://doi.org/10.1016/j.ceramint.2003.12.197>.
- [192] L.-J. Meng, M.P. dos Santos, Influence of the target-substrate distance on the properties of indium tin oxide films prepared by radio frequency reactive magnetron sputtering, *Journal of Vacuum Science & Technology A.* 18 (2000) 1668–1671. <https://doi.org/10.1116/1.582404>.
- [193] D. Horwat, A. Billard, Effects of substrate position and oxygen gas flow rate on the properties of ZnO: Al films prepared by reactive co-sputtering, *Thin Solid Films.* 515 (2007) 5444–5448. <https://doi.org/10.1016/j.tsf.2006.12.188>.
- [194] W. Chamorro, J. Ghanbaja, Y. Battie, A.E. Naciri, F. Soldera, F. Mücklich, D. Horwat, Local Structure-Driven Localized Surface Plasmon Absorption and Enhanced Photoluminescence in ZnO-Au Thin Films, *J. Phys. Chem. C.* 120 (2016) 29405–29413. <https://doi.org/10.1021/acs.jpcc.6b09974>.
- [195] P.B. Barna, M. Adamik, Fundamental structure forming phenomena of polycrystalline films and the structure zone models, *Thin Solid Films.* 317 (1998) 27–33. [https://doi.org/10.1016/S0040-6090\(97\)00503-8](https://doi.org/10.1016/S0040-6090(97)00503-8).
- [196] P.A. Korzhavyi, B. Johansson, Literature review on the properties of cuprous oxide Cu_2O and the process of copper oxidation, (2011). <https://www.osti.gov/etdeweb/biblio/1039386> (accessed July 11, 2023).
- [197] A.A. Ogwu, E. Bouquerel, O. Ademosu, S. Moh, E. Crossan, F. Placido, An investigation of the surface energy and optical transmittance of copper oxide thin films prepared by reactive magnetron sputtering, *Acta Materialia.* 53 (2005) 5151–5159. <https://doi.org/10.1016/j.actamat.2005.07.035>.

- [198] K. Mech, R. Kowalik, P. Żabiński, Cu thin films deposited by DC magnetron sputtering for contact surfaces on electronic components, *Archives of Metallurgy and Materials*. 56 (2011) 903–908. <https://doi.org/10.2478/v10172-011-0099-4>.
- [199] W. Wang, D. Wu, Q. Zhang, L. Wang, M. Tao, p H -dependence of conduction type in cuprous oxide synthesized from solution, *Journal of Applied Physics*. 107 (2010) 123717. <https://doi.org/10.1063/1.3452383>.
- [200] D.O. Scanlon, G.W. Watson, Undoped n-Type Cu₂O: Fact or Fiction?, *J. Phys. Chem. Lett.* 1 (2010) 2582–2585. <https://doi.org/10.1021/jz100962n>.
- [201] S. Ishizuka, K. Akimoto, Control of the growth orientation and electrical properties of polycrystalline Cu₂O thin films by group-IV elements doping, *Applied Physics Letters*. 85 (2004) 4920–4922. <https://doi.org/10.1063/1.1827352>.
- [202] M. Tibério, T. Calmeiro, S. Nandy, D. Nunes, R. Martins, E. Fortunato, J. Deuermeier, Orientation dependence of electrical properties of polycrystalline Cu₂O thin films, *Semiconductor Science and Technology*. 35 (2020) 075016. <https://doi.org/10.1088/1361-6641/ab883b>.
- [203] D. Wee, G. Parish, B. Nener, Investigation of the accuracy of the spectral photocurrent method for the determination of minority carrier diffusion length, *Journal of Applied Physics*. 111 (2012) 074503. <https://doi.org/10.1063/1.3700246>.
- [204] Q. Gan, F.J. Bartoli, Z.H. Kafafi, Plasmonic-Enhanced Organic Photovoltaics: Breaking the 10% Efficiency Barrier, *Advanced Materials*. 25 (2013) 2385–2396. <https://doi.org/10.1002/adma.201203323>.
- [205] H.A. Atwater, A. Polman, Plasmonics for improved photovoltaic devices, *Nature Mater.* 9 (2010) 205–213. <https://doi.org/10.1038/nmat2629>.
- [206] S.M. Sze, *Semiconductor devices: physics and technology*, John wiley & sons, Inc, New York, 2002.
- [207] G. Tagliabue, J.S. DuChene, A. Habib, R. Sundararaman, H.A. Atwater, Hot-Hole versus Hot-Electron Transport at Cu/GaN Heterojunction Interfaces, *ACS Nano*. 14 (2020) 5788–5797. <https://doi.org/10.1021/acsnano.0c00713>.
- [208] R. Jia, G. Lin, D. Zhao, Q. Zhang, X. Lin, N. Gao, D. Liu, Sandwich-structured Cu₂O photodetectors enhanced by localized surface plasmon resonances, *Applied Surface Science*. 332 (2015) 340–345. <https://doi.org/10.1016/j.apsusc.2015.01.194>.
- [209] T. Bora, M.T.Z. Myint, S.H. Al-Harhi, J. Dutta, Role of surface defects on visible light enabled plasmonic photocatalysis in Au–ZnO nanocatalysts, *RSC Adv.* 5 (2015) 96670–96680. <https://doi.org/10.1039/C5RA16569E>.

- [210] W. Ouyang, F. Teng, M. Jiang, X. Fang, ZnO Film UV Photodetector with Enhanced Performance: Heterojunction with CdMoO₄ Microplates and the Hot Electron Injection Effect of Au Nanoparticles, *Small*. 13 (2017) 1702177. <https://doi.org/10.1002/sml.201702177>.
- [211] Y. Wang, Y. Zhu, H. Gu, X. Wang, Enhanced Performances of n-ZnO Nanowires/p-Si Heterojunctioned Pyroelectric Near-Infrared Photodetectors via the Plasmonic Effect, *ACS Appl. Mater. Interfaces*. 13 (2021) 57750–57758. <https://doi.org/10.1021/acsami.1c14319>.
- [212] N. Patra, M. Manikandan, V. Singh, I.A. Palani, Investigations on LSPR effect of Cu/Al nanostructures on ZnO nanorods towards photodetector applications, *Journal of Luminescence*. 238 (2021) 118331. <https://doi.org/10.1016/j.jlumin.2021.118331>.
- [213] Y. Zheng, L. Zhang, J. Guan, S. Qian, Z. Zhang, C.K. Ngaw, S. Wan, S. Wang, J. Lin, Y. Wang, Controlled Synthesis of Cu⁰/Cu₂O for Efficient Photothermal Catalytic Conversion of CO₂ and H₂O, *ACS Sustainable Chem. Eng.* 9 (2021) 1754–1761. <https://doi.org/10.1021/acssuschemeng.0c07702>.
- [214] I. Barba-Nieto, N. Gómez-Cerezo, A. Kubacka, M. Fernández-García, Oxide-based composites: applications in thermo-photocatalysis, *Catalysis Science & Technology*. 11 (2021) 6904–6930. <https://doi.org/10.1039/D1CY01067K>.
- [215] F. Xu, H.-F. Lv, S.-Y. Wu, H.-P. Ho, Light-activated gas sensing activity of ZnO nanotetrapods enhanced by plasmonic resonant energy from Au nanoparticles, *Sensors and Actuators B: Chemical*. 259 (2018) 709–716. <https://doi.org/10.1016/j.snb.2017.12.128>.
- [216] T. Gries, R. Catrin, S. Migot, F. Soldera, J.-L. Endrino, A.R. Landa-Canovas, F. Cleymand, D. Mangin, F. Mücklich, D. Horwat, Local Modification of the Microstructure and Electrical Properties of Multifunctional Au–YSZ Nanocomposite Thin Films by Laser Interference Patterning, *ACS Applied Materials & Interfaces*. 6 (2014) 13707–13715. <https://doi.org/10.1021/am503160w>.
- [217] T. Minami, Y. Nishi, T. Miyata, J. Nomoto, High-Efficiency Oxide Solar Cells with ZnO/Cu₂O Heterojunction Fabricated on Thermally Oxidized Cu₂O Sheets, *Appl. Phys. Express*. 4 (2011) 062301. <https://doi.org/10.1143/APEX.4.062301>.
- [218] C. Wang, J. Xu, S. Shi, Y. Zhang, Y. Gao, Z. Liu, X. Zhang, L. Li, Optimizing performance of Cu₂O/ZnO nanorods heterojunction based self-powered photodetector with ZnO seed layer, *Journal of Physics and Chemistry of Solids*. 103 (2017) 218–223. <https://doi.org/10.1016/j.jpcs.2016.12.026>.

- [219] J. Xie, C. Guo, C.M. Li, Interface functionalization with polymer self-assembly to boost photovoltage of Cu₂O/ZnO nanowires solar cells, *International Journal of Hydrogen Energy*. 39 (2014) 16227–16233. <https://doi.org/10.1016/j.ijhydene.2014.04.108>.
- [220] K. Cheng, Q. Li, J. Meng, X. Han, Y. Wu, S. Wang, L. Qian, Z. Du, Interface engineering for efficient charge collection in Cu₂O/ZnO heterojunction solar cells with ordered ZnO cavity-like nanopatterns, *Solar Energy Materials and Solar Cells*. 116 (2013) 120–125. <https://doi.org/10.1016/j.solmat.2013.04.021>.
- [221] M.H. Tran, J.Y. Cho, S. Sinha, M.G. Gang, J. Heo, Cu₂O/ZnO heterojunction thin-film solar cells: the effect of electrodeposition condition and thickness of Cu₂O, *Thin Solid Films*. 661 (2018) 132–136. <https://doi.org/10.1016/j.tsf.2018.07.023>.
- [222] Y. Zhang, P. Zhang, S. Feng, J. Cao, J. Wang, Y. Zheng, L. Shi, C. Li, J. Pan, Transparent p–n Junction in Cu₂O/ZnS/ZnO Core–Shell Nanoarrays via In Situ Sulfuration for Enhanced Photovoltaic Stability, *ACS Appl. Nano Mater.* (2023). <https://doi.org/10.1021/acsnm.3c01653>.
- [223] S. Noda, H. Shima, H. Akinaga, Cu₂O/ZnO Heterojunction Solar Cells Fabricated by Magnetron-Sputter Deposition Method Films Using Sintered Ceramics Targets, *J. Phys.: Conf. Ser.* 433 (2013) 012027. <https://doi.org/10.1088/1742-6596/433/1/012027>.
- [224] R. Kumar, K. Bergum, H.N. Riise, E. Monakhov, A. Galeckas, B.G. Svensson, Impact of post annealing and hydrogen implantation on functional properties of Cu₂O thin films for photovoltaic applications, *Journal of Alloys and Compounds*. 825 (2020) 153982. <https://doi.org/10.1016/j.jallcom.2020.153982>.
- [225] P.L. Khoo, Y. Kikkawa, K. Satou, T. Shinagawa, M. Izaki, Improvements in external quantum efficiency of electrochemically constructed n-ZnO/p-Cu₂O photovoltaic devices by rapid thermal annealing, *Thin Solid Films*. 653 (2018) 158–164. <https://doi.org/10.1016/j.tsf.2018.03.026>.
- [226] J.H. Hsieh, P.W. Kuo, K.C. Peng, S.J. Liu, J.D. Hsueh, S.C. Chang, Opto-electronic properties of sputter-deposited Cu₂O films treated with rapid thermal annealing, *Thin Solid Films*. 516 (2008) 5449–5453. <https://doi.org/10.1016/j.tsf.2007.07.097>.
- [227] S. Raheman AR, B.M. Momin, H.M. Wilson, U.S. Annapure, N. Jha, Optimal fabrication of 0D/1D Cu₂O quantum dots sensitized CdS nanorods heterojunction: Efficient photoredox catalyst for H₂ generation under visible light irradiation, *Journal of Alloys and Compounds*. 835 (2020) 155262. <https://doi.org/10.1016/j.jallcom.2020.155262>.

- [228] Y. Lou, Y. Zhang, L. Cheng, J. Chen, Y. Zhao, A Stable Plasmonic Cu@Cu₂O/ZnO Heterojunction for Enhanced Photocatalytic Hydrogen Generation, *ChemSusChem*. 11 (2018) 1505–1511. <https://doi.org/10.1002/cssc.201800249>.
- [229] R. Borah, S.W. Verbruggen, Effect of size distribution, skewness and roughness on the optical properties of colloidal plasmonic nanoparticles, *Colloids and Surfaces A: Physicochemical and Engineering Aspects*. 640 (2022) 128521. <https://doi.org/10.1016/j.colsurfa.2022.128521>.
- [230] J. Chen, C. Li, D.W. Zhao, W. Lei, Y. Zhang, M.T. Cole, D.P. Chu, B.P. Wang, Y.P. Cui, X.W. Sun, W.I. Milne, A quantum dot sensitized solar cell based on vertically aligned carbon nanotube templated ZnO arrays, *Electrochemistry Communications*. 12 (2010) 1432–1435. <https://doi.org/10.1016/j.elecom.2010.08.001>.
- [231] A. Guerrero, N. F. Montcada, J. Ajuria, I. Etxebarria, R. Pacios, G. Garcia-Belmonte, E. Palomares, Charge carrier transport and contact selectivity limit the operation of PTB7-based organic solar cells of varying active layer thickness, *Journal of Materials Chemistry A*. 1 (2013) 12345–12354. <https://doi.org/10.1039/C3TA12358H>.
- [232] D. Pitarch-Tena, T.T. Ngo, M. Vallés-Pelarda, T. Pauporté, I. Mora-Seró, Impedance Spectroscopy Measurements in Perovskite Solar Cells: Device Stability and Noise Reduction, *ACS Energy Lett.* 3 (2018) 1044–1048. <https://doi.org/10.1021/acsenergylett.8b00465>.
- [233] T.-F. Zhang, X.-G. Tang, Q.-X. Liu, S.-G. Lu, Y.-P. Jiang, X.-X. Huang, Q.-F. Zhou, Oxygen-vacancy-related relaxation and conduction behavior in (Pb_{1-x}Ba_x)(Zr_{0.95}Ti_{0.05})O₃ ceramics, *AIP Advances*. 4 (2014) 107141. <https://doi.org/10.1063/1.4900610>.
- [234] L. Nkhaili, A. Narjis, A. Outzourhit, A. El Kissani, R. El Moznine, Investigation of the Optical and Electrical Properties of ITO/ZnO/CdS/CuO:Co/Ag Structure for Solar Cell, *Advances in Materials Science and Engineering*. 2020 (2020) e3907203. <https://doi.org/10.1155/2020/3907203>.
- [235] R. Tan, Z. Wei, J. Liang, Z. Lv, B. Chen, J. Qu, W. Yan, J. Ma, Enhanced open-circuit photovoltage and charge collection realized in pearl-like NiO/CuO composite nanowires based p-type dye sensitized solar cells, *Materials Research Bulletin*. 116 (2019) 131–136. <https://doi.org/10.1016/j.materresbull.2019.04.025>.
- [236] E.D. Palik, *Handbook of Optical Constants of Solids*, Academic Press, 1998.
- [237] A. Ziashahabi, T. Ghodselahi, Localized Surface Plasmon Resonance properties of copper nano-clusters: A theoretical study of size dependence, *Journal of Physics and Chemistry of Solids*. 74 (2013) 929–933. <https://doi.org/10.1016/j.jpics.2013.02.009>.




- [238] Ü. Özgür, Y.I. Alivov, C. Liu, A. Teke, M.A. Reshchikov, S. Doğan, V. Avrutin, S.-J. Cho, and H. Morkoç, A comprehensive review of ZnO materials and devices, *Journal of Applied Physics*. 98 (2005). <https://doi-org.bases-doc.univ-lorraine.fr/10.1063/1.1992666>.
- [239] A. Niv, Z.R. Abrams, M. Gharghi, C. Gladden, X. Zhang, Overcoming the bandgap limitation on solar cell materials, *Applied Physics Letters*. 100 (2012) 083901. <https://doi.org/10.1063/1.3682101>.
- [240] M.A. Green, Third generation photovoltaics: ultra-high efficiency at low cost, Springer-Verlag. 25 (2003) 241–256. <https://doi.org/10.1002/pip.360>.
- [241] J. Edmundo Mastache Mastache, R. López, E. Viguera Santiago, O. Soriano Vargas, Platinum (Pt), gold (Au), and silver (Ag) ohmic contacts to cupric oxide (CuO) films deposited by air-based sputtering and thermal annealing, *Results in Physics*. 46 (2023) 106292. <https://doi.org/10.1016/j.rinp.2023.106292>.
- [242] A. Kahn, Fermi level, work function and vacuum level, *Materials Horizons*. 3 (2016) 7–10. <https://doi.org/10.1039/C5MH00160A>.







Yerila RODRÍGUEZ-MARTÍNEZ

M.Sc. Materials Science - Ph.D candidate

CONTACT

 Yerila Rodriguez Martínez
 Cuban
 13/04/1992
 yerih@gmail.com

NETWORKS

 Y. Rodriguez-Martínez
 Yerila Rodríguez Martínez
 Yerila Rodríguez Martínez
 0000-0001-5314-0101

LANGUAGES

English Fluent
Spanish First language
French Beginner

UPDATED

 September 2023

EDUCATION

Ph. D. - Materials Science / Physics

Sept 2020 - Present

Université de Lorraine - Nancy (France) / UH - Havana (Cuba)

Dissertation: Cu nanoparticles inclusion in ZnO and Cu₂O matrices for enhanced photoconversion of all-oxide optoelectronics.

M. Sc. - Physics

2017 - 2018

UH - Havana (Cuba)

Dissertation: Inorganic core-shell structures for emerging solar cells.

B. Eng. - Physics

2010 - 2015

UH - Havana (Cuba)

Dissertation: Development of a temperature control system for a Mettler TG50 thermobalance.

WORK EXPERIENCE

Associate Researcher

2022 - Present

UH - Havana (Cuba)

Photovoltaics Research Laboratory, Institute of Materials Science and Technology (IMRE)

Young Researcher

2018 - 2022

UH - Havana (Cuba)

Photovoltaics Research Laboratory, Institute of Materials Science and Technology (IMRE)

Researcher in Training

2011 - 2015

UH - Havana (Cuba)

Photovoltaics Research Laboratory, Institute of Materials Science and Technology (IMRE)

INTERNATIONAL EXPERIENCE

- **2023**, Institut Jean Lamour, Université de Lorraine, Nancy, France, 6 months (in progress).
- **2022**, Institut Jean Lamour, Université de Lorraine, Nancy, France, 6 months.
- **2021**, Institut Jean Lamour, Université de Lorraine, Nancy, France, 7 months.
- **2019**, Institut Jean Lamour, Université de Lorraine, Nancy, France, 2 months.
- **2017**, Humboldt University of Berlin, Institute of Physics and IRIS Adlershof, Berlin, Germany, 3 months.

PUBLICATIONS

One-step formation of plasmonic Cu nanodomains in p-type Cu₂O matrix films for enhanced photoconversion of n-ZnO/p-Cu₂O heterojunctions.

2022

ACS Applied Electronic Materials, 4(11), 5527-5537

Y. Rodríguez-Martínez, L. Vaillant-Roca, J. Ghanbaja, S. Migot, Y. Battie, S. Ould Saad Hamady, D. Horwat

In-situ pulsed laser induced growth of CdS nanoparticles on ZnO nanorods surfaces.

2020

Materials Research Bulletin, 125, 110790

Y. Rodríguez-Martínez, J. Alba-Cabañas, O. Cruzata, S. Bianco, E. Tresso, F. Rossi, L. Vaillant-Roca

Impact of solvent exposure on the structure and electronic properties of CH₃NH₃PbI(3-x)Cl_x mixed halide perovskite films.

2019

Applied Physics A, 125(7), 470

Ralairisoa, M., Rodríguez, Y., Salzmann, I., Vaillant, L., and Koch, N.

Laser activation to grow ZnO nanostructures.

2018

Revista Cubana de Física, 35(1E), E21-E23

Y. Rodríguez-Martínez, J. A. Alba-Cabañas, O. Cruzata-Montero and L. Vaillant-Roca

New Design Concepts for Inorganic Solar Cells: From Thin Films to Functional Nanostructures: Using a pulsed laser for in-situ growth of semiconductor core-shell nanostructures.

2017

IEEE Proceedings of Photonics North (PN)

Lidice Vaillant Roca, Yerila Rodríguez-Martínez, Jesús Antonio Alba Cabañas, and Osmel Cruzata Montero,

AWARDS

IOP Best poster presented by a Young Researcher.

2020

Physics Faculty, UH, Havana (Cuba)

SCHOLARSHIPS

Funding granted for research mobility to France.

2023

APS-EPS-ICTP Travel Award Fellowship Programme (ATAP)

Hosted by: Institut Jean Lamour, University of Lorraine, Nancy, France

Funding granted for doctoral formation in France.

2022 - 2023

Campus France

Hosted by: Institut Jean Lamour, University of Lorraine, Nancy, France

Funding granted for research mobility to France.

2019 - 2021

Service de Coopération et d'Action Culturelle (SCAC) of the French Embassy in Cuba

Hosted by: Institut Jean Lamour, University of Lorraine, Nancy, France

WORKSHOPS & CONFERENCES

| | |
|--|-----------|
| PLATHINIUM'23 - Plasma Thin Film International Union Meeting Antipolis Convention Centre, Antibes, Francia | Sept 2023 |
| Cuban-Canadian Workshop on Clean Energy Materials and Technologies IMRE - UH, Havana, Cuba. | Feb 2023 |
| Journées des doctorants du département CP2S Université de Lorraine, Nancy, France. | Jun 2022 |
| Séminaire scientifique 2022 de l'école doctorale C2MP Université de Lorraine, Nancy, France. | Jun 2022 |
| Jornada Científica y Fórum de Ciencia y Técnica IMRE - UH, Havana, Cuba. | Jun 2022 |
| LatinXChem Twitter Conference 2021 IMRE - UH, Havana, Cuba. | Sep 2021 |
| XV Symposium of the Cuban Physical Society UH, Havana, Cuba. | Mar 2020 |
| II Cuban Physics Meeting for Graduate Students ICIMAF, Havana, Cuba. | Jan 2020 |
| Scientific Conference and Forum on Science and Technology IMRE - UH, Havana, Cuba. | Jun 2019 |
| Scientific Conference and Forum on Science and Technology IMRE - UH, Havana, Cuba. | Jun 2018 |
| First Nanosciences Workshop / International Science, Technology and Innovation Convention 2018 Havana, Cuba. | Mar 2018 |
| I Cuban Physics Meeting for Graduate Students UH, Havana, Cuba. | Jan 2018 |
| VII International Workshop Cuba-Fotovoltaica Palacio de las Convenciones, Havana, Cuba. | Dec 2017 |

Inclusion de nanoparticules de Cu plasmoniques dans des matrices de ZnO et de Cu₂O pour améliorer la photoconversion de l'optoélectronique tous oxydes.

Résumé : Dans ce travail, nous présentons dans une première partie les résultats de la croissance in situ de nanoparticules (NPs) plasmoniques de cuivre (Cu) dans une matrice de p-Cu₂O en utilisant la pulvérisation cathodique magnétron réactive d'une cible de Cu et en ajustant le débit d'oxygène. Il a été possible d'observer, dans des conditions pauvres en oxygène, la formation de films composites CuNPs-Cu₂O présentant la signature du phénomène de résonance plasmon de surface localisée (LSPR). Les dispositifs basés sur les nanocomposites étudiés interfacés avec de l'oxyde de zinc (ZnO) ont été caractérisés par des mesures J-V et des mesures spectrales de photocourant, montrant une augmentation de la densité de photocourant sous illumination optique comme conséquence de l'incorporation des particules plasmoniques et de l'injection conséquente de porteurs chauds. La deuxième partie du manuscrit présente les résultats du recuit thermique rapide (RTA) des films composites CuNPs-Cu₂O dans des conditions pauvres en oxygène et l'évolution de leurs propriétés lorsque la température augmente. Après un recuit à une température de recuit supérieure à 150 °C, il a été possible de constater une ségrégation du cuivre vers la surface, une augmentation de l'orientation cristalline préférentielle du Cu₂O et une amélioration du signal LSPR. La réponse électrique des dispositifs constitués des composites interfacés avec ZnO puis recuits à 200 °C a montré une augmentation supplémentaire du photocourant en raison de la LSPR des nanoparticules de Cu à la surface des dispositifs. Enfin, la synthèse de nanoparticules de Cu par une source d'agrégation de gaz (GAS) et la fabrication ultérieure de structures multicouches ZnO-CuNPs avec une réponse plasmonique ont été étudiées. Le composite obtenu a révélé une réponse LSPR et la présence de particules de Cu agissant comme points de nucléation pour des grains coniques de ZnO hautement orientés.

Mots-clés : *nanoparticules de cuivre, oxyde de cuivre, résonance plasmonique de surface localisée, pulvérisation magnétron réactive, porteurs chauds, photoconversion.*

Plasmonic Cu nanoparticles inclusion in ZnO and Cu₂O matrices for enhanced photoconversion of all-oxide optoelectronics

Abstract: In this work we present the results on in-situ growth of plasmonic copper (Cu) nanoparticles (NPs) into a p-Cu₂O matrix by using reactive magnetron sputtering of a Cu target and adjusting the oxygen flowrate. It was possible to observe, for oxygen-poor conditions, the formation of CuNPs-Cu₂O composites presenting the signature of the localized surface plasmon resonance (LSPR) phenomenon. Devices based on the studied nanocomposites interfaced with zinc oxide (ZnO) were characterized by J-V and spectral photocurrent measurements, showing a photocurrent density increase under optical illumination as a result of the plasmonic particles incorporation and consequent hot carriers injection. In the second part of the manuscript, the results about the rapid thermal annealing (RTA) of the CuNPs-Cu₂O composites under oxygen-poor conditions and their properties evolution when temperature increases are presented. At temperature higher than 150 °C it was possible to see a copper segregation towards the surface, increase in the crystal preferential orientation of Cu₂O and improvement of the LSPR signal. Electrical response of devices constituted by the composite layers interfaced with ZnO and annealed at 200 °C showed a further increase in the photocurrent resulting from the LSPR of Cu NPs at the devices surface. Finally, the synthesis of Cu nanoparticles through a gas aggregation source (GAS) and the subsequent fabrication of ZnO-CuNPs multilayer structure with plasmonic response were studied. The resulted composite revealed LSPR response and the presence of Cu particles acting as nucleation points for highly oriented ZnO conical grains.

Keywords: *copper nanoparticles, copper oxide, localized surface plasmon resonance, reactive magnetron sputtering, hot carriers, photoconversion.*